ABSTRACT

Title of Document:	FATIGUE CRACK MONITORING WITH COUPLED PIEZOELECTRIC FILM ACOUSTIC EMISSION SENSORS
	Changjiang Zhou, Doctor of Philosophy, 2013
Directed By:	Associate Professor Yunfeng Zhang Civil and Environmental Engineering

Fatigue-induced cracking is a commonly seen problem in civil infrastructures reaching their original design life. A number of high-profile accidents have been reported in the past that involved fatigue damage in structures. Such incidences often happen without prior warnings due to lack of proper crack monitoring technique. In order to detect and monitor the fatigue crack, acoustic emission (AE) technique, has been receiving growing interests recently. AE can provide continuous and real-time monitoring data on damage progression in structures. Piezoelectric film AE sensor measures stress-wave induced strain in ultrasonic frequency range and its feasibility for AE signal monitoring has been demonstrated recently. However, extensive work in AE monitoring system development based on piezoelectric film AE sensor and sensor characterization on full-scale structures with fatigue cracks, have not been done. A lack of theoretical formulations for understanding the AE signals also hinders the use of piezoelectric film AE sensors. Additionally, crack detection and source

localization with AE signals is a very important area yet to be explored for this new type of AE sensor.

This dissertation presents the results of both analytical and experimental study on the signal characteristics of surface stress-wave induced AE strain signals measured by piezoelectric film AE sensors in near-field and an AE source localization method based on sensor couple theory. Based on moment tensor theory, generalized expression for AE strain signal is formulated. A special case involving the response of piezoelectric film AE sensor to surface load is also studied, which could potentially be used for sensor calibration of this type of sensor.

A new concept of sensor couple theory based AE source localization technique is proposed and validated with both simulated and experimental data from fatigue test and field monitoring. Two series of fatigue tests were conducted to perform fatigue crack monitoring on large-scale steel test specimens using piezoelectric film AE sensors. Continuous monitoring of fatigue crack growth in steel structures is demonstrated in these fatigue test specimens. The use of piezoelectric film AE sensor for field monitoring of existing fatigue crack is also demonstrated in a real steel I-girder bridge located in Maryland. The sensor couple theory based AE source localization is validated using a limited number of piezoelectric film AE sensor data from both fatigue test specimens and field monitoring bridge. Through both laboratory fatigue test and field monitoring of steel structures with active fatigue cracks, the signal characteristics of piezoelectric film AE sensor have been studied in real-world environment.

FATIGUE CRACK MONITORING WITH COUPLED PIEZOELECTRIC FILM ACOUSTIC EMISSION SENSORS

By

Changjiang Zhou

Dissertation submitted to the Faculty of the Graduate School of the
University of Maryland, College Park, in partial fulfillment
of the requirements for the degree of
Doctor of Philosophy
2013

Advisory Committee:
Associate Professor Yunfeng Zhang, Chair/Advisor
Professor Amde M. Amde
Professor Bilal M. Ayyub
Research Professor Chung C. Fu
Professor Sung W. Lee

Acknowledgements

The research work in this dissertation was partially supported by National Science Foundation under Award No. CMMI-1031304 (Program Director: Dr. M.P. Singh) and US Department of Transportation's RITA Program (Grant No. RITARS11HUMD; Program Director: Caesar Singh). Additional financial supports from the University of Maryland and Minta Martin Aerospace Fund are also gratefully acknowledged.

I am very grateful to my thesis supervisor Yunfeng Zhang, for his five years of support and guidance. It was my fortune to be able to work with him. I learned a lot from him, from both academic and non-academic aspects. I also thank him for numerous comments and suggestions on the thesis. My gratitude also goes to the dissertation committee members: Dr. Chung C. Fu, Dr. Amde M. Amde, Dr. Bilal M. Ayyub and Dr. Sung W. Lee.

I would like to thank Maryland State Highway Administration for their assistance and arrangement in the field test. The technique help of Dr. Y. Edward Zhou from URS Corporation is also appreciated. Special thanks goes to Dr. Hoon Sohn and his students at KAIST for their help of the field test in South Korea. This is a memorable trip and I really enjoyed my time there. I also thank Dr. Lane Johnson at UC Berkeley for sharing with me his Fortran code and I'm grateful to his quick response to my questions.

I always enjoyed working here and would like to thank my colleagues, Zhen Li, Linjia Bai, Timothy K. Saad, Noah C. Blum. Discussion with them on both scientific problems and daily life has always been enlightening and fun. I also thank

my friends at University of Maryland. We share so many memories and so many wonderful stories of our youth.

For my girlfriend, Shuo, an astrophysicist, thank you for your sweat love all these years. The days when we are in different cities perusing Ph.D. degrees are finally going to an end.

Last but most important, I thank my parents and my sister, Guangwen Zhou, Xingqun Hu and Xiaohua Zhou. They have always been encouraging, supportive and understanding. This thesis is dedicated to my family.

Table of Contents

List of Tables

List of Figures

Nomenclature

In summary, following notation is used in this dissertation:

α = P wave speed

β = Shear wave speed

c = Rayleigh wave speed

ω = Angular frequency

ε = Strain

k = Wave number

a = Radius of the sensor

d = Clear spacing of sensing dots in the sensor couple

J_1 = First order Bessel function of the first kind

f_s = Trough frequency caused by space phase shift effect.

f_a = Trough frequency caused by aperture effect.

μ = Shear modulus

r = Distance from AE source to sensor

R_1 , R_2 , R_3 = Roots of the Raleigh cubic

T_r = Rise time

$S(t)$ =Source function

μ = Shear modulus

C_{pqij} = Elastic constants

ΔV = Crack volume

n = Crack normal

l = Crack motion vector

G = Green's function

g_{ij} = Component of Green's function

M = Moment tensor

λ = Lamé's first parameter

$\mathbf{u}$ = Displacement vector

$\mathbf{f}$ = Body force

∇ = Del operator

ρ = Density of a material

H = Heaviside step function

ν = Poisson's ratio

D_i = Electric displacement

[d] = The piezoelectric constant matrix

q = Electric charge

E_i = Electric field

R_f = Resistance of the feedback loop of the amplifier

C_f = Capacity of the feedback loop of the amplifier

Chapter 1: Introduction

1.1 Research Motivation

Fatigue-induced cracking is a commonly seen problem in civil infrastructures reaching their original design life, e.g. highway bridges, traffic signal pole, etc. These aged structures have experienced a large number of stress cycles. A number of cases have been reported recently that involve fatigue damages. For example, in September 2009, fatigue induced cracks were found unexpectedly in the eye-bars of the existing San Francisco Bay Bridge and in October 2009 further cracking led to the falling of 5000 pounds of steel parts to the roadway during rush hour and the traffic was stopped. Such incidences happen frequently without prior warnings due to lack of proper crack monitoring and localization technique.

There are a few nondestructive evaluation (NDE) techniques available for fatigue crack detection, such as eddy current, magnetic particle inspection, radiography, thermography, acoustic emission (AE) and ultrasonic testing. In particular, AE techniques have been receiving growing popularity in use for fatigue crack monitoring, especially on bridges (e.g., Holford *et al.*, 2001; Kosnik, 2009; McKeefry and Shield, 1999). AE is the elastic wave generated by sudden energy releases within a material. As AE sensor passively listens to the signals, it can provide real-time information on damage progression in a structure. This is different from ultrasonic test, which excites elastic stress waves into a solid to be received by ultrasonic probes.

There are a variety of types of AE sensors based on distinct operation or sensing principles. The conventional AE sensor measures the dynamic out-of-plane displacement based on second order dynamic oscillator principle. This type of AE sensors usually has a high sensitivity but relatively narrow band (i.e., resonant transducer). However, broadband AE transducer is also available with conical piezoelectric sensing element. A representative broadband AE sensor is the one developed by Proctor (1982). This broadband AE sensor exhibits a broad bandwidth up to 1 MHz. However, this type of sensor is usually very expensive (several hundred dollars) due to its complex design and fabrication process, which limits its massive application in practice.

Another type of piezoelectric AE sensors attracts growing interests recently is piezoelectric film AE sensor. Piezoelectric film AE sensor measures in-plane strain induced by surface stress waves. Therefore, it is a zero order sensor unlike the 2nd-order conventional AE sensor that measures displacement. The piezoelectric film AE sensor can have adjustable properties, which is achieved by using different sensing materials. For example, using PZT-5A as the sensing element material would provide a high sensitivity comparable to the conventional AE sensors, while using flexible piezoelectric paint would enable the sensor conform to curved surface of structures and yield a flat frequency response over a broad frequency bandwidth. Piezoelectric paint's ability of acoustic emission signal sensing has been verified by many researchers, including Egusa and Iwasawa (1998), Wenger *et al*. (1996, 1999a, 1999b), Sakamoto *et al*. (2001), Zhang and Li (2006), Li and Zhang (2008). However, extensive work in AE monitoring system development based on

piezoelectric film AE sensor and sensor characterization on full-scale structures with fatigue cracks, have not be reported. A lack of theoretical formulations for understanding the AE signals also hinders the use of piezoelectric film AE sensors. Successful application of piezoelectric film AE sensor in practice also requires long-term field test of piezoelectric film AE sensor so that its field monitoring issues and durability can be examined and potential problems can be fixed. Additionally, crack detection and source localization with AE signals is a very important area yet to be explored for this new type of AE sensor.

1.2 Research Objective

The primary goal of this research is to study the signal characteristics of surface stress-wave induced AE strain signals measured by piezoelectric film AE sensors in near-field both analytically and experimentally as well as develop an AE source localization method based on sensor couple theory. By doing so, the technology of using piezoelectric film AE sensor for fatigue crack monitoring can be further advanced. The following specific objectives are defined to accomplish the main goal:

(1) To establish theoretical formulas for characterizing AE-induced strain signals measured by piezoelectric film AE sensors; moment tensor theory will be used in the formulation.

(2) To theoretically derive the Green's function for AE-induced strain signals using elastodynamic solution approach. The derived Green's function will be verified with experimental data collected by piezoelectric film AE sensor under surface load.

(3) To develop an AE monitoring system that includes piezoelectric film AE sensors, preamplifier, high-speed data acquisition hardware, and software programs for user interface and data recording.

(4) To experimentally characterize and verify the AE sensing performance of piezoelectric film AE sensor in both laboratory test and field test of steel structures with active fatigue cracks.

(5) To develop a AE source localization method based on sensor couple theory and experimentally validate this method using AE data from piezoelectric film AE sensors installed on fatigue test specimens and field test bridge.

1.3 Organization of Dissertation

This dissertation consists of eight chapters, including the research motivation presented in this chapter and the conclusions and future work summarized in Chapter 8. The remaining chapters are organized as follows,

- Chapter 2 offers a review of acoustic emission technique for crack monitoring. AE signal analysis methods are presented including waveform-based methods and feature-based methods.
- Chapter 3 provides a background view of piezoelectric film AE sensor development. The ultrasonic sensing principle of piezoelectric film AE sensor is briefly described. The material properties of piezoelectric materials commonly used for piezoelectric film AE sensor are examined. Other aspects of the piezoelectric film AE sensor such as signal conditioning circuit (preamplifier and filter), frequency bandwidth and sensor configuration are also studied.

- Chapter 4 conducts an analytical study of near-field AE strain signals. Based on moment tensor theory, generalized expression for AE strain signal is formulated. The Green's function for expressing AE strain signals in half space is also derived using elastodynamic solution approach. A special case involving the response of piezoelectric film AE sensor to surface load is also studied, which could potentially be used for sensor calibration of this type of sensors.
- Chapter 5 proposes a new concept of sensor couple theory based AE source localization technique, which is based on the space phase shift of the AE signals between two identical AE sensors spaced apart. Parametric studies are performed to evaluate the proposed AE source localization method and experimental tests were conducted to validate the method.
- Chapter 6 presents two laboratory tests of fatigue crack monitoring using piezoelectric film AE sensors. Continuous monitoring of fatigue crack growth in steel structures is demonstrated. The AE source localization method using coupled piezoelectric film strain sensors are also validated using the lab test data.
- Chapter 7 demonstrates the use of piezoelectric film AE sensor for field monitoring of existing fatigue crack in a real steel I-girder bridge located in Maryland. A variety of AE features of the acquired field test data are calculated and analyzed. The sensor couple theory based AE source localization is validated again using a limited number of piezoelectric film AE sensor data.

Chapter 2: Acoustic Emission (AE) Sensor and Signal Analysis

2.1 AE Technology for Crack Monitoring

Acoustic emission (AE), as defined by the Acoustic Emission Working Group (Spanner, 1974), is "*the transient stress wave generated by the rapid release of energy from localized sources within a material*". The studies on AE were first documented in the 1950s. Through a series of tensile tests of conventional engineering materials, Kaiser studied the acoustic processes, including frequency levels and its relationship with the stress-strain curve (Miller, 1987). Nowadays, AE technology has been applied to a variety of engineering areas, from bridge to oil pipeline monitoring, from heavy engine to aircraft body. It can be used for nondestructive evaluation (NDE) of materials, real-time monitoring of structures and failure analysis of systems. It has been proved to be a useful NDE technique. Different from ultrasonic test, which excites elastic waves into a solid, AE sensor passively listens to the stress-wave signals emitted from the structure, typically at locations with structural defects or damage such as crack. If measured properly, the AE signals contain the source information. As a lot of AE sources are damage related, the recorded AE signals would reveal the flaw information of the structure after signal analysis. Thus, it could be used for damage detection, which has also been demonstrated in structural members made of various materials, such as fiber-reinforced polymer (FRP) and metallic materials (Grosse and Ohtsu, 2008; Vahaviolos, 1999).

Fatigue crack monitoring is a common type of damage assessment problem encountered in civil infrastructures. Many structures including pressurized storage

tanks, pipelines, rocks, concrete, bridges, traffic signal poles and other cyclically loaded structures, would potentially have fatigue cracking and fracturing issues. These cracking processes, if undetected, can grow and disrupt service, even cause catastrophic failures (see, e.g., NTSB 1989). Such incidences happen frequently without early warnings due to lack of proper crack monitoring technique. Because of the real-time monitoring ability of AE sensor technology, AE monitoring may provide early warning signs for those fractures. For large structures, such as bridges, conventional inspection process for fatigue cracks requires extensive labor and is thus time-consuming and not cost-effective. With the development of AE technology, which has a high sensitivity and can be implemented for continuous monitoring, automatic data recording and analysis for early warning before catastrophic failure is likely to be achievable.

Experimental study of fatigue crack monitoring with AE technology has been conducted by researchers. Ono and Ohtsu proposed a generalized theory of acoustic emission and Green's function for signal analysis (Ono and Ohtsu, 1984). Their work gives a generalized expression for synthesizing AE signals based on the moment tensor theory. Good agreement between the measured AE signals and the simulated AE signals due to crack source have been observed in a fatigue test (Ono and Ohtsu, 1984; Yuyama *et al.*, 1988).

By implementing inverse analysis of the AE signal, characteristics of the AE source could be determined, including the crack mode, crack orientation and source location (Grosse and Ohtsu, 2008). These waveform based AE signal analysis usually requires the AE sensor have high fidelity (i.e., broadband) when recording the AE

data. This implies that broadband AE sensors with non-resonance over operating frequency range are favorable to this analysis. However this type of broadband AE sensor usually requires high precision in fabrication and technique for enhancing its sensitivity; therefore, they are expensive than other resonance-type AE sensors which prevent their wide application.

In order to make the AE application cost-effective, resonance-type AE sensors or narrow-band AE sensors might be used alternatively. Near field AE monitoring strategy with lower-sensitivity broadband AE sensor such as piezoelectric paint has been proposed by researchers recently (Zhou and Zhang, 2012).The near-field AE monitoring strategy is intended to make AE sensor focus on the local area near the sensor. Because of the relatively small monitoring area, AE signals measured by low-sensitivity broadband sensor are still strong enough to be used for inverse waveform analysis which is simplified by short wave travel path. However due to its sensitivity, some AE events with very low energy release might still be missed.

An alternative way of performing AE monitoring is to use resonance-type AE sensors and statistical AE feature values derived from such narrowband AE sensors can be calculated and correlated with fatigue crack growth characteristics. Good correlation of the fatigue crack growth rate and statistical AE feature values (such as AE counts and counts rate) were observed in relatively simple fatigue test specimens by Roberts and Talebzadeh (2003a, 2003b). The stress intensity factor and the whole fatigue life could also be studied based on the AE data (Yu *et al*., 2011; Yu and Ziehl, 2012; Han *et al*., 2011).

2.2 AE Signal Analysis

In general, AE signal analysis methods can be divided into two main categories : the parameter-based method and the signal waveform-based method (Grosse *et al.*, 2003). As described in the previous section, both methods are applied in practice.

2.2.1 Waveform-based Method

Comprehensive AE source information could be derived with the waveform-based method. Broadband AE sensor has to be used for AE data collection before waveform based method can be applied. Since AE signal is recorded without much distortion, waveform-based method generates more accurate results for many applications, for example, AE source localization. The main advantage of the waveform-based method is the ability to do inverse analysis. If the Green's function for wave propagation and the transfer function of the AE sensor are available, the AE source characteristics could be solved inversely. For example, the crack mode (tension or shear) and orientation are of particular interest for AE source study. By using the inverse analysis methods, such source features can be solved from the recorded AE signals (Grosse *et al.*, 2003). Common inverse analysis methods include 3-D source localization along with fault plane solution technique and moment tensor inversion (Dahlen and Tromp, 1998). Among the inverse analysis methods, moment tensor inversion is the most popular and have been studied by many researchers (Dahm, 1993; Grosse, 1996; Weiler, 2000).

2.2.2 AE Parameter-based Method

AE parameter-based signal analysis processes the data from a statistical perspective. It's also called *classical method*. Some pre-defined parameters or features are used to describe the whole signal. This type of method tries to correlate the AE parameters or features with the known physical parameters of the AE source. For example, researchers are trying to correlate the AE counts with the fatigue crack length (or fatigue life) in metallic structures (Roberts and Talebzadeh, 2003a and 2003b; Talebzadeh and Roberts, 2001; Yu *et al*., 2011) or to correlate the RA value with the fracture mode of the AE source.

In general, AE features can be potentially related with one or more physical quantities. Some of them are related based on physical mechanism while others are solely based on empirical relationship regressed with measured data. Commonly used AE features include: rise time, counts rate, b value, energy, RA value and so on. In civil engineering, AE signals from reinforced concrete or steel structure subjected to cracking are of great interest. In these areas, RA value, b value (improved b value), AE counts rate and energy have been more popular for AE feature analysis. The following subsections give a brief review of the afore-mentioned AE features.

2.2.2.1 AE Counts and Hits Rate

AE counts rate is defined as the derivative of AE counts with respect to time, often in load cycles for fatigue test data. AE counts refer to be the number of times the AE signal amplitude exceeds a given threshold value, as shown in Figure 2.1. It is found that the AE counts rate versus load cycles follows a power law that is analogous to the Paris-Erdogan law for fatigue crack growth modeling (Talebzadeh and Roberts, 2001). Thus, the AE counts rate may have an inherent connection with the fatigue

crack growth rate and could be potentially used for describing fatigue crack growth. Good relationship has been observed between the AE counts rate and crack growth rate in fatigue test of simple steel specimens (Berkovits and Fang, 1995; Roberts and Talebzadeh, 2003a) and has been applied for fatigue life prediction (Roberts and Talebzadeh, 2003b). Besides AE counts rate, cumulative AE counts are also used to study fatigue crack propagation (Yu and Ziehl, 2012; Yu *et al*., 2011).

In addition to AE counts, AE hits is also a popular AE feature for damage quantification (Shi *et al*., 2000). Different from the AE counts, AE hits is the number of AE events acquired during the test and the user needs to define the time interval to separate two AE events. Thus, it is more closely related to the occurrence frequency of AE activity in comparison with AE counts.

2.2.2.2 RA Value

RA value is defined as the rise time (the time between the signal first crossing the threshold value and the peak amplitude arrival) divided by the peak amplitude of the signal (JCMS-IIIB5706, 2003). It is another important AE feature in parameter based AE signal analysis method. It is also known as the reciprocal of gradient in AE waveforms (for rock materials, Shiotani *et al*., 2001). Researchers believe that RA value is a very good index for classifying the fracture type and identify failure modes of the AE events. For example, it's found that higher RA value is more related to shear type crack (Anastassopoulos and Philippidis, 1995; Shiotani *et al*., 2001), which might be able to indicate the damage condition in structures. Some successfully demonstrated applications of this AE feature include compressive failure in concrete with recycled aggregate (Watanabe *et al.*, 2007), corrosion process in reinforced concrete (Ohtsu and Tomoda, 2008), cracking of steel fibre reinforced concrete under

bending (Soulioti *et al.*, 2009), degradation of cross ply fiber reinforced composites (Aggelis *et al.*, 2010), etc. According to the definition of RA value, only two points are needed for calculation although the whole AE signal record might be needed to identify these two points.

2.2.2.3 b Value

b value is another important index in analyzing AE signals. *b* value is originally from seismology field and is used to imply the amplitude distribution of earthquakes within a certain period. It's a parameter associated with the well-known Gutenberg–Richter law (Gutenberg and Richter, 1954) which describes the relationship between the magnitude of earthquake events and the total number of earthquakes of at least that magnitude. This can be expressed in Eq. (2.1)

$$\log_{10} N_M = a - bM \tag{2.1}$$

Where M is the magnitude of earthquake and N_M is the total number of earthquakes of an amplitude at least M. b is a parameter referred to as b value. a is another parameter. Since b value is of great interest in seismology area, due to the AE phenomenon analogous to earthquake fault rupture, b value is also believed to be applicable in AE study and some remarkable research has being done by Hirata (1989); Shiotani *et al.*(1994, 2001 and 2007);Weiss (1997); Colombo *et al.*(2003); Rao and Lakshmi (2005). Findings include the correlation between AE amplitude distributions (b values) and the attenuation(Weiss, 1997), the correlation between the b value and the fractal dimension of fractures (i.e. earthquake) (Aki, 1981; Hirata, 1989), the correlation between the improved b value and the quantification of damage level in concrete structures (Rao and Lakshmi, 2005; Shiotani *et al*., 2007). Although the peak amplitudes of AE signals are well known to be closely related to the scale of

damage (fracture dimension, damage level, etc.), the analysis is not adequate if only taking consideration of the amplitudes. As crack progresses gradually, the mechanical property of the host structures near crack might change, which could possibly cause a higher AE signal attenuation rate due to wave reflection and refraction, and results in lower amplitude in the received AE signal even when an AE event of higher amplitude happened (Shiotani *et al*., 2007). Thus, the distribution of the amplitude (i.e. *b* value) outperforms the absolute peak amplitude, especially when the peak amplitude is subject to influence of monitoring conditions.

2.2.2.4 AE Energy

AE energy is defined in a way that it could be used to quantify the damage. AE energy release in different composites has been studied for concrete and used in damage quantification in CFRP composites (Bourchak *et al*., 2007). However, the definitions of AE energy are different in different AE monitoring systems (Harris and Bell, 1977; Mohan and Prathap, 1980; Landis and Baillon, 2002).

For the piezoelectric paint AE sensor, the signal amplitude is proportional to the strain of the structure (at the sensor location) due to the AE events (Li and Zhang, 2008) . The strain-based AE energy can be defined as

$$V_\varepsilon \propto \int \sigma d\varepsilon = E \int \varepsilon d\varepsilon \tag{2.2}$$

As $V \propto \varepsilon$, we have

$$V_\varepsilon \propto \int \sigma d\varepsilon = E \int \varepsilon d\varepsilon \propto \int V dV \propto V^2 \tag{2.3}$$

The cumulative AE energy can be calculated as

$$\int V_\varepsilon dt \sim \int V^2 dt \tag{2.4}$$

$\int V^2 dt$ will be used as the AE energy index in this study, which is equal to the area under the squared AE signal curve. This energy is actually cumulative AE energy. AE energy rates (first order derivate of the cumulative AE energy curve with respect to time) can also be calculated for AE feature analysis if needed.

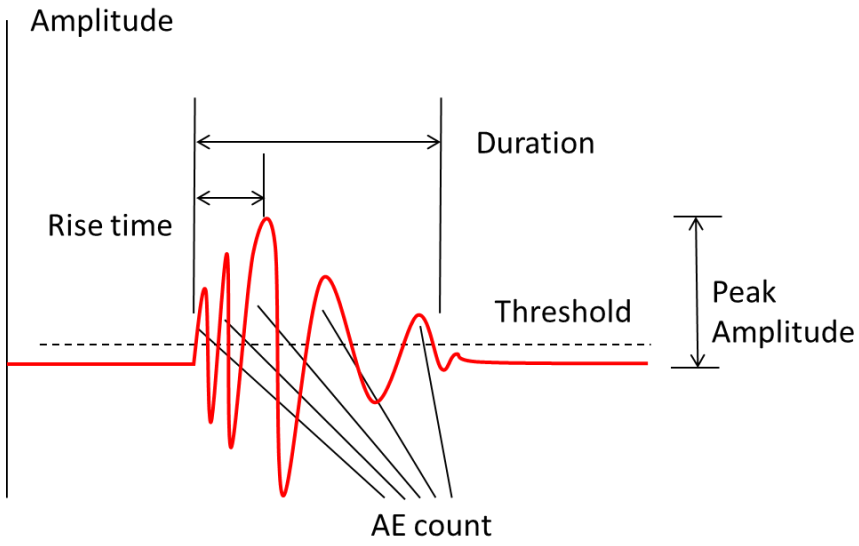

Figure 2.1: AE parameters definition of an output signal

Chapter 3: Background of Piezoelectric Film AE Sensor

3.1 Historical Development of Piezoelectric Film AE Sensor

Piezoelectric AE sensor converts a mechanical stimulus to an electric signal based on its sensing principle. Several sensing principles can be used for piezoelectric AE sensor design. For conventional piezoelectric AE sensor, it measures the dynamic out-of-plane displacement. This type of piezoelectric AE sensors usually have a special backing and wear plate (Proctor, 1982). The backing serves as a damping block while the wear plate is used to protect the active sensing element. This type of AE sensors can be configured as a broadband transducer or a resonant transducer through judicious selection of backing size and active element (usually piezoelectric crystals like quartz or piezoelectric ceramics). A typical AE sensor of this type is the conical shape AE sensor developed by Proctor (1982). This sensor has a small contact area, which reduce the aperture effect as much as possible. As a result of using conical shaped piezoelectric sensing element, this AE sensor exhibits a broad bandwidth up to 1 MHz. However, the design of this type of sensor is not perfect due to the trade-off between broad bandwidth and high sensitivity. The fabrication cost is also higher due to complex sensor design with conical shaped piezoelectric sensing element.

There are some other types of piezoelectric AE sensors. For example, piezoelectric film AE sensor is one among those who attracts growing interests recently. In contrast with conventional piezoelectric AE sensor which is based on a 2nd-order dynamic oscillator operating principle measuring out-of-displacement

displacement, piezoelectric film AE sensor measures stress-wave-induced in-plane strain. Piezoelectric film AE sensor is thus a zero-order sensor. The dynamic strain within the sensing area of the piezoelectric film AE sensor is transformed into electrical signal according to piezoelectric material sensing principle. This type of sensor is usually bonded to the monitored structure using epoxy.

Piezoelectric materials present an important factor in AE sensor design. Among all the piezoelectric materials for AE signal sensing, Lead zirconate titanate (PZT) and Polyvinylidene Fluoride (PVDF) are most popular. To date, most of the piezoelectric AE sensors are made of PZT, which is usually in the form of ceramics. Quite a few research works are reported using PZT wafers (Crawley, 1994; Kawai, 1969; Lee and O'Sullivan, 1991; Liu *et al*., 1995; Yu *et al*., 2011). The advantages of using PZT include low cost, commercial availability and relatively high sensitivity. However, it is difficult to form PZT into complex shape and apply it on curved structure due to its brittleness. Other characteristics of PZT may not be favorable to AE application, such as resonance peak within operation frequency range and mismatch of acoustic impedance with some materials. In contrast, PVDF has properties of flexibility, ability to resist corrosion, and toughness (Wang *et al*., 1999). It can be made into large sheets of thin films easily. The disadvantages of PVDF are its relatively low sensitivity, low transmitting constant, large dielectric loss, high-cost and low Curie temperature (Gu *et al*., 2002; Harsanyi, 2010). This limits its application to metallic structures.

Recently, a new type of piezoelectric material – piezoelectric paint has attracted growing attentions from researchers. Piezoelectric paint is a composite

material. Within the material, tiny piezoelectric particles are randomly dispersed in a polymer matrix phase. Adjustable material properties can be achieved compared with a single-phase material. The flexibility of polymer matrix could make piezoelectric paint easily conformable to curved surface of structures. The piezoelectric paint's ability of acoustic emission signal sensing has been verified by many researchers including Egusa and Iwasawa (1998),Wenger *et al.* (1996, 1999a, 1999b),Sakamoto *et al.* (2001), Kobayashi *et al.* (2002, 2007), Zhang and Li (2006), Li and Zhang (2008) and Li (2009). A thorough study of piezoelectric paint's material properties has been conducted by Li (2009), including the effects of various volume fractions of piezoelectric materials on its sensitivity. Previous work also shows piezoelectric paint AE sensor can be used as a promising technology for acoustic emission based nondestructive evaluation of structural damages or defects in either metallic or composite structure. However, extensive work in AE monitoring system development based on piezoelectric film AE sensor and sensor characterization on full-scale structures with fatigue cracks, have not be reported. A lack of theoretical formulations for understanding the AE signals also hinders the use of piezoelectric film AE sensors. Successful application of piezoelectric film AE sensor in practice also requires long-term field test of piezoelectric film AE sensor so its field monitoring issues and durability can be examined and potential problems can be fixed. Additionally, crack detection and source localization with AE signals is a very important area yet to be explored for this new type of AE sensor.

3.2 Sensing Principle of Piezoelectric Film AE Sensor

For piezoelectric film AE sensor, in the absence of external electric field, the electric charge generated by stretching its sensing element can be expressed as,

$$\begin{Bmatrix} D_1 \\ D_2 \\ D_3 \end{Bmatrix} = \begin{bmatrix} 0 & 0 & 0 & 0 & d_{15} & 0 \\ 0 & 0 & 0 & d_{24} & 0 & 0 \\ d_{31} & d_{32} & d_{33} & 0 & 0 & 0 \end{bmatrix} \{\sigma_1 \quad \sigma_2 \quad \sigma_3 \quad \sigma_4 \quad \sigma_5 \quad \sigma_6\}^T \tag{3.1}$$

where $\{\sigma_1 \quad \sigma_2 \quad \sigma_3 \quad \sigma_4 \quad \sigma_5 \quad \sigma_6\}^T = \{\sigma_{11} \quad \sigma_{22} \quad \sigma_{33} \quad \sigma_{23} \quad \sigma_{31} \quad \sigma_{12}\}^T$; σ_1, σ_2 and σ_3 are tensile stress; σ_4, σ_5 and σ_6 are shear stress; d_{31}, d_{32}, d_{33}, d_{24} and d_{15} are piezoelectric constants; D_1, D_2 and D_3 are the electric charge displacements. If shear stress is negligible and considering the fact that AE sensor is placed on the surface (meaning σ_{33} equals zero), Eq. (3.1) is simplified as,

$$D_3 = d_{31}\sigma_1 + d_{32}\sigma_2 + d_{33}\sigma_3 = d_{31}E_{11}\varepsilon_{11} + d_{32}E_{22}\varepsilon_{22} \tag{3.2}$$

If the piezoelectric sensing material is homogeneous and the sensor sensitivity in both directions 1 and 2 are the same, the resulting charge could be written as $D_3 = d_{31}E_{11}(\varepsilon_{11} + \varepsilon_{22})$. This is different from AE displacement sensor which measures the displacement in a single direction (usually direction 3). Assuming the dimension of the sensor is $l \times w \times t$, where l, w and t are sensing element length, width and thickness respectively, as a result, the generated electric charge is related to the dielectric displacement D_3 by the following relationship,

$$q = \iint D_3 dA = \iint D_3 dA = \iint (d_{31}E_{11}\varepsilon_{11} + d_{32}E_{22}\varepsilon_{22})dxdy = \int_l \int_w (d_{31}E_{11}\varepsilon_{11} + d_{32}E_{22}\varepsilon_{22})dxdy \tag{3.3}$$

It can be shown that piezoelectric film AE sensor can be configured as either strain sensor or strain rate sensor because of the mechanical coupling property of piezoelectric materials (Lee and O'Sullivan, 1991; Sirohi and Chopra, 2000). Li (2009) summarized the two types of signal conditioning circuit. In summary, if a current amplifier is used as the signal conditioning circuit, the output voltage from the sensor is linear proportional to the total strain change rate and can be express as,

$$V_{out}(t) = -R_f \dot{q} = -R_f \int_l \int_w (d_{31} E_{11} \dot{\varepsilon}_{11} + d_{32} E_{22} \dot{\varepsilon}_{22}) dxdy \tag{3.4}$$

If a charge amplifier is used as the signal conditioning circuit, the output voltage from the sensor is linear proportional to the average strain with the sensor area and can be express as,

$$V_{out}(t) = -\frac{q}{C_f} = -\frac{1}{C_f} \int_l \int_w (d_{31} E_{11} \varepsilon_{11} + d_{32} E_{22} \varepsilon_{22}) dxdy \tag{3.5}$$

In this study, piezoelectric film AE sensors are mainly used as a strain sensor and a charge amplifier is designed and used.

3.3 Piezoelectric Paint AE Sensor

3.3.1 Material Properties of Piezoelectric Paint

Piezoelectric paint typically comprises tiny piezoelectric particles mixed within polymer matrix and therefore belongs to the "0-3" piezoelectric composite. The "0-3" means that the ceramic particles are randomly dispersed in a polymer matrix. Compared with other connectivity types, "0-3" has the advantage of ease of fabrication into complex shapes and may conform to any curved surface. The piezoelectric paint offers the unique blending of the high piezoelectric properties of

ferroelectric ceramics (e.g., PZT) and the mechanical compliance and conformability of polymers (e.g., PVDF). Li (2009) carried out a series of studies on piezoelectric paint sensors for different volume fractions of PZT particles and experimentally characterized the material properties. The material properties of piezoelectric paint and other piezoelectric materials are listed in Table 3.1. It can be concluded from d_{31} values that the piezoelectric paint has a sensitivity comparable to PVDF but is much lower (about 1/30) than PZT.

Table 3.1. Typical piezoelectric material properties (Li, 2009)

	PZT-5A[a]	PVDF	Piezoelectric Paint (PZT% by volume)			
			40%	50%	60%	70%
d_{33} [pC/N]	390	-22.1	6.1	13.7	27.1	48.1
$-d_{31}$ [pC/N]	175	-6.2	2.1	4.4	8.6	15.0
k^p	0.63	0.03	0.02	0.06	0.10	0.19
g_{31} [10^{-3}Vm/N]	12.4	-70.8	18.4	24.0	29.1	30.7
k_{31}	0.36	0.03	0.02	0.04	0.7	0.13
$\varepsilon/\varepsilon_0$[b]	1800	9.9	12.9	20.7	33.4	55.2
Z [MRayl]	30	2	4.9	6.0	7.3	9.2
Tc Curie Point [°C]	350	150 (melt)	Degradation temperature of resin >200			

[a] Material parameters are provided by APC International Inc, Pennsylvania.

[b] $\varepsilon_0 = 8.85\times10^{-12}$ F/m, is the permittivity of free space (vacuum)

3.3.2 Signal Conditioning Circuitry

The charge output from the piezoelectric sensor is usually very small. It also attenuates very fast along transmission cables and is very easy to be affected by noise. In order to measure these weak signals, a signal conditioning circuit is needed to amplify the signal and potentially filter the signal to remove unwanted noise. Piezoelectric sensor can be modeled as either a voltage source in series with the combination of its internal capacitance and internal resistance as shown in Figure

3.1.(a) or a current source in parallel with its internal capacitance and resistance shown in Figure 3.1.(b). In this study, a voltage follower design shown in Figure 3.1 (a) is utilized to amplify the AE signals in piezoelectric film AE sensors. The detailed amplification circuit is shown in Figure 3.2.

For piezoelectric sensor, its signal is very easy to be contaminated by noise, such as power source and EMI noise. In order to enhance the signal-to-noise ratio (SNR) and for ease of post processing, a filter is usually necessary to eliminate the unwanted noise from the signal. Due to huge amount of AE data at high sampling rate, an analog filter is preferred over a digital filter in order to perform real-time filtering without overwhelming the computation capacity of the data acquisition system. As the piezoelectric paint sensors are operating in ultrasonic range and the typical frequency range of interest is above 5 kHz based on the author's experience, a low cutoff frequency of 5 kHz is selected for the filter design; for most of applications with piezoelectric paint sensor, the signal frequency contents are usually below 600 kHz, thus the filter's high cutoff frequency is set to be 600 kHz. The design of the analog filter is based on Sallen–Key topology, which is usually used as the implementation of a second order active filter. It is a pure second order Butterworth filter with a gain of 0 dB. A schematic of the filter circuitry is shown in Figure 3.2.

By inputting signals of different frequency contents to the signal conditioning circuit using a function generator and measuring the output from the circuit, its frequency response curve can be experimentally determined which is shown in Figure 3.3. It can be seen the signal conditioning circuit has a nearly flat frequency response

within the filter's pass band, thus would not affect the frequency response of the piezoelectric film AE sensor over the specified frequency range.

3.3.3 Frequency Response Characteristics of Piezoelectric Film AE Sensor

Step force on the surface of half space is a simulated AE source commonly used in experiment. Both pencil lead break and breaking glass capillary are good candidates for generating such kind of surface AE source with an approximate step force. In this study, glass capillary breakage is used to simulate the surface AE force. Figure 3.4(a) shows the experimental set up for characterizing the frequency response curve of piezoelectric film AE sensor. The test setup includes a large 4-inch thick steel block with a plan dimension of 20 inches by 20 inches to simulate the half space medium. Two piezoelectric paint AE sensors are bonded onto the steel surface, including one PZT sensor and one piezoelectric paint sensor. The PZT sensor has a diameter of 5mm while the piezoelectric paint sensor has a diameter of ½ inch. Both are in circular shape. Each sensor is connected to a 40 dB amplifier and a filter with a pass band of 5 to 600 kHz, which is described in the previous section. A commercial broadband AE sensor (Dunegan Engineering model SE 1000-HI, broadband AE sensor with a sensitivity of 1000 V/μm if used with a 20-dB preamplifier) is also mounted to the steel block at equal distance to the simulated AE source point. The SE 1000-HI has a 20-dB gain amplifier. The three sensors are equally distanced from their centers to the AE source point (i.e., glass capillary breakage), which is 50 mm.

Figure 3.4(b) shows the AE signals acquired by the three sensors as well as their corresponding frequency spectra. The signal in the commercial AE sensor shown in Figure 3.4(b) agrees with the anticipated waveform due to a breaking glass

capillary (e.g., shown in Johnson 1974; Proctor 1982). For the piezoelectric film AE sensors, they behave very well under 600 kHz. Starting from 600 kHz, the frequency response begins to roll down. This can be explained by the fact that the upper cut-off frequency of the filter used with the piezoelectric film AE sensor is 600 kHz. Particularly, piezoelectric paint AE sensor has a peak response level (about 1/3) not far from that of the commercial AE sensor with signal conditioning. It can also be seen that the frequency response of this piezoelectric paint AE sensor is relatively flat over its operating frequency range, which is consistent with the sensing material characteristics reflected by impedance measurements (Li, 2009) and frequency response of associated signal conditioning circuitry.

3.3.4 Signal Attenuation by Backing Film

A typical approach to installing piezoelectric film AE sensor is to bond it onto host structure surface using adhesive material like epoxy or glue. In order to enhance the ease of installing the piezoelectric film AE sensor, a polyimide backing film is used in the sensor design. The backing film is a thin polyimide film so that it does not affect the strain transmission. The sensing element, e.g. PZT and piezoelectric paint is first bonded onto the backing film using conductive epoxy and the backing film can then be bonded to the monitored structure surface with glue such as superglue or M-bond from Vishay. Since the super glue only takes several seconds to cure, the installation time is considerably shortened, which is especially convenient in field. Another advantage of this backing film is to apply on non-conductive materials, such as concrete and FRP.

Detailed configuration of piezoelectric film AE sensor with backing film can be found in Figure 3.5. In order to ensure that the sensor performance is not affected by the backing film, a comparison test was conducted, with a standard pencil lead break test in order to simulate the AE source. Pencil lead break is also referred to as Hsu-Nelson source. Figure 3.6 shows a typical signal measured by piezoelectric film AE sensor and PZT disc in a pencil lead break test. It is seen that the backing film does reduce the amplitude of the AE signal, in both P and Raleigh wave arrivals. The tests were repeated 20 times and the results were used to statistically assess the reduction of AE signal peak amplitude by the backing film, which is experimentally determined to be 82%.

Compared with the PZT disc without any backing film, the signal measured by the piezoelectric film AE sensor with backing film has more ring-down signals, suggesting some non-uniform amplification effect in its frequency response. To provide an insight of the amplification effect at different frequencies, the frequency spectra of both sensor signals is presented in Figure 3.7(a). The frequency spectra are averaged from 20 sets of data to minimize the noise effect. The amplification ratios at different frequencies are also calculated and shown in Figure 3.7(b).

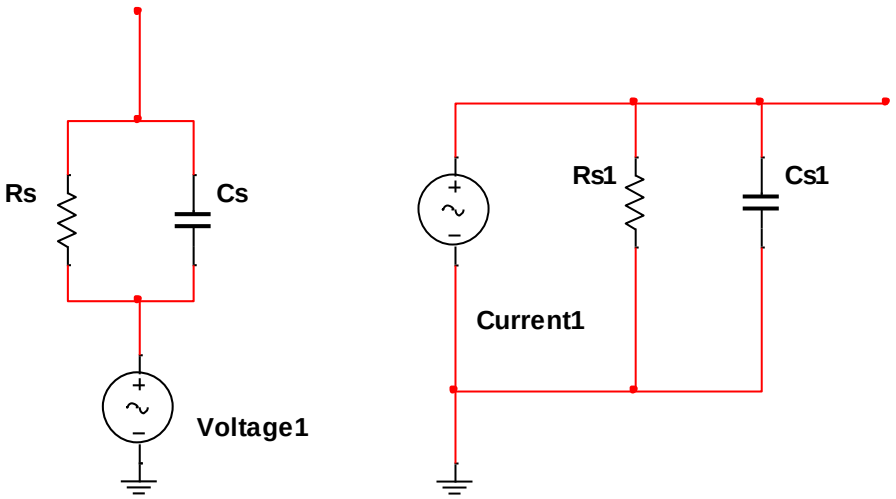

(a) (b)

Figure 3.1: Piezoelectric sensor models: (a) voltage source; (b) current source

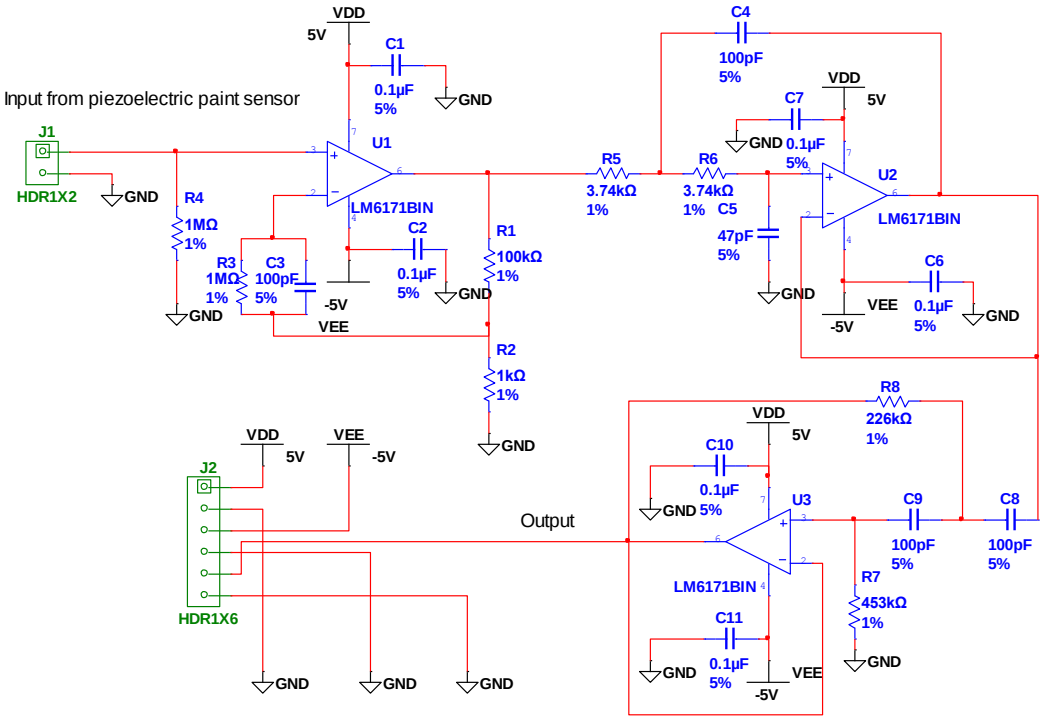

Figure 3.2: Signal conditioning circuit for piezoelectric paint AE sensor

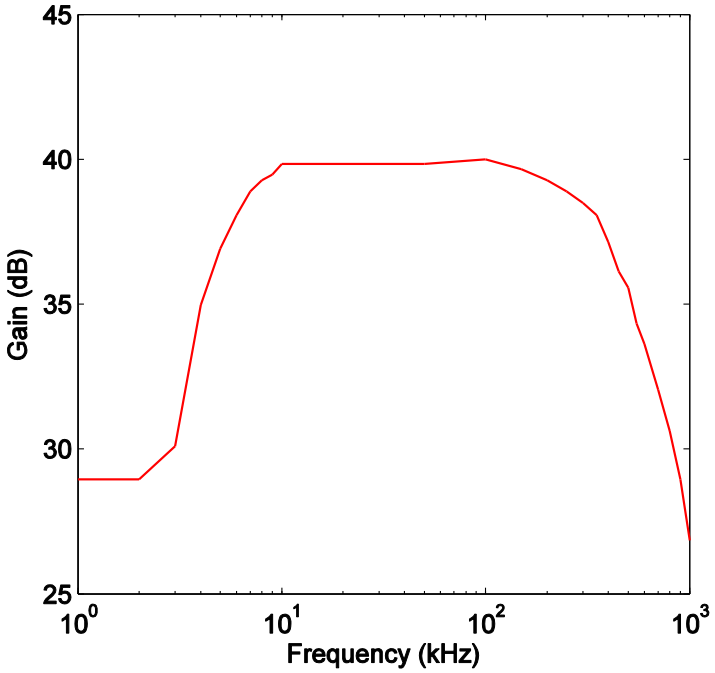

Figure 3.3: Measured frequency response curve of the signal conditioning circuit in Figure 3.2

(a)

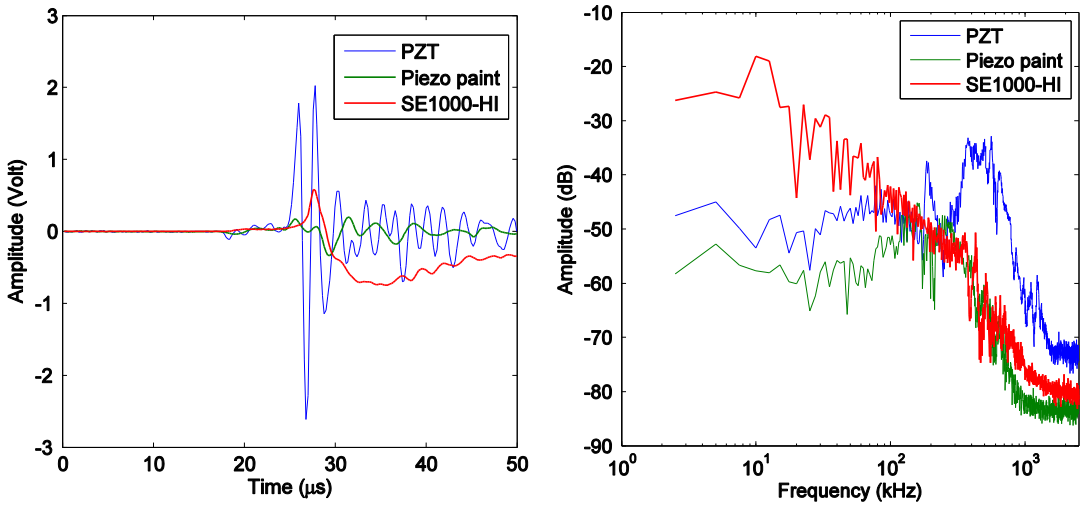

(b)

Figure 3.4: AE signal measured by piezoelectric paint AE sensor and commercial AE sensor (Dunegan Engineering model SE-1000HI) due to simulated surface pulse (glass capillary breakage): (a) test setup; (b) Signal time history (left figure) and frequency spectra (right figure, frequency spectra are averaged of 20 sets of data).

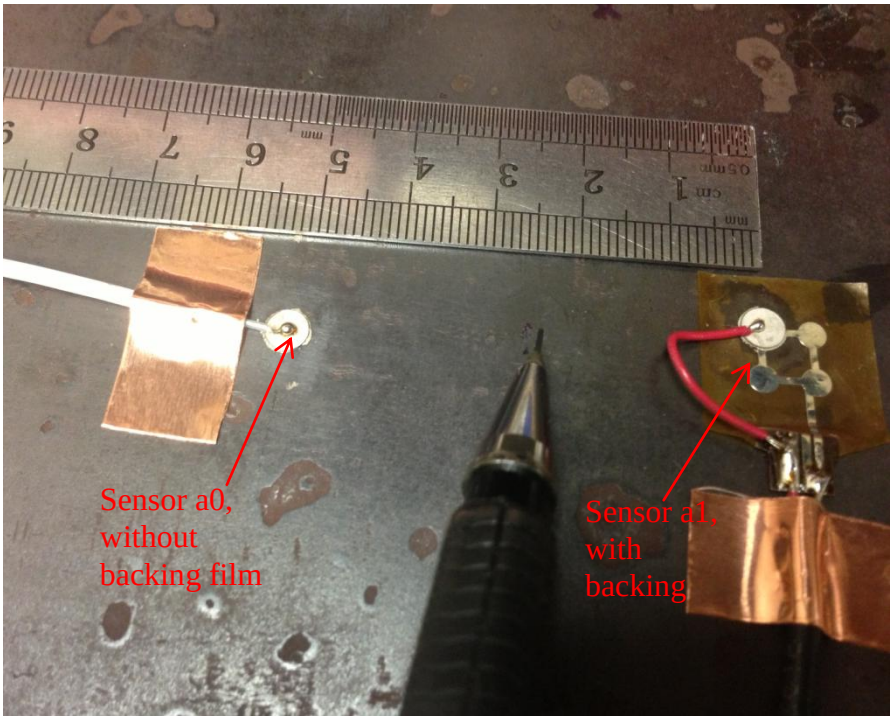

Figure 3.5: Experimental set up for studying the attenuation by backing film

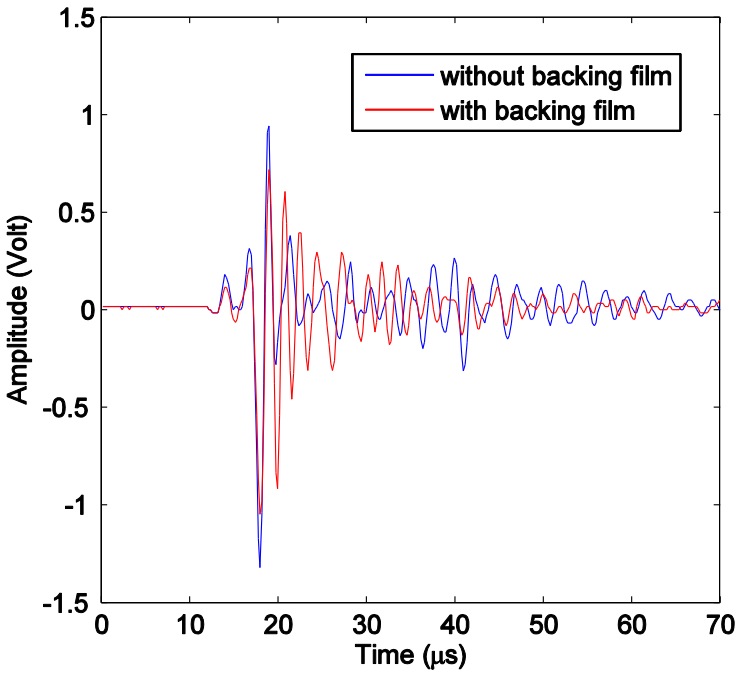

Figure 3.6: AE waveform comparison of thin-film AE sensor with and without backing film

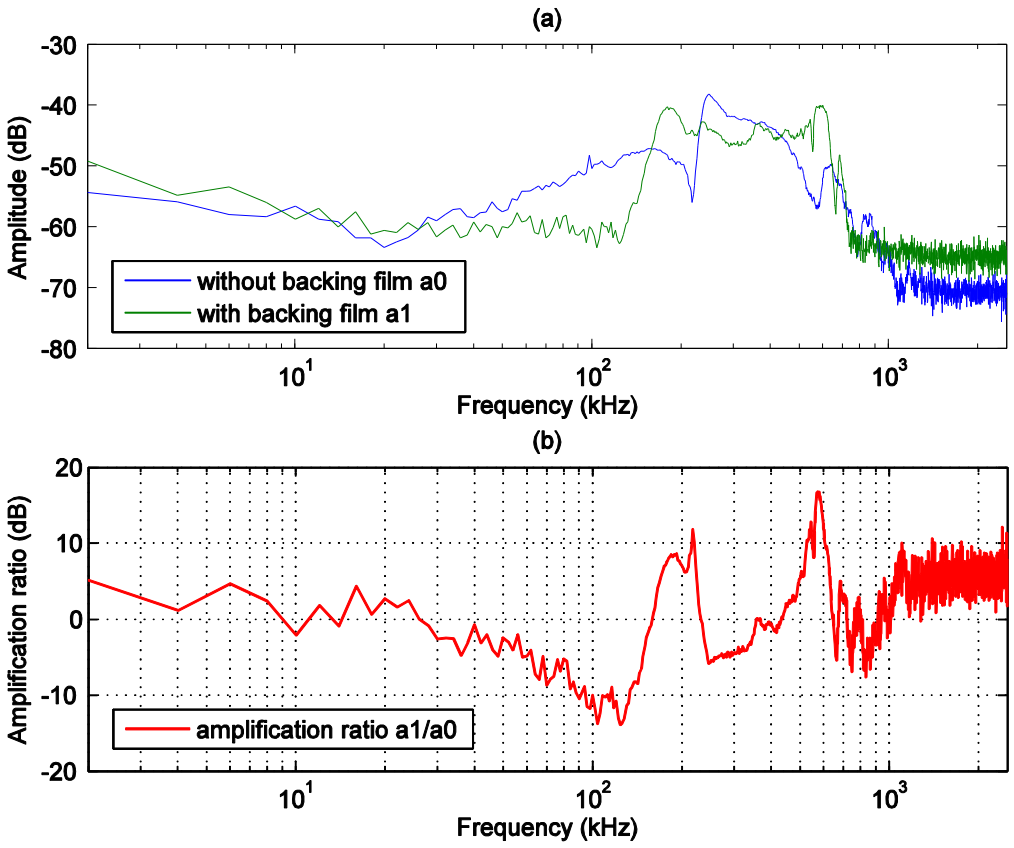

Figure 3.7: (a) Frequency spectra of piezoelectric film AE sensor with and without backing film (averaged with 20 sets of data); (b) amplification ratio by backing film (determined from Figure 3.7(a))

Chapter 4: Analytical Study of Near-field AE Induced Strain Signal

4.1 Introduction

Using piezoelectric film sensor to detect surface stress wave signals has been receiving growing interests lately (e.g., Ihn and Chang, 2004; Park *et al*., 2006; Yun *et al*., 2010). Conventional acoustic emission (AE) sensors are based on a 2^{nd}-order dynamic oscillator operating principle which measures displacement perpendicular to the monitored surface. Piezoelectric film strain sensor is based on measuring stress-wave-induced strain in its plane. Some strain-based piezoelectric film AE sensors such as those made of piezoelectric paint have a lower sensitivity than the conventional AE sensors, especially those resonant type AE sensors. Therefore, near-field AE signal monitoring is most suitable for such strain-based piezoelectric film AE sensors placed in close proximity to potential AE source (e.g., crack) locations. Near-field here refers to a distance from the AE source within which the AE-induced strain signal level is greater than a pre-specified intensity value, which will be discussed in later section.

Ohtsu employed the Green's function and moment tensor theory for AE signal analysis, with a focus on surface displacement sensor (Ohtsu, 1995; Ono and Ohtsu, 1984; Yuyama *et al*., 1988). In Ohtsu's work, good agreement between the measured and simulated signals was observed, which verified the validity of applying moment tensor and Green's function method in AE signal analysis. While generalized AE theory has been proposed for displacement-based AE signal sensing (Fortunko *et al*., 1992; Ohtsu, 1995; Ono and Ohtsu, 1984; Proctor, 1982; Yuyama *et al*., 1988), little

research have been reported for strain-based AE signal sensing such as signal characteristics and calibration of this type of AE signals collected in near-field. Currently most research on strain sensor has been limited to low frequency use (Sirohi and Chopra, 2000). The successful application of near-field AE monitoring with piezoelectric film AE sensor is hindered by a lack of knowledge of such AE signals and influential parameters.

This chapter aims to elucidate the underlying sensing principle of near-field AE monitoring with piezoelectric film AE sensor and its signal characteristics. Moment tensor theory and Green's function are used to synthesize the AE strain signal, in which the moment tensors represent the cracking source while the Green's functions yield the transfer function between the source and AE sensor. The derivation of the theoretical formulation starts from the well-established solution of the Green's function in half space due to a Heaviside step force originally derived by Johnson (Johnson, 1974). As a special case with potential use for sensor calibration, stress wave-induced surface strain response to a nearby surface pulse load is presented. A parametric study follows, with varying parameters including two structural materials (steel and aluminum), two different types of crack mode (tensile type of cracking and shear type of cracking) and two depth values for the crack source are examined (1 mm and 5 mm). As an example of application, analytical solution of the stress wave-induced surface strain due to a surface pulse is presented, which can be used as the basis for calibrating such AE strain sensors. To verify the formulations, experiments were carried out with glass capillary breakage on a large steel block and the result is compared with the theoretical predictions.

4.2 Moment Tensor Theory for AE Strain Signal

4.2.1 Moment Tensor Theory

Moment tensor analysis is commonly used for AE waveform simulation (Ohtsu, 1995). The basics of moment tensor theory are reviewed below before formulation for AE strain signal is presented.

4.2.1.1 General Expression for Strain Signal Due to AE Source

Moment tensor analysis can be used for synthesizing AE-induced stress waves due to crack initiation. It has been long used in seismology field (Aki and Richards, 2002) and has also been employed for AE signal analysis (see e.g. Ono and Ohtsu, 1984; Ohtsu, 1995). In moment tensor analysis, moment tensors (dipoles or double couples) weighted Greens' functions are employed to represent the signal. According to the generalized AE theory (Ono and Ohtsu, 1984), signals emanating from a hidden fatigue crack can be expressed as,

$$u_k(\mathbf{x},t) = G_{kp,q'}(\mathbf{x},t;\mathbf{x}',t') * S(t) C_{pqij} n_j l_i \Delta V \tag{4.1}$$

Where C_{pqij} are elastic constants, ΔV is the crack volume, n is the crack normal and l is the crack motion vector; S(t) is the source function; $G_{kp,q}$ is the spatial derivative of the Green's function G_{kp} with respect to the spatial coordinate q', where G_{kp} represents the displacement in the k direction at point $\mathbf{x}$ and time t due to a unit force in the p direction at point $\mathbf{x}'$ and time t', q' here means that the spatial derivate is with respect to the source's coordinate.

Denoting $C_{pqij}\ n_j\ l_i\ \Delta V$ as M_{pq}, which is also referred to as moment tensor, yields Eq. (4.2).

$$u_k(\mathbf{x},t) = \sum G_{kp,q'}(\mathbf{x},t;\mathbf{x}',t') * S(t) M_{pq} \tag{4.2}$$

With different choice of moment tensors and Green's functions, a variety of crack modes can be represented with Eq. (4.2). For example, an explosive source can be modeled as $M_{11} + M_{22} + M_{33}$, while a double couple source can be modeled as $M_{ij} + M_{ji}$, depending on the source coordinate (Lay and Wallace, 1995). For buried cracks, summation about p and q should be done. For surface cracks, the signal could be generated by a double couple/ dipole, in which case there is no summation for indices p and q in Eq. (4.2).

The generalized moment tensor components M_{pq} in Eq. (4.2) can be expressed as follows (Aki and Richards, 2002),

$$M_{pq} = \begin{bmatrix} \lambda l_k n_k + 2\mu l_1 n_1 & \mu(l_1 n_2 + l_2 n_1) & \mu(l_1 n_3 + l_3 n_1) \\ \mu(l_1 n_2 + l_2 n_1) & \lambda l_k n_k + 2\mu l_2 n_2 & \mu(l_2 n_3 + l_3 n_2) \\ \mu(l_1 n_3 + l_3 n_1) & \mu(l_2 n_3 + l_3 n_2) & \lambda l_k n_k + 2\mu l_3 n_3 \end{bmatrix} \Delta V \tag{4.3}$$

The above theory as expressed in Eq. (4.2) applies to surface displacement. With some manipulation, it can be adapted for surface strain,

$$\begin{aligned} \varepsilon_{kk}(\mathbf{x},t;\mathbf{x}',t') &= \lim_{\Delta x_k \to 0} \frac{u_k(\mathbf{x}+\Delta\mathbf{x}_k,t;\mathbf{x}',t') - u_k(\mathbf{x},t;\mathbf{x}',t')}{\Delta x_k} \\ &= \lim_{\Delta x_k \to 0} \frac{G_{kp,q'}(\mathbf{x}+\Delta\mathbf{x}_k,t;\mathbf{x}',t') - G_{kp,q'}(\mathbf{x},t;\mathbf{x}',t')}{\Delta x_k} * S(t) M_{pq} \\ &= G_{kp,q'k}(\mathbf{x},t;\mathbf{x}',t') * S(t) M_{pq} \end{aligned} \tag{4.4}$$

In the general case, the resulting strain can be calculated with Eq. (4.3) and (4.4).

4.2.1.2 Crack Induced AE Strain Signal Formula

There are two crack modes of interest to AE monitoring. The first is the tensile mode, in which the suddenly released stress from crack propagation is in parallel with the crack normal. The other mode is the shear mode, in which the stress direction is

perpendicular to the crack normal. Figure 4.1 shows a schematic of both the shear crack and tensile crack. If the forces are expressed using the notation of moment tensor and the corresponding moment tensor is denoted as M_{pq} (assuming the sensor lies in the x_1-x_2 plane, as shown in Figure 4.2), the resulting strain in direction 1 can be expressed as,

$$\varepsilon_{11}(\mathbf{x},t;\mathbf{x}',t') = G_{1p,q'1}(\mathbf{x},t;\mathbf{x}',t') * S(t)M_{pq} \tag{4.5}$$

It should be noted that only the in-plane strains (i.e., x_1-x_2 plane in Figure 4.2) are considered because of the sensing principle of strain-based piezoelectric film AE sensor as discussed in Chapter 3. The index *kk* in Eq. (4.4) thus only takes a value of either 11 or 22.

4.2.1.2.1 Tensile mode crack

For the case of a tensile crack buried inside the material, the crack normal is assumed to be l = (1, 0, 0) and the crack propagates along the direction of the vector n = (1, 0, 0), without loss of generality. Accordingly, its moment tensor can be written as,

$$M_{pq} = \begin{bmatrix} \lambda+2\mu & 0 & 0 \\ 0 & \lambda & 0 \\ 0 & 0 & \lambda \end{bmatrix} \Delta V \tag{4.6}$$

Consequently, the stress-wave induced strain in direction 1 only at the sensor location due to a tensile crack source is,

$$\begin{aligned} \varepsilon_{11}(\mathbf{x},t;\mathbf{x}',t') = {} & G_{11,1'1}(\mathbf{x},t;\mathbf{x}',t') * S(t)\Delta V(\lambda+2\mu) + G_{12,2'1}(\mathbf{x},t;\mathbf{x}',t') * S(t)\Delta V\lambda \\ & + G_{13,3'1}(\mathbf{x},t;\mathbf{x}',t') * S(t)\Delta V\lambda \end{aligned} \tag{4.7}$$

The strain in direction 2 could also be obtained in a similar way. With the strain in both directions 1 and 2, the total stress wave induced strain response of the AE sensor can be obtained.

4.2.1.2.2 Shear mode crack

Similarly, for the case of a buried shear type crack, the crack normal is assumed to be l= (1, 0, 0) while the crack propagates along the direction defined by the vector n= (0, 0, 1). The corresponding moment tensor can be expressed as,

$$M_{pq} = \begin{bmatrix} 0 & 0 & \mu \\ 0 & 0 & 0 \\ \mu & 0 & 0 \end{bmatrix} \Delta V \tag{4.8}$$

The resulting strain in direction 1 is,

$$\varepsilon_{11}(\mathbf{x},t;\mathbf{x}',t') = [G_{11,3'1}(\mathbf{x},t;\mathbf{x}',t') + G_{13,1'1}(\mathbf{x},t;\mathbf{x}',t')] * S(t)\Delta V \mu \tag{4.9}$$

For displacement-based AE signal monitoring, the spatial derivative of the Green's function is of most interest. However, for strain -based AE signal sensing, as strain is the spatial derivative of the in-plane displacement with respect to the corresponding coordinate, it's the second partial derivative of the Green's function rather than the first derivative of Green's function. This can also be seen in Eq. (4.4). This is distinct to the displacement -based AE signal analysis, which is concerned with the first derivative of the Green's function. Thus, in order to show the characteristics of stress-wave-induced AE strain signals, the second order derivative of the Green's function needs to be calculated.

4.2.2 Equation of Motion

The general equations of motion for wave propagation can be expressed as,

$$\mu\nabla^2\mathbf{u}+(\lambda+\mu)\nabla\nabla\cdot\mathbf{u}+\mathbf{f}=\rho\ddot{\mathbf{u}} \tag{4.10}$$

where λ is Lamé's first parameter, and μ is the shear modulus, or Lamé's second parameter; **u** is the displacement vector; **f** is the body force, which can be reduced to a concentrated force; ∇ is the Del operator and ρ denotes the density.

For a half space with a free surface of x_3=0, the boundary conditions are specified in such a way that the following stresses vanish on the free surface,

$$\begin{cases} T_{13}=\mu\left(\dfrac{\partial}{\partial x_3}u_1+\dfrac{\partial}{\partial x_1}u_3\right) \\ T_{23}=\mu\left(\dfrac{\partial}{\partial x_3}u_2+\dfrac{\partial}{\partial x_2}u_3\right) \\ T_{33}=\lambda\left(\dfrac{\partial}{\partial x_1}u_1+\dfrac{\partial}{\partial x_2}u_2+\dfrac{\partial}{\partial x_3}u_3\right)+2\mu\dfrac{\partial}{\partial x_3}u_3 \end{cases} \tag{4.11}$$

Currently, two approaches are available to solve the equations of motion with the boundary conditions in Eq. (4.11). The first approach is the Cagniard-de Hoop method (De Hoop, 1960) which was also used by Johnson in deriving Green's function as well as the first order spatial derivative of Green's function (Johnson, 1974). The other approach which was first introduced by Willis (Willis, 1973), expresses the results in a series of generalized rays and was also used by other researchers (Hsu, 1985; Pao *et al*., 1979; Ren *et al*., 2002). For the latter method, as the results are expressed in a series of rays, one needs to calculate the arrival time of each ray and summates the contribution from each arrival ray. For the Cagniard-de Hoop method, only one integral term appears in the final formula, although the integration path needs to be constructed carefully. Therefore, the expression in the Cagniard – de Hoop approach is more concise. Furthermore, the differentiation with respect to spatial coordinate is also simpler than the Willis method. In addition, the

existing results of Green's function can be utilized. Therefore, in this study, the formulation will be based on the Cagniard- de Hoop method.

4.2.3 Second Order Spatial Derivative of Green's Function for Half Space

Green's function for half space is usually referred to as the Lamb's Problem, which was first studied by Lamb (Lamb, 1904). Lamb studied the surface displacement response due to a vertical line source with impulsive load. Most of the discussions have been limited to force perpendicularly applied to the surface. In order to study the transient dynamic response of an half space, studies concerning loads with arbitrary shape and orientations have been investigated by others. For example, Pinney (Pinney, 1954) obtained the closed-form solutions of surface motion due to a point source in a semi-infinite medium for a special case $\lambda = \mu$, where λ and μ are the Lamé's first and second parameters respectively. Pekeris dealt with the general case of arbitrary Poisson's ratio for both surface pulse (Pekeris, 1955a) and buried pulse (Pekeris, 1955b), for which a closed-form solution was determined. Both horizontal and vertical displacements have been studied for vertical sources with varying depth. The case of a double-couple source in a half space has also been examined by Kawasaki *et al*. (1972a and b).

Based on the Knopoff-de Hoop representation theorem, Johnson (1974) presented a unified result and extended the solutions to the spatial derivatives of Green's function, which are useful for AE application since crack source mechanism is related to the spatial derivative of the Green's function. Following Johnson's work (1974), many studies have been carried out for semi-infinite medium. Richard (1979) derived exact solutions to the Lamb's problem involving only arithmetic operation

and square roots computation, in which both the source and receiver lies on the same free surface. Richard's result simplified the theoretical computation for the calibration of surface-mount displacement-measurement-based AE sensors. Later Ohtsu employed the Green's function and moment tensor method in AE signal analysis, with a focus on surface displacement sensor (Ohtsu, 1984; Yuyama *et al*. 1988; Ohtsu, 1995). In Ohtsu's work, good agreement between the measured signal and simulated signal was observed, which verified the validity of applying moment tensor and Green's function method in AE signal analysis.

As stated before, few theoretical formulations have been reported for stress wave-induced AE strain signal, e.g., using piezoelectric film AE sensors, and applications involving the use of piezoelectric film-based strain sensors fall within relatively low frequency ranges, i.e. below 10 kHz. Therefore, a theoretical study is needed to relate AE source with stress-wave induced AE strain signal over a broad ultrasonic frequency range. The key issue here is to derive the dynamic Green's function for strain. Generally speaking, analytical form of Greens' function can only be derived for a limited number of cases of geometrical configuration (e.g., the Green's function of a homogeneous, isotropic infinite space). In practice, the Green's function of half space and Green's function of infinite plate are of most interest since these solutions provide good approximations under many real application conditions. As for civil structures, the plate thickness is relatively large and a lot of times can be treated as half space, thus the studies in this chapter will mainly focus on the case of half space.

Let g_{ij} (x_1, x_2, 0, t ; x_1', x_2', x_3',t') represent the displacement in the i-th direction at the sensor location (x_1,x_2,0) due to a unit impulse force in the j-th direction applied at location (x_1', x_2', x_3'). Without loss of generality, the values of x_1' and x_2' are assumed to be zero. Figure 4.2 shows the relative positions and dimensions of the sensor and AE source. If G denotes a matrix whose components are g_{ij}, then G is the Green's function.

For the Green's function and first order spatial derivative of Green's function for a half space, theory has been well established as summarized by Johnson (1974). The Green's function for a half space when the sensor lies on the free surface can be written in the transformed domain s as (Johnson, 1974),

$$G(x_1,x_2,0,s;0,0,x_3^{'},0)=\frac{-1}{4\pi^2\mu}\int_{-i\infty}^{i\infty}\int\left[\frac{\exp(-v_\alpha x_3^{'})}{d}M(\xi_1,\xi_2,0,s,x_3^{'},0)F\right] + \left[\frac{\exp(-v_\beta x_3^{'})}{d}N(\xi_1,\xi_2,0,s,x_3^{'},0)F\right]\exp(\xi_1 x_1+\xi_2 x_2)d\xi_1 d\xi_2 \tag{4.12}$$

The corresponding Green's functions in the time domain can be obtained accordingly. However, for stress wave-induced AE strain signal analysis, second order spatial derivative of the Green's function is needed. As only in-plane strain is of interest to the application of stress wave-induced AE strain sensor, only $G_{1i,j1'}$ and $G_{2i,j2'}$ will be formulated here. Taking the $G_{11,11'}$ as an example, the second order spatial derivative can be made inside the integral as follows,

$$G_{11,1'1'}(x_1,x_2,0,s;0,0,x_3^{'},0)=\frac{1}{4\pi^2\mu}\int_{-i\infty}^{i\infty}\int\left[\frac{\exp(-\nu_\alpha x_3^{'})}{d}M_{11}(\xi_1,\xi_2,0,s,x_3^{'},0)F\right]$$
$$+\left[\frac{\exp(-\nu_\beta x_3^{'})}{d}N_{11}(\xi_1,\xi_2,0,s,x_3^{'},0)F\right](-\xi_1)\xi_1\exp(\xi_1x_1+\xi_2x_2)d\xi_1d\xi_2$$

(4.13)

Following the general Cagniard - de Hoop method with modification made by de Hoop (1960 and 1961), solutions in the time domain could be obtained as shown in Eq. (4.14). Details of obtaining the solutions in the time domain from the transformed domain have been expounded by de Hoop (1960, 1961). Although it is for the case of Green's function and the first order of Green's function, the general approach can be extended to the solution of the second order spatial derivatives. Therefore, the details on how to obtain the solutions in time domain for second order spatial derivatives of Green's function are omitted here, with only the final results presented below,

$$G_{11,1'1}(x_1,x_2,0,t;0,0,x_3^{'},0)=$$
$$\frac{1}{\pi^2\mu r}\frac{\partial^3}{\partial t^3}\int_0^{((t/r)^2-\alpha^{-2})^{1/2}}H(t-r/\alpha)$$
$$\times\mathrm{Re}[\eta_\alpha\sigma^{-1}((t/r)^2-\alpha^{-2}-p^2)^{-1/2}M_{11,1'1}(q,p,0,t,x_3^{'})]Fdp$$
$$+\frac{1}{\pi^2\mu r}\frac{\partial^3}{\partial t^3}\int_0^{p_2}H(t-t_2)$$
$$\times\mathrm{Re}[\eta_\beta\sigma^{-1}((t/r)^2-\beta^{-2}-p^2)^{-1/2}N_{11,1'1}(q,p,0,t,x_3^{'})]Fdp$$

(4.14)

In which, *H* is the unit Heaviside step function and Re denotes the real part. Also,

$$\begin{cases}M_{11,1'1}=2\eta_\beta(q^4\cos^4(\phi)-6p^2q^2\sin^2(\phi)\cos^2(\phi)+p^4\sin^2(\phi))\\ N_{11,1'1}=\eta_\beta{}^{-1}[\eta_\beta{}^2\gamma(q^2\cos^2(\phi)-p^2\sin^2(\phi))+(4\eta_\alpha\eta_\beta-\gamma)\cdot\\ \qquad((q^4+p^4+4p^2q^2)\sin^2(\phi)\cos^2(\phi)-p^2q^2(\sin^4(\phi)+\cos^4(\phi)))]\end{cases}\quad(4.15)$$

In order to be consistent with the Green's function and the first order derivative of the Green's function, the same notations for the variables in Johnson's paper (1974) are used here to formulate the second order spatial derivative of Green's function. These parameters are p_2, t_2, γ, σ, η_α, η_β, q, as defined by Johnson (1974) as,

$$p_2 = \begin{cases} ((t/r)^2 - \beta^{-2})^{1/2} & \sin(\theta) \le \beta/\alpha \\ \left[\left(\dfrac{t/r - (\beta^{-2} - \alpha^{-2})^{1/2} \cos(\theta)}{\sin(\theta)} \right)^2 - \alpha^{-2} \right]^{1/2} & \sin(\theta) > \beta/\alpha \end{cases} \tag{4.16}$$

$$t_2 = \begin{cases} r/\beta & \sin(\theta) \le \beta/\alpha \\ r/\alpha \sin(\theta) + r(\beta^{-2} - \alpha^{-2})^{1/2} \cos(\theta) & \sin(\theta) > \beta/\alpha \end{cases} \tag{4.17}$$

$$\gamma = \eta_\beta + p^2 - q^2 \tag{4.18}$$

$$\sigma = \gamma^2 + 4\eta_\alpha \eta_\beta (p^2 - q^2) \tag{4.19}$$

$$\begin{aligned} \eta_\alpha &= (\alpha^{-2} + p^2 - q^2)^{1/2} \qquad \mathrm{Re}\{\eta_\alpha\} \ge 0 \\ \eta_\beta &= (\beta^{-2} + p^2 - q^2)^{1/2} \qquad \mathrm{Re}\{\eta_\beta\} \ge 0 \end{aligned} \tag{4.20}$$

It's worth noting that in the first integral term of Eq. (4.14)

$$q = -t/r \sin(\theta) + i((t/r)^2 - \alpha^{-2} - p^2)^{1/2} \cos(\theta) \qquad \mathrm{Re}\{\eta_\alpha\} \ge 0 \tag{4.21}$$

While in the second integral term of Eq. (4.14),

$$q = -t/r \sin(\theta) + i((t/r)^2 - \beta^{-2} - p^2)^{1/2} \cos(\theta) \qquad \mathrm{Re}\{\eta_\alpha\} \ge 0 \tag{4.22}$$

A full list of the corresponding components in the above equations are expressed as follows,

$$
\begin{cases}
M_{11,1'1} = -2\eta_\beta(q^4\cos^4(\phi) - 6p^2q^2\sin^2(\phi)\cos^2(\phi) + p^4\sin^2(\phi)) \\
M_{11,2'1} = -2\eta_\beta(q^4\cos^2(\phi) - p^4\sin^2(\phi) + 3p^2q^2(\cos^2(\phi) - \sin^2(\phi)))\sin(\phi)\cos(\phi) \\
M_{11,3'1} = -2\eta_\alpha\eta_\beta(q^2\cos^2(\phi) - 3p^2\sin^2(\phi))q\cos(\phi) \\
M_{12,1'1} = M_{11,21'} \\
M_{12,2'1} = -2\eta_\beta[(q^2\cos^2(\phi) - p^2\sin^2(\phi))(q^2\sin^2(\phi) - p^2\cos^2(\phi)) \\
\qquad +4p^2q^2\sin^2(\phi)\cos^2(\phi)] \\
M_{12,3'1} = -2\eta_\alpha\eta_\beta[q^2\cos^2(\phi) - p^2\sin^2(\phi) + 2p^2\cos^2(\phi)]q\sin(\phi) \\
M_{13,1'1} = -2\eta_\alpha\eta_\beta(q^2\cos^2(\phi) - 3p^2q\sin^2(\phi))q\cos(\phi) \\
M_{13,2'1} = -2\eta_\alpha\eta_\beta(q^2\cos^2(\phi) - p^2\sin^2(\phi) + 2p^2\cos^2(\phi))q\sin(\phi) \\
M_{13,3'1} = -2\eta_\alpha^2\eta_\beta(q^2\cos^2(\phi) - p^2\sin^2(\phi))
\end{cases}
$$

(4.23)

$$
\begin{cases}
M_{21,1'2} = M_{12,21'} \\
M_{21,2'2} = -2\eta_\beta(q^4\sin^2(\phi) - p^4\cos^2(\phi) + 3p^2q^2(\sin^2(\phi) - \cos^2(\phi)))\sin(\phi)\cos(\phi) \\
M_{21,3'2} = -2\eta_\alpha\eta_\beta(q^2\sin^2(\phi) - p^2\cos^2(\phi) + 2p^2\sin^2(\phi))q\cos(\phi) \\
M_{22,1'2} = M_{21,22'} \\
M_{22,2'2} = -2\eta_\beta(q^4\sin^4(\phi) - 6p^2q^2\sin^2(\phi)\cos^2(\phi) + p^4\cos^2(\phi)) \\
M_{22,3'2} = -2\eta_\alpha\eta_\beta(q^2\sin^2(\phi) - 3p^2\cos^2(\phi))q\sin(\phi) \\
M_{23,1'2} = -2\eta_\alpha\eta_\beta[q^2\sin^2(\phi) - p^2\cos^2(\phi) + 2p^2\sin^2(\phi)]q\cos(\phi) \\
M_{23,2'2} = -2\eta_\alpha\eta_\beta(q^2\sin^2(\phi) - 3p^2\cos^2(\phi))q\sin(\phi) \\
M_{23,3'2} = -2\eta_\alpha^2\eta_\beta(q^2\sin^2(\phi) - p^2\cos^2(\phi))
\end{cases}
$$

(4.24)

While

$$
\begin{cases}
N_{11,1'1} = -\eta_\beta^{-1}[\eta_\beta^{\,2}\gamma(q^2\cos^2(\phi) - p^2\sin^2(\phi)) + (4\eta_\alpha\eta_\beta - \gamma)\cdot \\
\qquad ((q^4 + p^4 + 4p^2q^2)\sin^2(\phi)\cos^2(\phi) - p^2q^2(\sin^4(\phi) + \cos^4(\phi)))] \\
N_{11,2'1} = -\eta_\beta^{-1}[\eta_\beta^{\,2}\gamma(q^2 + p^2) + (4\eta_\alpha\eta_\beta - \gamma)\cdot \\
\qquad (q^4\sin^2(\phi) - p^4\cos^2(\phi) + 3p^2q^2(\sin^2(\phi) - \cos^2(\phi)))]\sin(\phi)\cos(\phi) \\
N_{11,3'1} = -[\eta_\beta^{\,2}\gamma + (4\eta_\alpha\eta_\beta - \gamma)\cdot(q^2\sin^2(\phi) - p^2\cos^2(\phi) + 2p^2\sin^2(\phi))]q\cos(\phi) \\
N_{12,1'1} = -\eta_\beta^{-1}(\gamma - 4\eta_\alpha\eta_\beta)[(q^2\cos^2(\phi) - 3p^2\sin^2(\phi))q^2 + \\
\qquad p^2(3q^2\cos^2(\phi) - p^2\sin^2(\phi))]\sin(\phi)\cos(\phi) \\
N_{12,2'1} = -\eta_\beta^{-1}(\gamma - 4\eta_\alpha\eta_\beta)[(q^2\cos^2(\phi) - p^2\sin^2(\phi))(q^2\sin^2(\phi) - p^2\cos^2(\phi)) \\
\qquad +4p^2q^2\sin^2(\phi)\cos^2(\phi)] \\
N_{12,3'1} = -(\gamma - 4\eta_\alpha\eta_\beta)[q^2\cos^2(\phi) - p^2\sin^2(\phi) + 2p^2\cos^2(\phi))]q\sin(\phi) \\
N_{13,1'1} = \gamma(q^3\cos^2(\phi) - 3p^2q\sin^2(\phi))\cos(\phi) \\
N_{13,2'1} = \gamma(q^3\cos^2(\phi) - 3p^2q\sin^2(\phi) + 2p^2q\cos^2(\phi))\sin(\phi) \\
N_{13,3'1} = \eta_\beta\gamma(q^2\cos^2(\phi) - p^2\sin^2(\phi))
\end{cases}
\tag{4.25}
$$

$$
\begin{cases}
N_{21,1'2} = N_{12,21'} \\
N_{21,2'2} = -\eta_\beta^{-1}(\gamma - 4\eta_\alpha\eta_\beta)[(q^4\sin^2(\phi) - 3p^2q^2\cos^2(\phi)) + \\
\qquad 3p^2q^2\sin^2(\phi) - p^4\cos^2(\phi)]\sin(\phi)\cos(\phi) \\
N_{21,3'2} = -(\gamma - 4\eta_\alpha\eta_\beta)[q^2\sin^2(\phi) - p^2\cos^2(\phi) + 2p^2\sin^2(\phi)]q\cos(\phi) \\
N_{22,1'2} = -\eta_\beta^{-1}[\eta_\beta^{\,2}\gamma(q^2 + p^2) + (4\eta_\alpha\eta_\beta - \gamma)\cdot \\
\qquad (q^4\cos^2(\phi) - p^4\sin^2(\phi) + 3p^2q^2(\cos^2(\phi) - \sin^2(\phi)))]\sin(\phi)\cos(\phi) \\
N_{22,2'2} = -\eta_\beta^{-1}[\eta_\beta^{\,2}\gamma(q^2\sin^2(\phi) - p^2\cos^2(\phi)) + (4\eta_\alpha\eta_\beta - \gamma)\cdot \\
\qquad ((q^4 + p^4 + 4p^2q^2)\sin^2(\phi)\cos^2(\phi) - p^2q^2(\sin^4(\phi) + \cos^4(\phi)))] \\
N_{22,3'2} = -[\eta_\beta^{\,2}\gamma + (4\eta_\alpha\eta_\beta - \gamma)\cdot(q^2\cos^2(\phi) - p^2\sin^2(\phi) + 2p^2\cos^2(\phi))]q\sin(\phi) \\
N_{23,1'2} = \gamma(q^2\sin^2(\phi) - p^2\cos^2(\phi) + 2p^2\sin^2(\phi))q\cos(\phi) \\
N_{23,2'2} = \gamma(q^2\sin^2(\phi) - 3p^2\cos^2(\phi))q\sin(\phi) \\
N_{23,3'2} = \eta_\beta\gamma(q^2\sin^2(\phi) - p^2\cos^2(\phi))
\end{cases}
\tag{4.26}
$$

When implementing the above equations for numerical computation, singularity at either $((t/r)^2-\alpha^{-2})^{1/2}$ or $((t/r)^2-\beta^{-2})^{1/2}$ might happen. In order to avoid errors due to numerical instability, substitutions are recommended, including

$$p=((t/r)^2-\alpha^{-2}-p^2)^{1/2}-v^2 \text{ Or}$$

$$p=((t/r)^2-\alpha^{-2})^{1/2}\sin(v) \tag{4.27}$$

With the above substitution, singularity is avoided in the integrand.

4.3 Response of Piezoelectric Film AE Sensor to Surface Point Load

For the cases involving horizontal and vertical surface displacements, exact solutions have already been derived (Pinney, 1954; Pekeris, 1955a; Richard, 1979) and the results have been applied for AE displacement sensor calibration. However, few research works has been done for in-plane surface strain, especially for arbitrary values of Poisson's ratio. Due to the emerging use of piezoelectric film AE sensors, it is of importance to study the surface strain response to a vertical surface load. The result could be extended to the solution of surface crack source. Additionally, the formulations presented in this section can also be used for the calibration of such AE strain sensor.

In this section, the response of piezoelectric film AE sensor to a vertical force (acting in direction 3) is discussed. As indicated in Eq. (4.4), the AE strain sensor measures the summation of strains in direction 1 and 2. Thus, the fundamental solution represents the total surface strain response due to a vertical force.

4.3.1 Theoretical Formula

In order to study AE strain sensor's signal, the components of the Green's function $G_{13,1}$ and $G_{23,2}$ need to be known. Since it is known that

$$G_{13,1}(x_1, x_2, 0, t; 0, 0, x_3^{'}, 0) = -G_{13,1'}(x_1, x_2, 0, t; 0, 0, x_3^{'}, 0) \tag{4.28-a}$$

$$G_{23,2}(x_1, x_2, 0, t; 0, 0, x_3^{'}, 0) = -G_{23,2'}(x_1, x_2, 0, t; 0, 0, x_3^{'}, 0) \tag{4.28-b}$$

The total response is

$$G = G_{13,1} + G_{23,2} = -(G_{13,1'} + G_{23,2'}) \tag{4.28-c}$$

From Johnson's work (Johnson, 1974), it's known that

$$\begin{aligned} G(x_1, x_2, 0, t; 0, 0, x_3^{'}, 0) = & -\frac{1}{\pi^2 \mu r} \frac{\partial^2}{\partial t^2} \int_0^{p_1} H(t - r/\alpha) \\ & \times \mathrm{Re}[\eta_\alpha \sigma^{-1}((t/r)^2 - \alpha^{-2} - p^2)^{-1/2}(M_{13,1'} + M_{23,2'})]Fdp \\ & -\frac{1}{\pi^2 \mu r} \frac{\partial^2}{\partial t^2} \int_0^{p_2} H(t - t_2) \\ & \times \mathrm{Re}[\eta_\beta \sigma^{-1}((t/r)^2 - \beta^{-2} - p^2)^{-1/2}(N_{13,1'} + N_{23,2'})]Fdp \end{aligned} \tag{4.29}$$

Where

$$\begin{aligned} M_{13,1'} + M_{23,2'} &= -2\eta_\alpha \eta_\beta (q^2 - p^2) \\ N_{13,1'} + N_{23,2'} &= \gamma (q^2 - p^2) \end{aligned} \tag{4.30}$$

This can be further simplified following a similar procedure employed by Richards (1979) in his work on calculating the Green's function for surface displacement due to a surface impulse. Here, the total in-plane surface strains due to a surface impulse are derived and the result is shown in Eq. (4.31)

$$\varepsilon(t)=\frac{1}{\pi\mu r}\begin{cases} 0 & \text{for T < 1} \\ \dfrac{\partial^2}{\partial t^2}\left\{\dfrac{2A}{\pi\alpha}\displaystyle\int_0^{\pi/2}\frac{(P^2-1)(A-P^2)^{1/2}(A-2P^2)P^2}{(A-2P^2)^4-16X^2Y^2P^4}d\chi\right\} & \text{for1} < T < \alpha/\beta \\ \dfrac{\partial^2}{\partial t^2}\left\{\dfrac{2A}{\pi\alpha}\displaystyle\int_0^{\pi/2}\frac{(P^2-1)(A-P^2)\ (A-2P^2)P^2}{(T^2-P^2)^{1/2}[(A-2P^2)^4-16X^2Y^2P^4]}d\chi-\frac{H(T-R_3^{1/2})R_3c_8}{\alpha(T^2-R_3)^{1/2}}\right\} & \text{for } \alpha/\beta < T \end{cases} \tag{4.31}$$

Where in the first integral term of Eq. (4.31),

$$P^2=(T^2-1)\sin^2\chi+1 \tag{4.32-a}$$

While in the second integral term of Eq. (4.31),

$$P^2=(A-1)\sin^2\chi+1 \tag{4.32-b}$$

In Eq. (4.31), when $\alpha/\beta< T$, the second part results from the residual of complex integral at the pole of the integrand, where

$$c_8=\frac{1}{2}cA(A-2R_3)^3/R_3 \tag{4.33}$$

$$c=1/[16(A-1)(R_3-R_1)(R_2-R_3)] \tag{4.34}$$

R_3 is the largest root of the Rayleigh cubic which is always real and directly related to the Rayleigh wave speed; R_1 and R_2 are the other two roots of the Rayleigh cubic which are real if the Poisson's ratio is smaller than 0.263 and two complex conjugates if Poisson's ratio is greater than 0.263 respectively.

4.3.2 Simulation Study

For sensor calibration, a large steel block is used in this study, which has its parameter values listed in Table 1. The large steel block can be considered as a half space. AE strain sensors are mounted on the surface of the steel block, and the sensors are placed 5 cm away from a step force simulating a surface impulse. This forms a standard sensor calibration setup similar to that used for calibrating

conventional AE sensor (ASTM, 2007). Assume that the source function $S(t)$ is expressed as

$$dS(t)/dt = \sin^4(\pi t/T_r), \quad (0 < t < T_r) \tag{4.35}$$

Where T_r is the rise time and set to be 2 μs and the sampling rate is 10 MHz. The response of the AE strain sensor can be calculated from Eq. (4.31) as shown in Figure 4.3 (a). Figure 4.3(b) shows the corresponding frequency spectrum. It can be seen the frequency spectrum is broadband and it is observed that the flat frequency characteristics of AE strain signal is similar to AE displacement signal due to an impulsive force. This broadband frequency characteristics is favorable to AE strain sensor calibration.

Figure 4.4 shows the comparison of strains from numerical spatial derivative of displacement and from analytical calculation. Two results agree with each other at P arrival and S arrival. However, the numerical differentiation misses the Rayleigh peak, while the analytical result could accurately predict this peak, which has been verified with experimental data as shown in Figure 4.7 (a). From this comparison it can be seen that the analytical solution is more accurate than taking derivative of displacement signals

Discussion of stress wave attenuation relationship in the context of implementing the AE strain sensor is now in order. It is known that the P wave decays faster than the Rayleigh wave. In this study, it is found that for the in-plane AE strain signal, the amplitude of P wave decays at a rate of $r^{-1.1330}$ while the amplitude of Rayleigh wave attenuates at a rate of $r^{-0.4114}$ with distance r. This is consistent with the $r^{-1/2}$ Rayleigh wave attenuation relationship reported elsewhere

(Mooney, 1974). It should be noted that the trough and the peak of the Rayleigh wave amplitude decay at almost the same rate. Figure 4.5 plots the attenuation rates of P wave and Rayleigh wave amplitudes for vertical displacement, horizontal displacement and total in-plane strain respectively. It is seen that the P wave amplitude of strain decays fastest while the P wave amplitude of horizontal and vertical displacement decays at almost the same rate. For Rayleigh wave amplitude, there isn't much difference among these three modes. Both displacements decay at almost the same rate while the strain response decays at a slightly lower rate. This also suggests that AE features adopted for AE strain sensor can be based on the peak or trough of the Rayleigh wave because they are measurable at a greater distance than the P waves.

The concept of near-field AE monitoring could also be defined more precisely in terms of amplitude decay of P wave amplitude. Specifically, the near-field is defined here as the region where the P wave amplitude decay is no more than 90% percent of the value at 1-inch distance from the crack source. For example, for surface step force on a large steel block, the near-field area would be ten inches according to this criterion.

4.3.3 Experimental Study

Impulsive force acting on the surface of a half space is a very popular AE source that has been long used for experimental validation test of AE instrumentation (ASTM, 2007). Glass capillary break and pencil lead break are commonly used for simulating the step force. In this study, glass capillary break was used to generate surface force since it is closer to a step force (Kim and Kim, 1993).

Figure 4.6 shows the experimental stet up used for this study. The half space medium is physically simulated by a large steel block with a dimension of 508 x 508 x 102 mm (20 x 20 x 4 inches) and glass capillary break is used to simulate the step AE source. The procedure of breaking glass capillary follows the ASTM standard E1106-07. An 18×18×0.13 mm cover glass was put on the steel surface. The glass capillary has a 0.4 mm outer diameter and was rest on the cover glass plate. A glass rod of a 2 mm diameter was put on the top of the capillary. This rod is to transfer the force to the glass capillary from the loading screw. Three circular PZT based strain sensors with diameters of 5 mm, 7 mm and 10 mm respectively were mounted on the steel surface using conductive epoxy. Signal conditioning units consisting of a 40 dB pre-amplifier and a 5 to 600-kHz band-pass filter were connected to the three AE strain sensors before data acquisition. For comparison purpose, a commercial broadband AE sensor (model # SE 1000-HI) made by Dunegan Engineering Company, Inc. was also used in the test. Unlike the AE strain sensor, this commercial AE sensor measures the out-of-plane displacement (i.e., the displacement perpendicular to the steel block surface) with a 20 dB pre-amplifier. The Four sensors are equally distanced from their centers to the impulsive AE source simulated with glass capillary break.

The signal acquired by the PZT-based AE strain sensors with a diameter of 5-mm is shown in Figure 4.7(a) and its corresponding frequency spectrum is shown in Figure 4.7 (b). Compared with the theoretical strain signal in Figure 4.4 (a), the experimental data agrees very well with the theoretical prediction. The P, S and Rayleigh wave arrival can be clearly identified. The frequency spectrum of the

experimental signal is relatively flat. This also matches the frequency spectrum characteristics of the theoretical curve and suggests the suitability of using glass capillary break for AE strain sensor calibration.

Figure 4.8 shows the signals collected by all four AE sensors. The signal from the commercial AE sensor (SE 1000-HI) is easily recognized as a displacement waveform due to an approximate step force generated by glass capillary breakage (Proctor, 1982). For the three AE stain sensors, comparing the waveforms from 5-mm, 7-mm and 10-mm diameter PZT sensors, the waveforms from 5-mm diameter sensor is closer to the theoretical one and it is much cleaner. For sensor with larger aperture, such as the 10-mm PZT sensor, the duration of the Rayleigh arrival gets larger due to larger sensor size, which is also verified by the numerical simulation shown in Figure 4.9. When the sensor size gets larger, this averaging effect will get stronger and the shape of the signal would also change. Furthermore, from the test result, it's seen that not only the wave pulse gets wider but also the wave arrival becomes more difficult to identify. Considering S arrival identification in Figure 4.8 as an example, it's much harder for a 10-mm diameter PZT disc sensor than those for the 5-mm and 7-mm PZT disc sensors. Thus to detect strain signal with high fidelity, smaller sensor aperture is desirable. All the three sensors agree very well with each other in terms of the general waveform shape and the arrival time of each wave component. This confirms the suitability of using piezoelectric film strain sensor for near field AE signal monitoring in ultrasonic frequency range.

4.4 Signal Characteristics: Parametric Study

4.4.1 Source Location

To understand the signal characteristics of stress-wave-induced AE strain signals in near-field monitoring, a parametric study was carried out. The concerned parameters are: depth of source locations (surface crack or buried crack), cracking types (tensile crack or shear crack), sensor distance from the crack source and structural materials (steel or aluminum). Two crack depth values (1 mm and 5 mm) and horizontal projection distance (0.05 and 0.1 m) from the AE source to the sensor are considered. The values of material properties used in the parametric study are listed in Table 1. All of the case studies are based on a buried fatigue crack with a crack volume of 1×10^{-15} m^3 and a source time function shown in Eq. (4.35). The AE strain data are sampled from elastodynamic solutions at a sampling rate of 5 MHz.

Table 4.1. Material properties adopted for the parametric study

Material	Poisson's ratio	Density (kg/m^3)	Young's modulus (GPa)	P-wave speed (km/s)	S-wave speed (km/s)
Steel	0.3	7850	200	5.8564	3.1304
Aluminum	0.33	2700	72	6.2857	3.1662

Instead of studying individual second order spatial derivative of Green's function component, a combination of several second order spatial derivative of Green's function components are used to represent the crack mode, since real AE sources are usually represented by a combination of several Greens' function components (Ohtsu, 1995). Among all possible AE sources, cracking is of most interest, such as fatigue crack in metallic structure or smeared cracks in concrete structure. Particularly, two common crack modes are chosen for parametric study - the tensile crack and shear crack.

In Figures 4.10 to 4.13, sharp rise can be seen in the AE strain signal. In general, the amplitude of Raleigh wave arrival is much larger than P arrival and S wave arrival. In some cases, the Raleigh wave arrival even goes to infinite (if the source lies on the surface and has an infinitesimal rise time). The P arrival is larger than the S arrival. Compared with P arrival and Raleigh arrival, the S arrival is negligible.

Additionally, in Figures 4.10 and 4.11 which have a small crack source depth value of 1-mm, it is seen that the Rayleigh waves become more dominant compared with the P waves when the AE sensor moves away from the source (from 0.05 m to 0.1 m). In another word, P wave attenuates at a faster rate than the Raleigh wave. The waveform of the Rayleigh arrival looks closer to a tone-burst signal. The same conclusion can be drawn by comparing the signals shown in Figures 4.12 and 4.13. It can also be seen that the AE signals generated by shear crack attenuate faster than the signal generated by tensile type crack. In Figures 4.11 and 4.13, it is observed that the peak value of the shear type crack signal is one order of magnitude lower when the depth of the crack source increases from 1mm to 5mm. However, the peak value of the tensile type crack signal magnitude is nearly on the same order when the sensor depth changes from 1mm to 5mm as shown in Figures 4.10 and 4.12.

By comparing the AE strain signals shown in Figures 4.10 to 4.13, it is observed that deeper crack source would have weaker AE signals. Furthermore, the signal attenuation with distance becomes more apparent when the crack source depth increases. If the signal is expressed using the normalized time of $t\alpha/r$, its magnitude would be inversely proportional to the source depth r.

4.4.2 Comparison of Different Materials

Steel and aluminum are commonly used materials in civil engineering. They are different in Poisson's ratio, material density and Young's modulus. These differences would be reflected in the signal waveform. In this study, the simulation was based on one of the previous case - a buried tensile crack at a depth of 5 mm. It is seen from Figures 4.14 that the AE signal in steel has a slightly larger amplitude than the signal in aluminum (the starting point of signals have been shifted to the same point for comparison). That's to say, a stronger signal would be expected in steel structure. This is especially significant for P arrival. Also, the elapsed time between the P arrival and Raleigh arrival in steel is shorter than that of the aluminum, which is similar to the findings reported for displacement signal by Mooney (1974).

4.5 Application of AE Strain Sensors

Crack induced AE signal is related to force couples/dipoles, which have certain directions and usually can be predetermined in practice based on engineering experience. To make some useful suggestions to choose the location for installing AE strain sensors, two cases are considered: sensor in the crack's propagation direction (e.g. station A) and in the normal of crack's propagation direction (e.g. station B). Since different combinations of Green's functions and moment tensors are used for tensile and shear cracks, the conclusion might depend on the crack type. In Figure 4.15 (a), it shows the simulated AE signals due to tensile crack when AE strain sensors are placed at these two stations. The signal at station A is significantly larger than the signals at station B, that's to say, placing AE strain sensor towards the fatigue crack propagation direction would give stronger signals thus higher SNR

value. However, it's another story for out-of-plane tensile crack, which would make the stations A and B have the same response as shown in Figure 4.15(b).

For shear crack, the conclusion might be different. Figure 4.16(a) shows the simulated AE signal for shear crack with crack surface parallel with x_1- x_2 plane (sensor surface plane). In this case, signals at two locations are identical, which means there is no preference for AE sensor placement for in plane shear crack. For out of plane shear crack (e.g. in plane x_2-x_3), there do exist some significant difference for different locations as shown in Figure 4.16 (b). It can be seen that there would be no signal output if sensors are put at station B while at station A good measurement with higher SNR value could be made. According to this study, it's suggested that putting AE strain sensors on the normal of tensile crack surface or in the plane of shear crack surface.

4.6 Conclusions

This chapter presents the elastodynamic solutions of stress-wave induced AE strain signal in near-field. Its signal characteristics are analyzed through moment tensor weighted Green's function. The generalized expression for strain signal is presented. The theoretical formulation of Green's function for the surface strain due to AE source is derived from the well-established solution of the Green's function in half space due to a Heaviside step force.

A formulation of AE strain sensor's response to surface pulse was presented to provide the theoretical basis for the calibration of piezoelectric film AE sensors. Compared with direction numerical solutions, this analytical formula is more accurate

since it avoids the error that could be generated from numerical differentiation of displacement signals with respect to spatial coordinates.

To understand the signal characteristics of stress-wave-induced AE strain signals in near-field monitoring, a parametric study that investigate the effects of different materials, source depths and cracking modes are conducted. These signal characteristics include the arrival time and distance attenuation relationship of the P, S and Raleigh waves. Sharp rise can be seen in the AE strain signal. In general, the amplitude of Raleigh wave arrival is much larger than P arrival and S wave arrival. It is also observed that deeper crack source would have weaker AE signals. Furthermore, the signal attenuation with distance becomes more apparent when the crack source depth increases. In terms of different structural materials, the AE strain signal in steel has a slightly larger amplitude than the signal in aluminum.

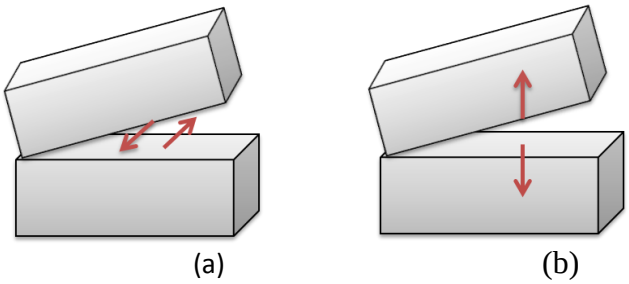

Figure 4.1 : Schematics of fracture mode: (a) shear crack mode; (b) tensile crack mode

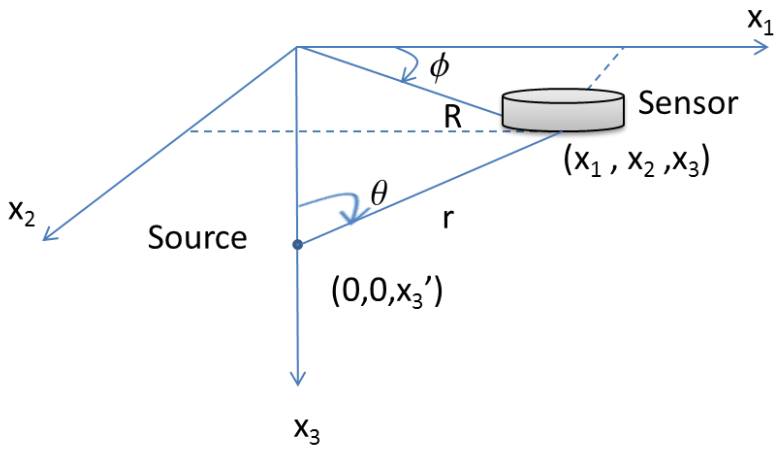

Figure 4.2: Schematics of AE strain sensor and crack source locations in a half space

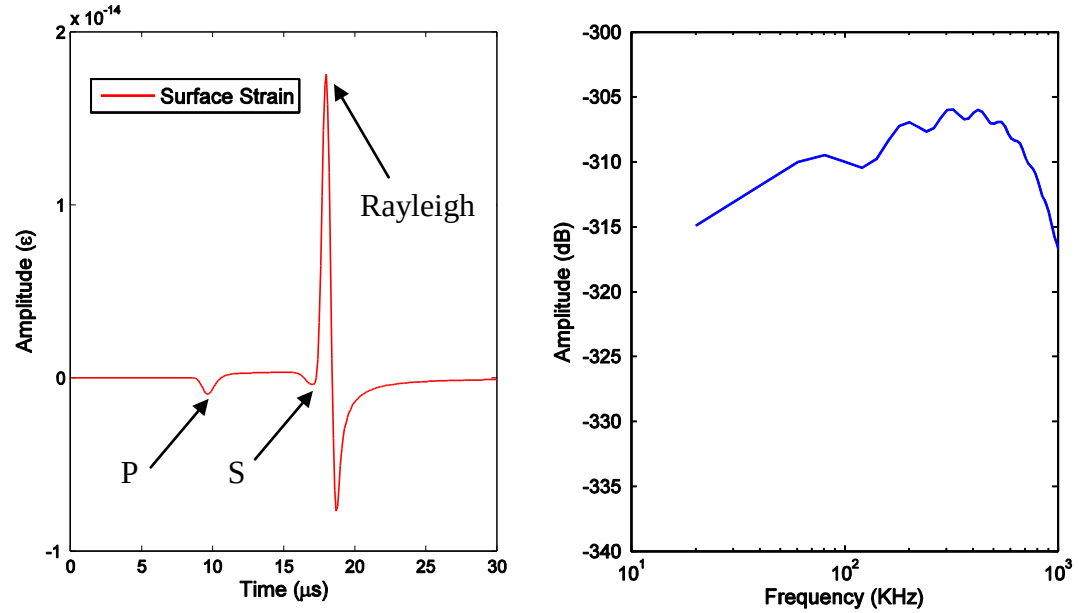

(a) (b)

Figure 4.3: AE strain sensor calibration curve (aperture effect not considered): (a) signal waveform; (b) frequency spectrum

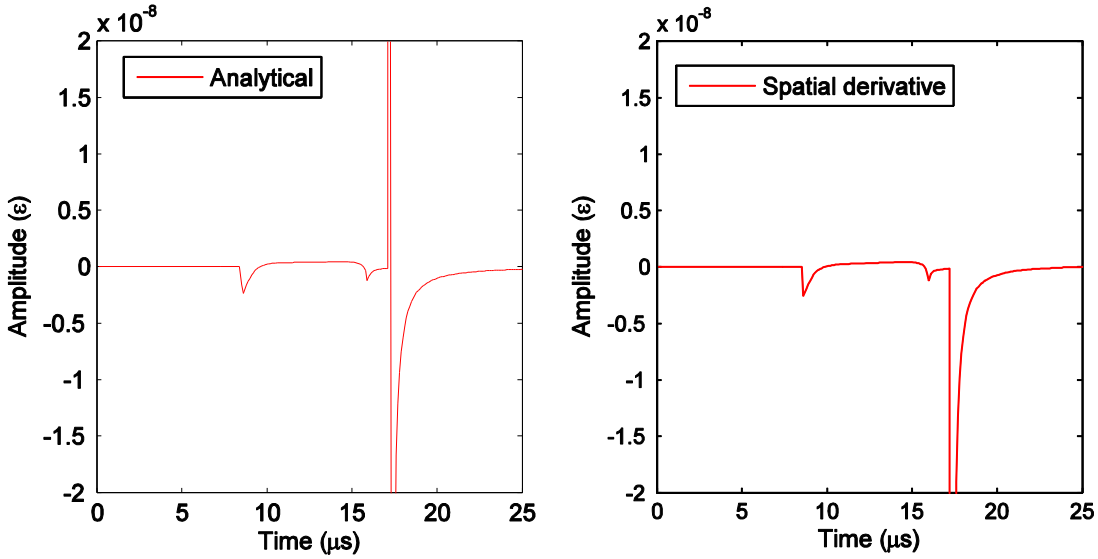

(a) (b)

Figure 4.4: Comparison of strains from analytical result and numerical differentiation of displacement: (a) analytical solution; (b) spatial derivation of displacement

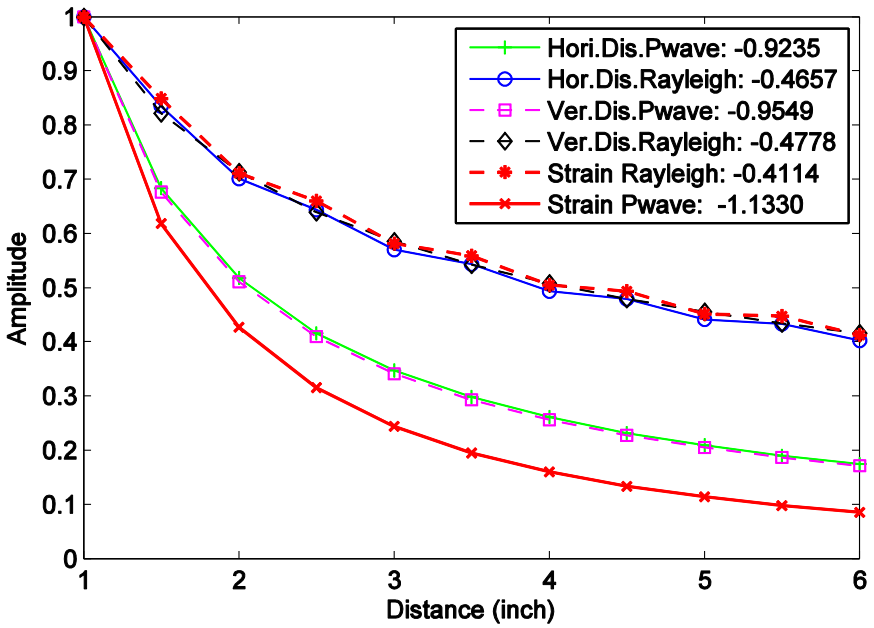

Figure 4.5: Attenuation relationship of AE strain signal in half space with distance

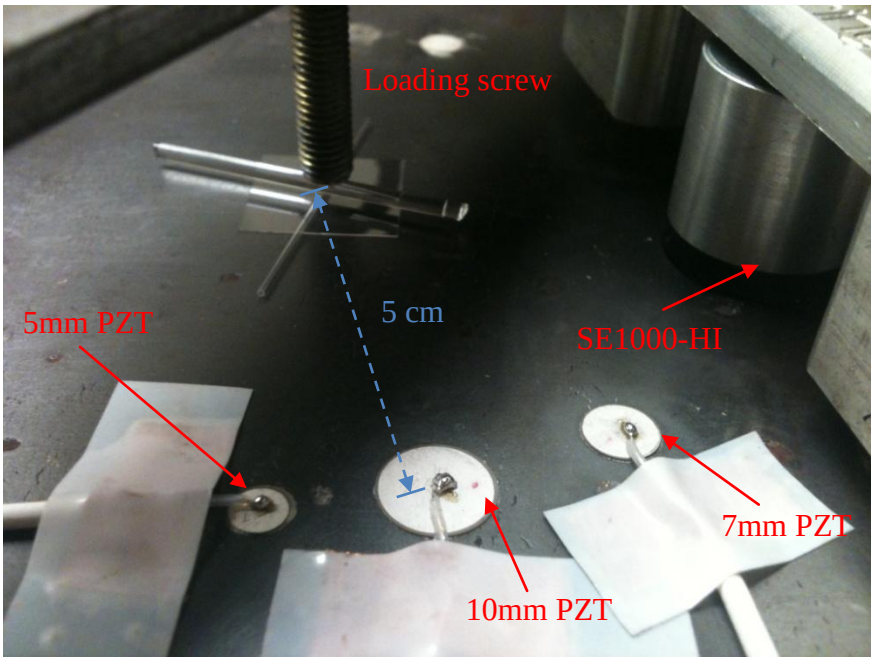

Figure 4.6: Experimental setup for AE signal calibration on steel block

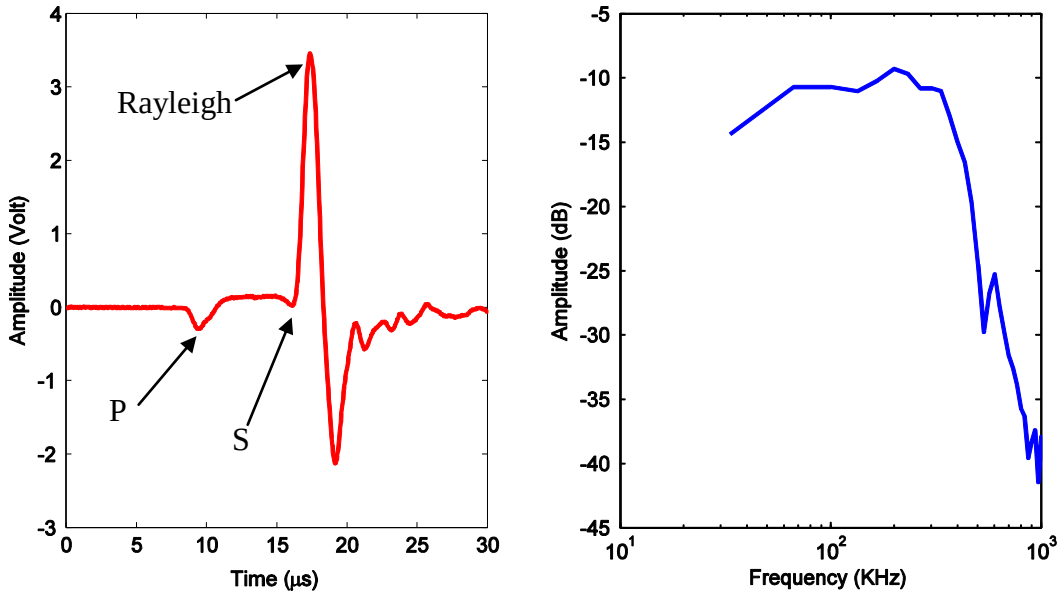

Figure 4.7: AE strain response to a glass capillary breaking event obtained by a PZT sensor with 5-mm diameter: (a) AE Signal; (b) frequency spectrum

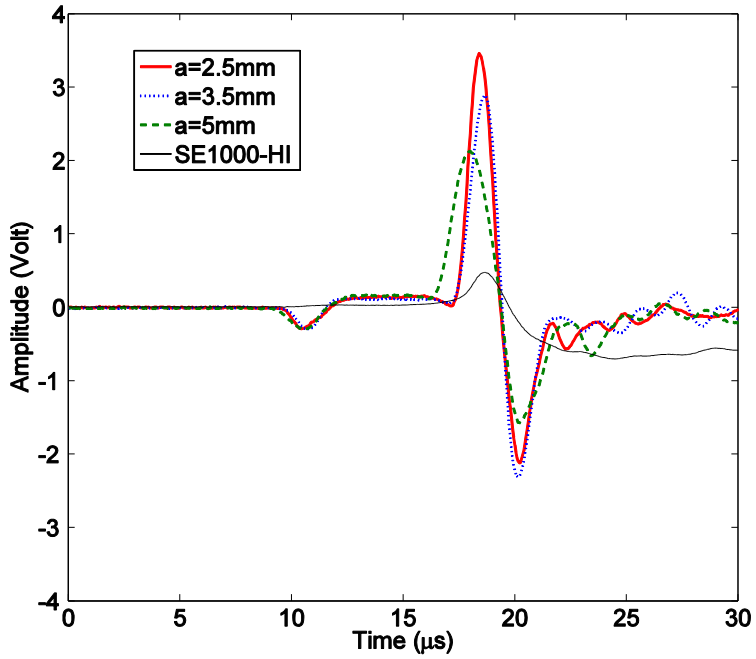

Figure 4.8: Comparison of experimental AE signals measured by different AE sensors in glass capillary breaking test (a is the PZT sensor radius)

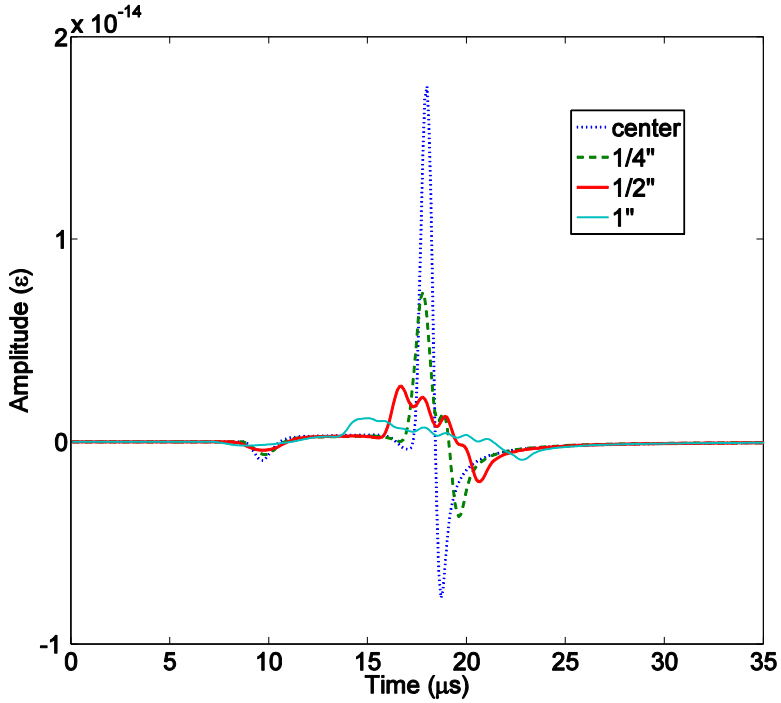

Figure 4.9: Simulated AE strain signals by sensors with different sensor diameters

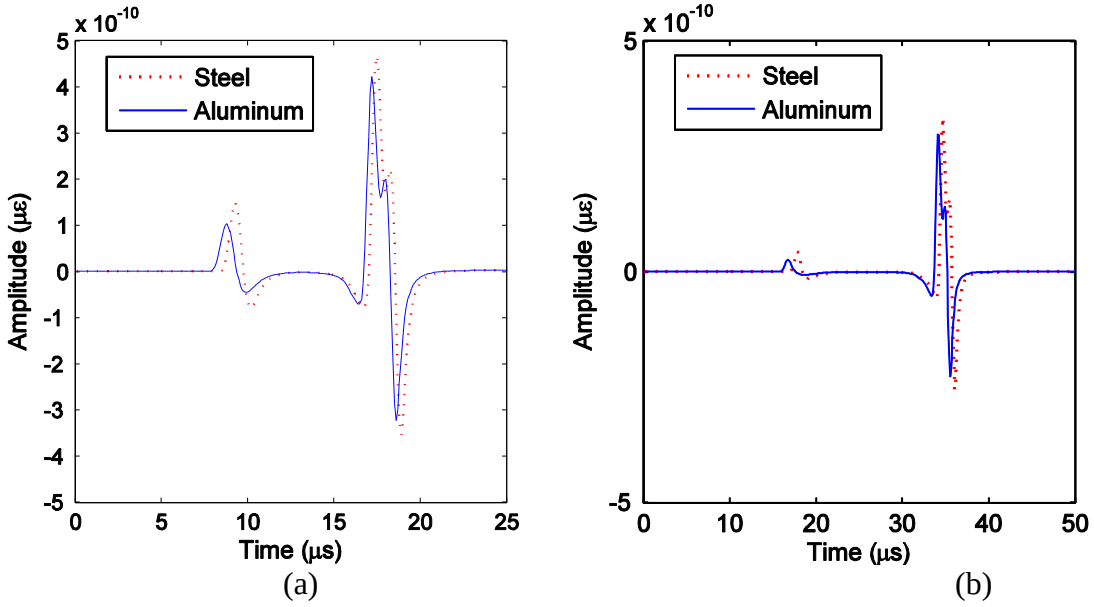

Figure 4.10: Comparison of surface AE strains due to tensile cracking simulated with a buried step source at a depth of 1-mm in a half space: (a) distance = 0.05 m; (b) distance = 0.1 m

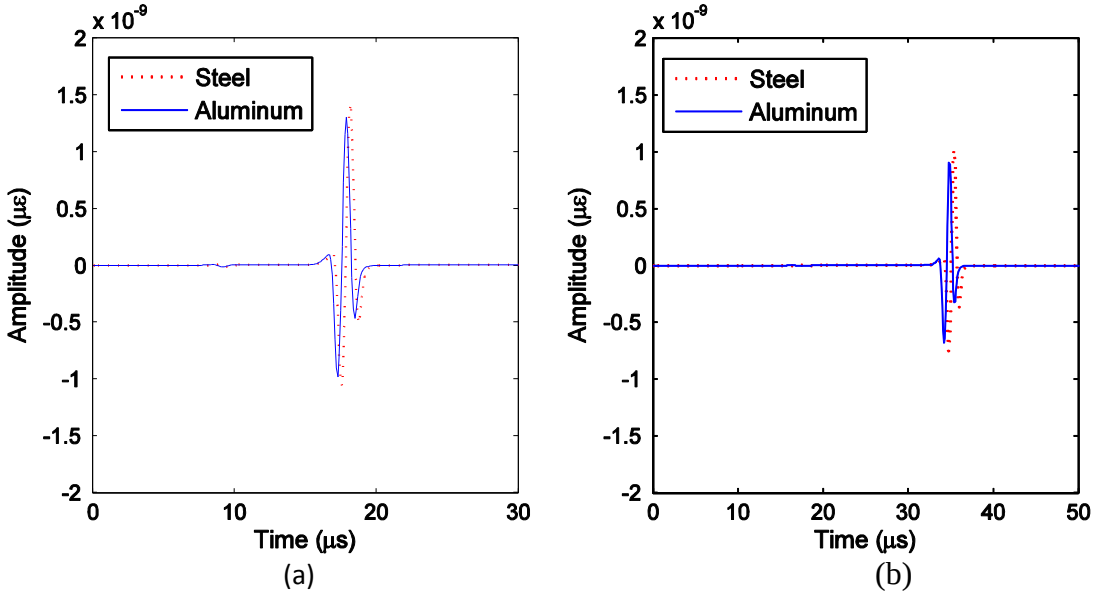

Figure 4.11: Comparison of surface AE strains due to shear cracking simulated with a buried step source at a depth of 1-mm in a half space: (a) distance = 0.05 m; (b) distance = 0.1 m

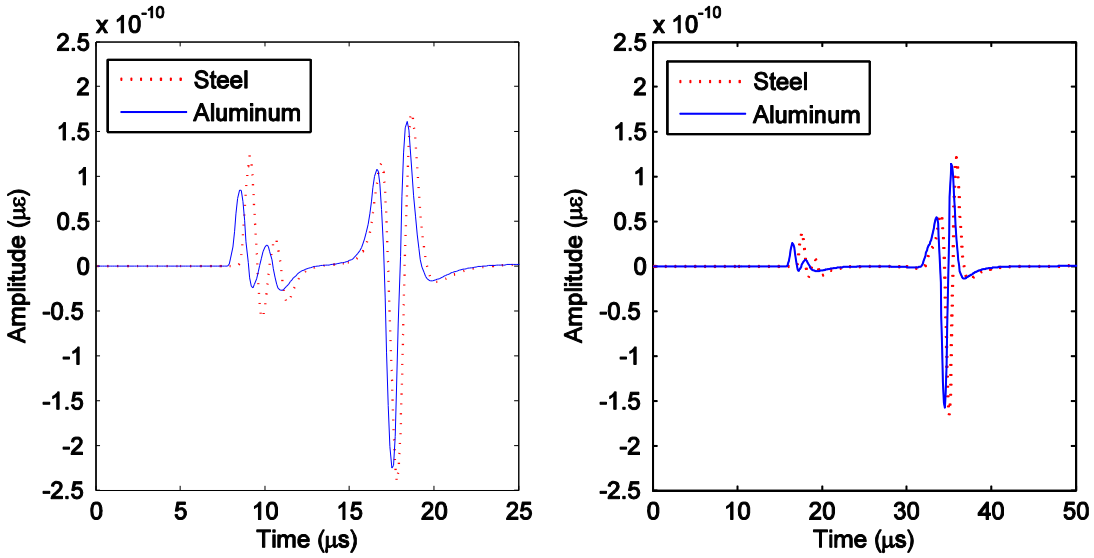

Figure 4.12: Comparison of surface AE strains due to tensile cracking simulated with a buried step source at a depth of 5-mm in a half space: (a) distance = 0.05 m; (b) distance = 0.1 m

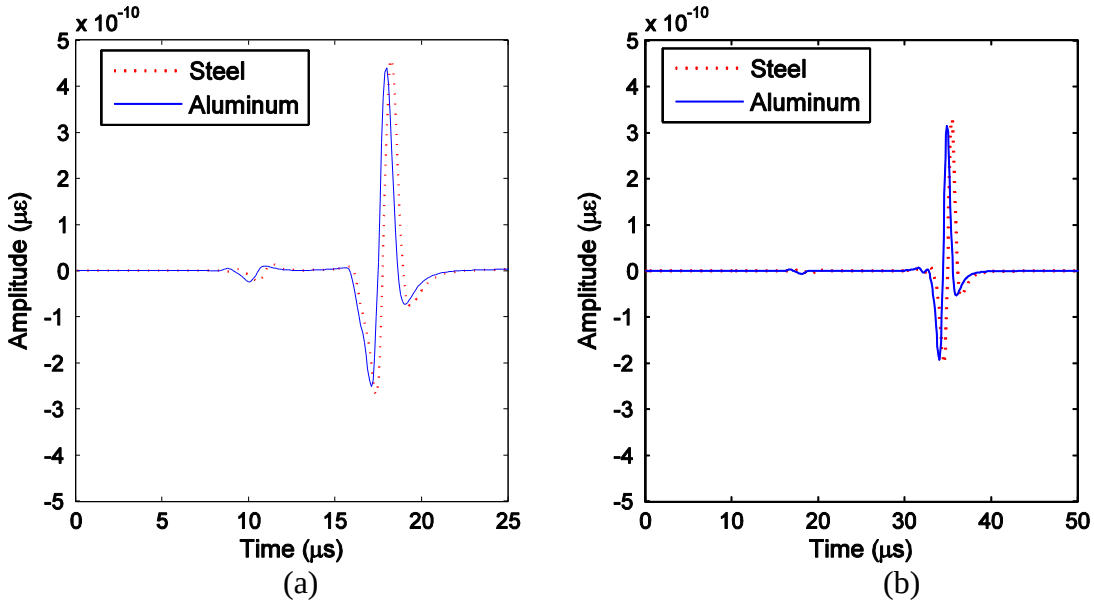

Figure 4.13: Comparison of surface AE strains due to shear cracking simulated with a buried step source at a depth of 5-mm in a half space: (a) distance = 0.05 m; (b) distance = 0.1 m

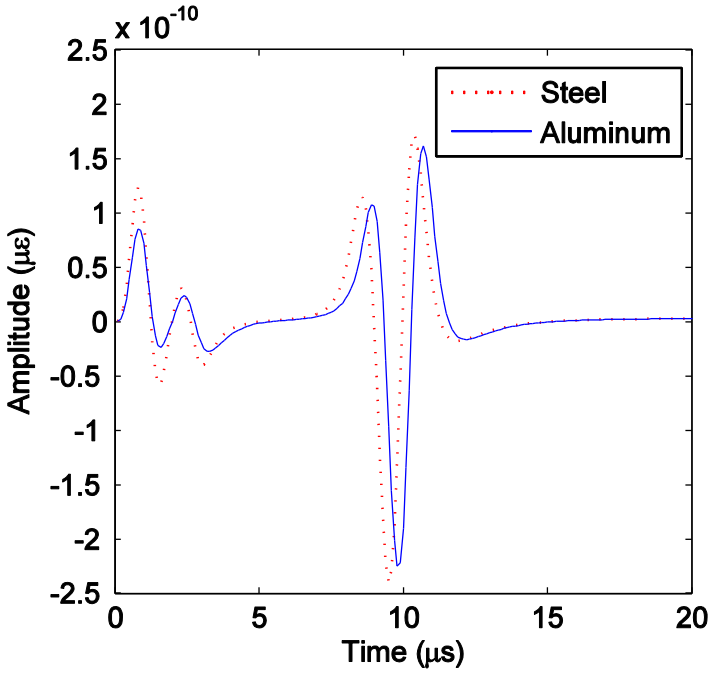

Figure 4.14: Comparison of AE strain signals in different materials

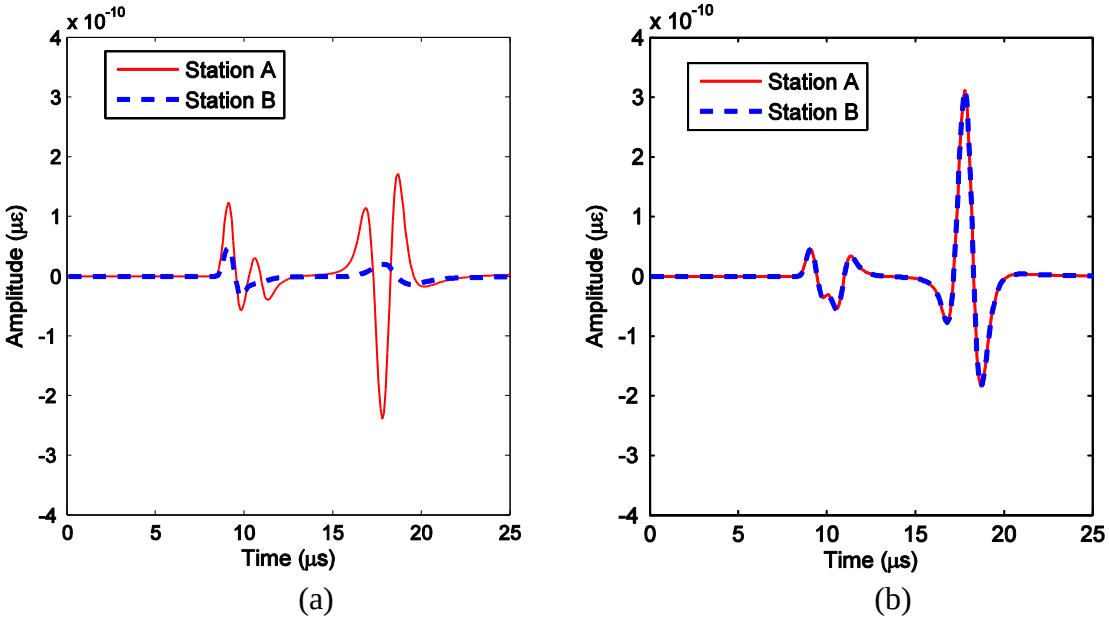

Figure 4.15: Comparison of AE strains at different measurement station due to tensile cracking simulated with a buried step source at a depth of 5-mm in a half space: (a) in plane crack; (b) out of plane crack

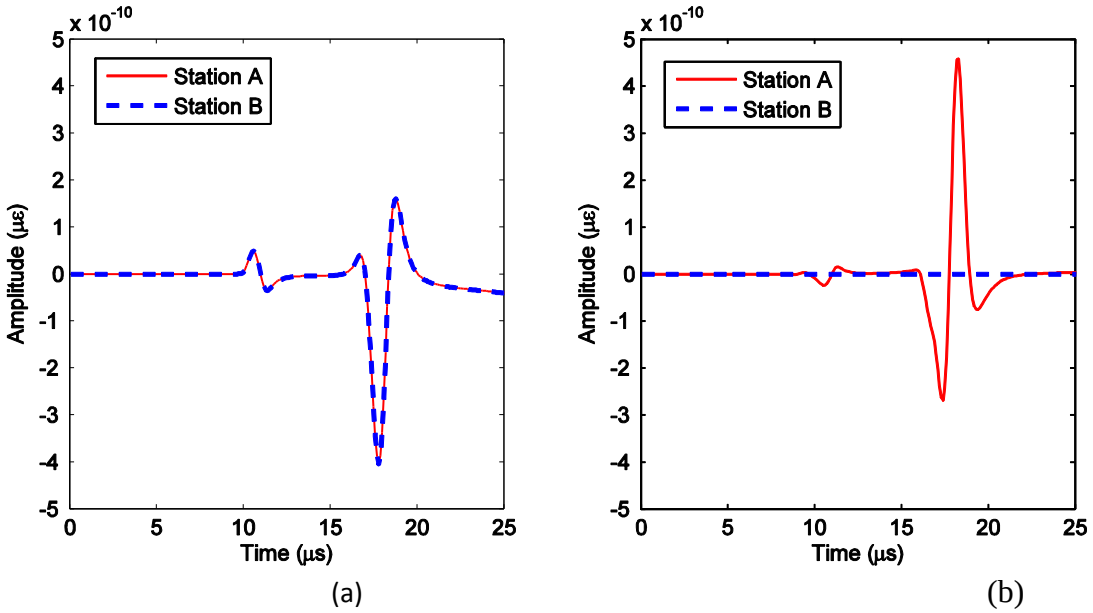

Figure 4.16: Comparison of AE strains at different measurement station due to shear cracking simulated with a buried step source at a depth of 5-mm in a half space: (a) in plane crack; (b) out of plane crack

Chapter 5: Acoustic Emission Source Localization Using Coupled Piezoelectric Film AE Sensors

5.1 Introduction

Acoustic emission (AE) techniques have been receiving growing popularity in use for fatigue crack monitoring on bridges (e.g., Holford *et al*., 2001; Kosnik, 2009; Roberts and Talebzadeh, 2003; Yu *et al*., 2011). AE consists of a propagating elastic wave generated by a sudden release of energy within a material. The elastic wave generated by structural damage propagates through the solid to the surface where it can be detected by surface mount sensors. The AE sensor captures AE signals that contain information about the damage source such as location, crack size, and etc. It is possible to extract such information through a signal analysis of those signals. Knowing the AE source location will provide useful information such as crack growth rate. Additionally, with the source location information, certain irrelevant AE events can be excluded to enhance the accuracy of AE feature and waveform interpretation.

Piezoelectric materials have been used as surface-mount sensors to measure physical movement or strain by directly bonding or embedding piezoelectric thin sheets onto the structure. Piezoelectric ceramics are perhaps the most popular piezoelectric materials for sensing purpose. In particular, sensors made of piezoelectric ceramic patches (e.g., PZT) have recently gained increasing popularities for NDE applications (see, e.g., Ihn and Chang, 2004; Park *et al*., 2006).

Presently, there are two main approaches for source location: time of arrival location (TOA) and single sensor modal analysis location (SSMAL). For the TOA

method, wave speed information needs to be known a priori, and time-frequency analysis has to be performed which involves determining the time of wave propagation to overcome the dispersive nature of flexural wave modes and uncertainty caused by noise. A constant wave speed is generally required in order to determine the source position through triangulation. Moreover, the accuracy in determining the time arrival is critical to the success of this method. This is especially challenging when the first portion of the waveform is attenuated (Ziola and Gorman, 1991).

The SSMAL method is also based on the time arrival difference between different wave modes. In order to separate different wave components from the measured signals, the following methods have been proposed: the cross-correlation method (Ziola and Gorman, 1991), band pass filtering separation (Maji and Satpathi, 1995; Holford *et al*., 2001) and wavelet analysis (Ciampa and Meo, 2010). These techniques have been developed to improve the arrival time measurement of fundamental flexural mode (A_0) with AE instrumentation. Since the SSMAL method is derived from the dispersive nature of Lamb waves, it is only suitable for thin plate applications where the Lamb wave occurs. This method also requires constant wave speed.

For this study, an energy-based AE source localization technique is presented which utilizes the phase difference in the measured AE signals of two piezoelectric film strain sensors to determine the AE source direction angle. Based on the energy spectral information, the AE source direction (azimuth) can be determined from the trough frequency values. The source location can be identified as the intersection of

two converging lines such as the azimuth line and structural geometrical conditions (e.g., weld line) usually known a priori. For example, fatigue crack in metallic structures usually initiates from weldments under high cyclic stress. Therefore, if the AE source direction angle can be determined, the AE source location can be determined in conjunction with the geometry information of fatigue detail.

The proposed AE source localization technique is not based on the time arrival information of the AE signals and the two fundamental factors governing its performance are the relative positions between the two coupled piezoelectric film strain sensors and AE source. Since this localization procedure is based on the trough frequency of the combined signal instead of time arrival difference, averaging of multiple AE signals' frequency spectra can be performed to reduce noise effect. Although the proposed method also requires constant wave speed, this should not pose much problems for the following reasons: for surface AE sources on thick plates (e.g., steel plates with a thickness greater than ¾ inches), the Rayleigh wave arrival usually dominates in energy spectra compared to other wave components such as P and S wave arrivals. Secondly, the Rayleigh wave speed in isotropic half space is constant and therefore it can be used for constant wave speed of the traveling waves. For thin plates, as the extensional mode has a constant wave speed in the frequency range of interest (i.e., <1 MHz for AE monitoring), this method can also be used for source localization as long as the extension part is recognizable.

5.2 Theoretical Formulation

5.2.1 Operation Principal of Sensor Couple

It's well known that phase cancellation would reduce the sensitivity of a sensor at certain frequencies when surface waves pass under the sensor with finite sensing element size (Greenspan, 1987). This is called the aperture effect of a sensor. When two sensing elements are placed next to each other, phase cancellation would also occur if the signals from these two sensing elements are combined. In this case, the phase cancellation comes from the following two sources: the first source is the aperture effect of each individual sensing element and the other is due to the spatial separation of the two sensing elements. This AE source localization method proposed here is based on the phase cancellation due to the spatial separation of two piezoelectric film strain sensors. Since there are two sensing elements separated by a fixed distance in this coupled AE sensor system, this system is termed as "sensor couple" hereto forth.

Figure 5.1 shows the schematic of a sensor couple comprised of two sensing dots and the coordinate system. The sensor couple has two local axes x'_1 and x'_2. The direction angle (i.e., azimuth) of the source is denoted as θ (i.e., the angle between x'_1 and x axis). Without loss of generality, it is assumed that the center of the sensor couple is located at the origin of the coordinate system, and AE source lies on the x-axis.

Any given frequency component ω_i of the AE signal at the sensor can be expressed as,

$$\varepsilon(\omega_i) = A_i \cos(\omega_i t + kx) \tag{5.1}$$

Where A_i is the amplitude of given frequency component ω_i. Assuming the AE source is far enough, for any arbitrary point (x,y) within sensor dot #1, the strain on a narrow stripe with a width of dx is (Greenspan, 1987; Kinsler *et al*., 1999),

$$d\varepsilon_1(\omega_i) = 2\sqrt{a^2-(x-x_{01})^2}\,dx \cdot A_i \cos(\omega_i t + kx) \tag{5.2}$$

Where $k = 2\pi f / c$, c is the Rayleigh wave speed; a is the radius of the sensing dot; f is the Rayleigh wave frequency. The total strain over the whole sensing dot area can be expressed as,

$$\begin{aligned}
\varepsilon_1(\omega_i) &= \int d\varepsilon_{1,i} = \int_{-a+x_{01}}^{a+x_{01}} 2\sqrt{a^2-(x-x_{01})^2}\,A_i \cos[\omega_i t + kx_{01} + k(x-x_{01})]dx \\
&= \int_{-a+x_{01}}^{a+x_{01}} 2\sqrt{a^2-(x-x_{01})^2}\,A_i\{\cos(\omega_i t + kx_{01})\cos[k(x-x_{01})] \\
&\quad -\sin(\omega_i t + kx_{01})\sin[k(x-x_{01})]\}dx \\
&= \int_{-a+x_{01}}^{a+x_{01}} 2\sqrt{a^2-(x-x_{01})^2}\,A_i \cos(\omega_i t + kx_{01})\cos[k(x-x_{01})]dx \\
&\quad -\int_{-a+x_{01}}^{a+x_{01}} 2\sqrt{a^2-(x-x_{01})^2}\,A_i \sin(\omega_i t + kx_{01})\sin[k(x-x_{01})]dx
\end{aligned} \tag{5.3}$$

The second integral in the above equation vanishes because the sinusoidal function is an odd function Eq. (5.3) thus becomes,

$$\begin{aligned}
\varepsilon_1(\omega_i) &= \int_{-a+x_{01}}^{a+x_{01}} 2\sqrt{a^2-(x-x_{01})^2}\,A_i \cos(\omega_i t + kx_{01})\cos[k(x-x_{01})]dx \\
&= A_i' \frac{J_1(ka)}{ka}\cos(\omega_i t + kx_{01})
\end{aligned} \tag{5.4}$$

Where A_i' is a constant and J_1 is the first order Bessel function of the first kind. Similarly, for sensor dot #2, the total strain over its sensing area is,

$$\varepsilon_2(\omega_i) = \int d\varepsilon_2 = \int_{-a+x_{02}}^{a+x_{02}} 2\sqrt{a^2-(x-x_{02})^2}\, A_i \cos[\omega_i t + kx_{02} + k(x-x_{02})]dx$$
$$= \int_{-a+x_{02}}^{a+x_{02}} 2\sqrt{a^2-(x-x_{02})^2}\, A_i \{\cos(\omega_i t + kx_{02})\cos[k(x-x_{02})]$$
$$-\sin(\omega_i t + kx_{02})\sin[k(x-x_{02})]\}dx$$
$$= \int_{-a+x_{02}}^{a+x_{02}} 2\sqrt{a^2-(x-x_{02})^2}\, A_i \cos(\omega_i t + kx_{02})\cos[k(x-x_{02})]dx$$
$$-\int_{-a+x_{02}}^{a+x_{02}} 2\sqrt{a^2-(x-x_{02})^2}\, A_i \sin(\omega t + kx_{02})\sin(k(x-x_{02}))dx$$

(5.5)

The second integral in Eq. (5.5) is zero. Thus, total strain on sensor dot #2 is,

$$\varepsilon_2(\omega_i) = \int_{-a+x_{02}}^{a+x_{02}} 2\sqrt{a^2-(x-x_{02})^2}\, A_i \cos(\omega_i t + kx_{02})\cos[k(x-x_{02})]dx$$
$$= A_i' \frac{J_1(ka)}{ka}\cos(\omega_i t + kx_{02})$$

(5.6)

Collectively, the combined strain signal in the sensor couple made up of the two sensor dots is,

$$\varepsilon(\omega_i) = \varepsilon_1(\omega_i) + \varepsilon_2(\omega_i)$$
$$= A_i' \frac{J_1(ka)}{ka}\cos(\omega_i t + kx_{01}) + A_i' \frac{J_1(ka)}{ka}\cos(\omega_i t + kx_{02})$$
$$= A_i' \frac{J_1(ka)}{ka}[\cos(\omega_i t + kx_{01}) + \cos(\omega_i t + kx_{02})]$$
$$= A_i' \frac{J_1(ka)}{ka}[\cos(\omega_i t)\cos(kx_{01}) - \sin(\omega_i t)\sin(kx_{01}) + \cos(\omega_i t)\cos(kx_{02}) - \sin(\omega_i t)\sin(kx_{02})]$$

Noting that $x_{01} = -x_{02} = (\frac{d}{2} + a)\cos\theta$, the above equation is simplified into,

$$\varepsilon(\omega_i) = 2A' \frac{J_1(ka)}{ka}\cos[k(\frac{d}{2} + a)\cos\theta]\cos(\omega_i t) \qquad (5.7)$$

Eq. (5.7) describes the frequency response of the sensor couple which is governed by two terms. The first is the aperture effect due to the finite size of each sensing dot itself and the second term is related to the fact that the two sensing dots of this sensor

couple are spaced apart (this is called space phase shift effect hereto). Both terms have zeros at certain frequencies, leading to troughs on the frequency response curves. Here the troughs are the frequencies where the frequency response is zero.

From Eq. (5.7), the space phase-shift-induced troughs can be determined using the formula below,

$$k_s(\frac{d}{2}+a)\cos\theta = \frac{\pi}{2}+n\pi \tag{5.8}$$

where n = 0, 1, 2, …, and $k_s = 2\pi f_s / c$. f_s is used to represent the trough frequencies caused by the space phase shift effect.

Solving Eq. (5.8) yields

$$f_s = \frac{\left(\frac{1}{2}+n\right)c}{2\left(\frac{d}{2}+a\right)\cos\theta} \tag{5.9}$$

On the other hand, the aperture-effect-caused troughs can be solved by letting $J_1(ka)$ term in Eq. (5.7) equal to zero, which are listed below,

$$k_a a = 3.83, 7.02, 10.17... \tag{5.10}$$

For which 3.83, 7.02, 10.17… are the zero points of the first order Bessel function of the first kind and $k_a = 2\pi f_a / c$, here f_a is used to represent the trough frequencies caused by the aperture effect due to the finite size of sensor area.

Solving Eq. (5.10) yields the first trough frequency caused by the aperture effect as,

$$f_{a1} = \frac{3.83c}{2\pi a} \tag{5.11}$$

Eq. (5.9) reveals that the projection of the clear spacing between the two sensing dots on the source direction line (x_1 axis in Figure 5.1) determines the value of f_s. It should also be noted that the first two or three trough frequency values due to space phase shift should be made smaller than the first trough frequency due to the aperture effect, that is, $f_{si} < f_{a1}$, i = 1, 2, so these two types of trough frequencies would not be mixed up in practice. This is generally true as long as the source direction angle θ is not close to 90° (thus the denominator in Eq. (5.9) is not near zero). To demonstrate this, an example is given here in which a sensor couple with two identical sensing dots positioned 15-mm apart from center to center and each sensing dot has a radius of 2.5-mm. For steel structures, a typical value for the Rayleigh wave speed is 2950 m/s, and the first trough on the frequency response curve caused by the aperture effect is

$$f_{a1} = \frac{3.83c}{2\pi a} = \frac{3.83 \times 2950}{2\pi \times 2.5 \times 10^{-3}} = 719 \text{ kHz}$$

The first trough caused by the space phase shift can be calculated below using Eqn. (5.9) (for illustration purpose, θ is assumed to be 45° here),

$$f_{s1} = \frac{0.5c}{2(d/2 + a)\cos(\pi/4)} = \frac{2950 \times \sqrt{2}}{4(7.5 \times 10^{-3} + 2.5 \times 10^{-3})} = 104 \text{ kHz}$$

The second trough occurs at frequency 104 × 3 = 312 kHz, which is still smaller than the one caused by the aperture effect. The second trough frequency is often very useful and can be used along with the first trough to further enhance the accuracy in source localization, especially when the first trough does not show up for a number possible reasons, e.g., the plate thickness is not large enough, or noise in lower frequency range. This is particularly true when source lies on the axis of x'_1. When

the source direction angle θ gets larger and larger, f_s also increases accordingly and will eventually exceed the trough frequency due to the aperture effect. For example, when the source lies on the axis of x'_2, f_s would become infinite, that is, space phase-shift-induced trough frequency would vanish for the sensor couple when θ = 90°. Therefore, when using the sensor couple to locate an AE source, it's recommended that the first two or three frequency troughs caused by space phase-shift should be made smaller than the one caused by the aperture effect to avoid confusion and thus error. This can be achieved by adjusting the clear spacing between the two sensing dots and sensor dot radius, as well as orienting the sensor couple so the direction angle is not close to 90°.

5.2.2 Sensitivity Analysis of Frequency Change to Direction Angle

According to Eq. (5.9), the space phase-shift caused trough frequency f_s of the AE signal acquired by a sensor couple is characterized by a secant function of the source direction angle. Since the secant function is nonlinear, the variation of frequency f with θ will not follow a linear relationship. In practical applications such as fatigue crack monitoring, it is important to know the rate of change in trough frequency f due to the direction angle θ change, df/dθ. This rate of change can be determined by taking derivative of Eq. (5.9) with respect to θ, as expressed in Eq. (5.12),

$$\frac{df}{d\theta} = \frac{(0.5+n)c}{d+2a} \times \frac{\sin\theta}{\cos^2\theta} \tag{5.12}$$

The change rate $df/d\theta$ is plotted in Figure 5.2 for one case: d = 12.7 mm, a = 3.175 mm. It can be seen that although the zero degree direction (i.e., along the x'_1 axis) yields the lowest trough frequency value, the rate of change $df/d\theta$ is zero at θ=0.

Therefore it's hard to detect the source's moving when the direction angle is near zero since the trough frequency value changes very little. When the direction angle θ approaches 90°, the change rate goes to infinity. However, as stated in the previous section, before reaching the direction angle of 90°, the trough frequency due to the aperture effect of single sensing dot would occur first and thus may be mixed up with the trough frequencies due to space phase shift effect. Due to this potential interference, the trough frequencies caused by the sensor couple's space phase-shift effect cannot be used for source localization when the direction angle θ is getting close to 90°. Therefore it is suggested that when applying the sensor couple for source localization using space phase-shift induced trough frequency change, the direction angle should be initially chosen somewhere in between 30° and 60° by carefully arranging the sensor couple orientation. In practice, users often can determine the possible source location ranges based on engineering experiences and calculations to estimate most likely AE source locations.

5.3 Parametric Study Using Elastodynamic Solution

5.3.1 Strain Signal from Surface Pulse

Surface pulse is a popular AE source in studying AE sensor characteristics. It can be simulated by pencil lead break or glass capillary breakage. The Rayleigh wave generated by the surface pulse is dominant in the stress wave received by the sensor couple and its derivation from elastodynamic theory is presented in Chapter 4. Under surface pulse, the strain signal measured by piezoelectric film AE sensor is expressed in Eq. (4.31).

The source function S(t) for surface pulse force can be expressed as in Eq. (4.35), which is

$$dS(t)/dt = \sin^4(\pi t/T_r), \quad (0 < t < T_r) \tag{5.13}$$

The rise time T_r is assumed to be 2 μs in this study based on the number given by Ohtsu (1995). The sampling interval is 0.1 μs. The material of the half space is steel with Poisson's ratio of 0.3, density of 7580 kg/m^3 and Young's modulus of 200 GPa, which is given in Table 4.1. The mesh size over the sensing dot area is 1/30 of its diameter. The AE source is placed at the origin of the coordinate system while the center of the sensor couple is located 25-mm and 50-mm away from the AE source, respectively. Two radius values of the sensor dots were considered in this study: 2.5-mm and 5-mm. It is worth noting that in each case study both sensor dots have identical radius value. The two sensor dots in the sensor couple are separated by a center-to-center distance of 15-mm and 20-mm respectively.

5.3.2 Case Study of Different Source Direction Angles

Three cases are discussed below: 0° direction, 90° degree direction and arbitrary direction which correspond to maximum space phase-shift, minimum space phase-shift and the one between. This discussion will shed some lights on how trough frequencies are affect by space phase-shift.

5.3.2.1 CASE 1: θ = 0 degree (AE Source on Axis x'_1)

Figure 5.3 shows the sensor couple response to stress waves due to a surface force expressed in Eqn. (5.13). The appearance of the first and second trough frequencies can be clearly seen in Figure 5.3. Although the four case studies have different combinations of parameter values in terms of sensing dots' radius *a*, clear space *d* and

source distance x_0, they can be grouped in to two sets in terms of trough frequencies. Thus the elastodynamic solutions confirm the theoretical prediction (given by Eqn. (5.9)) that the trough frequencies due to sensor couple's space phase-shift is controlled by the center-to-center distance between the two sensing dots in the sensor couple. Figure 5.3 also shows the analytical curve (given by Eqn. (5.9)) represented by J_1x, which matches the elastodynamic results very well. This is very encouraging after noting the fact that the analytical curve and the elastodynamic results are obtained with independent methods.

5.3.2.2 CASE 2: θ = 90 degrees (AE Source on Axis x'$_2$).

For the case where the AE source lies on axis x'_2, no space phase-shift effect induced troughs should be seen on the frequency spectrum of the sensor couple response. All the trough frequencies seen in the frequency spectra are due to the single sensor dot's aperture effect, which can be expressed as the first order Bessel function of the first kind as expressed in Eqn. (5.7). This theoretical prediction is also verified with the elastodynamic results. Figure 5.4 shows the frequency spectra of the sensor couple's response to a surface force described by Eqn. (5.13). Troughs are clearly seen in the frequency spectra. However, they are due to the aperture effect of a single sensor dot and matches the theoretical prediction curve $2J_1(ka)/(ka)$ very well. No space phase-shift effect caused troughs are seen regardless of how far the sensor couple is located from the source in this case.

5.3.2.3 CASE 3: Various Direction Angle θ

For the case where the AE source does not lie on either axis x'_1 or x'_2, According to Eq. (5.9) all the trough frequencies in the frequency spectra should be only related to the projection of the center-to-center distance (d+2a) on the direction of source to the

center of the sensor couple. This theoretical prediction is also verified with the elastodynamic results. The elastodynamic calculations are performed for the cases of direction angle from 0 to 60 degrees with an increment of 5 degrees. The identified trough frequencies are then compared with the theoretical prediction from Eq. (5.9) and the result is plotted in Figure 5.5. It can be seen that the elastodynamic results are classified into two groups by the projected distance of (d+2a). Each group can be predicted by theoretical values from Eq. (5.9) very well. This again verifies that the trough frequencies are only related to the projection of center-to-center distance (d+2a) on the source's directions (direction to the center of the sensor couple).

5.3.3 Noise Effect

The proposed method could still yield accurate trough frequency results even in the presence of strong noise since sensor noise usually does not exhibit the space phase-shift effect. Moreover, multiple AE data sets can be averaged in the frequency spectrum to cancel out noise, as demonstrated in Figure 5.7. In Figure 5.6, a Gaussian white noise was superimposed onto the original AE signal shown in Figure 5.3 (case of "50mm a=2.5mm d=10mm") numerically. Noisy signals with Signal-to-noise ratio (SNR) of 10 and 20 dB were examined. Figure 5.6 shows the AE signal with added Gaussian white noise of SNR equal to 10 dB along with the original signal and their corresponding frequency spectra are shown in Figure 5.7. Looking at the original signal and the noisy signal, the arrival time of the surface wave is hard to recognize for the case of 10-dB SNR. However, in the frequency domain, the trough frequency can still be clearly identified.

When the noise level further increases, trough frequency might become harder to identify because of noise contamination although an average of multiple sets of data in frequency domain can be easily done to solve this problem. The average of three sets of noisy data with SNR equal to 10dB is also shown in Figure 5.7. The result is closer to the signal without any noise. For AE signals with even higher level of noise, accurate result can be achieved with more data to average. It should be noted that averaging can be done in frequency domain even if they are different type of AE signals as long as they originate from the same AE source point. In applications such as fatigue crack monitoring, propagation of the crack is generally very slow compared to AE signal duration (on the order of milliseconds). Therefore, many AE signals can be collected that could be considered emanating from the same AE source location. Averaging of these data in the frequency domain could thus enhance the accuracy of AE source localization.

As the trough frequency identification is performed in frequency domain, the AE signal duration is a very important since it is inversely proportional to the frequency resolution. Longer record will give smaller resolution thus would deliver more accurate results of the frequency identification. However longer signals might introduce noise contents and make the trough frequency unable to be identified. This is especially true when the signal amplitude is small.

5.4 Experimental Validation

5.4.1 PZT Disc based Sensor Couple

A sensor couple system comprised of two PZT discs (i.e., sensor dots) is adopted for the experimental setup, as shown in Figure 5.8. Each PZT sensor dot has a diameter

of 5-mm and a thickness of 0.2-mm. The fundamental resonance frequency of the PZT disc is 445 kHz. The PZT material is PZT-5A. The two sensor dots are separated apart at a distance of 19-mm from center to center. Pencil lead break on a large steel block is employed to generate a step force (Sause, 2011), which generates a surface stress wave signal having a wideband frequency spectrum on the half space. This study thus adopted pencil lead break to simulate wideband AE source.

Figure 5.8 shows a close-up view of the sensor couple that is mounted on a the surface of a 100 mm thick steel block that measures 500 mm by 500 mm in its plane. A signal conditioning unit that consists of a 40-dB pre-amplifier and a band-pass filter with 5 to 600 kHz pass band was connected to the sensor couple and a high-speed data acquisition system (National Instruments model # PCI-5105). The sampling rate used in this experimental study was 10 MHz. A series of pencil-break tests were conducted 25mm and 50 mm away from the center of the sensor couple system with a variety of direction angles: 0°, 10°, 20°, 30°, 40°, 50° and 60°.

As an example, Figure 5.9 shows the signal measured by the sensor couple and its corresponding frequency spectrum when the pencil-break source is located at a direction angel of 60° from the sensor couple center. The troughs in the frequency spectrum shown in Figure 5.9(b) can be fairly easily identified. After examining the frequency spectrum, three troughs are identified which corresponds to the n =0, 1, and 3 respectively (as given by Eqn. (5.9)). The three trough frequencies in Figure 9(b) are identified as 154.1 kHz, 470.0 kHz and 770.4 kHz respectively. As the Rayleigh wave speed has been determined to be 2872 m/s and the source is located 50 mm away from the sensor couple's center, the first analytically predicted trough frequency

would be 151 kHz according to Eqn. (5.9) ,the second trough would locate at 453 kHz and the third would be 755 kHz. There are some small discrepancies between experimental values and theoretical predictions, which might be due to the error of measurement of the sensor and source positions. For the experimental data itself, the three frequency troughs are related to each other with a linear relationship. Generally, this agrees well with the experimental result shown in Figure 5.9(b).

Figure 5.10 shows the frequency spectrum of signal from the coupled sensor system along with that of each individual sensor acquired when the source is at 30° direction. For the signal measured by each sensor dot, the frequency spectrum of the AE signal is expected to have no space phase shift effect caused troughs up to the upper cutoff frequency (at 600 kHz) of the signal conditioning unit. This matches with the experimental test shown in Figure 5.10. The troughs on the frequency spectrum of the sensor couple are prominent when comparing these three curves. For example, the sensor couple signal has a clear trough at the frequency of 92.45 kHz while both of the two individual sensors have a flat frequency spectrum near this frequency range. The only reason for this frequency trough occurrence is the space-phase shift effect of the two sensors, so do the troughs at 269.6 kHz, 439.1 kHz and 631.7 kHz. These three troughs could be predicted theoretically and correspond to the 1^{st}, 2^{nd}, 3^{rd} and 4^{th} troughs given in Eqn. (5.9). It is worth noting that even though the frequency spectra are not flat here, the trough frequencies can still be identified without much difficulty. This demonstrates that the requirement of flat frequency spectrum is unnecessary as long as the signal's frequency content is sufficiently large over the sensor couple's operating frequency range.

5.4.2 Comparison with Analytical Results at Various Angles

Figure 5.11 shows the trough frequencies identified from experimental data for pencil lead breakage source located at various angles for the PZT disc based sensor couple system. The sensor couple has the same configuration as that given in section 4.1. The pencil lead break tests were conducted 25 mm and 50mm away from the sensor couple's center but with different direction angles. In order to reduce the noise effect, results from six tests for each source direction have been averaged to generate a smooth frequency spectrum from which the trough frequencies can be identified with ease. The theoretical prediction results from Eqn. (5.9) are also included in Figure 5.11 for comparison purpose. It can be seen that the theoretical predictions and experimental results agree very well with each other. This again demonstrates the validity of this source localization method. It's also seen in Figure 5.11 that the trough frequency f_s changes very slowly with the direction angle θ when θ is close to 0. The trough frequencies identified from experimental data at source direction 0° and 10° can be hardly differentiated. Therefore, it is difficult to narrow down the increment in the source direction when the direction angle is very small. When the direction angle gets larger, the trough frequency changes more rapidly and as such the source direction can be identified more accurately. This is clearly seen in Figure 5.11.

It is worth noting that although the above formulation is derived for stress wave induced strain, the same methodology can be equally well applied to other type of AE sensors such as those commercially available AE sensors based on out of displacement measurements. This has been verified in this experimental study, but due to space limit, the results are not included in this chapter.

5.6 Conclusions

This chapter presents a new concept of energy based AE source localization technique, which is based on the phase shift of AE signals between the two sensing elements in the coupled AE sensor system. Since this approach is conducted in frequency domain and it does not rely on arrival time difference, it could still exhibit good performance for AE signals with low SNR through averaging multiple records. Once the direction (azimuth) is identified, the location of AE source can be determined as the intersection of two converging lines such as the azimuth line and geometrical conditions (e.g., weld line) usually known a priori. From analytical derivation, it is seen that the key parameters are only related to the source direction and the distance between the centers of two sensing elements in the coupled AE sensor system.

To demonstrate the technique, a series of numerical simulation for a Heaviside force on the surface of half space are carried out. The Heaviside force is known to generate a wideband AE source. To experimentally validate this technique, pencil lead break tests on a large steel block were also conducted. It is seen that the theoretical predictions and experimental results agree very well with each other. This agreement is also verified with the real data from field monitoring of an existing fatigue crack on a steel bridge girder. These demonstrate the validity of this source localization method. Although broadband AE signals with flat frequency spectra would make the localization technique easy to use, this is not required as long as the frequency contents are spread over the sensor couple's bandwidth.

This study also investigates the sensitivity of sensor couple. It is suggested that for practical application the azimuth angle range is determined to be from 30° to 60° for best accuracy. The characteristic of AE signals may affect the performance of the coupled AE sensor system in locating AE source. Single wave component is required to ensure the accuracy of the localization technique. When the source is close to or on the surface, Rayleigh wave arrival usually has much larger amplitude than other components and thus dominates the waveform, consequently good performance can be achieved.

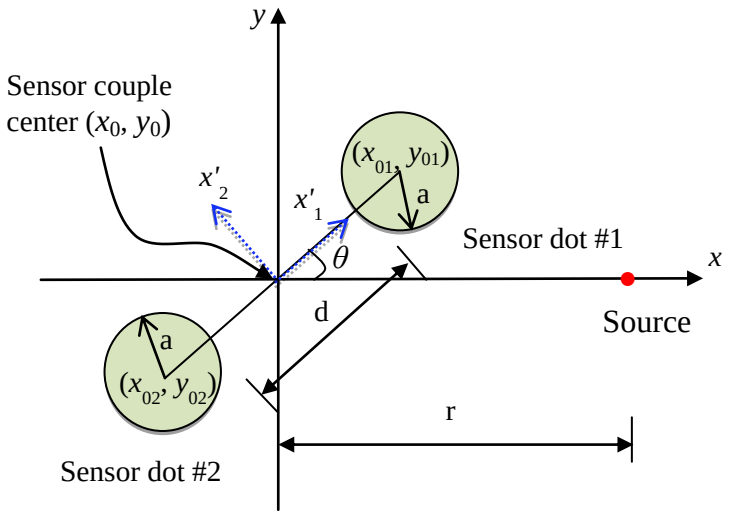

Figure 5.1: Schematic of sensor couple and coordinate system

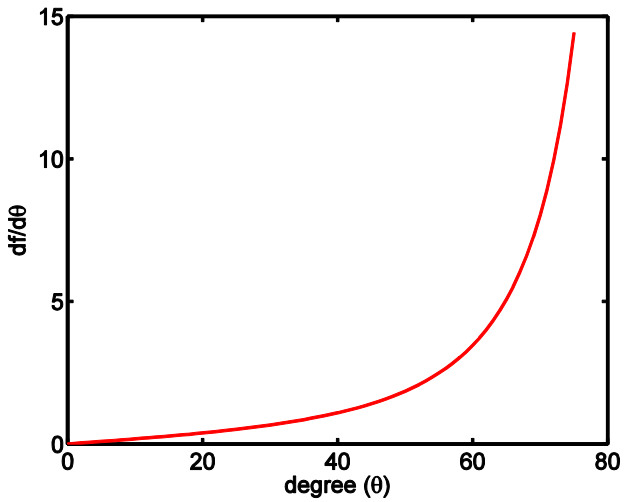

Figure 5.2: Frequency shift rate $df/d\theta$ of sensor couple versus source direction angle θ

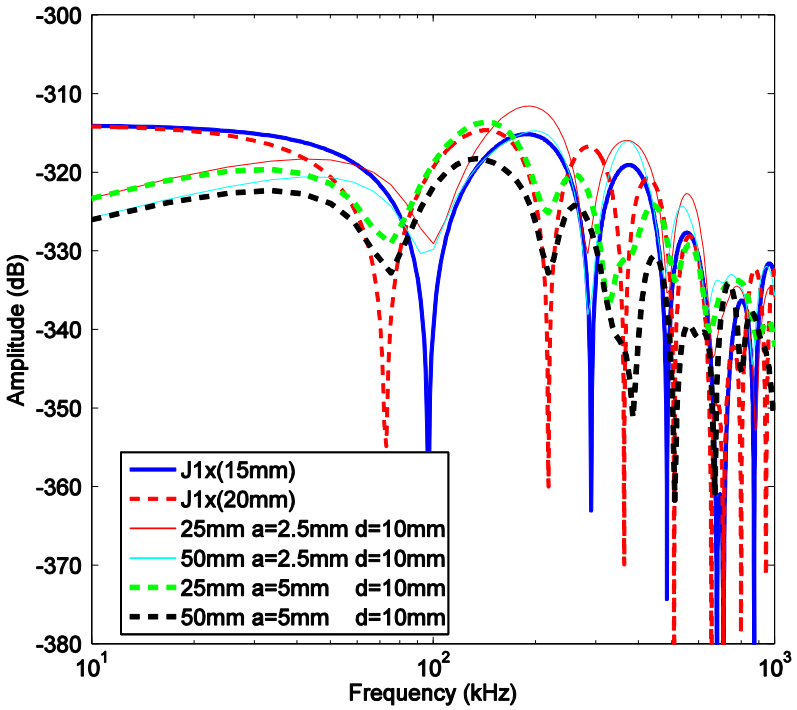

Figure 5.3: Frequency spectra of sensor couple's signal with varying parameter values (θ=0)

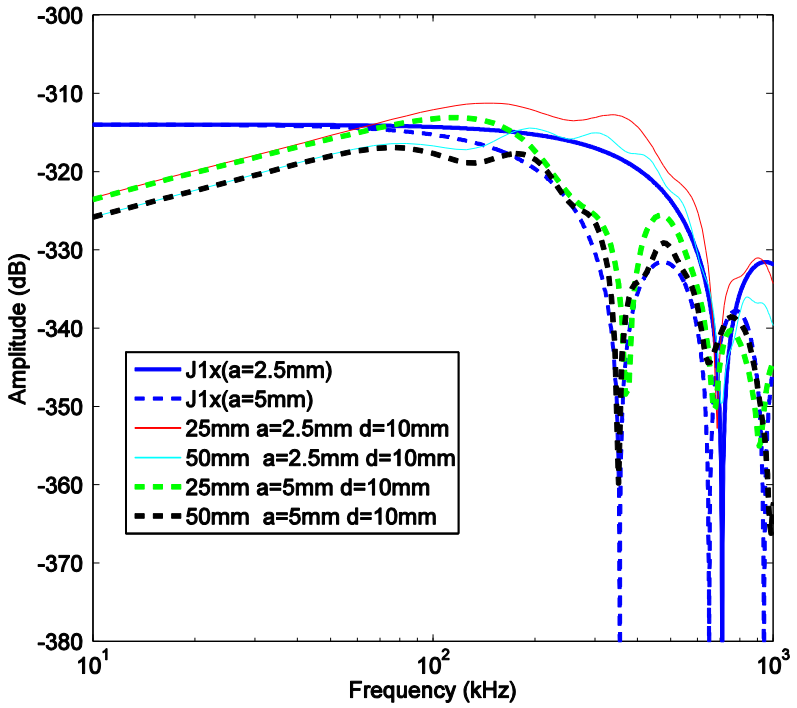

Figure 5.4: Frequency spectra of sensor couple's signals with varying parameter values (θ=90°)

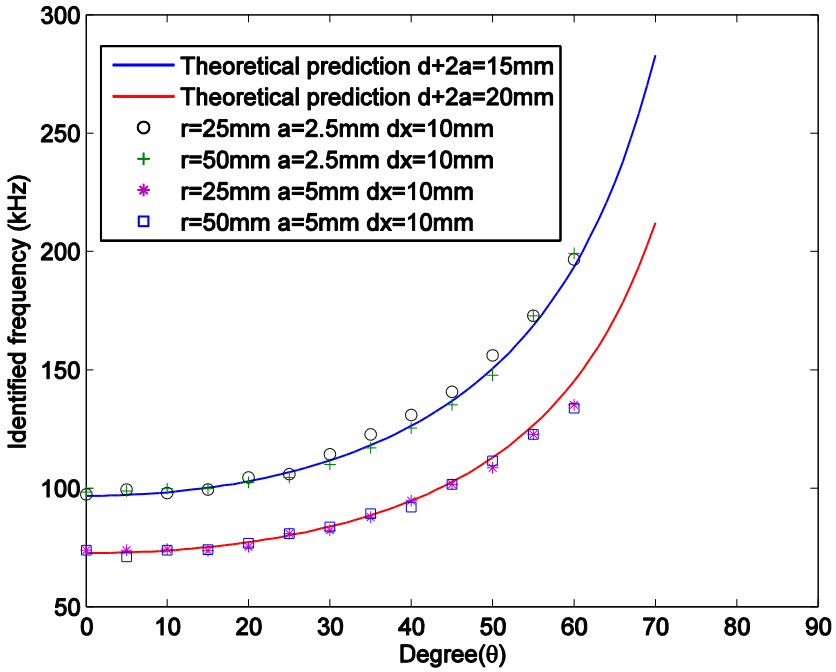

Figure 5.5: Comparison of trough frequencies obtained from theoretical prediction and elastodynamic simulation for various direction angles and source distances

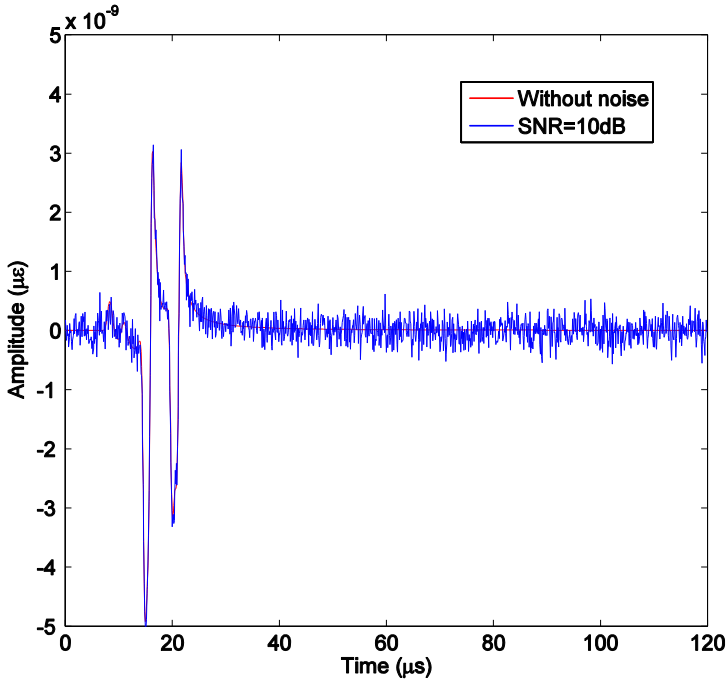

Figure 5.6: Time history of sensor couple's signal with noise

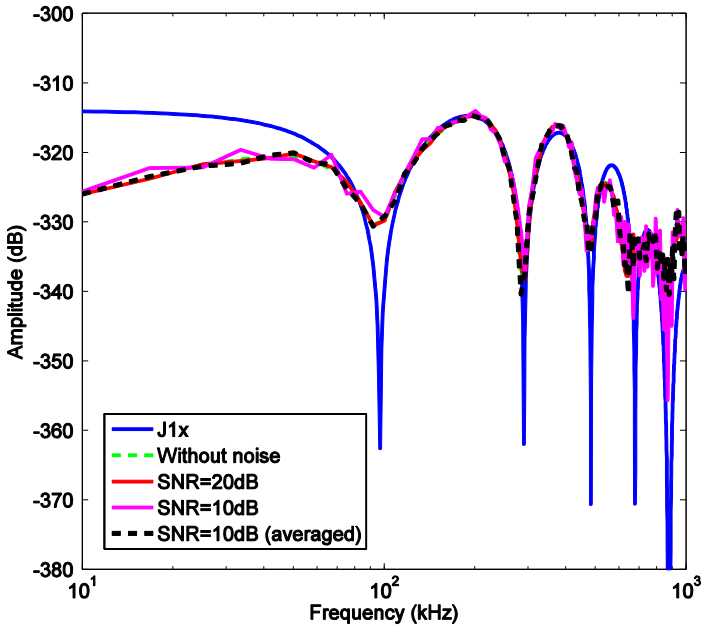

Figure 5.7: Frequency spectra of sensor couple's signals with varying noise levels

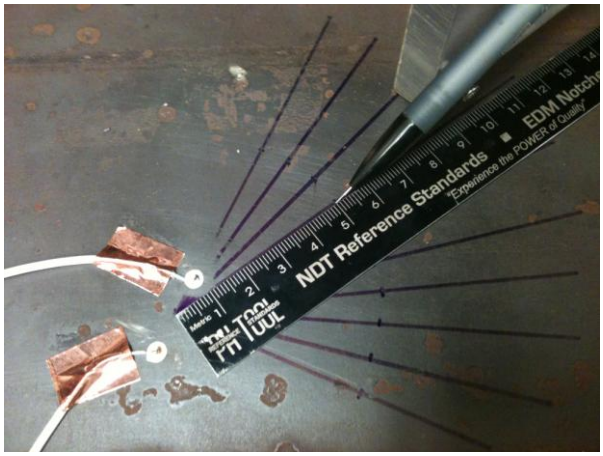

Figure 5.8: Close-up view of the experimental setup

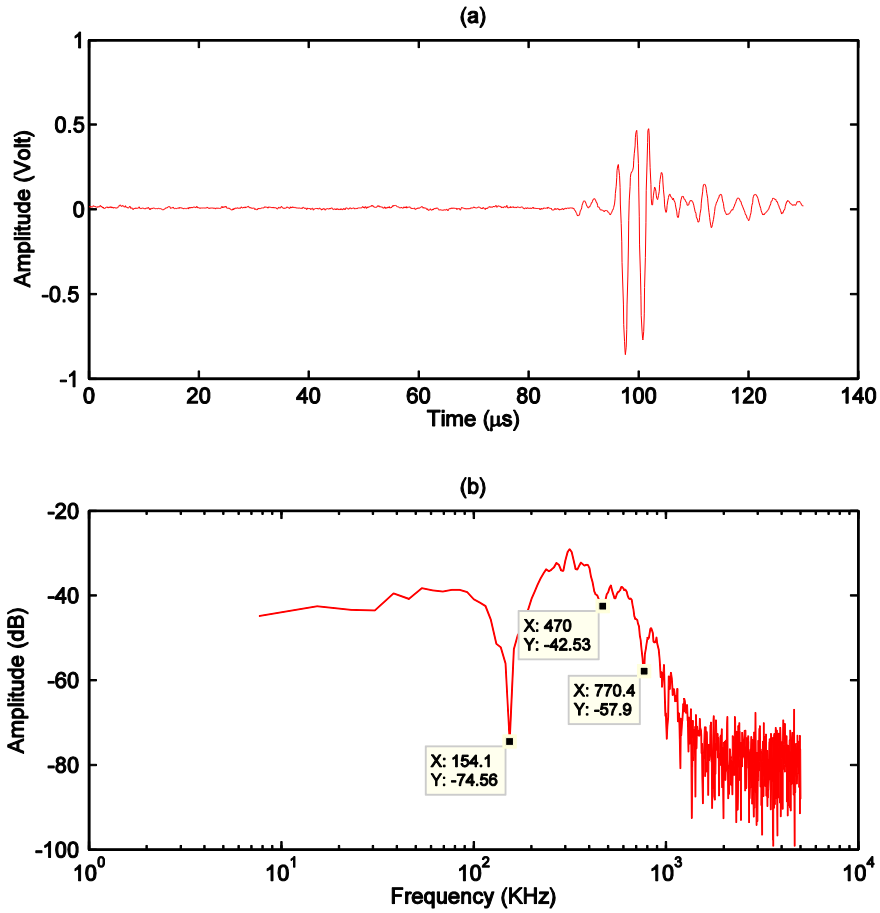

Figure 5.9: Signal from the sensor couple due to pencil lead break source at 60° direction: (a) AE signal; (b) frequency spectrum

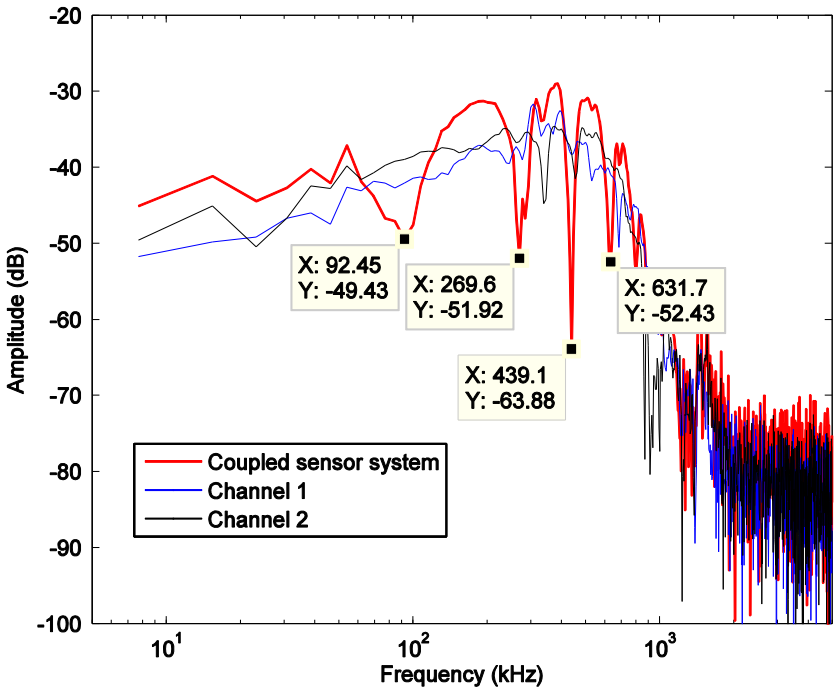

Figure 5.10: Frequency spectra of sensor couple signal and each individual sensor due to pencil lead break source at 30° direction.

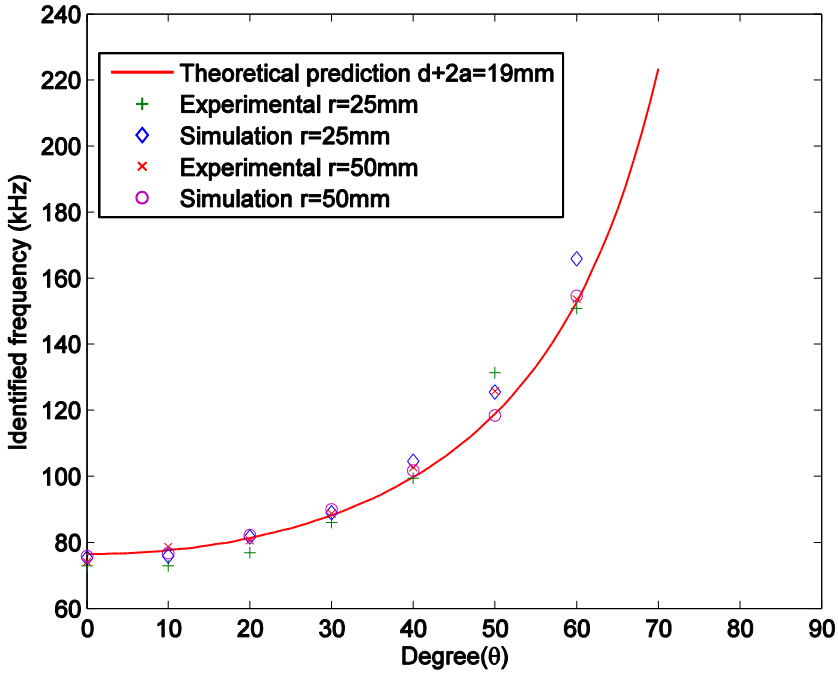

Figure 5.11: Comparison of trough frequencies obtained from theoretical prediction, elastodynamics simulation and experimental tests for various direction angles and source distances

Chapter 6: AE Signal Monitoring on Fatigue Test Specimens

6.1 AE Monitoring on Welded Tubular Joints

6.1.1 Review of Fatigue Crack Monitoring on Tubular Structures

Tubular structures have become increasingly popular for economic and aesthetic reasons, yet member deterioration and fatigue cracking of connections is often reported. Fatigue and fracture are at the root of more than 80% of the failures in steel structures. Circular hollow sections (CHS) are frequently used in structures subjected to fatigue loading such as cranes, sign support structures, wind turbine supports and offshore structures. These sections are generally connected by direct welding of the sections to each other. Brittle failures (e.g., structural collapse) subsequent to fatigue induced fracture in the past have been observed in tubular steel structures, mainly because specific details have a lower fatigue resistance than foreseen at design stage. One structure type receiving significant attention is the overhead welded highway sign support truss (both full span and cantilevered span) (Ocel *et al*., 2006). Many of these structures contain CHS members and connections that employ circumferential fillet welds. There have been many recent reports of cracking in these structures in the vicinity of the welded connections (Dexter and Ricker, 2002). Figure 6.1 shows a downed sign support structures that crashed a car passing by.

Application of tubular elements in welded lattice structures possesses several advantages, the main among them being low weight characteristics, reached owing to optimum geometric characteristics of sections and reduction of external loadings on the structure. The realization of these advantages requires the evaluation of the

strength in joints of the connections which are the most critical places in the structure. Fatigue failures typically begin at high stress concentration locations at weld terminations of specific structural details such as stiffeners, joints, brackets, due to the presence of secondary stresses or out of plane bending. Welded tubular nodes contain various stress concentrations, both by the welding process itself and by geometric discontinuities. Obviously, this situation reduces the fatigue strength in a decisive manner. In addition, the stresses reach high peak values near to the weld toe of the joints. The fatigue performance of welded tubular connections is also of particular importance for the safety of tubular steel structures regularly subjected to repeating loading such as tower cranes and wind turbine support structures. Crane components experience a spectrum of stresses while operating. Several recent crane accidents in the USA, have demonstrated the criticality of fatigue crack monitoring of cranes and developing an effective strategy for fatigue remaining life updating and scheduling maintenance. A fracture critical member is a tension member or the tension region of a component whose failure would be expected to result in collapse of the crane or trolley, or dropping the load. To maintain acceptable reliability, the crane needs periodic inspection and repair of fracture critical member or hot spot areas at connections.

The integrity of structural components in welded tubular steel structures is affected by damage due to fatigue, corrosion, and accidental impact, among which fatigue crack is the major causes for abrupt structural collapse without early warning. Damage may reduce the residual strength of the structure below what is needed to carry the service loads. Primary method for structural condition assessment is

qualitative based on visual observations. The quality of the inspection and condition rating input is subjective (visual inspection based on the inspector's view) and time delayed due to inspection cycles (every two years or even longer). Differences between theoretically calculated and observed life prediction may differ by an order of magnitude. Therefore, through modern online structural health monitoring (SHM) techniques, the length of fatigue cracks can be measured continuously in structures, and automated online updating of fatigue reliability assessment can be realized. Having detected flaws, the updated time-variation in fatigue reliability can be obtained through updating the fatigue failure models, then maintenance including corrective actions can be taken to prevent service failures. Structural safety can be maintained by continuous monitoring, optimized maintenance scheduling and timely repair action. Piezoelectric film AE sensor (specifically piezoelectric paint film AE sensor) conforms well to curved surface because of its flexibility - making it very promising for use on tubular steel structures, for which conventional sensors are ill equipped to do. This study will explore the use of piezoelectric paint film AE sensor for continuous monitoring of fatigue crack growth in welded tubular joints.

6.1.2 Fatigue Test of Welded Tubular Specimens

6.1.2.1 Details of Test Specimens

AE monitoring of fatigue crack growth in three identical full-scale test specimens is conducted. The test specimens were fabricated in accordance with the mast-arm-to-flange plate connection design for signal support structures in Maryland. The full-scale test specimens were fabricated by Millerbernd Manufacturing Co. These specimens are labeled as WTJ4 to WTJ6 for later reference. The specimen is comprised of two components - a tapered seam-welded steel tube made of ASTM

A572 steel and a traverse plate made of ASTM A36 steel. The steel tube is inserted into the transverse plate and welded together using fillet weld. The transverse plate is a rectangular plate measuring 0.4572 m (18 inches) x 0.3048 m (12 inches) x 0.0508 m (2 inches). The tube's length is 1.524 m (5 feet). A taper rate of 0.0118 m/m (0.14 inches/foot) for the diameter is applied, which leads to a variation of external diameter tapering from 0.254 m (10 in) to 0.236 m (9.3 in) at its open end. The thickness of the tube wall is 6.35 mm (1/4 inches) along the tube. The transverse plate of the test specimen is anchored to the reaction frame with bolts. The test specimen and fatigue test setup is shown in Figure 6.2 (Li, 2013).

6.1.2.2 Fatigue Loading and Crack Monitoring

MTS servo-hydraulic loading system (dynamic 244.31 linear hydraulic actuator and FlexTest GT controller) was used to apply cyclic loading to the test specimen. Cyclic load with constant amplitude (load range from 0.1 kips to 6 kips) is applied vertically at the free end of the specimen with the servo-controlled hydraulic actuator. However, test of WTJ6 used a different loading scheme in order to apply a beach-marking method for fatigue growth marking which employs an alternating loading scheme with two different load ranges. The loading frequency in this test is set to be 1.5 Hz. When the test specimen was close to the end of its fatigue life, loading frequency was reduced 1 Hz and then 0.1 Hz to maintain a constant load range amplitude applied to the specimen.

Two types of data are acquired during the fatigue test: surface crack length (only for three specimens WTJ4 toWTJ6) and strains at specified locations (for all 6 specimens). For strain measurement, metal foil strain gauges (Vishay model EA-06-125AC-350 and EA-06-250BF-350) were used. Each test specimen has ten strain

gauges, which are connected to the data acquisition system (Pacific Instruments 6000, strain gage card 6038) using cables.

In order to measure the crack length, a printed tape measure with 1-mm small tick marks was bonded to the test specimen along the circumference weld. For crack monitoring and sizing, a digital microscope (model AM7013MZTS polarizing microscope) is used. Typically, a magnification factor of 50 is sufficient to see the fatigue crack. In this test, larger magnification is not possible because of blocked view by the 90 degree angle between the transverse plate and the tube at the weld toe, which makes it impossible to get the smaller view depth required for higher magnification factor. The detection and size measurement of fatigue cracks using the digital microscope depends on crack opening displacement under cyclic loading. Once the crack opening width is large enough to be identified in microscope image, the crack is detected.

6.1.2.3 Instrumentation for AE Monitoring

As seen in Figures 6.3 to 6.5, six piezoelectric film AE sensors were installed near the circumferential weld. These sensors are evenly spaced at 1 inch from center to center. The sensors are also aligned in both the longitudinal and circumferential directions. The piezoelectric film AE sensors with a polyimide substrate film are bonded to the test specimen surface using super glue. The piezoelectric paint disc has a circular shape with ½" diameter. An additional piezoelectric film AE sensor was installed 12 inches away from the weld toe as shown in Figure 6.4 and is used as a guard sensor to watch for any AE sources outside the weld toe area.

A 40-dB gain pre-amplifier was used to amplify the voltage signal from the piezoelectric paint AE sensor and a second order Butterworth band pass filter was

used with a pass band from 5 to 600 kHz. The 6-ft. long coaxial cables (Belden 8240 coax, RG-58A/U Type, 20 AWG solid 0.033" bare copper conductor) and BNC connectors were used to connect the piezoelectric film AE sensors and corresponding preamplifiers. 15-ft. long shielded coaxial cables (PCB Piezotronics model # 002, with white Teflon jacket) are used for connecting the preamplifier to a high-speed data acquisition system (National Instruments model # PCI-5105 installed on an emachine® desktop computer). In general, the cable between the sensor and the preamplifier should be kept as short as possible since the raw signal coming out from the sensor is very weak and would be further weakened if the cable is too long. In this experiment, the lengths of the cables connecting sensors and amplifiers were all the same and were less than 2 meters.

The high-speed data acquisition system (National Instruments model # PCI-5105) has a sampling speed up to 60 MS/s and was used to monitor the AE signals generated by fatigue crack development in the welded tubular joint specimen. In this experiment, a sampling rate of 5 MHz was used, since a low-pass filter with a cutoff frequency of 600 kHz was used in the signal conditioning circuit.

A Labview-based software program was developed for continuous AE data collection with triggering. Once AE signal exceeds the preset threshold, the AE signals would be captured and stored on the computer hard drive and the monitoring system is reset automatically for next AE signal triggering. In order to prevent excessive amount of AE data, a threshold level for triggering AE signal data acquisition is set to be 35 mV in this test. This threshold level has to be adjusted based on ambient noise level and noise floor of the sensor for different applications.

In the late stage of fatigue tests, the crack propagated further away from its initiation region (generally at the intersection of circumferential weld and seam weld at the top spot of the tube). In order to capture the AE signals (typically low amplitude) associated with crack propagation, the trigger channel was changed to the sensor closer to the crack tip. In the test of WTJ4, since the trigger sensor a2 is not at the top of the specimen, the trigger sensor was not changed during the test. The reason to choose sensor a2 for triggering was that sensor a0 (which is made of PZT-5A) had a lot of false triggering as reported in Figure 6.6. In the test of specimen WTJ5, the trigger sensor was changed from sensor a0 to sensor a4 at load cycle number N = 373,643 cycles. In the test of specimen WTJ6, the trigger channel was switched from sensor a0 to sensor a4 at load cycle number N = 350,000 cycles.

As stated earlier, piezoelectric paint AE sensors are relatively flexible and can be bonded to curved surface without damaging the sensor. This poses a significant advantage compared with PZT-5A based piezoelectric film AE sensors which are brittle and very easy to break when pressing against curved surface at installation on the 10”-diameter steel tube. Figure 6.6 shows a signal collected by a PZT-disc based AE sensor (labeled as a0 in Figure 6.3) due to imperfect bonding between the sensor substrate film and curved steel surface during cyclic loading of specimen WTJ4. It is also seen in Figure 6.6 that the piezoelectric paint AE sensors (labeled a2 and a3 in Figure 6.3) didn’t have this problem. Therefore, in the subsequent fatigue test of specimens WTJ5 and WTJ6, PZT-disc based piezoelectric film AE sensors were dropped. The following discussion is limited to AE data acquired by ½”-diameter piezoelectric paint disc based piezoelectric film AE sensors.

Figure 6.7 (a) shows the measured fatigue crack growth curves of the three welded tubular joint specimens. The corresponding stress intensity factors for these crack growth curves are roughly estimated to change from 10 $MPa \cdot \sqrt{m}$ for the first several data points to 30 $MPa \cdot \sqrt{m}$ at the end of crack growth curve. Figure 6.7(b) shows the cumulative AE hits versus crack length for all three specimens.

Figures 6.8(a) to 6.10(a) show the variation of cumulative AE hits and crack length with load cycles. AE hits is defined as the detection and measurement of an AE signal on a channel (ASTM, 2005) It is seen in these figures that AE activities usually are quite active during certain time window followed by a calm period and this active-calm cycle repeats again. This phenomenon is also reported by others in the fatigue tests, such as fatigue test of compact tension specimens (Yu *et al*., 2011). This can also be seen from the da/d*N* versus load cycle graph shown in Figures 6.8(b), 6.9(b) and 6.10(b). The general trend in these curves is that AE activities become more intensive as crack growth rate increases. It is also seen that piezoelectric paint AE sensors didn't pick up many AE events at lower crack growth length due to its lower sensitivity. When the test specimens get near their fatigue lives, more AE signals were triggered, mostly due to friction rubbing of the two sides of the fracture surface.

As shown in Figure 6.8 (b) and Figure 6.9 (b), the AE hits rate was approximate 1 at the later stage for both specimens WTJ4 and WTJ5. That's to say every load cycle had generated an AE event. Based on the observation during the fatigue tests, AE signals were triggered when a friction sound could be heard at the same time. Thus it's believed a lot of signals were due to friction. This was also

further confirmed after examination of the friction rubbing marks shown in Figure 6.11. Both specimens WTJ4 and WTJ5 have very obvious friction rubbing marks. However, for specimen WTJ6, the surface is fairly clean and there is no friction rubbing mark, which should be the reason for why there were much less friction signals in specimen WTJ6.

6.1.3 Simulated AE Test on Welded Tubular Specimens

Pencil lead break and hammer impact (PCB Piezotronics impact hammer model # 086D05 with a medium hardness tip, hammer mass = 0.7 lb, tip diameter = 0.25") are used to generate simulated AE sources on the specimen's tube. The impact hammer test was controlled by hitting from a fixed distance, 1 inch in this case, so that it would be repeatable and the results are comparable while pencil lead break is done using a fixture. Typical signals collected by piezoelectric paint AE sensor a1 on specimen WTJ5 due to simulated AE sources 1.5 inches away from the sensor are shown in Figure 6.12. It can be seen that the hammer impact induced AE signal has a longer-period pulse than that due to pencil lead break.

Figure 6.13 shows the averaged frequency spectrum of ten AE signals induced by simulated AE source. It is seen that energy of the AE signal induced by hammer impact is concentrated to lower frequency range at several kHz. However, for the pencil lead break test, the AE energy can go up to several hundred kHz, although strong energy content is also seen in the lower frequency range. Pencil lead break test data can be used to examine time of arrivals in the piezoelectric film AE sensors as well as attenuation and filtering effect by the steel tube.

Figure 6.14 shows the signals collected by piezoelectric paint AE sensor a0 on specimen WTJ5 when the pencil lead break was made at 3”, 6’’, 9’’ and 12’’ away from the weld toe (i.e., 1.5’’, 4.5”,7.5’’ and 10.5” away from the sensor) respectively. Attenuation of signal amplitude is seen when the simulated AE source (i.e., pencil lead break) is moving away from the AE sensor. The attenuation rate is lower for larger distance between the AE source and sensor, that is to say, the attenuation between 3” and 6” is much larger than that between 9” and 12”. This is consistent with the results reported in Chapter 4. Thus significant attenuation should be expected in the guard sensor if the AE source is originating from the weld toe. This provides an alternative way to identify any noise from the actuator loading head direction in addition to the time of arrivals method.

6.1.4 AE Signal Analysis

For specimen WTJ5, all piezoelectric paint AE sensors were installed on the specimen at load cycle number N=277,139. After sensor installation, 120,000 additional load cycles were applied to the test specimen before the specimen failed. At its failure, the specimen had very large crack and was no longer able to carry the constant load range).

Figures 6.15 – 20 show some typical AE signals as well as their frequency spectra at various loading cycles. Taking signals shown in Figure 6.17 as an example, close examination suggests that the AE source should be very close to sensor a0, since all the other sensors did not have any response and signal in sensor a0 is also very weak. It is noted that since sensor a0 is used for triggering, other AE events

might occur near other sensors but were too weak to trigger sensor a0 due to wave attenuation.

If the AE signals are triggered by friction rubbing of the fracture surfaces, the number of cumulative AE hits would increase linearly with the load cycles so that the AE hits rate is the same as the loading rate. This phenomenon was also observed during the test. Sensors picked up signals when crack front was approaching. Figure 6.21 shows such AE signals caused by friction rubbing on the fatigue crack's rupture surfaces. These AE signals all have a very strong low frequency component, as evidenced by their frequency spectra and long period pulses in Figure 6.22.

Most of the AE events at this stage were due to the friction rubbing of the fracture surface although some AE signals were still caused by fatigue crack growth. Although friction induced AE signals dominated this stage, AE signals with high frequency components were seen mixed with those friction signals, such as the signal shown in Figure 6.30. This high-frequency signal is likely to be caused by fatigue crack growth after comparing with the fatigue crack induced AE signals obtained in this test shown in Figures 6.23 to 6.28.

Using the time of arrivals information from the AE signals to analyze a sample AE signal with higher frequency contents as shown in Figure 6.27, the result is shown in Figure 6.29 and it is very clear that the AE signal is different from the friction signal shown in Figure 6.21. Mostly likely it's due to a large energy release event associated with fatigue crack growth because of its higher frequency contents in comparison with friction induced AE signals. Additionally it can be seen that AE signals arrived at sensor #a0 and sensor #a1 at almost the same time, and arrived later

at other sensors. It's clearly seen that the corresponding stress wave gradually arrived at sensor #a0, #a2, #a4 and #a5 with almost a fixed time delay. This means the signals must initiate from the south side crack front. By comparing with the signal in the guard sensor a6, the possibility of noise from actuator loading is also eliminated since the stress wave has the latest arrival time and strong attenuation in its amplitude was observed. Therefore it is concluded that this AE event is very likely due to the fatigue crack growth. For this type of AE signals, energy is concentrated up to one hundred kHz and it gradually rolls down after that. This is also consistent with the wave propagation in relatively thin tube wall (thickness = 6.4 mm) which will filter out the frequency contents at several hundred kHz.

Although specimens WTJ4 and WTJ5 have different fatigue life values, they have similar AE hits characteristics as shown in Figure 6.7. Calm periods were observed on both of the cumulative AE hits curves. Similar types of signals were obtained from both tests. For example, Figures 6.31 and 6.32 are AE signals acquired by piezoelectric paint AE sensors during fatigue test of specimen WTJ4. These AE signals are similar to those shown in Figures 6.17 and 6.19 respectively.

Figure 6.33 shows a series of friction-induced signals acquired at six time points (load cycle numbers): 520k, 540k, 550k, 560k, 570k and 575k cycles respectively. These friction-induced AE signals are different from those presented in Figure 6.21, probably because there are some difference (both geometry and location) in the friction rubbing marks over the fracture surfaces. For the friction induced AE signals from specimen WTJ4, they were changing with the loading cycles, e.g. fatigue

life, while the friction induced AE signals from specimen WTJ5 nearly didn't change over the time (some amplitude change but no waveform shape change).

Close to the end of the fatigue life, at load cycle number N= 575k, both amplitudes and phases of the AE signals in sensor a2 and sensor a3 became the same in specimen WTJ4. This could only happen when the AE source was far away from both sensors, and thus the distances to both sensors were very close and the AE signals of both sensors would have almost the same time of arrivals and signal amplitude. At this point, the fracture surface at the location near sensor a2 could not close, therefore it is assured that no friction rubbing or crack surface pounding occurred at this moment. For these friction induced AE signals, their energy is usually concentrated in lower frequency range. This is confirmed by Figure 6.34, which displays the frequency spectra of the AE signal shown in Figure 6.33. The friction-induced signals also have a relatively low frequency contents as reported before. This characteristic is different from that of a fatigue crack growth induced AE signal. Thus, from the frequency characteristics, it might be possible to tell whether an AE signal is due to fatigue crack growth or not. However, for specimen WTJ6, as there is no friction observed during the tests, much fewer signals were acquired compared with the tests of specimens WTJ4 and WTJ5. Figure 6.35 presents a signal obtained during the tests of specimen WTJ6. It is similar to the one shown in Figure 6.30, especially for the overriding high-frequency signal component. This is also further confirmed by the frequency spectra shown in Figure 6.36.

6.2 AE Monitoring on Welded Plate

6.2.1 Test Setup and Loading Procedure

In order to experimentally verify the sensor couple based AE source localization method in steel plate, two specimens comprised of 1-inch thick steel plate with welded stiffener are fabricated and cyclically loaded to generate fatigue crack near the tip of welded stiffener. The test specimen is comprised of four ASTM A36 steel plates: 1" thick plate, ¼" thick longitudinal stiffener and transverse stiffeners. Stiffeners are welded to the 1"-thick plate with 3/16" fillet weld. Details of the test specimen dimensions are shown in Figure 6.37. The 1" plate is considered to be thick enough for Rayleigh wave to develop in the plate so that the sensor couple theory for AE source localization is applicable. The width of the stiffeners is 3.5" so that the neutral axis of the inverted T-section is located within the 1"-thick plate (0.35" below its top surface).

A picture of the fatigue test setup including the specimen and loading head of the servo-hydraulic actuator is shown in Figure 6.38. The specimen is anchored to a loading frame with two steel plate and bolts. The specimen is cyclically loaded as a cantilever beam with a load range of 0.26 to 2.76 kips at a loading frequency of 1.5 Hz. For strain measurement, metal foil strain gauges (Vishay model EA-06-125AC-350) were used. Each test specimen has three strain gauges, labeled as SG1 to SG3 for easy reference. The instrumentation plan for the strain gauges is shown in Figure 6.39 (c). The measured stress ranges (for SG1, SG2, and SG3 respectively) corresponding to the above-mentioned load range are (sign convention adopted here is: positive value for tension, negative value for compression): SG1= [150 με, 880

με], SG2=[-70 με, -190 με], and SG3=[140 με, 860 με]. The weld toe at the discontinued stiffener location has the largest tensile stress along the weld line and it also has an abrupt change in geometry leading to stress concentration. This is also evidenced by the fatigue crack initiation observed in that location, as shown in Figure 6.41.

6.2.2 Instrumentation for AE Monitoring

A total of six AE sensors are installed on the test specimen, including three piezoelectric film AE sensors made of 5-mm diameter PZT-5A disc, one piezoelectric film AE sensor made of ½”-diameter piezoelectric paint disc and two commercial AE sensors (Dunegan Engineering model # SE1000-HI, broadband AE sensor with a sensitivity of 1000 V/μm if used with a 20-dB preamplifier). Figure 6.39(b) shows the location of these sensors. The piezoelectric film AE sensors measure the in-plane strain while the two commercial AE sensors measure the out-of-plane displacement. All piezoelectric film AE sensors were used with a 40-dB gain amplifier and a 5 kHz to 600 kHz band-pass filter. The commercial AE sensors have a 20-dB gain preamplifier. Similar to the piezoelectric film AE sensors used for the fatigue monitoring of tubular joint specimens, all piezoelectric AE film sensors have polyimide backing film for ease of installation.

The PZT-5A disc has a circular aperture of 5 mm while the piezoelectric paint disc has a diameter of 12.7 mm (1/2”). Although the outer diameter of the SE1000-HI sensor was measured as 20 mm and its aperture is 1.5 mm according to data sheet supplied by the manufacturer. Two of the piezoelectric film AE sensors made of PZT-5A disc (sensors labeled as a0 and a1) were bonded to the steel plate and their

location are shown in Figure 6.39 (b). Sensor a0 and a1 are 25 mm and 40 mm away from the weld tip respectively. The third piezoelectric film AE sensor made of PZT-5A disc (labeled as sensor a2) was bonded 60 mm away from sensor a0 and served as guard sensor to eliminate any AE signals from sources outside of the area of interest.

The two commercial AE sensors (labeled as sensors a4 and a5, as shown in Figure 6.39(b)) were installed on the other side of the longitudinal stiffener. Sensors a5 and a6 were aligned to the same line with sensors a0 and a1. A thin layer of Vaseline was used as couplant between the SE1000-HI sensor and the steel plate for good AE signal transmission. The SE1000-HI sensor is mounted with a C-shape magnet mounting fixture. Since the SE1000-HI sensors respond to the loading noise at low frequency range, they were not used for triggering. For piezoelectric film AE sensors, they are used with a band-pass filter and are thus immune to the low frequency loading noise, and can be used for triggering. In this test, sensor a0, which is closer to the weld tip, was used for triggering. The AE signal acquisition used the same Labview program for the tubular joint specimen test and the same data acquisition hardware was used.

6.2.3 Simulated AE Test on Welded Tubular Specimens

As a standard way to simulate AE source, pencil lead break test was performed on Specimen #2 at the weld toe where the fatigue crack was first seen (for detailed location of the weld toe, see Figure 6.41). Typical AE signals due to pencil lead break are shown in Figure 6.42. It can be seen that piezoelectric film AE sensors (a0, a1 and a2) have a larger amplitude than sensors SE1000-HI (a4 and a5), while both

types of AE sensors have their signal amplitudes greater than that of the piezoelectric paint AE sensor (a3).

Figure 6.43 shows a zoomed-in view of the AE signals shown in Figure 6.42. It's seen that different types of AE sensors have different signal characteristics. For the same type of sensors, the signal characteristics (waveform, frequency content) are similar. As pencil lead break generates an out of plane pulse force, it is similar to the tensile force at the fatigue crack. Thus, similar waveforms should be expected for the fatigue induced AE signal from this test. This provides another way to verify that the AE source is due to fatigue cracking.

Figure 6.44 shows the frequency spectra of the data shown in Figure 6.42. It's seen that most of energy of the AE signals induced by pencil lead break goes up to several hundred kHz in piezoelectric film AE sensors, no matter it is made of PZT-5A or piezoelectric paint. For commercial AE sensors, the energy is spread towards lower frequency range although high frequency content is also visible.

For reference purpose, ambient background noise measured by piezoelectric film AE sensors was also studied. Fifty records were collected and Figure 6.45 shows measured ambient background noise (no fatigue loading applied at measurement). The frequency spectra of ambient background noise are also presented in Figure 6.46, which was obtained by averaging 50 records in frequency domain. It can be seen that the commercial AE sensors have a lower noise floor.

6.2.4 Analysis AE Signals Collected in this Fatigue Test

Specimen#1 was used for training and AE monitoring process adjustment purpose. Both specimens are subjected to the same cyclic loading range. Fatigue crack growth

pattern for specimen#1 is shown in Figure 6.40. Fatigue crack was first seen at load cycle number N = 39,000 cycles in specimen#1.

Fatigue crack in specimen #2 was first seen at the same location as specimen#1 at load cycle number N=170,000 cycles. A close-up view of the fatigue crack in specimen#2 is shown in Figure 6.41, it is noted that the picture was taken at load cycle number N= 182,000 cycles, so the crack is still small. It's clear that the fatigue crack is a tensile type which is also confirmed by strain measurement data.

Figure 6.47 shows typical AE signals captured by the six AE sensors after fatigue crack was seen in specimen#2. The waveform of the AE signals captured by the three piezoelectric film AE sensors made of PZT-5A discs is similar to those AE signals acquired from fatigue test by other researchers (e.g., Berkovits and Fang, 1995; Yu *et al*., 2011). The corresponding frequency spectra are shown in Figure 6.48. It is seen that the energy distribution of the AE signals acquired by sensor a0, a1 and a2 is fairly strong up to several hundred kHz, which is similar to the power spectra of fatigue induced AE signals obtained in the tubular joint tests as shown in Figures 6.23 to 6.28.

Due to the lower sensitivity of sensor a3 made of piezoelectric paint (about 1/30 of the PZT-5A sensitivity), its signal does not show any visible AE waveform at this stage because the fatigue crack is still small and the corresponding stress intensity factor value (estimated to be in the range of 1 to 4 $MPa\cdot\sqrt{m}$) is considered too low for the piezoelectric paint based AE sensor to respond.

The AE signals collected by the two commercial AE sensors a4 and a5 are also shown in Figure 6.47 (e) and (f). However, the signals shown in the figure are

already filtered with a high-pass filter (cut-off frequency = 25 kHz) because the loading noise dominates the original unfiltered signals. Compared frequency spectra with signals from sensors based on PZT, their energy spread over the entire frequency range, which behaviors like white noise. This is due to weak signal energy and the signal frequency contents are immersed in the noise.

A zoomed-in view of the AE signals is presented in Figure 6.49. Clearly, different sensor signals exhibit different values of Rayleigh wave time of arrivals. This suggests that these AE signals are not EMI noise. Close examination of the time of the Rayleigh wave arrivals reveals that sensors a0 and a4 has the earliest arrival, while sensors a1 and a5 have a delayed arrival time compared with sensors a0 and a4. The guard sensor a2 has the latest arrival time because it was placed furthest away from the fatigue crack. According to the above analysis of time of arrivals, it's believed that the acquired AE signals are associated with the fatigue crack at the weld tip.

Looking at the AE signals acquired by sensors a0 and a1, their time arrivals are clearly different and the difference in Rayleigh wave arrival time is approximately 4.8 μs. Using typical Rayleigh wave speed value 2950 m/s in steel, the distance between these two sensors can be calculated as 14.2 mm. This value is very close to the actual center-to-center distance of the two sensors, which was set to be 15mm. This further confirms that the AE source is located at the weld tip shown in Figure 6.41. However, it's more difficult to determine the time of Rayleigh arrival in the AE signals acquired by the two SE1000-HI sensors due to their weak amplitude.

With the high frequency contents (from 100 to 400 kHz) of the AE signal and 1”-thick plate (thick enough for Rayleigh wave development), the proposed sensor couple theory might be used for AE source localization. According to the sensor couple theory, the AE signals acquired by sensors a0 and a1 are combined and its frequency spectrum is shown in Figure 6.50. It can be seen clearly that there are three troughs: 100.9 kHz, 277.6 kHz and 504.6 kHz. Actually these three troughs on the frequency spectrum are the first three predicted values of the space phase shift induced trough frequency. The theoretical prediction of the first trough frequency is given below,

$$f_s = \frac{c}{2x_{01}} = \frac{2950}{2\times 15\times 10^{-3}} = 98.3 \text{ kHz}$$

where c is the Rayleigh wave speed, x_{01} is the center to center distance between the two piezoelectric film AE sensors a0 and a1. Similarly, the second and third trough frequencies are predicted to be 295 kHz and 491 kHz. The experimental results are found to agree well with these theoretical predictions by a small error (less than 6% in error).

Naturally, the sensor couple theory can also be tried on the AE signals acquired by the two commercial AE sensors a4 and a5. Figure 6.51 shows the frequency spectrum of the combined signal of sensors a4 and a5, on which the trough frequencies can also be seen. The trough frequency values predicted from the sensor couple theory are 74 kHz, 221 kHz and 369 kHz respectively. However, only the first trough frequency could be determined from the experimental results, which is 73.53 kHz. The experimental result matches the theoretical predictions at the first trough

frequency. The reason for missing the other two trough frequencies is the weak signal amplitude of the commercial AE sensors resulting in lack of energy in high frequency range, which is clearly seen from their spectra as shown in Figure 6.51. Thus, the second and third trough frequencies become invisible. The smaller amplitude due to lower sensor sensitivity leads to lower SNR value and in worst case it might even become not possible to see any frequency troughs.

According to the above analysis, the feasibility of using the piezoelectric AE film sensor and commercial AE sensor for AE source localization based on the sensor couple theory has been demonstrated on the 1”-thick plate with fatigue crack. The theoretical prediction by the sensor couple theory agrees with the results using the time of arrivals method.

6.3 Conclusions

The feasibility of using piezoelectric film AE sensor for continuous fatigue crack monitoring during fatigue test of steel test specimens in the lab has been demonstrated. Piezoelectric film AE sensor made of piezo paint was found to be especially suitable for fatigue crack monitoring on tubular structure due to its flexibility. It can avoid noise introduced by imperfect bonding, which was seen for PZT based sensor.

AE signals due to different source mechanisms were identified, including fatigue crack propagation and friction rubbing of the fatigue crack surface. It’s found that even on the same type of structure, friction induced AE signals can be very different from each other. However, all the friction induced AE signals were significantly different from those induced by fatigue crack propagation. Looking at

the frequency spectra, it can be seen that the friction induced signals had relatively low frequency contents while the fatigue crack induced AE signals lay in higher frequency range. This frequency characteristic might be used to tell whether an AE signal is due to fatigue crack growth or not.

Through the AE hits analysis, it was found that AE activities usually were quite active during certain time window followed by a calm period and this active-calm cycle repeated again. This phenomenon is consistent with the fatigue tests results reported by other researchers. Also from the AE hits rate, it can be seen that AE hits rate was equal to one at the later stage for both specimens WTJ4 and WTJ5. This indicates a lot of AE signals were due to friction.

For the welded plate specimen, Fatigue crack induced AE signals were also collected. This was proved by the delay of the time arrivals in the sensor array and the agreement between detected source location and the observed fatigue crack tip during the test. The pencil lead break test at the crack location, which generated similar force to the tensile stress that induced fatigue crack in this test, also confirmed that some of the acquired AE signals were associated with fatigue crack growth.

The sensor couple theory for AE source localization presented in Chapter 5 was experimentally verified using the data acquired from the fatigue test of the welded plate for both piezoelectric film AE sensor and commercial AE sensor. The localization results match that of the conventional Time of Arrival method. However, due to the smaller tube wall thickness of the tubular joint specimen and its curved surface, the sensor couple based AE source localization method cannot be verified using AE data from the tubular joint specimens.

Figure 6.1: Car crushed by down signal support structures due to fatigue (courtesy of late R. Dexter, University of Minnesota)

Figure 6.2: Fatigue test setup for welded tubular joint test specimen

Figure 6.3: Piezoelectric film AE sensors (big disc is piezoelectric paint disc and small disc is PZT-5A disc) installed near the circumferential weld of the tubular joint specimen (Specimen WTJ4)

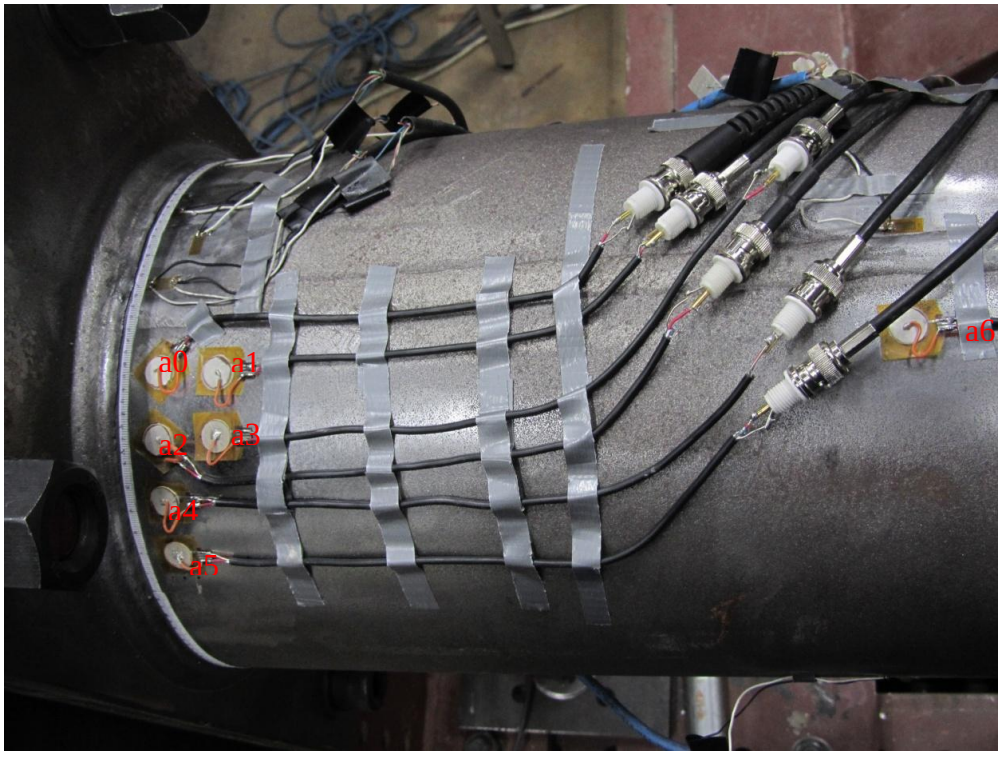

Figure 6.4: Piezoelectric film AE sensors (big disc is piezoelectric paint disc and no PZT-5A disc was used) installed near the circumferential weld on the tubular joint specimen (Specimen WTJ5)

Figure 6.5: Piezoelectric film AE sensors (big disc is piezoelectric paint disc and no PZT-5A disc was used) installed near the circumferential weld on the tubular joint specimen (Specimen WTJ6)

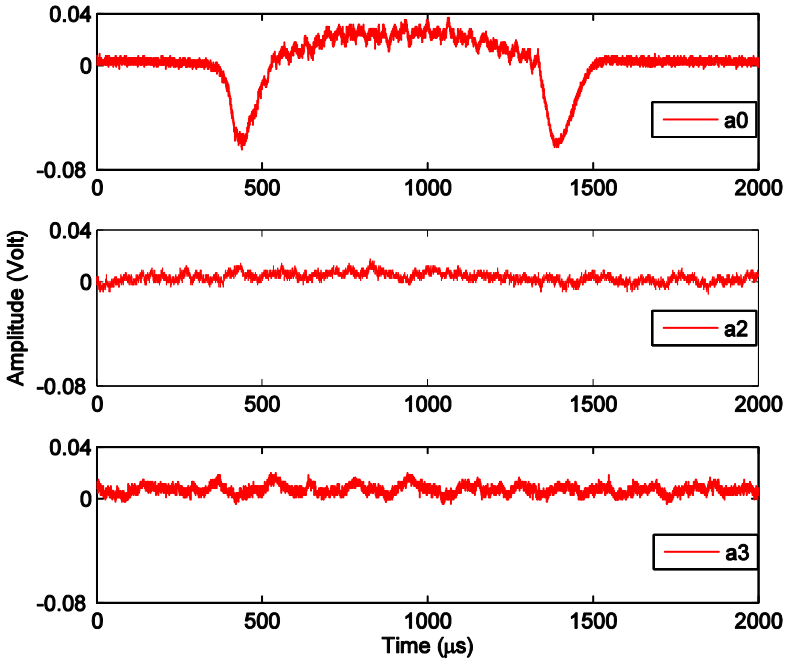

Figure 6.6: Signal from PZT-5A disc based piezoelectric film AE sensor (labeled a0 in Figure 6.3) on specimen WTJ4, due to flawed bonding layer between the sensor film and curved steel surface (a2 and a3 are piezoelectric paint AE sensors)

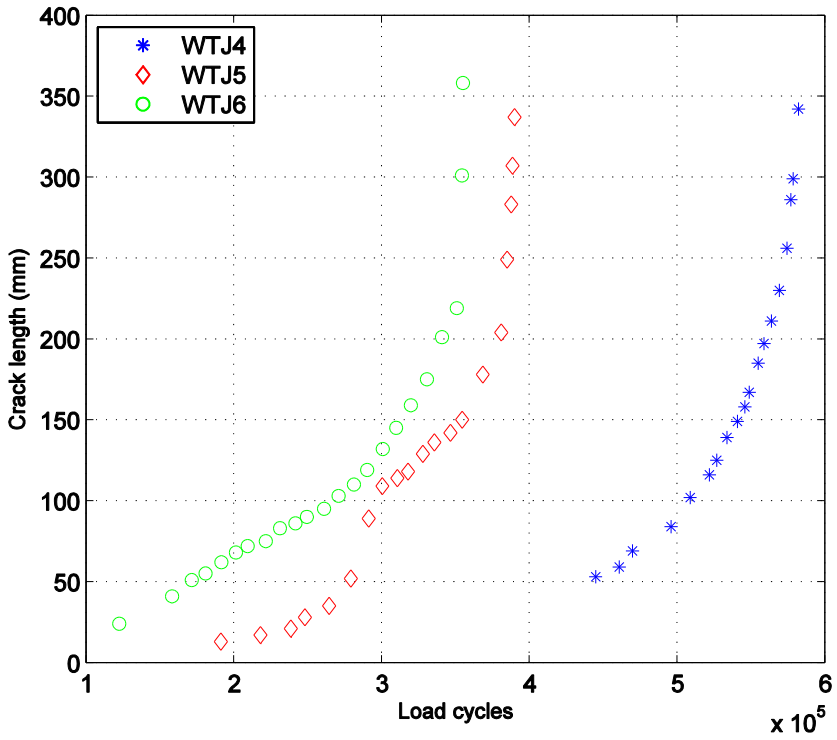

Figure 6.7: (a) see next page for caption

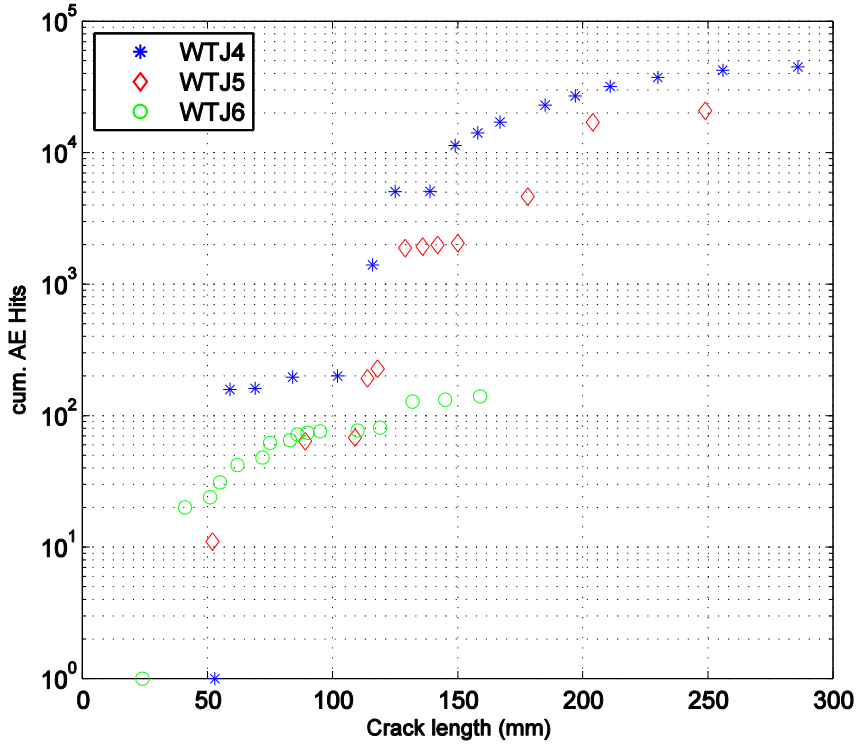

(b)

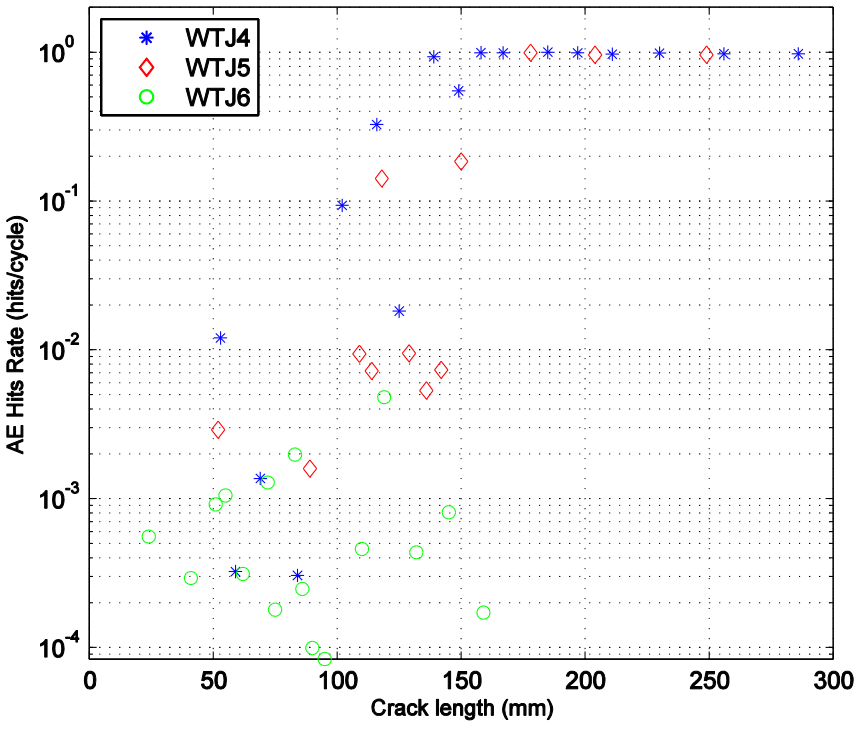

(c)

Figure 6.7: (a) Fatigue crack growth curves of three tubular joint specimens WTJ4, WTJ5 and WTJ6; (b) cumulative AE hits versus fatigue crack length (c) AE hits rate versus fatigue crack length

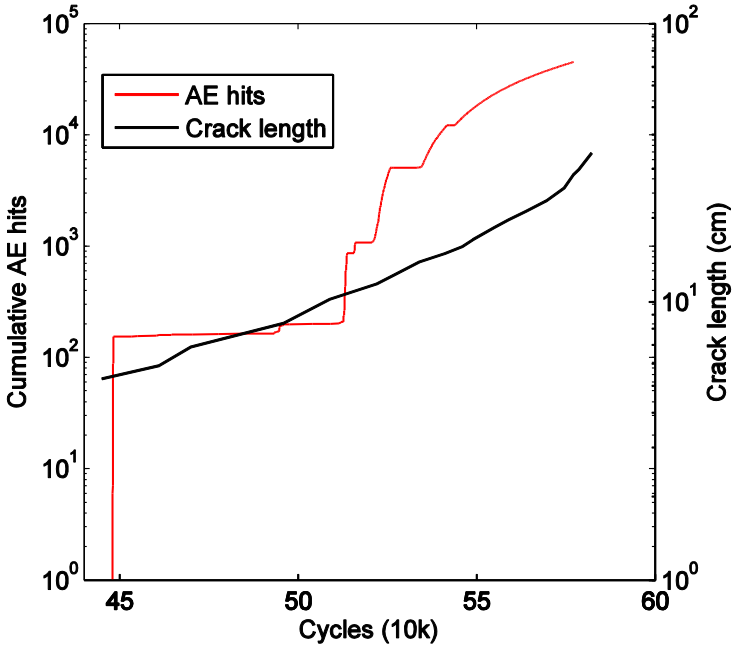

(a)

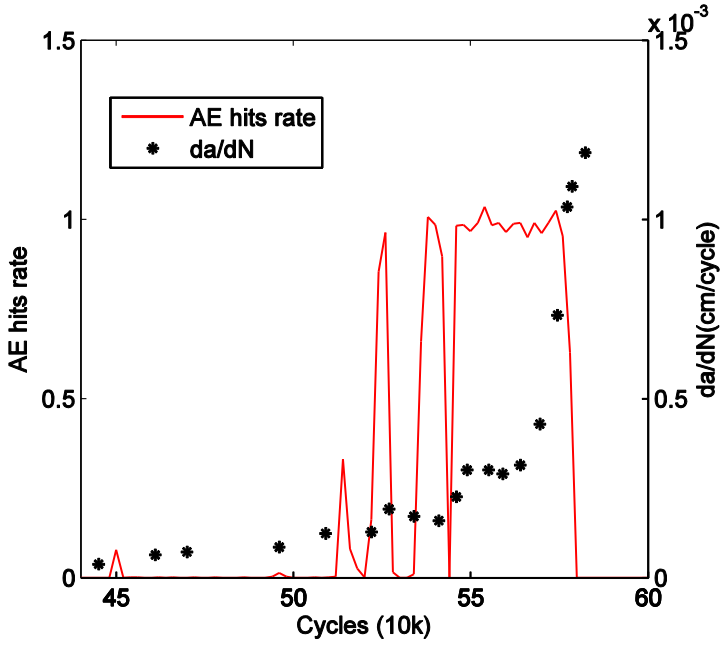

(b)

Figure 6.8: Test specimen WTJ4: (a) cumulative AE hits and crack length versus load cycles; (b) AE hits rate and crack growth rate da/dN along versus load cycles

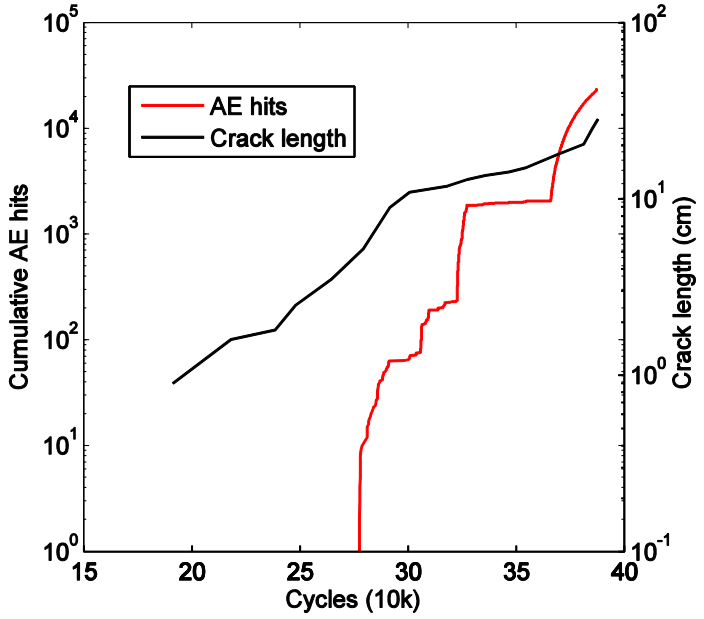

(a)

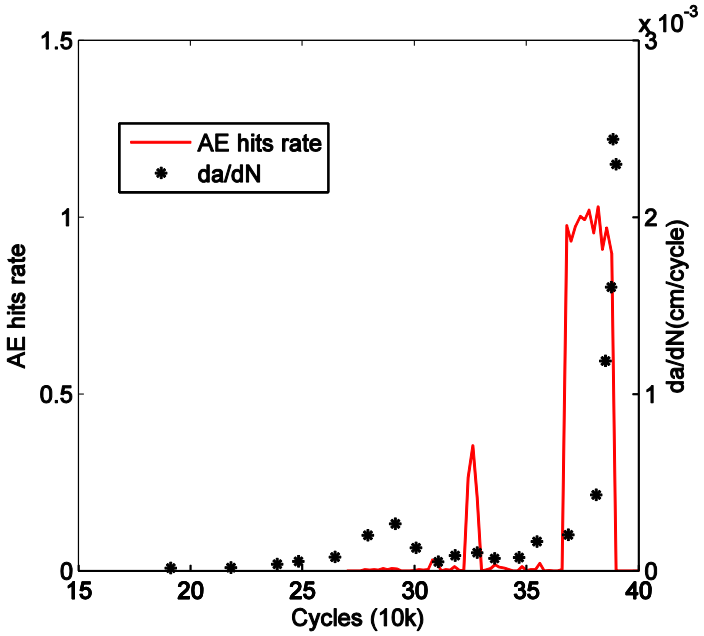

(b)

Figure 6.9: Test specimen WTJ5: (a) cumulative AE hits and crack length versus load cycles; (b) AE hits rate and crack growth rate da/dN along versus load cycles

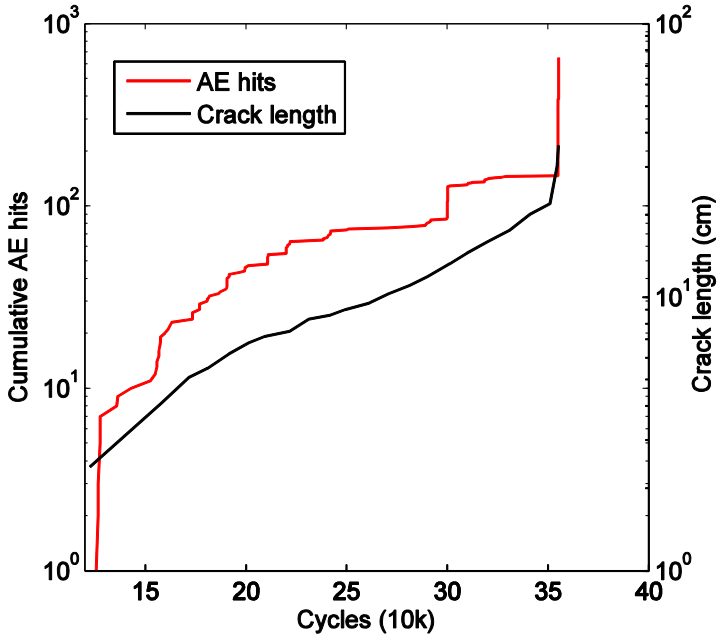

(a)

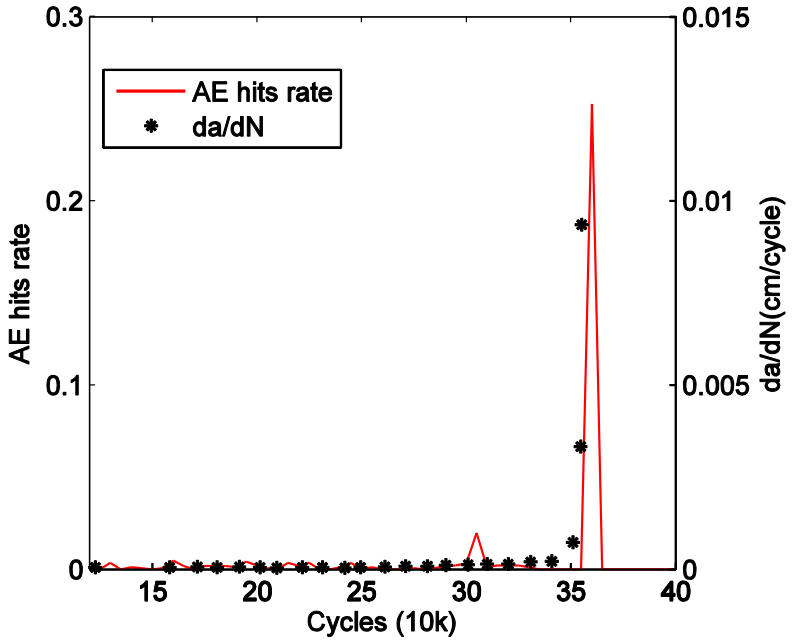

(b)

Figure 6.10: Test specimen WTJ6: (a) cumulative AE hits and crack length versus load cycles; (b) AE hits rate and crack growth rate da/dN along versus load cycles

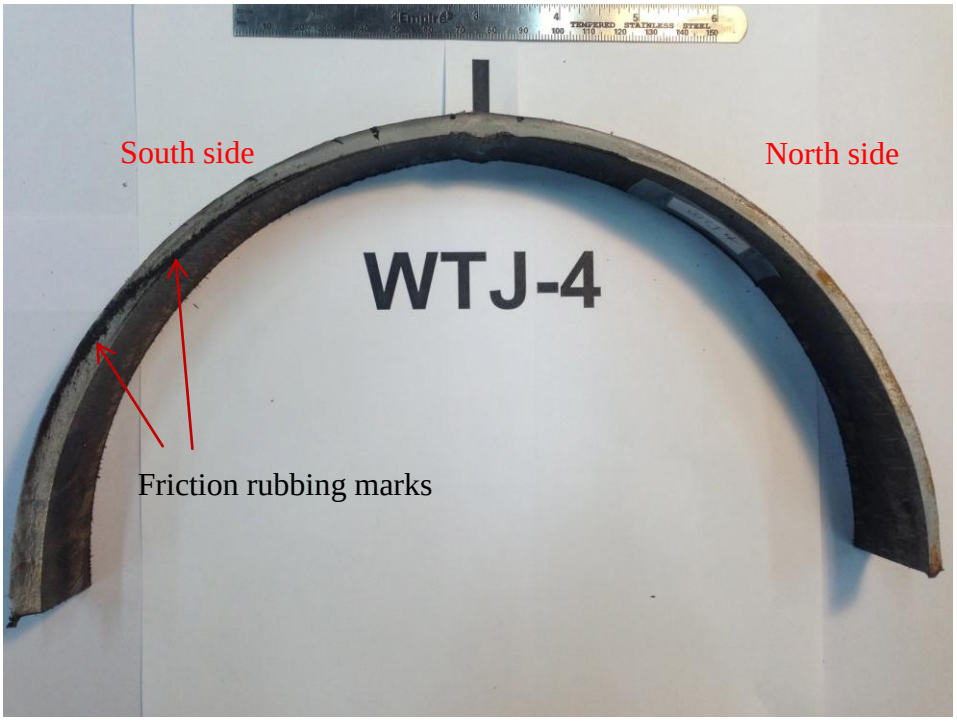

(a)

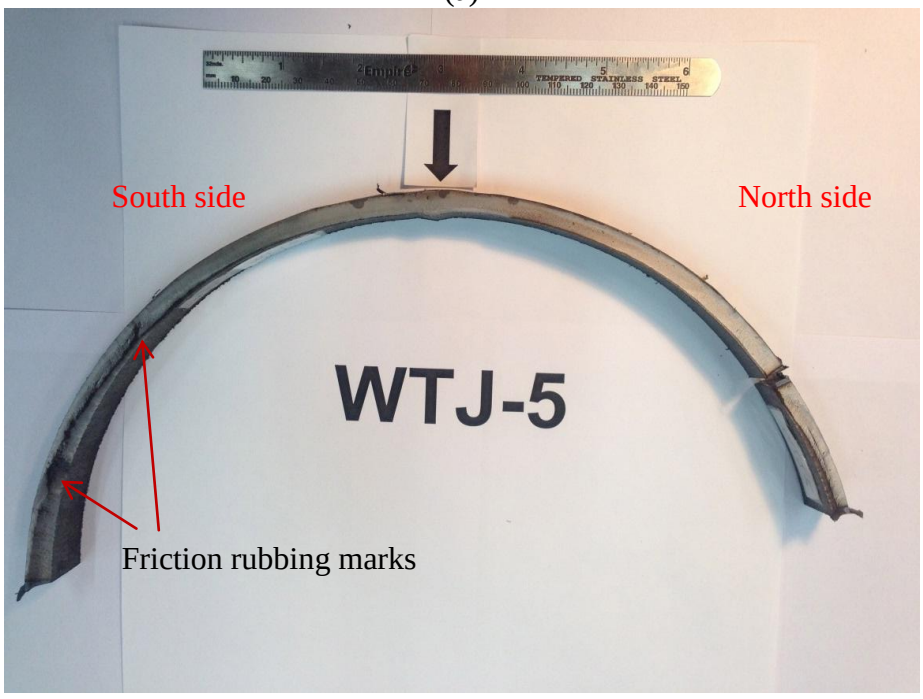

(b)

Figure 6.11: (a), (b) see next page for caption

(b)

Figure 6.11: Fracture surface of fatigue test specimens: (a) friction rubbing marks in WTJ4; (b) friction rubbing marks in WTJ5; (c) no friction rubbing marks in WTJ6

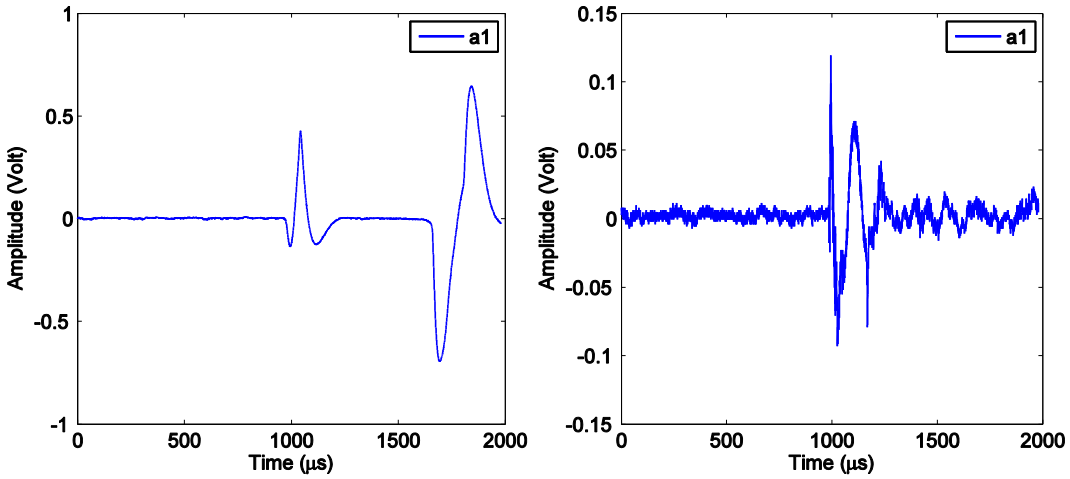

(a) (b)

Figure 6.12: Typical AE signals acquired by piezoelectric paint AE sensor (labeled as a1 in Figure 6.4) due to simulated AE source located 3-inch away from the sensor on specimen WTJ6: (a) hammer impact; (b) pencil lead break

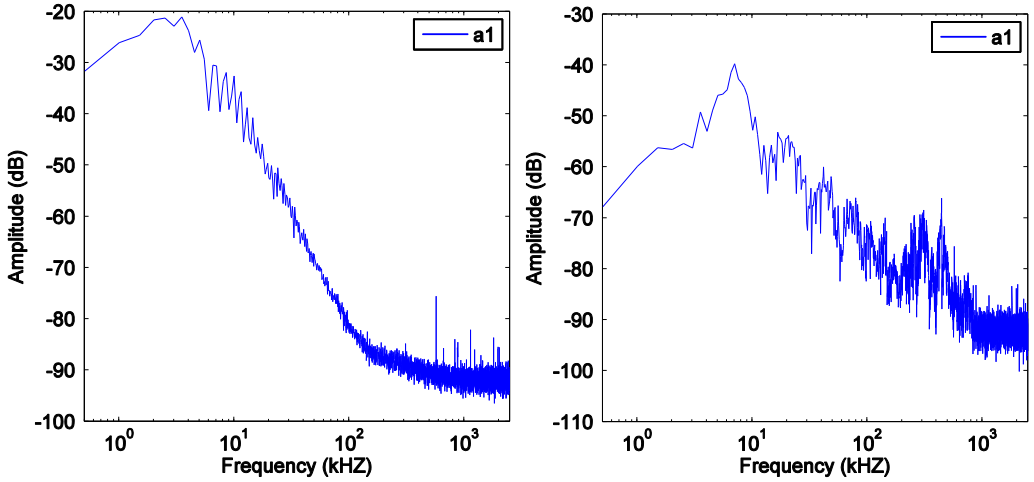

(a) (b)

Figure 6.13: Averaged frequency spectra of AE signals acquired by piezoelectric paint AE sensor (labeled as a1 in Figure 6.4) due to simulated AE source located 3-inch away from the sensor on specimen WTJ6: (a) hammer impact; (b) pencil lead break

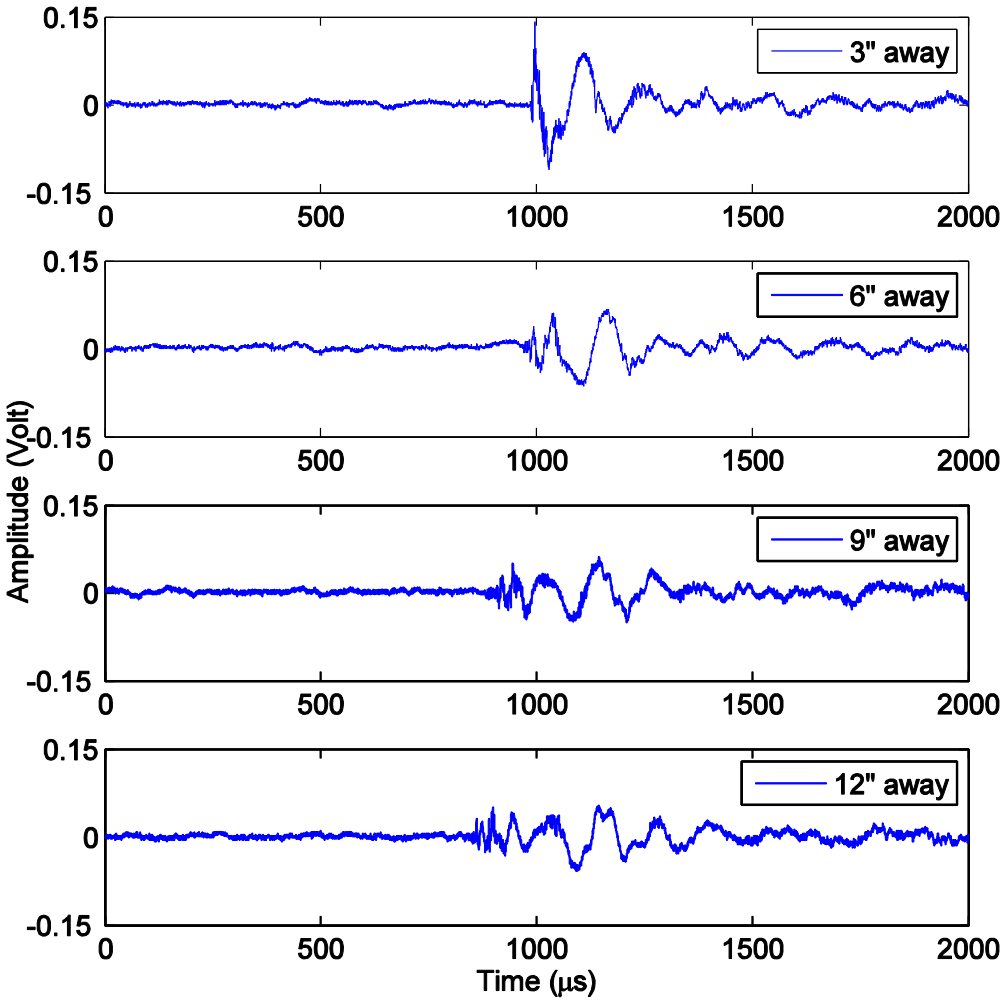

Figure 6.14: AE signals acquired by piezoelectric paint AE sensor (labeled a0 in Figure 6.4) due to simulated AE source (pencil lead break) with varying distances from the sensor in longitudinal direction

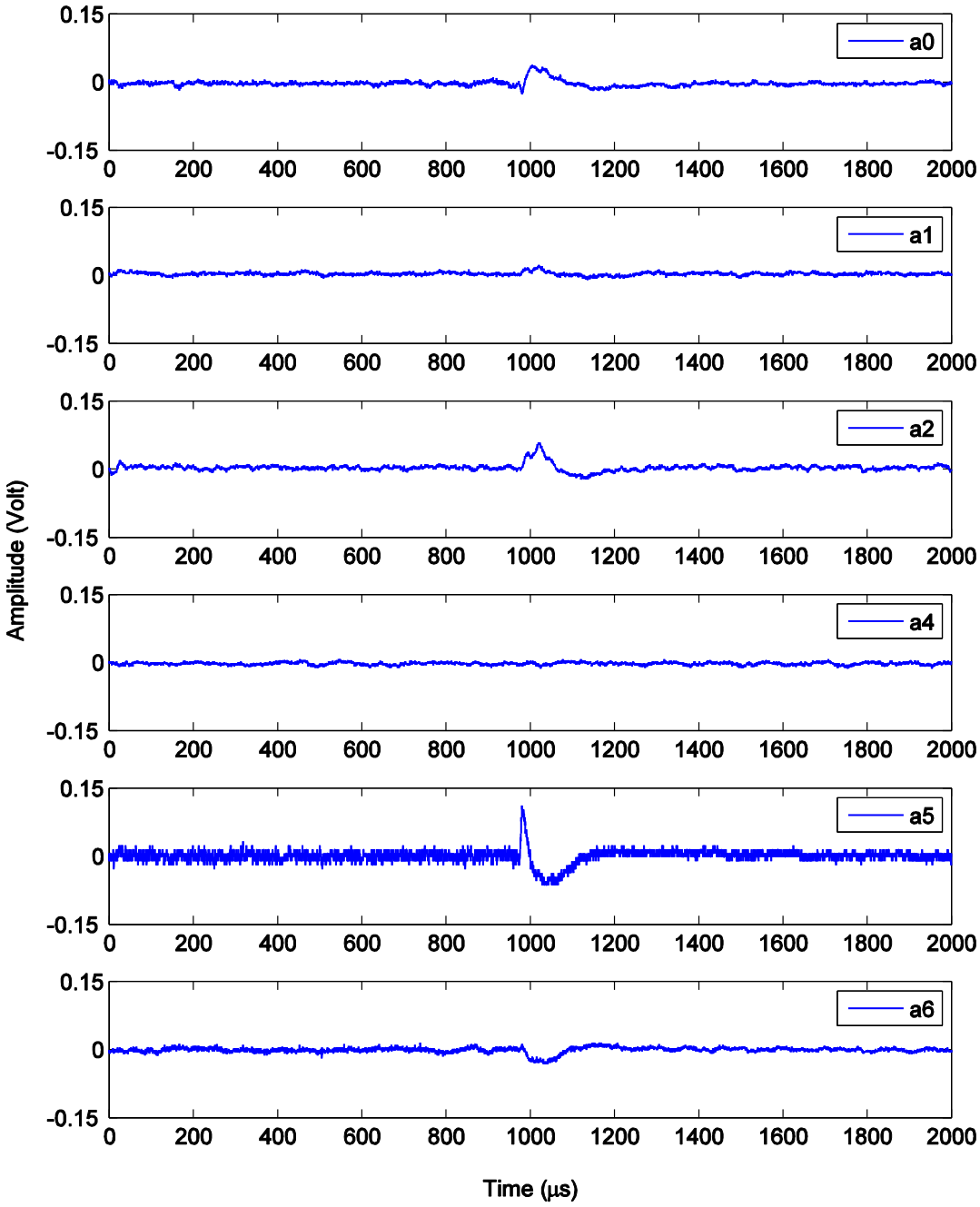

Figure 6.15: AE signals in piezoelectric paint AE sensors acquired at load cycle number N =309,269 cycles on specimen WTJ5

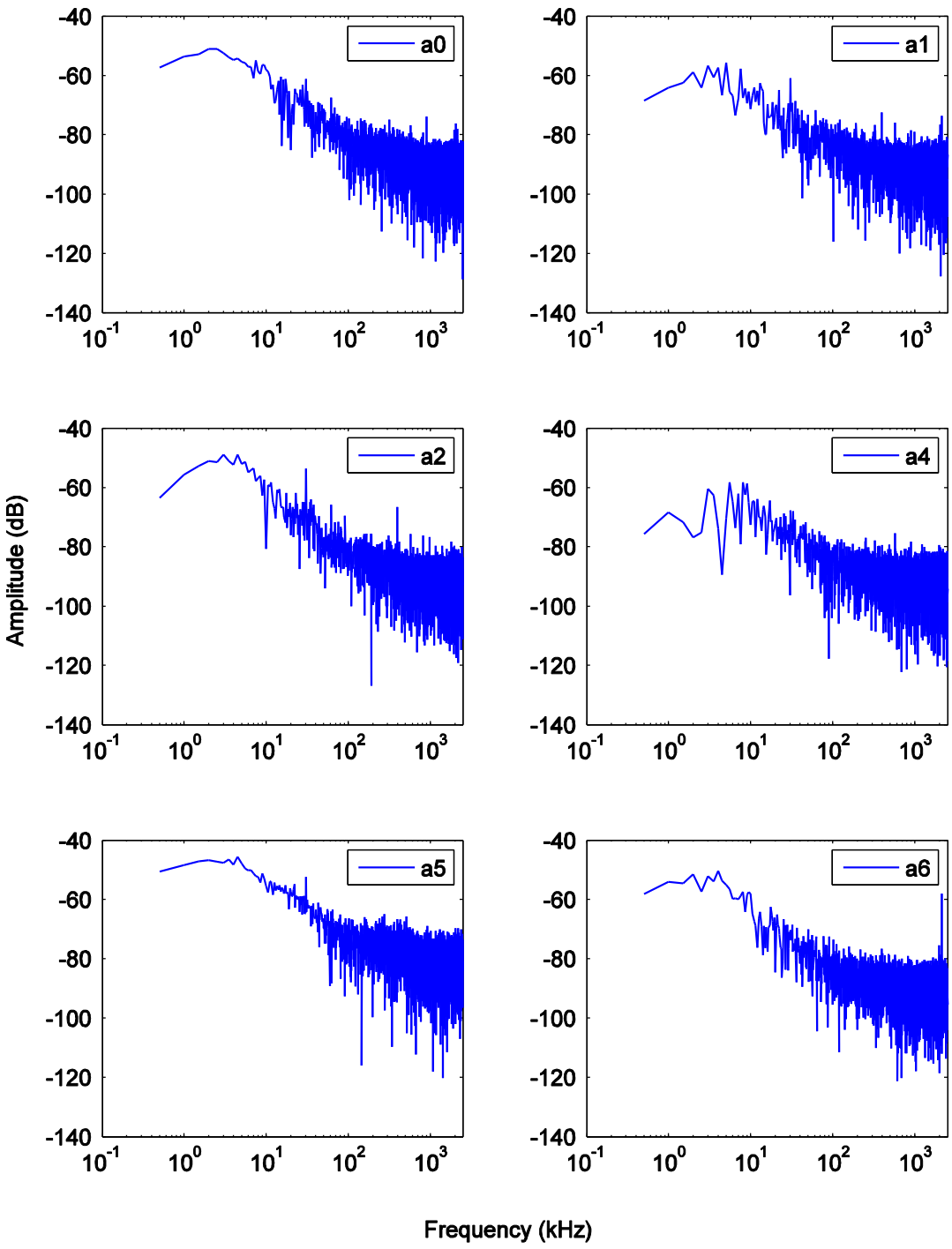

Figure 6.16: Frequency spectra of AE signals presented in Figure 6.15

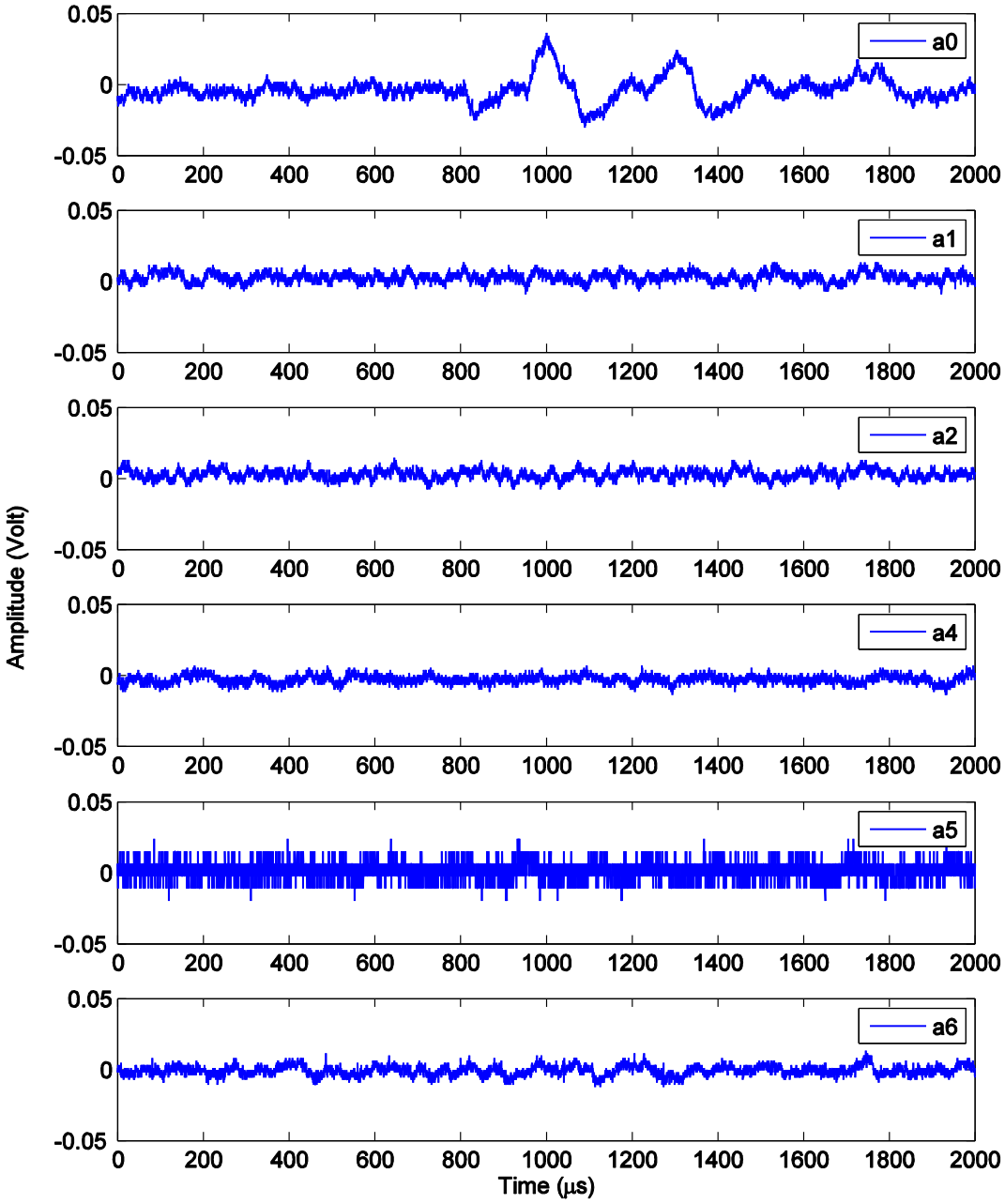

Figure 6.17: AE signals in piezoelectric paint AE sensors acquired at load cycle number N =327,359 cycles on specimen WTJ5

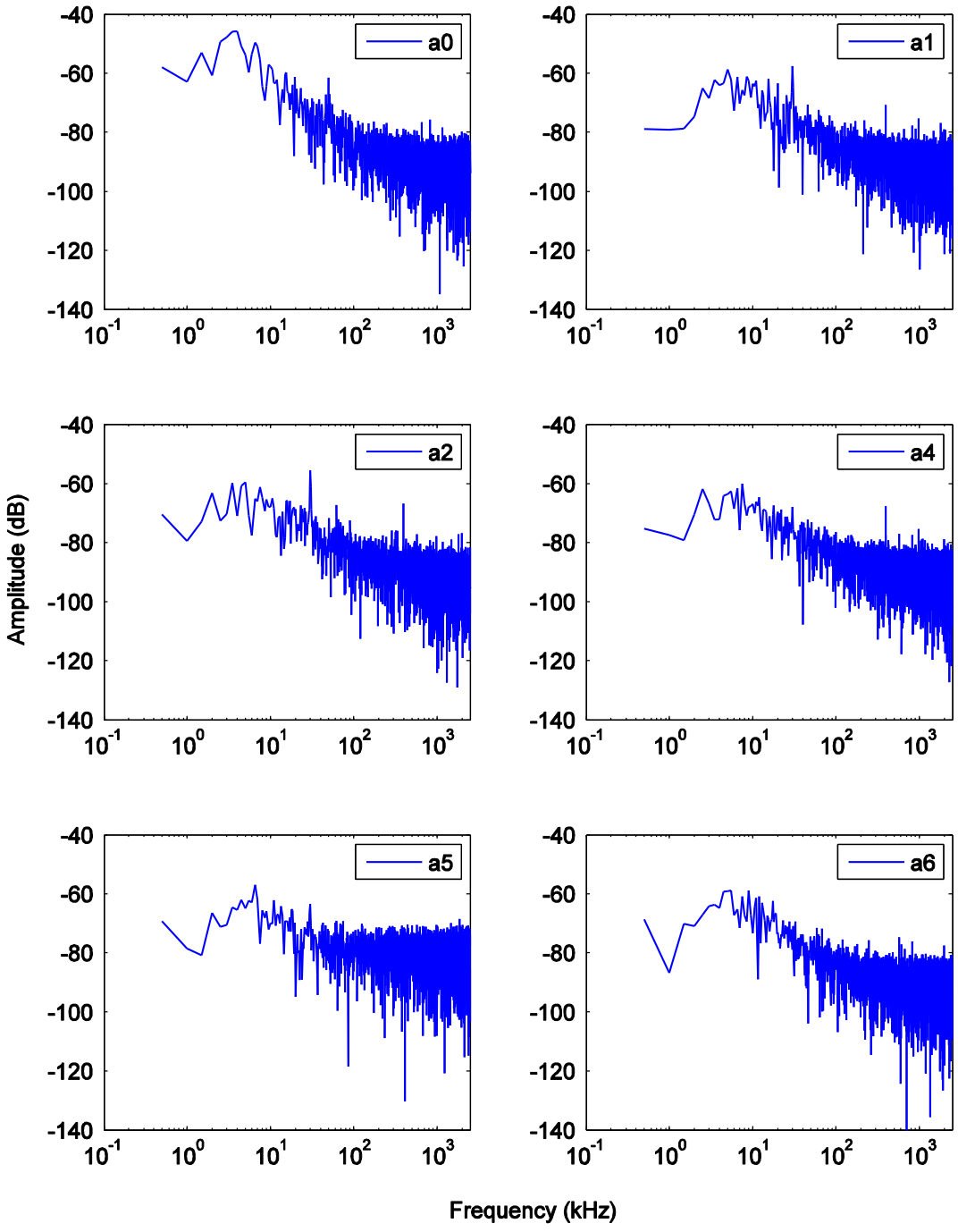

Figure 6.18: Frequency spectra of AE signals presented in Figure 6.17

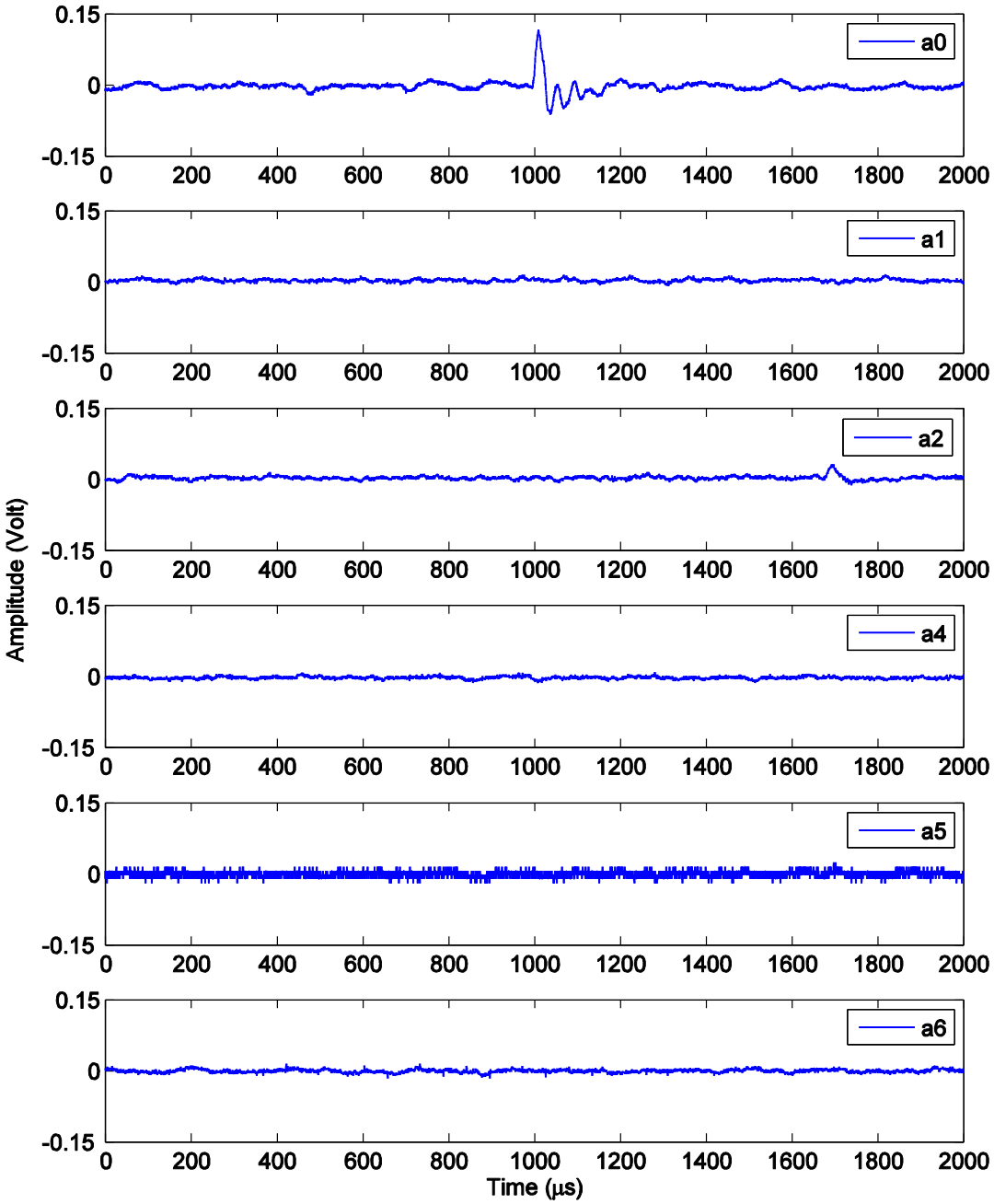

Figure 6.19: AE signals in piezoelectric paint AE sensors acquired at load cycle number N =346,337cycles on specimen WTJ5

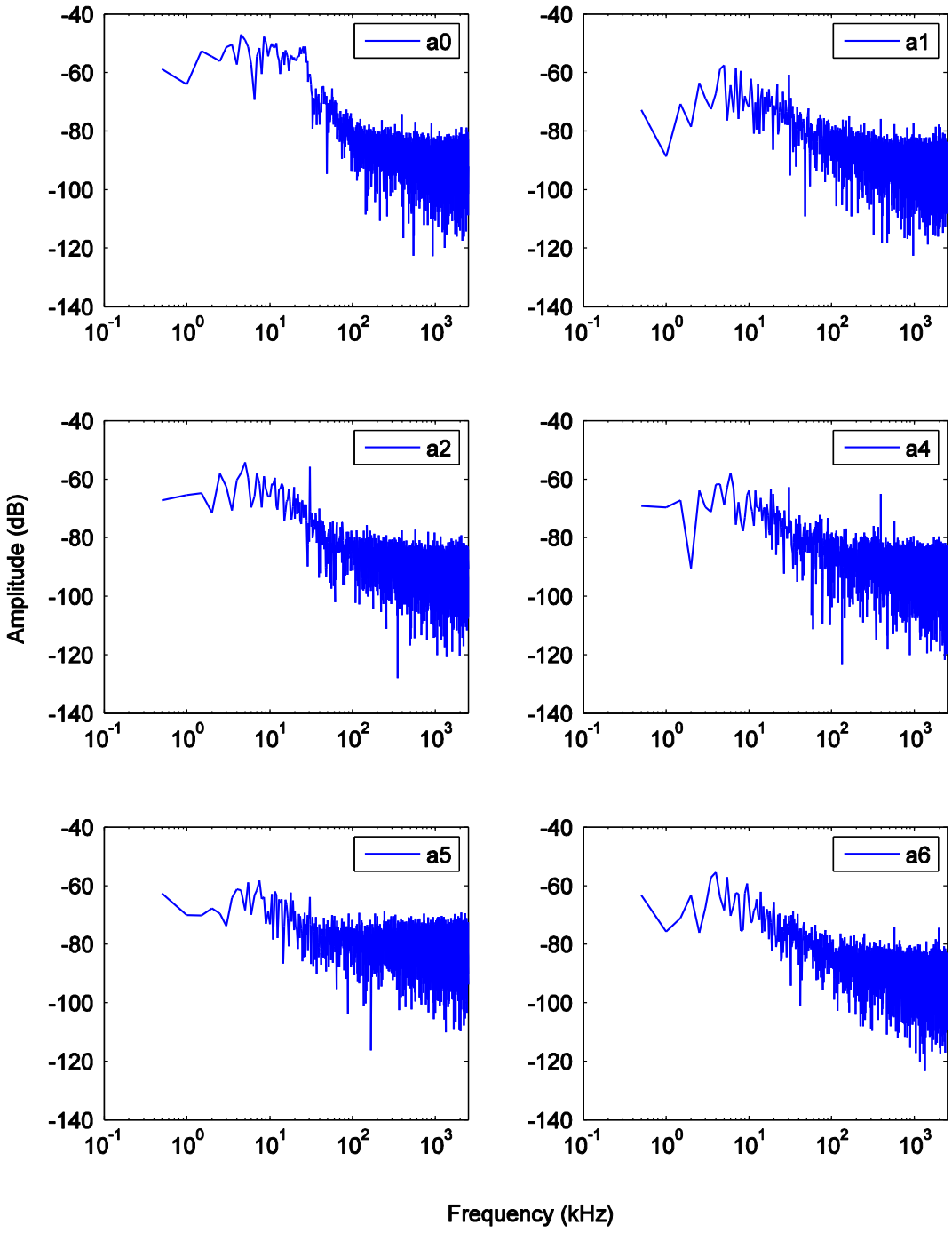

Figure 6.20: Frequency spectra of AE signals presented in Figure 6.19

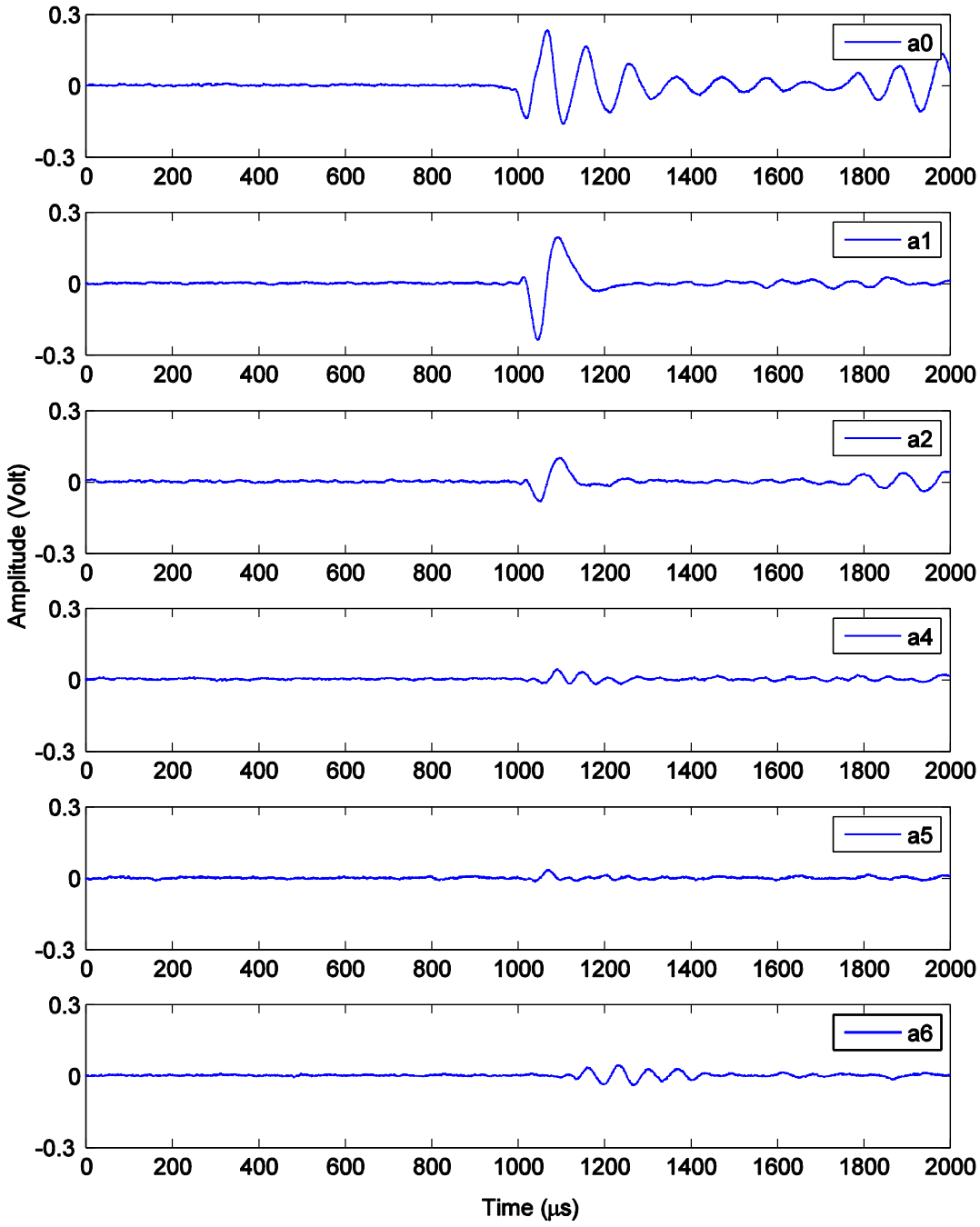

Figure 6.21: AE signals in piezoelectric paint AE sensors acquired at load cycle number N =367,899 cycles on specimen WTJ5

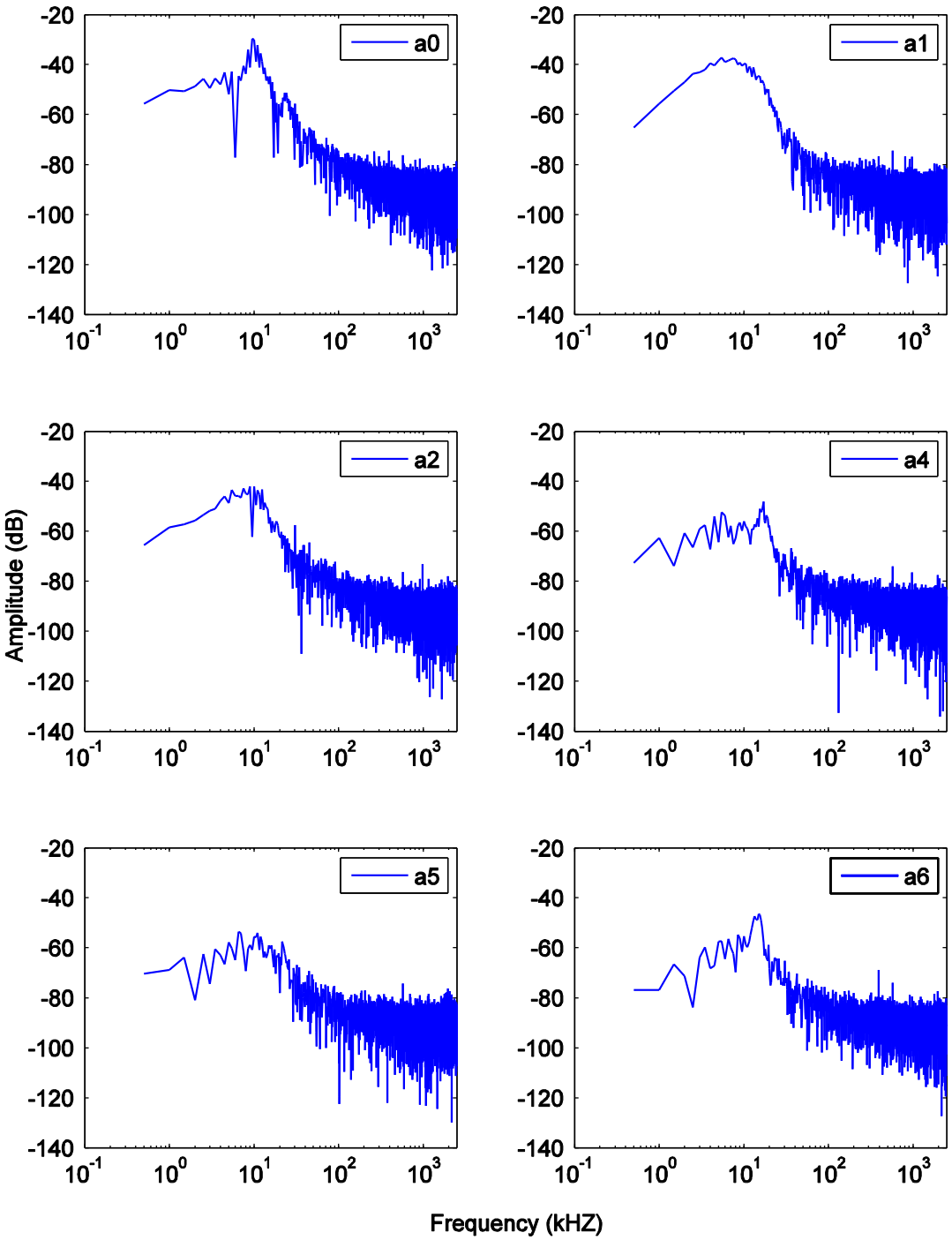

Figure 6.22: Frequency spectra of AE signals presented in Figure 6.21

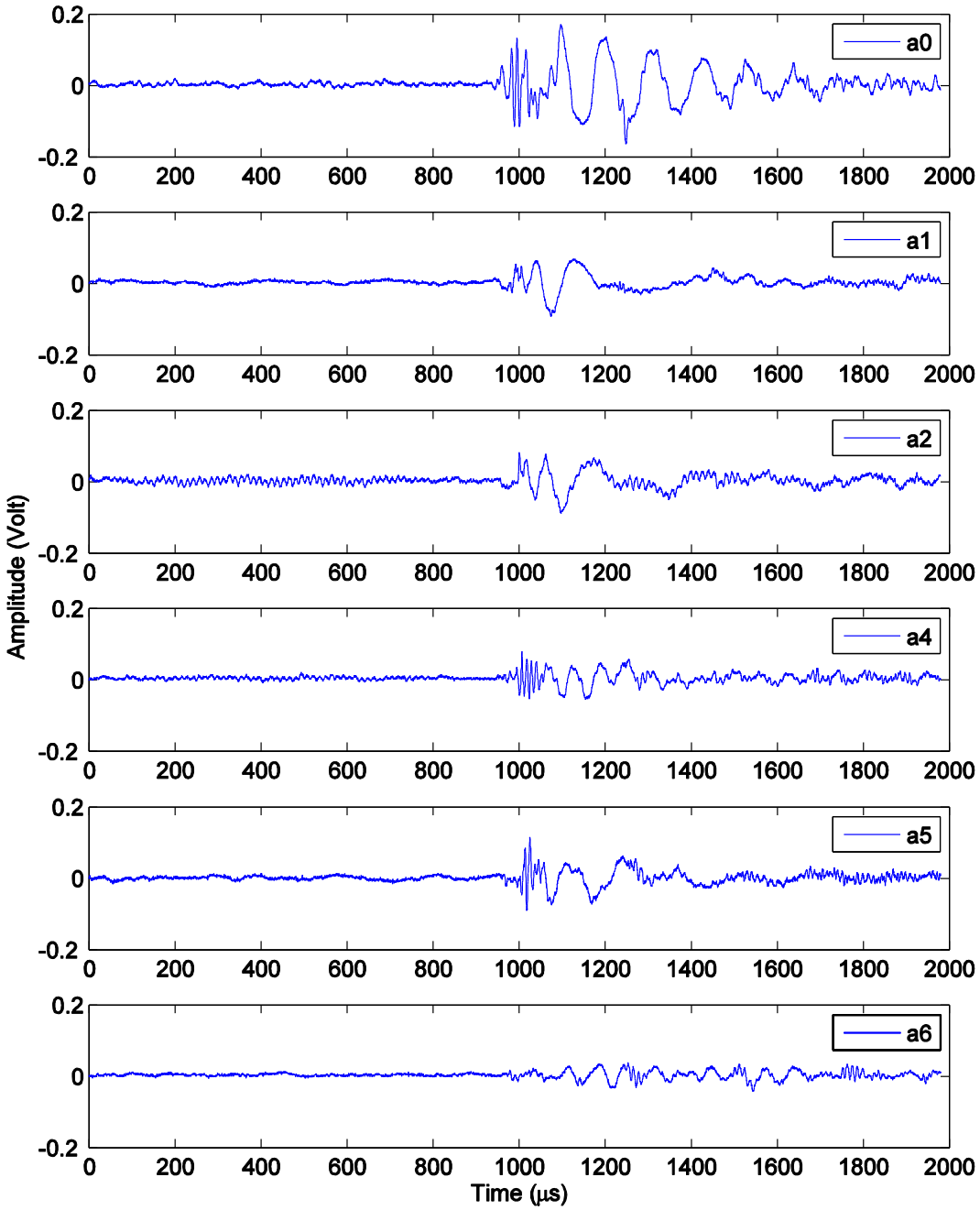

Figure 6.23: AE signals in piezoelectric paint AE sensors acquired at load cycle number N =374,679 cycles on specimen WTJ5

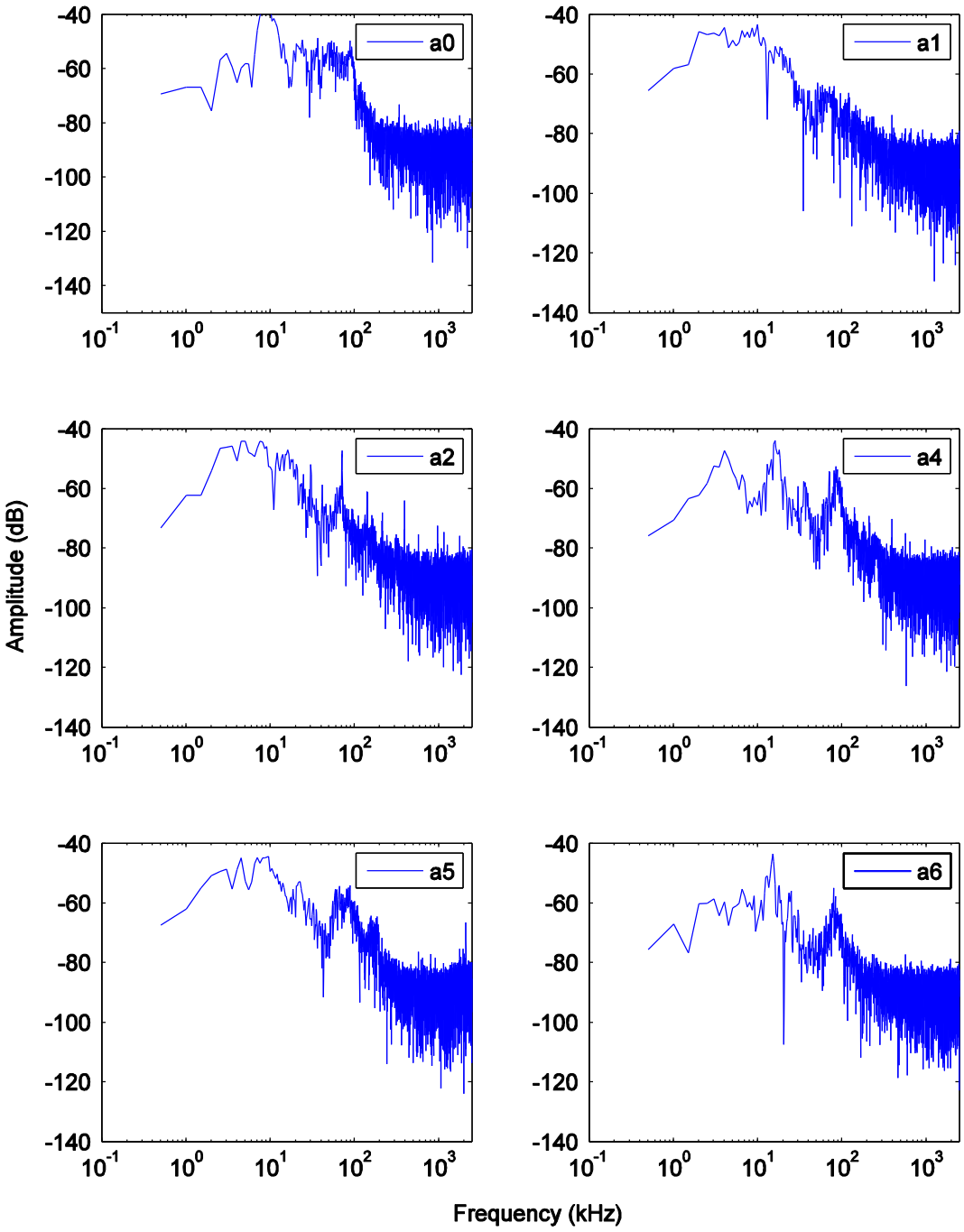

Figure 6.24: Frequency spectra of AE signals presented in Figure 6.23

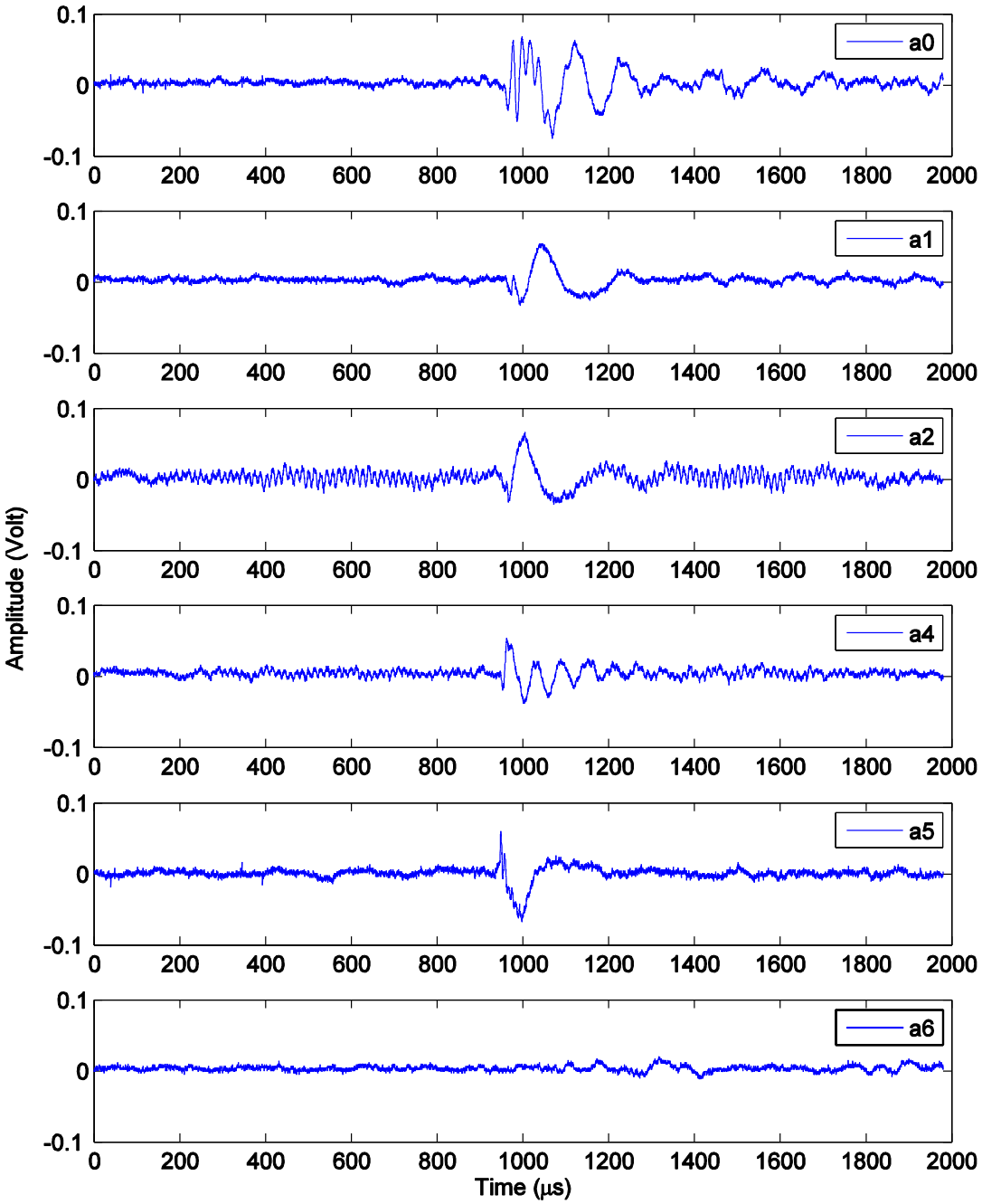

Figure 6.25: AE signals in piezoelectric paint AE sensors acquired at load cycle number N =374,731 cycles on specimen WTJ5

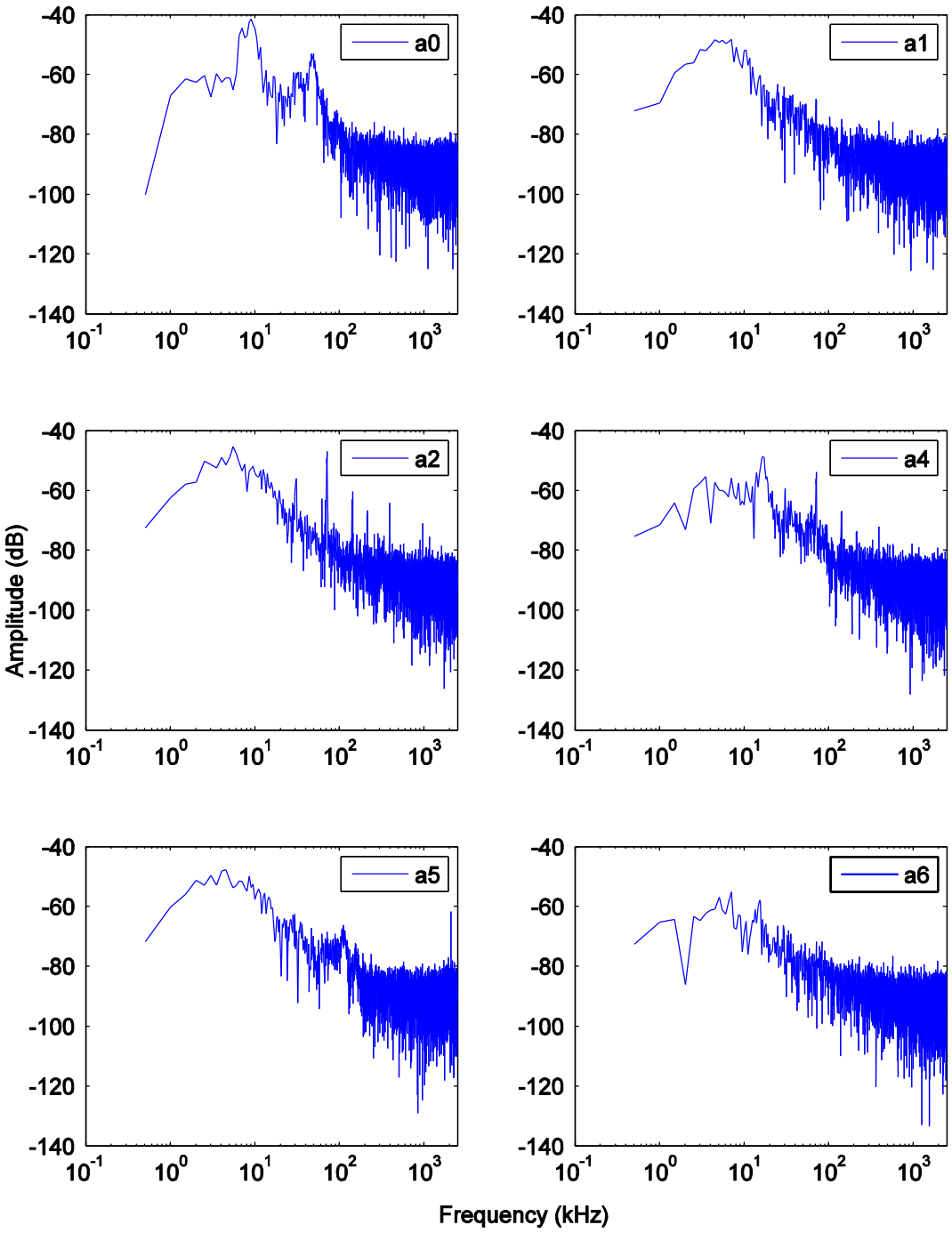

Figure 6.26: Frequency spectra of AE signals presented in Figure 6.25

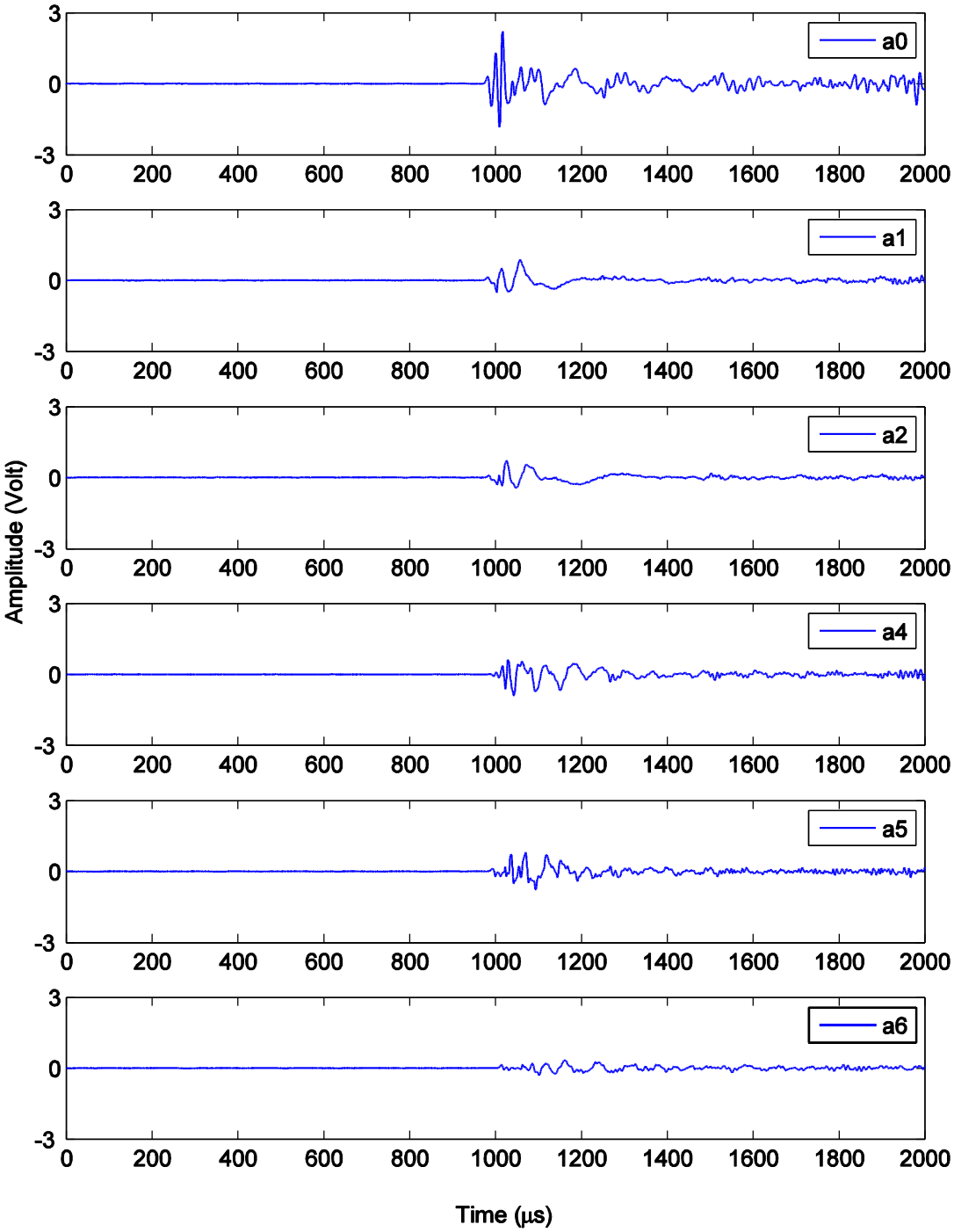

Figure 6.27: AE signals in piezoelectric paint AE sensors acquired at load cycle number N =386,775 cycles on specimen WTJ5

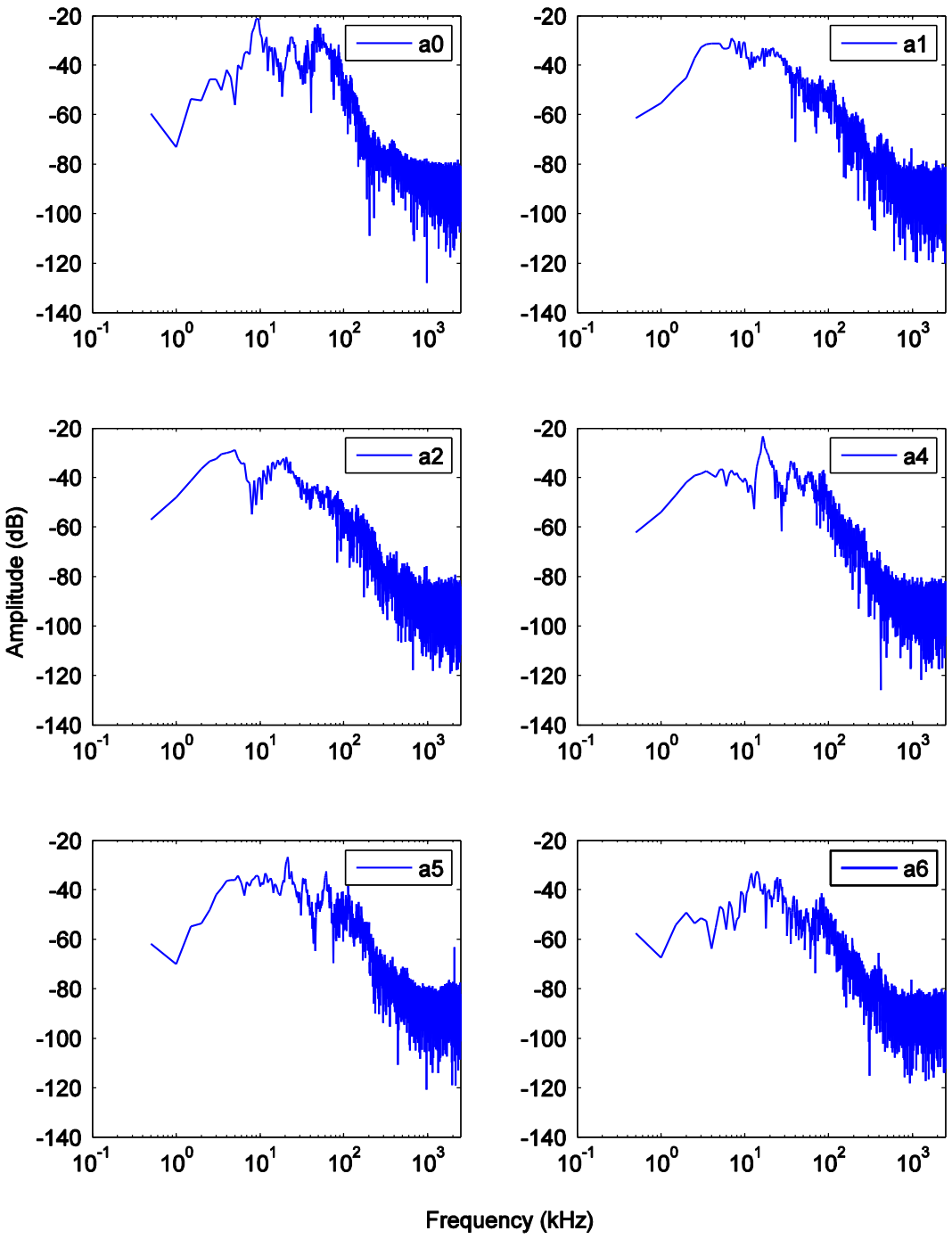

Figure 6.28: Frequency spectra of AE signals presented in Figure 6.27

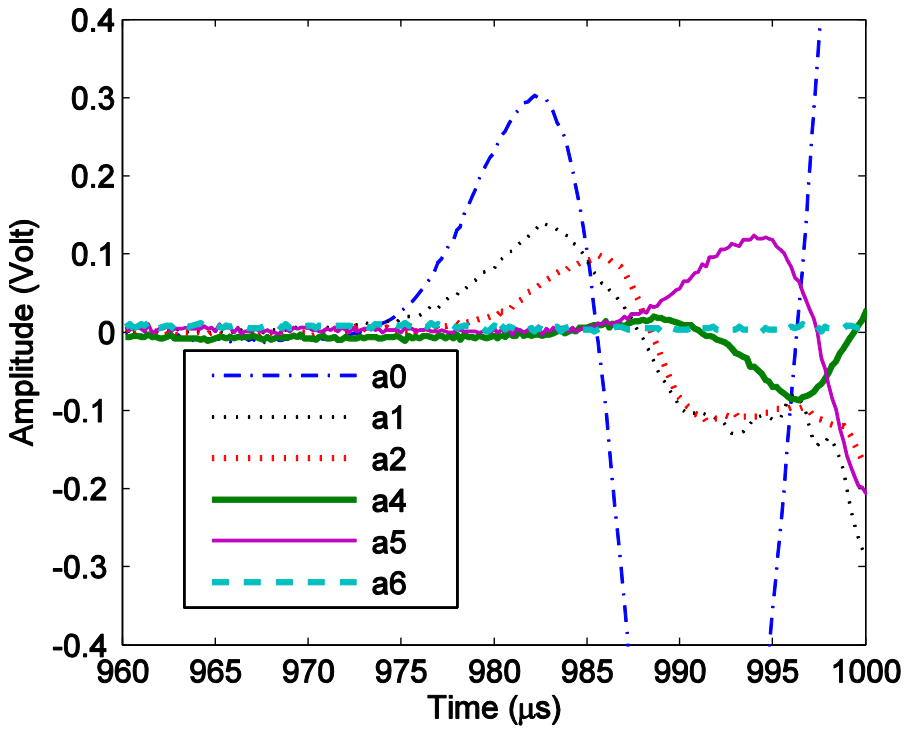

Figure 6.29: Zoomed-in view of AE signals in Figure 6.27 at load cycle *N* =386,775 for identifying time of arrivals on specimen WTJ5

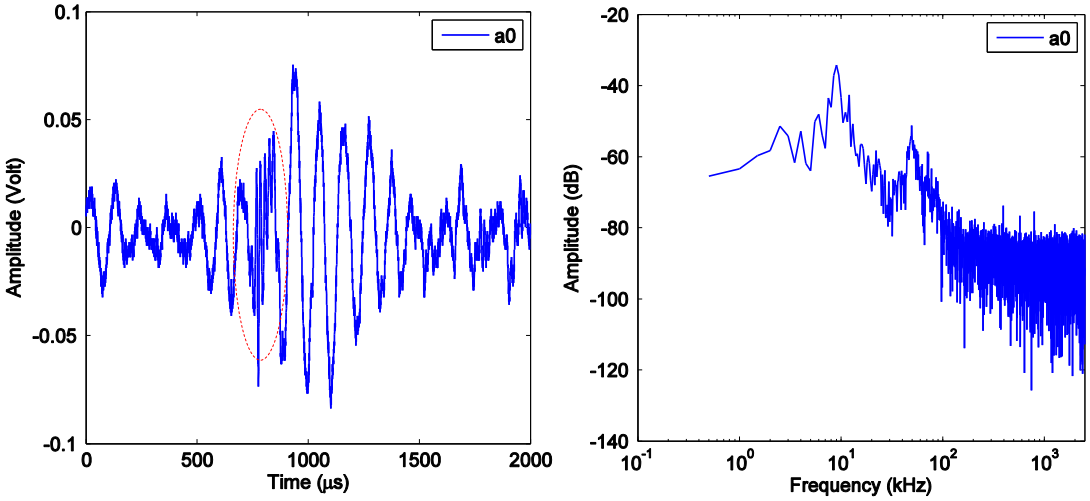

(a) (b)

Figure 6.30: Friction induced AE signal with overriding high-frequency signal component (encircled with dashed line) acquired by piezoelectric paint AE sensor a0 on specimen WTJ5at loading cycle *N* =387,233: (a) time history; (b) frequency spectrum

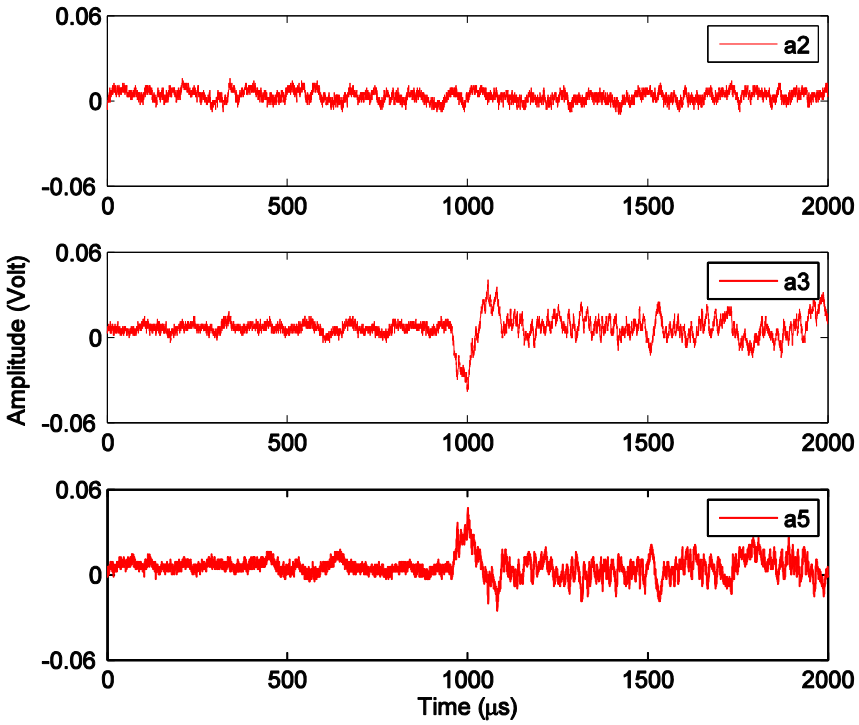

(a)

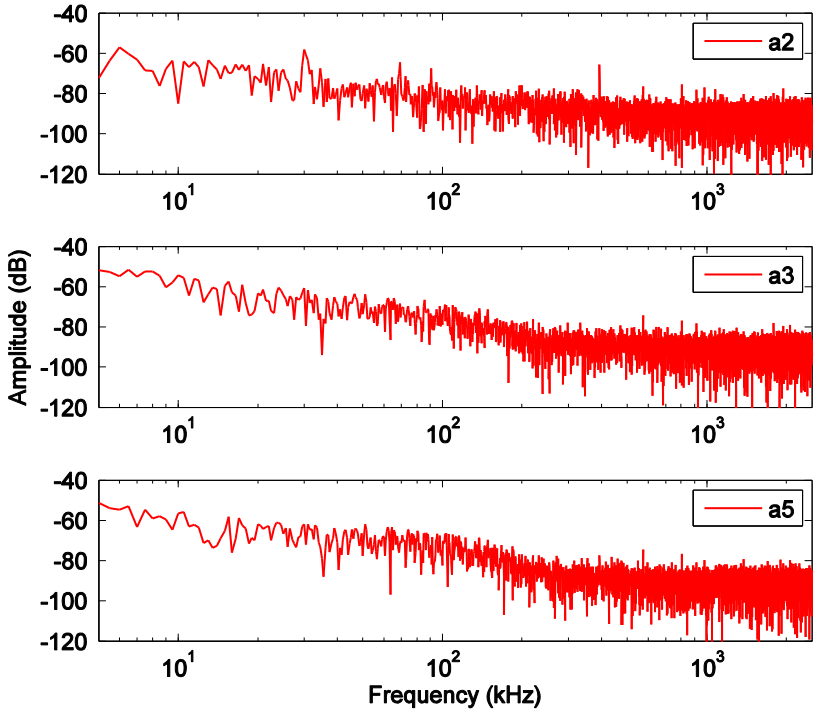

(b)

Figure 6.31: AE signals acquired by piezoelectric paint AE sensors at load cycle *N*= 490,236 cycles in test specimen WTJ4: (a) time history; (b) frequency spectra

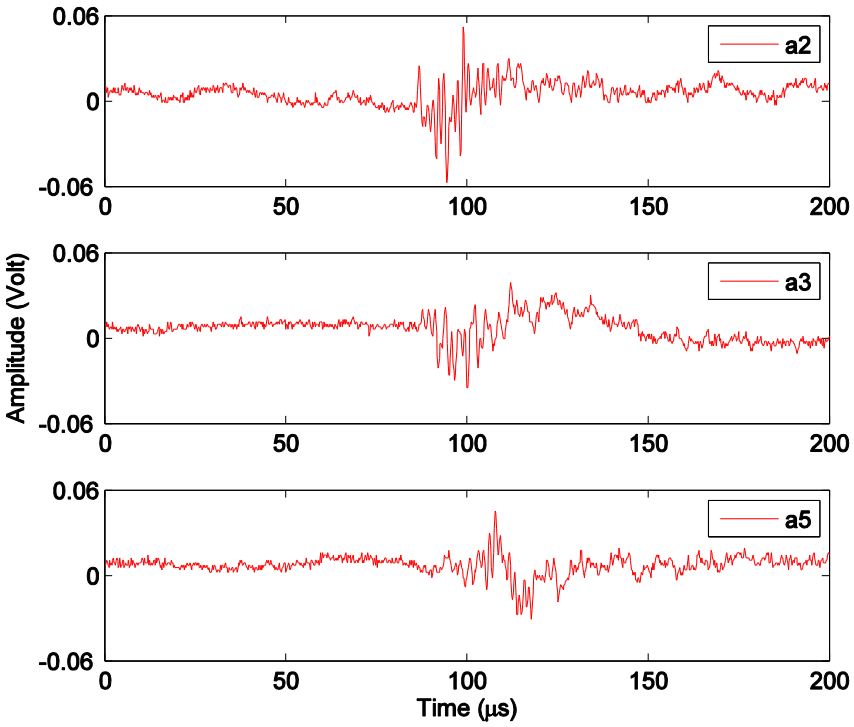

(a)

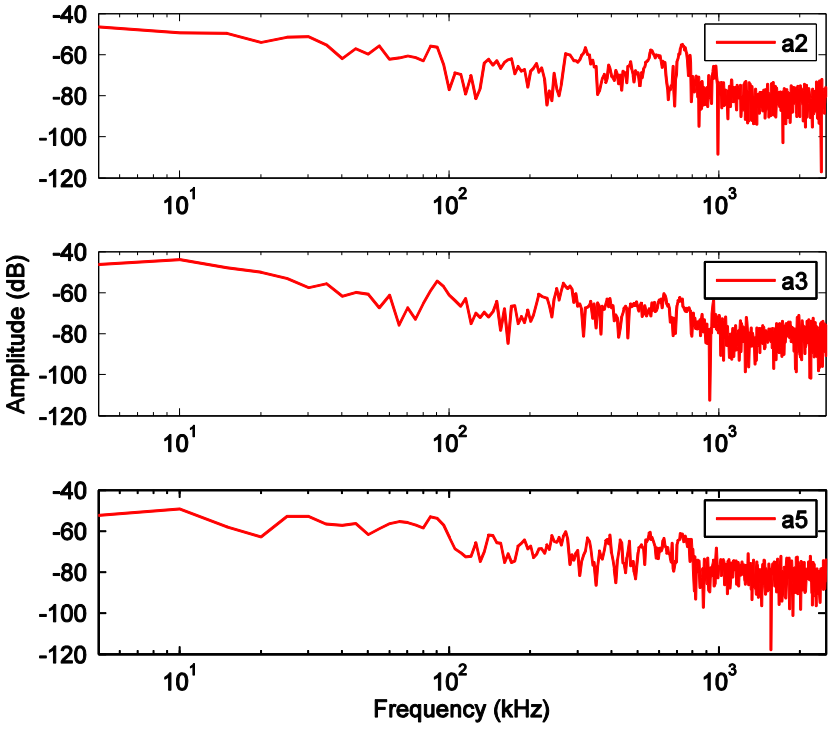

(b)

Figure 6.32: AE signals acquired by piezoelectric paint AE sensors at load cycle *N*= 506,382 cycles in test specimen WTJ4: (a) time history; (b) frequency spectra

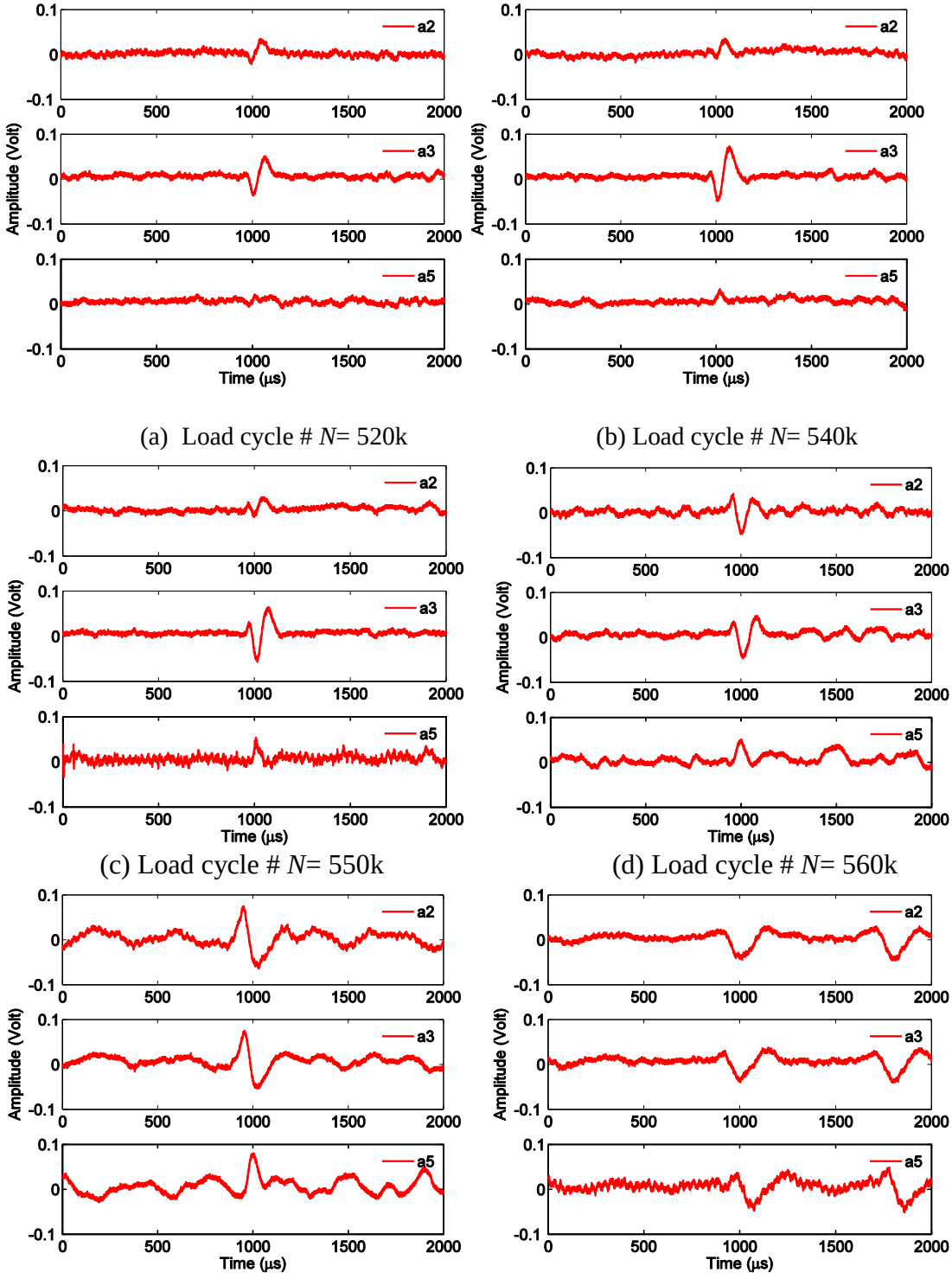

(a) Load cycle # *N*= 520k

(b) Load cycle # *N*= 540k

(c) Load cycle # *N*= 550k

(d) Load cycle # *N*= 560k

(e) Load cycle # *N*= 570k

(f) Load cycle # *N*= 575k

Figure 6.33: AE signals acquired by piezoelectric paint AE sensors on specimen WTJ4

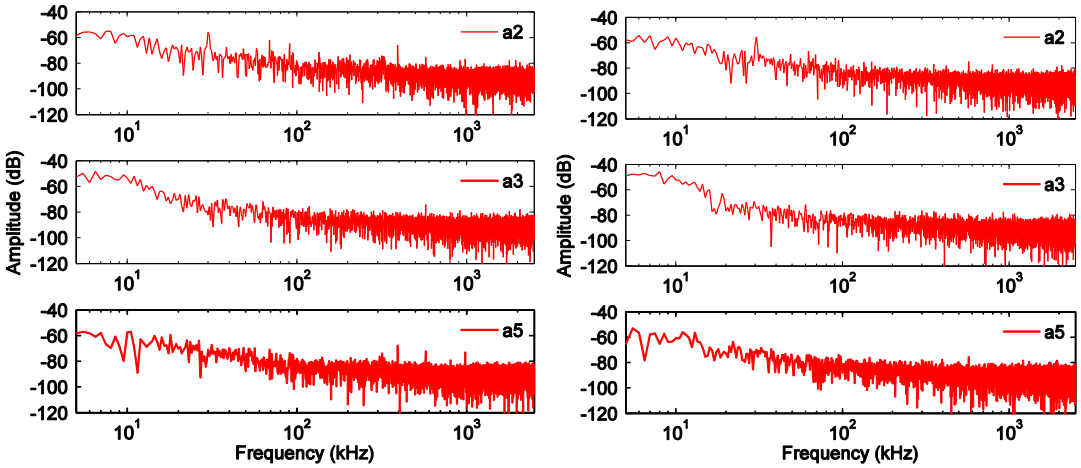

(a) Load cycle # N= 520k

(b) Load cycle # N= 540k

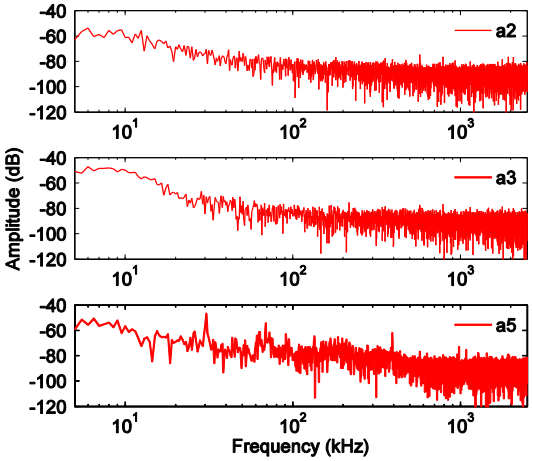

(c) Load cycle # N= 550k

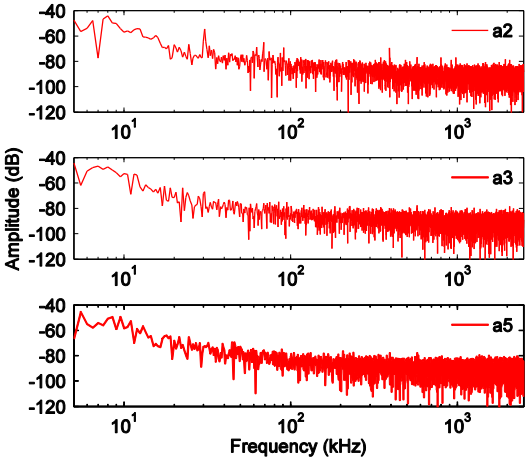

(d) Load cycle # N= 560k

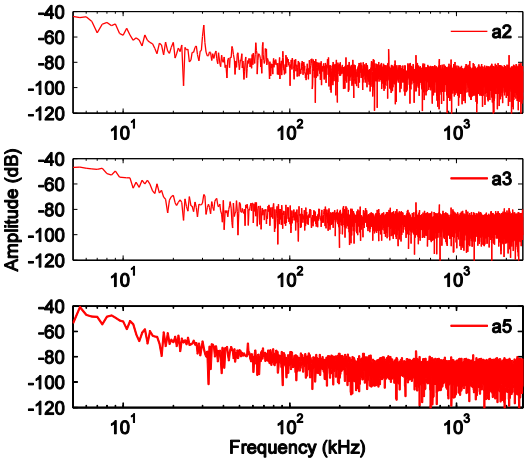

(e) Load cycle # N= 570k

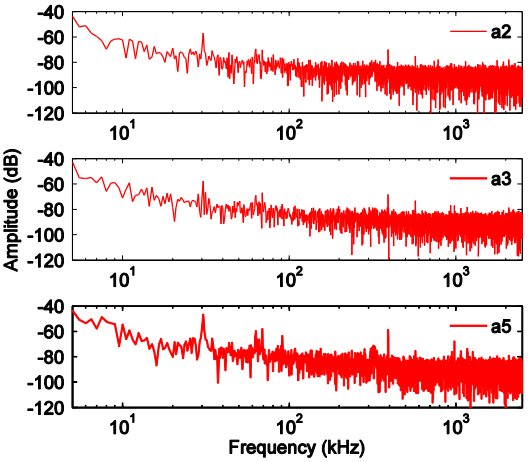

(f) Load cycle # N= 575k

Figure 6.34: Frequency spectra of AE signals shown in Figure 6.33

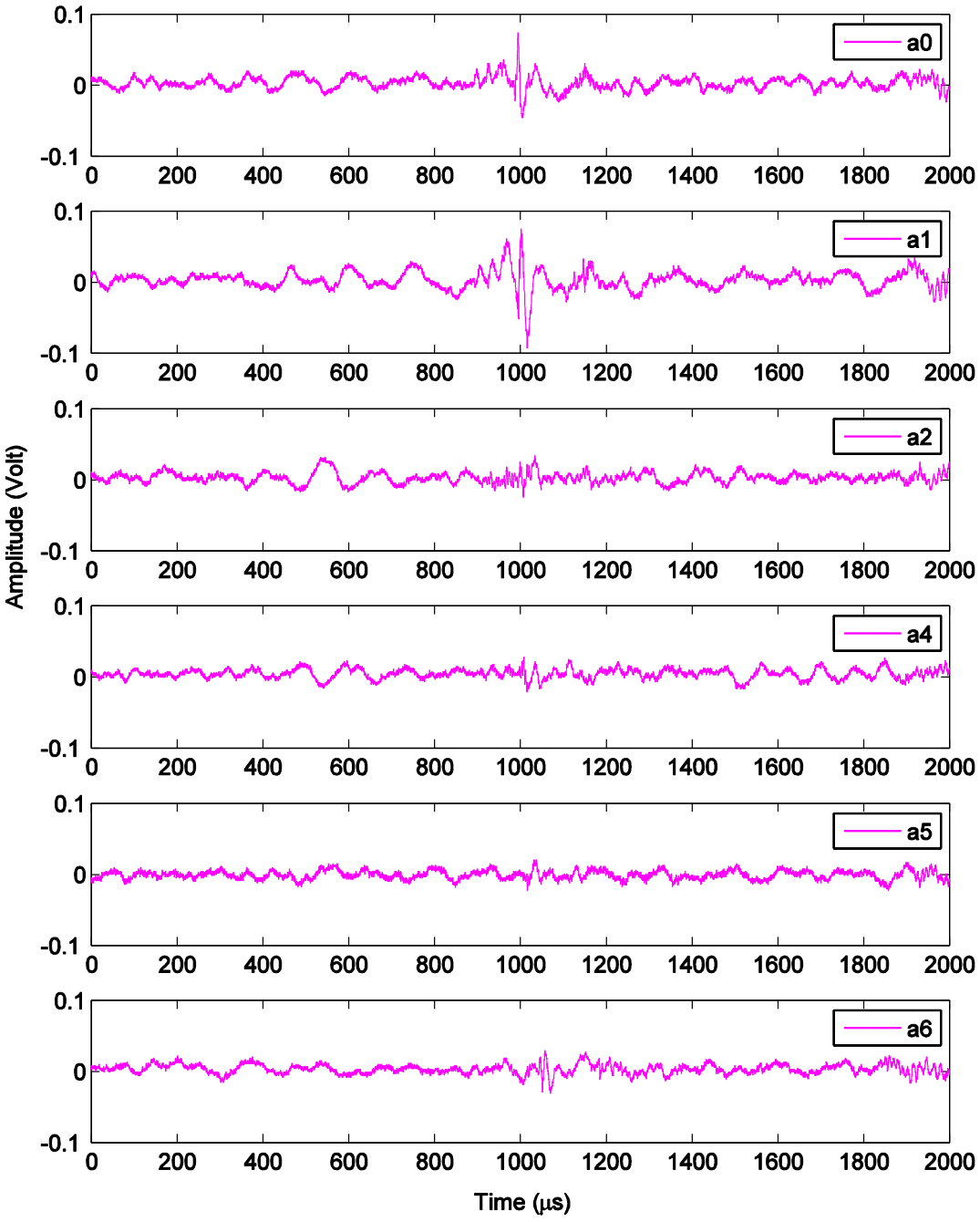

Figure 6.35: AE signals acquired by piezoelectric paint AE sensors on specimen WTJ6 at load cycle number N =299,876 cycles

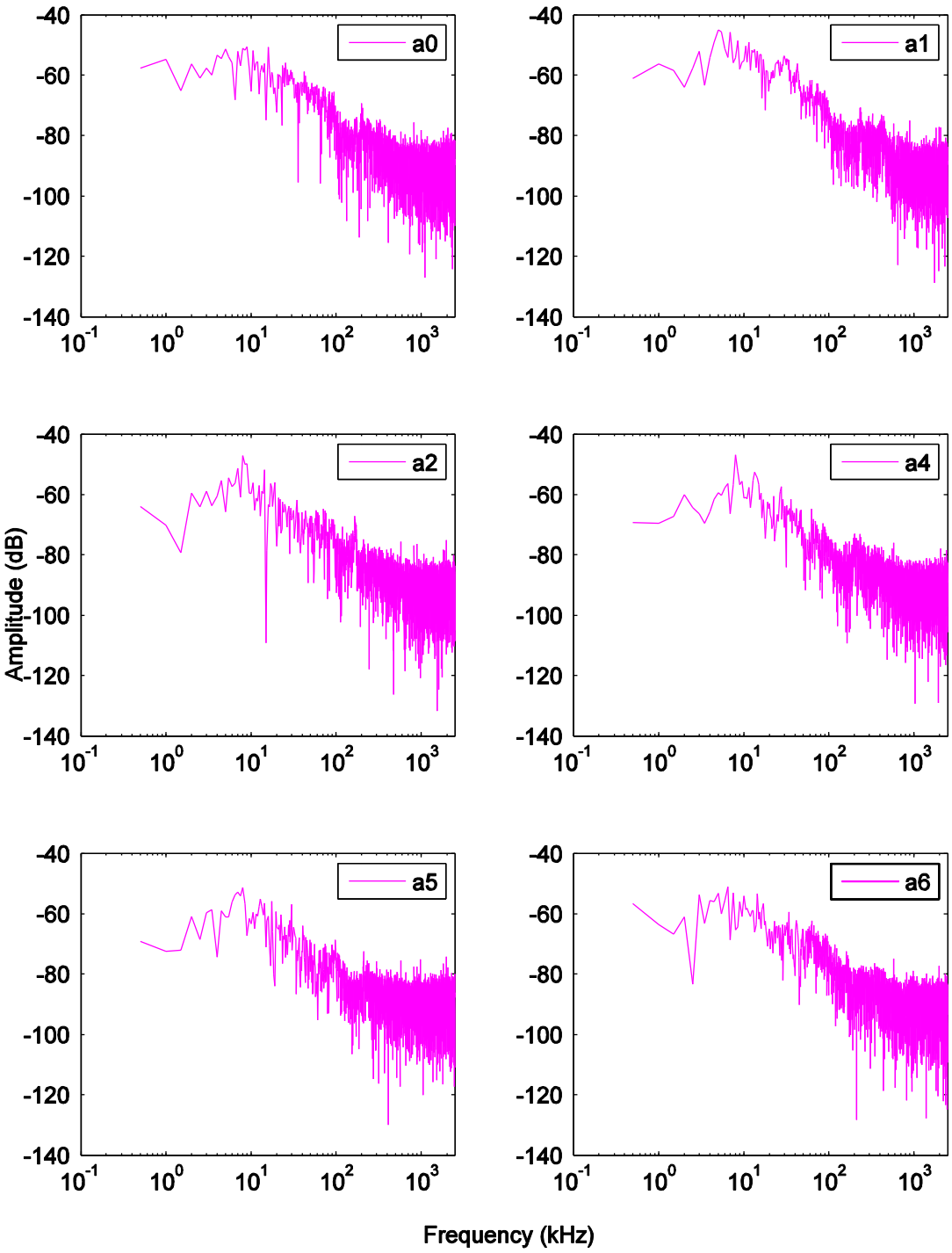

Figure 6.36: Frequency spectra of AE signals shown in Figure 6.35

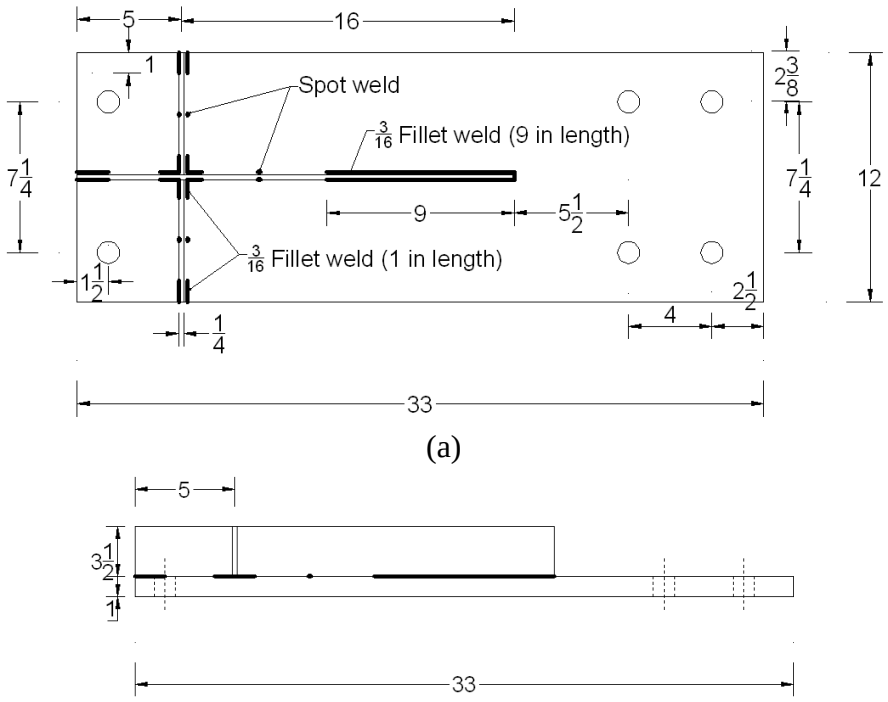

Figure 6.37: Dimensions of welded plate test specimen (unit: inch): (a) plan view; (b) side view

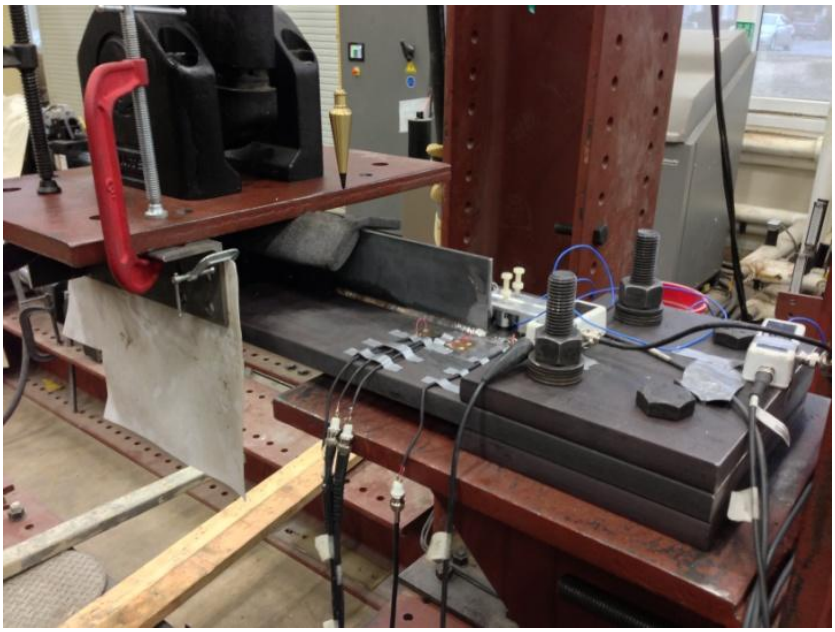

Figure 6.38: Picture of fatigue test setup for welded plate

(a)

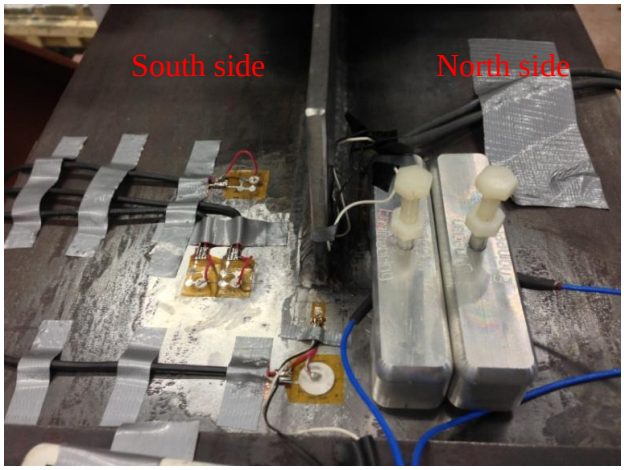

(b)

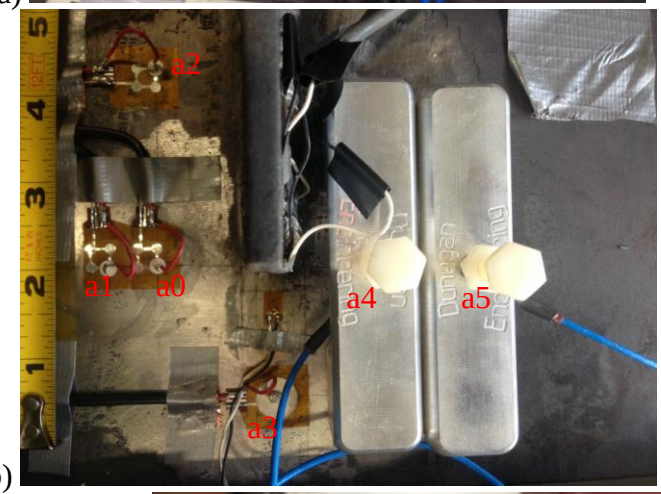

(c)

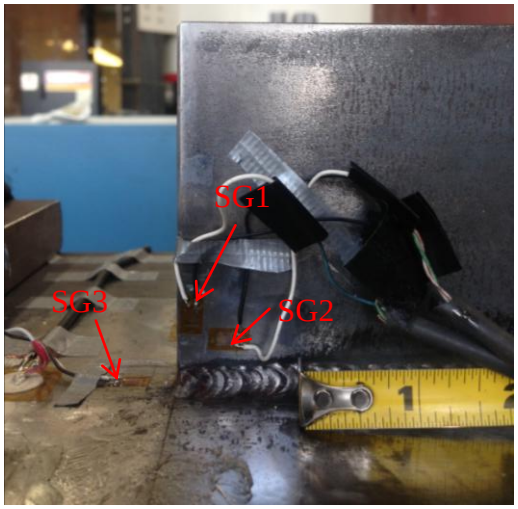

Figure 6.39: Configuration of piezoelectric film AE sensors and commercial AE sensors on the test specimen: (a) overall view; (b) top-down view; (c) strain gage location

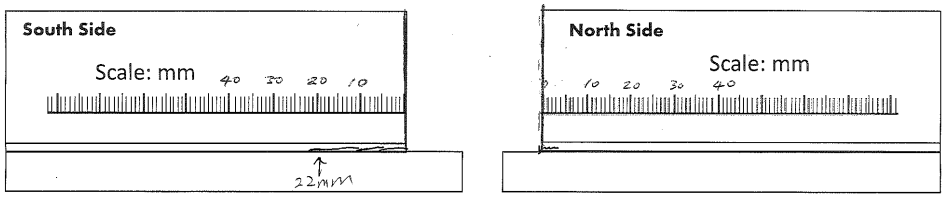

(a) Load cycle number = 100,000 cycles

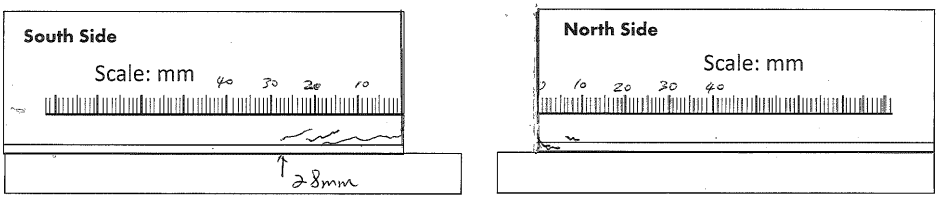

(b) Load cycle number = 126,000 cycles

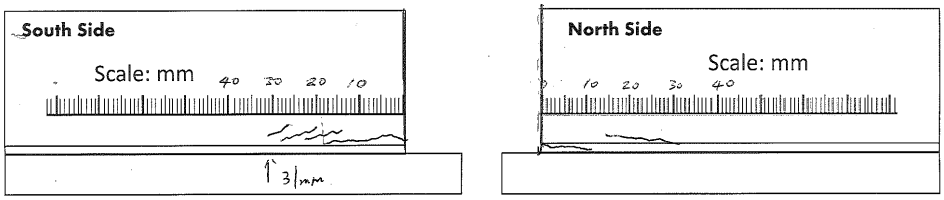

(c) Load cycle number = 165,000 cycles

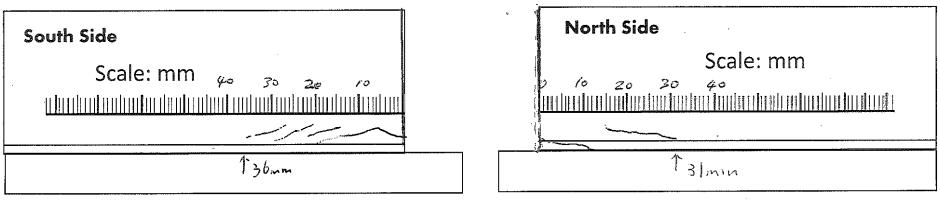

(d) Load cycle number = 185,000 cycles

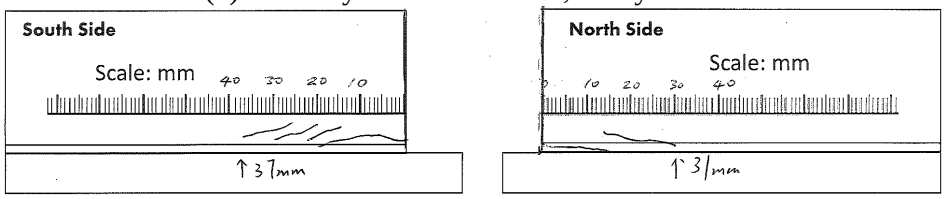

(e) Load cycle number = 205,000 cycles

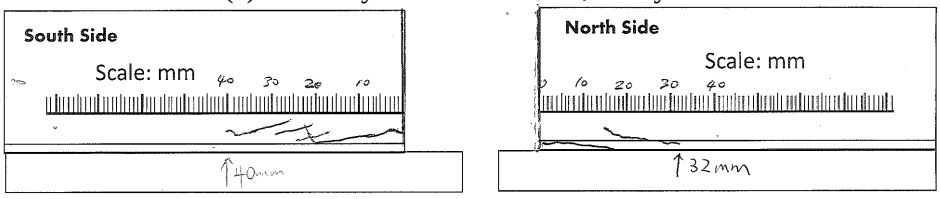

(f) Load cycle number = 237,000 cycles

Figure 6.40: Fatigue crack growth pattern in test specimen#1

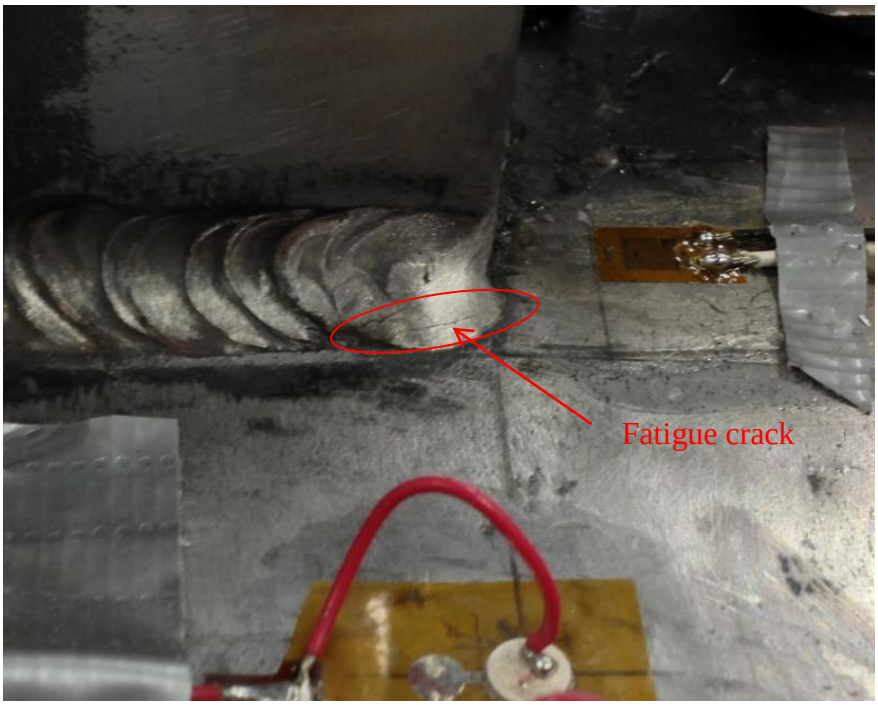

Figure 6.41: Close-up view of fatigue crack near longitudinal stiffener weld toe at load cycle number N =182,000 in specimen #2

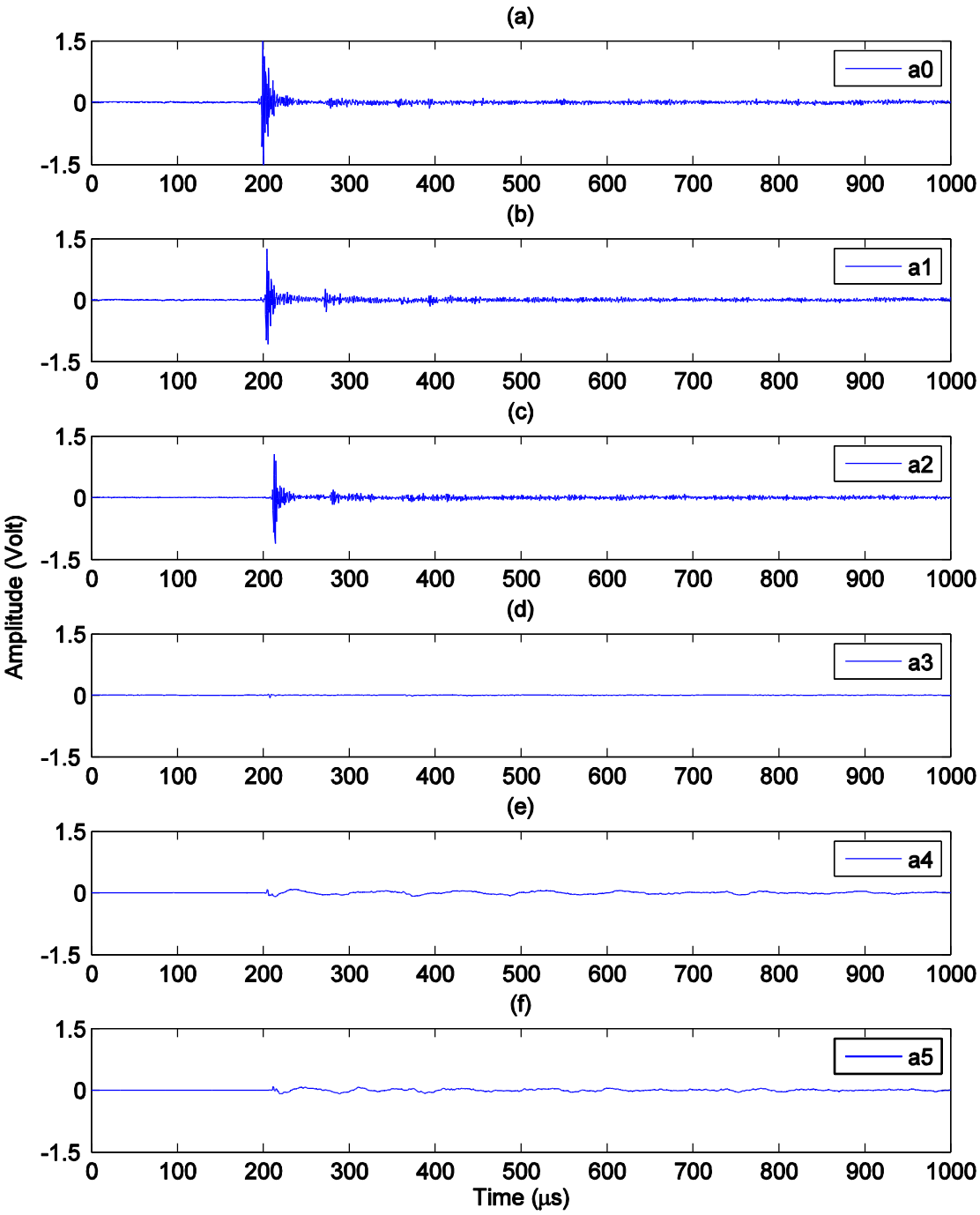

Figure 6.42: Pencil lead break induced signal measured by AE sensors on the test specimen #2 (pencil lead break at fatigue crack location shown in Figure 6.41): (a) piezoelectric film AE sensor closest to crack (5-mm diameter PZT-5A disc on backing film); (b) piezoelectric film AE sensor (5-mm diameter PZT-5A disc on backing film); (c) piezoelectric film AE sensor (12.27-mm diameter piezo paint disc on backing film); (d) commercial AE sensor (SE1000-HI) closer to the crack; (e) commercial AE sensor (SE1000-HI). (for detailed locations of these sensors, see Figure 6.39(b))

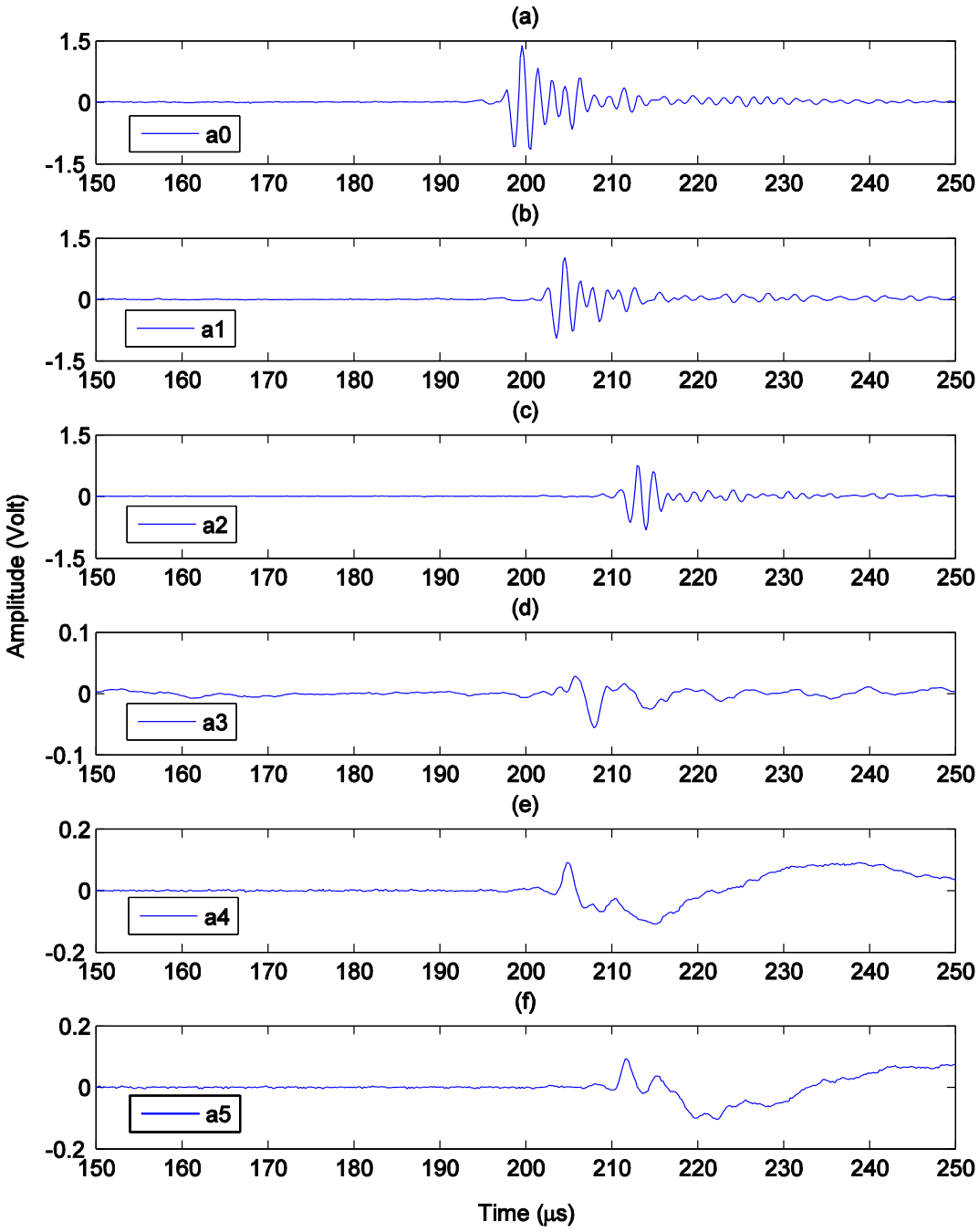

Figure 6.43: Zoomed-in view of the AE signals shown in Figure 6.30 (sensor labels shown in Figure 6.39(b))

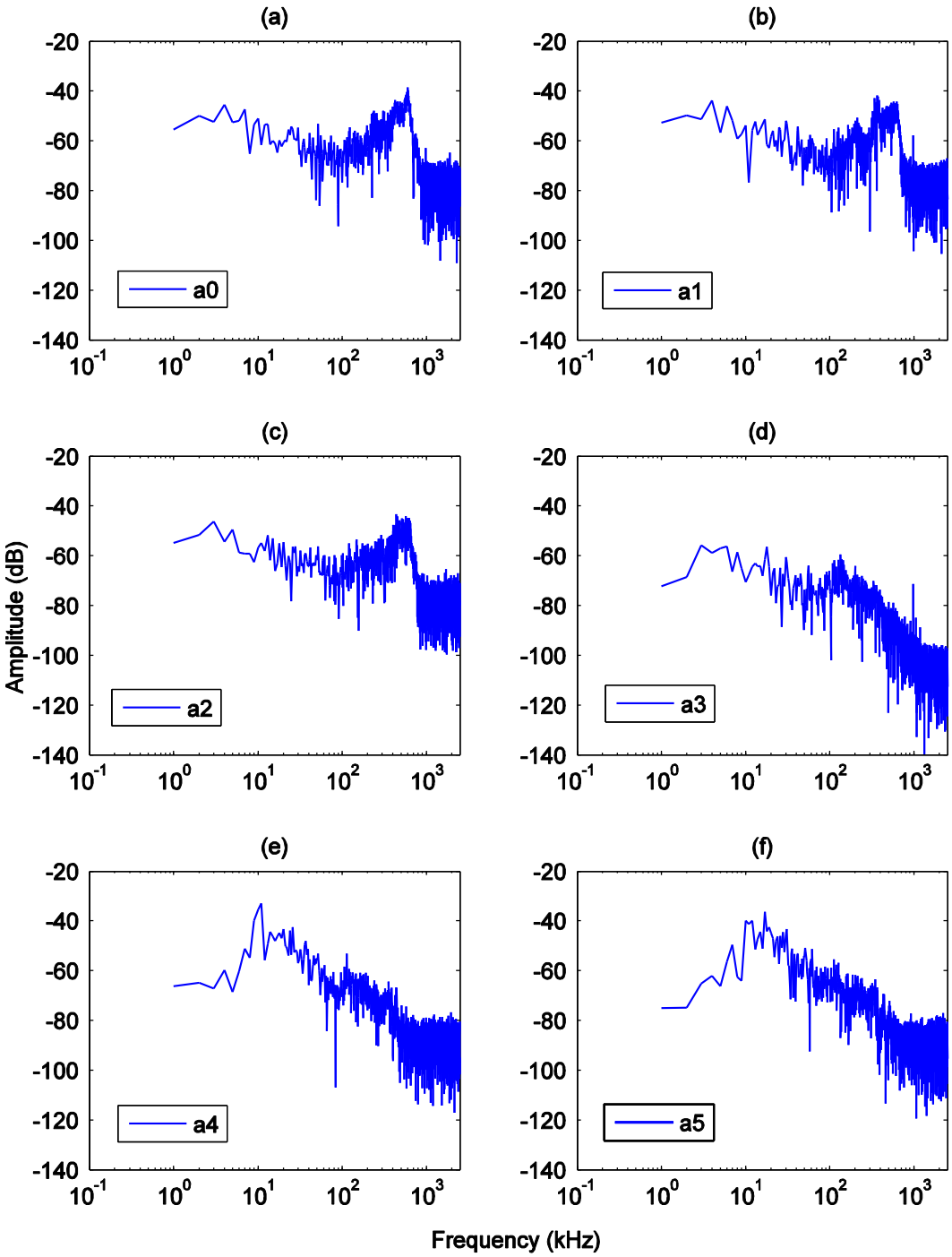

Figure 6.44: Frequency spectra of AE sensor signals in Figure 6.42 (sensor labels shown in Figure 6.39(b))

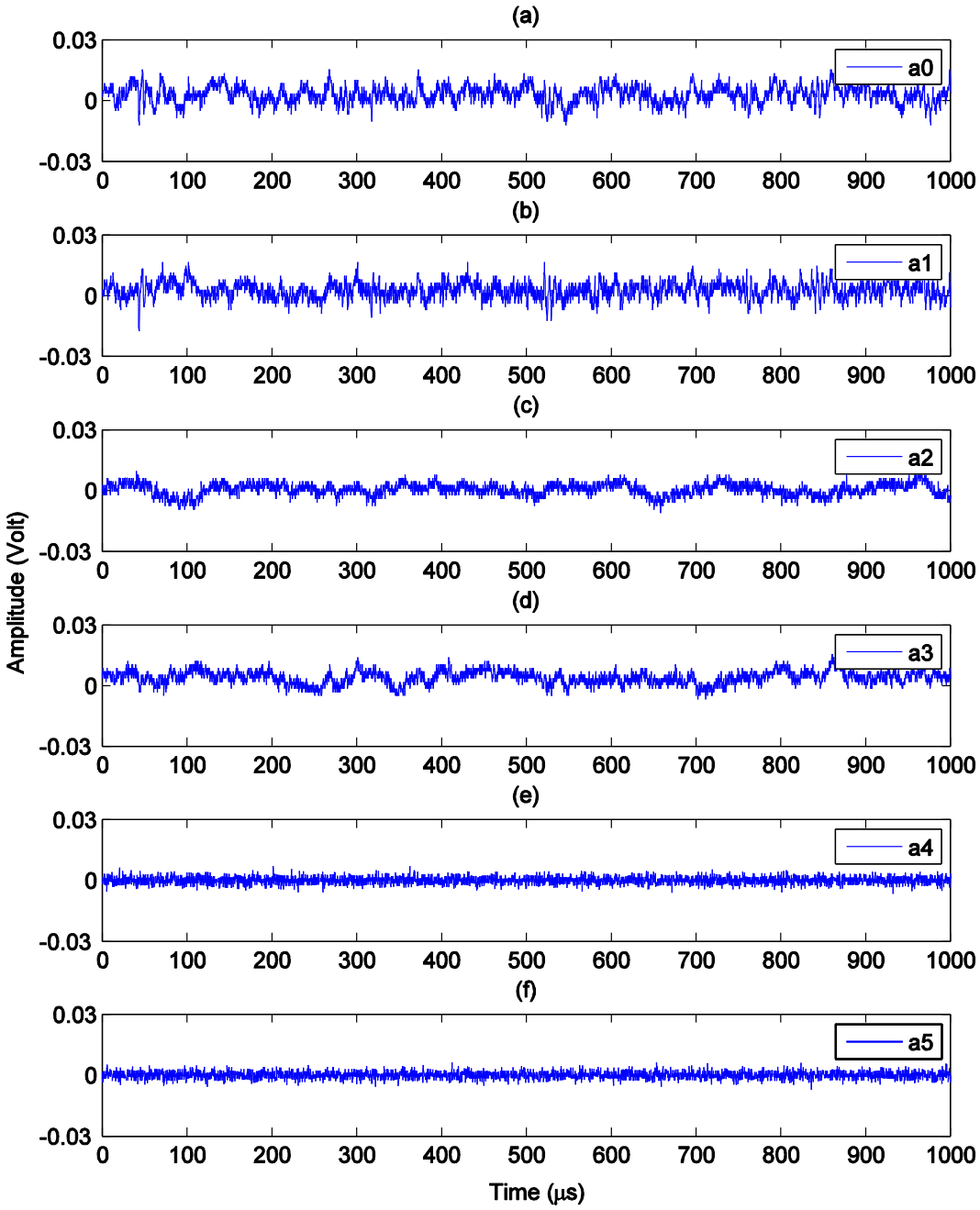

Figure 6.45: Ambient background noise signal measured by AE sensors (sensor labels shown in Figure 6.39(b))

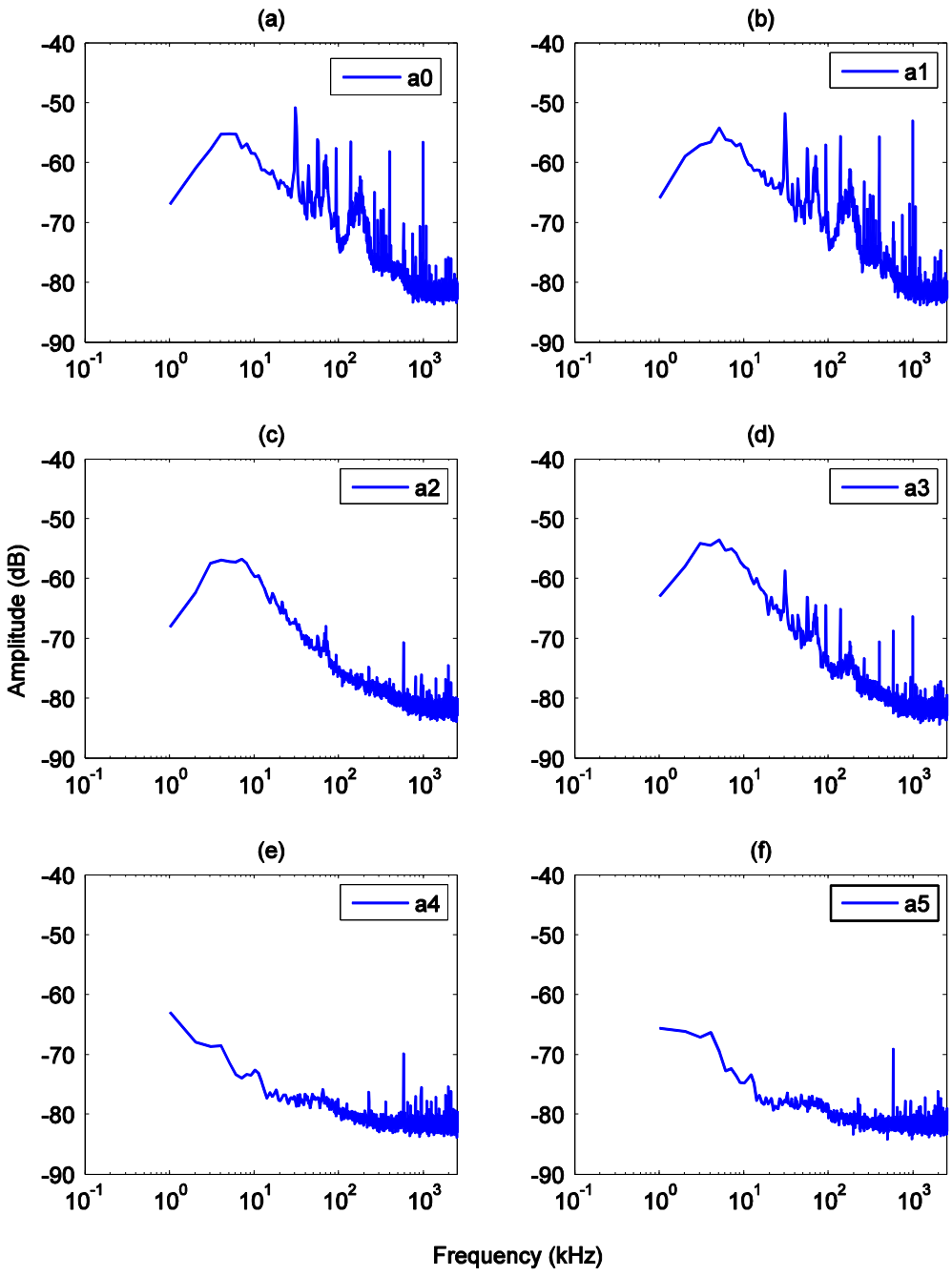

Figure 6.46: Frequency spectra of averaged ambient background noise signal measured by AE sensors (average of 50 records, sensor labels shown in Figure 6.39(b))

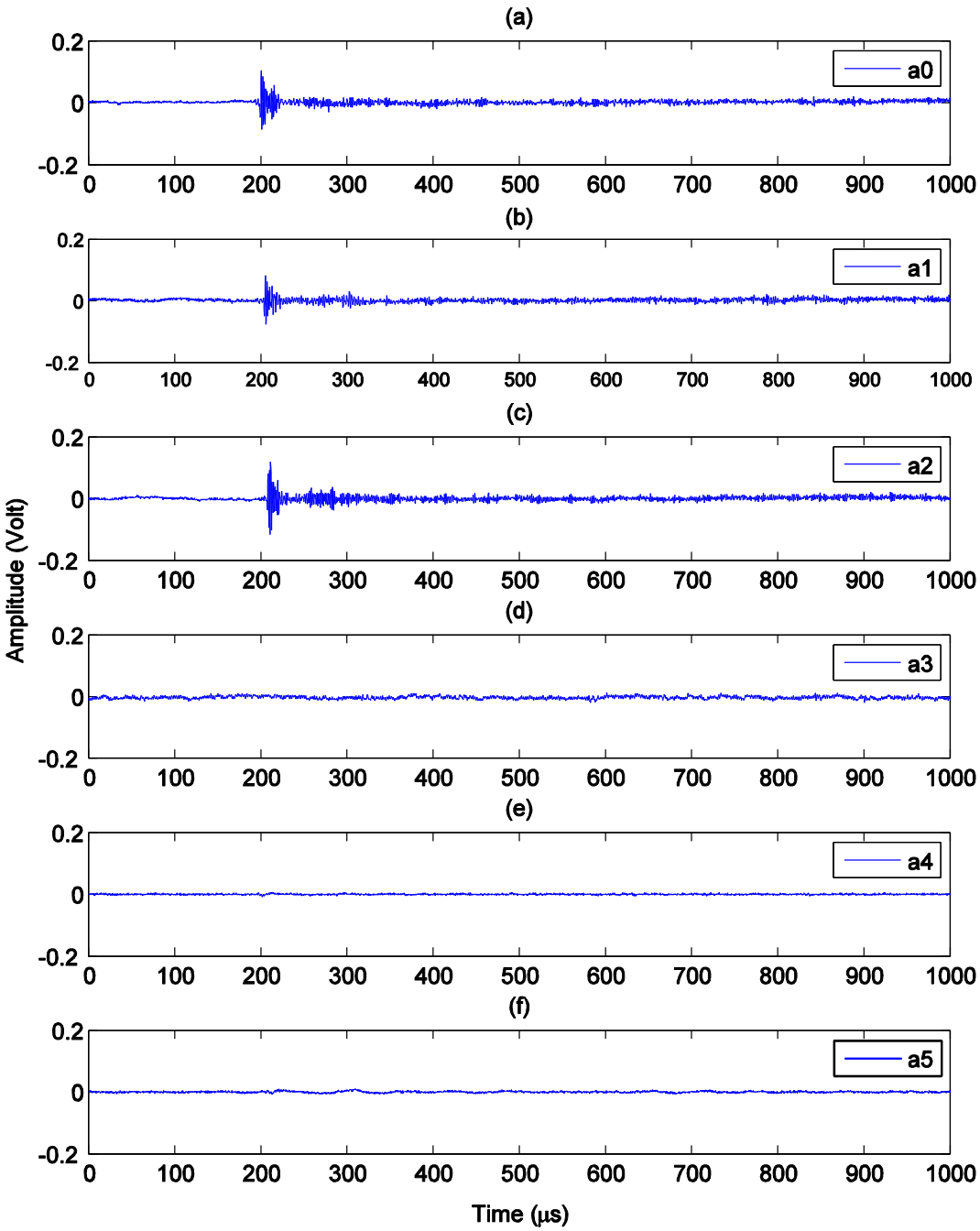

Figure 6.47: Fatigue crack induced AE signal measured by AE sensors at load cycle number N =185,300 cycles (sensor labels shown in Figure 6.39(b))

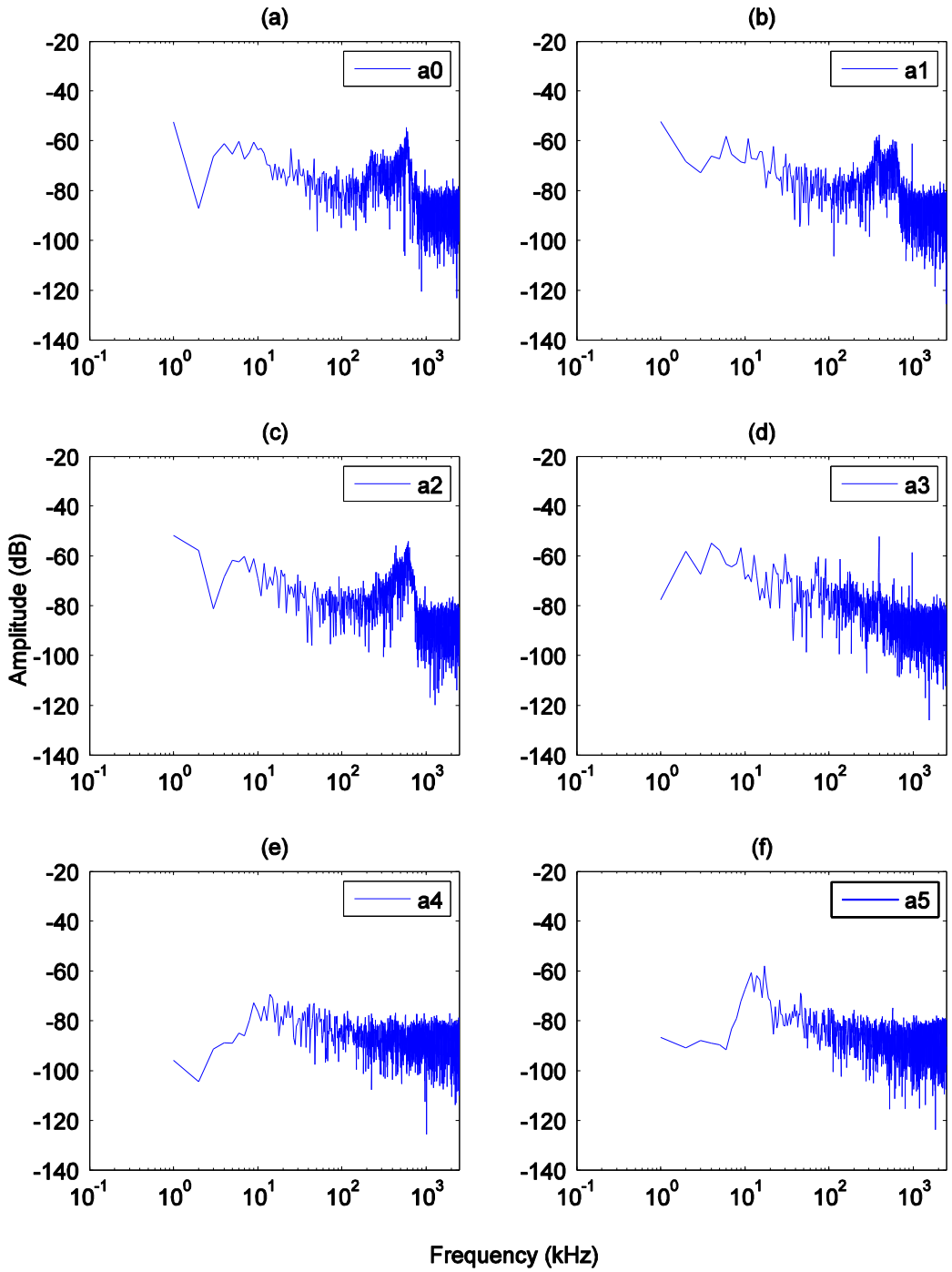

Figure 6.48: Frequency spectra of fatigue crack induced AE signal measured by AE sensors shown in Figure 6.47(sensor labels shown in Figure 6.39(b))

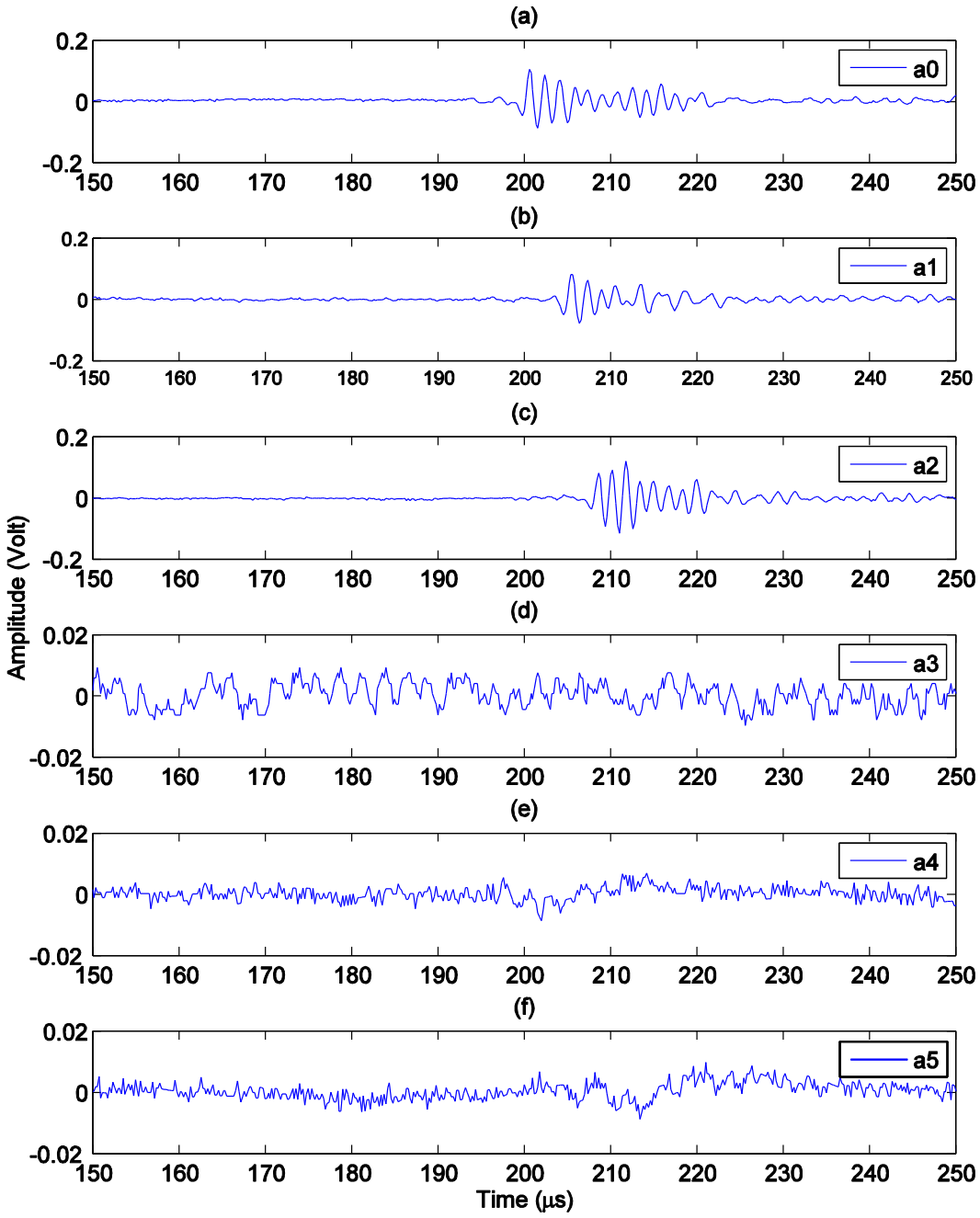

Figure 6.49: Zoomed-in view of the AE signals shown in Figure 6.47 (sensor labels shown in Figure 6.39(b))

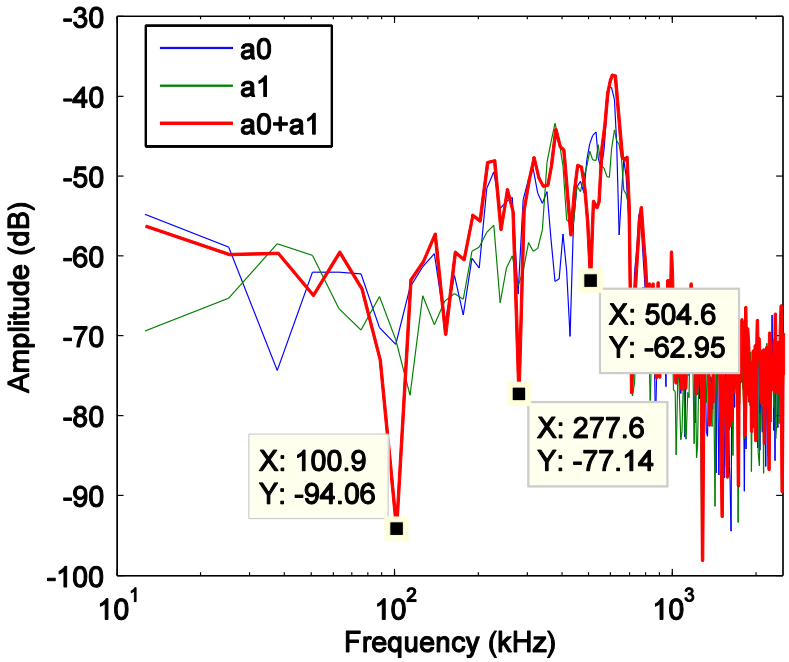

Figure 6.50: Frequency spectra of AE signals in sensor couple (a0+a1) comprised of two piezoelectric film AE sensors

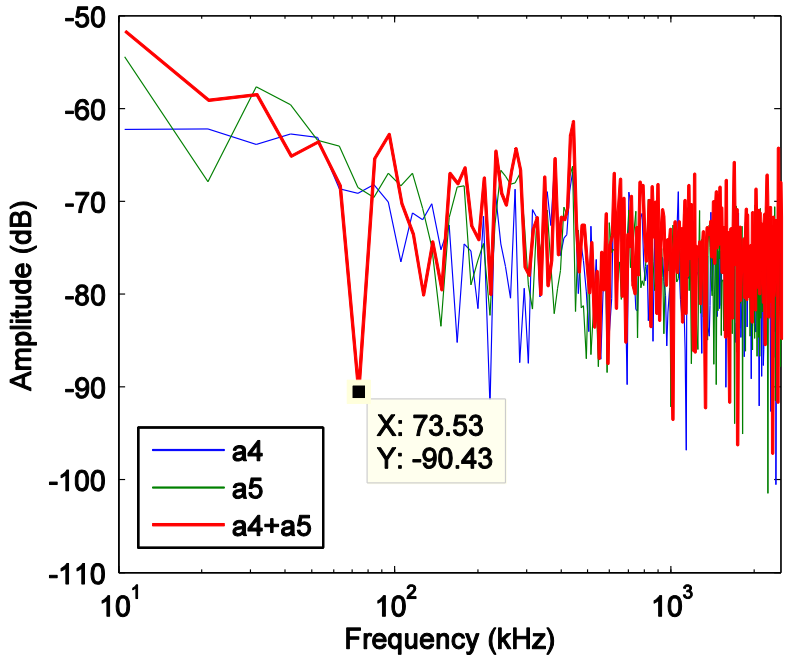

Figure 6.51: Frequency spectra of AE signals in sensor couple (a4+a5) comprised of two SE1000-HI AE sensors

Chapter 7: Field Test

7.1 Introduction

Fatigue-induced cracking may occur in steel bridges reaching their original design life. These aged structures have experienced increasing traffic volume and weight, deteriorating components, as well as a large number of stress cycles. A number of cases have been reported recently that involve fatigue damages in highway steel bridges. For example, fatigue cracks resulting from the typical web gap distortion near the bottom flange of welded plate girders were reported in a multi-girder steel bridge (Zhou, 2006). The distortion induced stresses initiated horizontal cracks in the web-to-flange welds and some propagated into vertical cracks at the end of the web-to-connection plate welds. On March 14, 2003, two large cracks were discovered in the webs of two welded plate girders on a multi-girder steel bridge (Zhou and Biegalski, 2010). The fracture was believed to have originated at the top of the web-to-stiffener weld. One crack propagated downward and diagonally fractured the full height of the 90-inch web plate.

Many nondestructive evaluation (NDE) techniques have been used for fatigue crack detection, including eddy current, magnetic particle inspection, radiography, thermography, acoustic emission (AE) and ultrasonic testing. In particular, AE technique has been receiving growing popularity in use for fatigue crack monitoring on bridges (e.g., Holford *et al*., 2001; Kosnik, 2009; McKeefry and Shield, 1999). AE is the elastic wave generated by sudden energy releases within a material and provides real-time information on damage progression in a structure. Since many AE

sources are damage-related, AE monitoring can be effectively used to diagnose impending structural material failure. Different from ultrasonic test, which excites elastic waves into a solid, AE sensor passively listens to the signals generated by crack initiation and progression within the monitored structure. In this chapter, field test results of the piezoelectric film AE sensor for fatigue crack monitoring on a steel I-girder bridge located at intersection of I-270 and Middlebrook Road are discussed.

7.2 AE Monitoring on I-270 Highway Steel Bridge

7.2.1 Bridge Description and Instrumentation

Field test was conducted on a multiple steel I-girders bridge (Bridge location, latitude=39.175296, longitude= -77.247046) located at I-270/Middlebrook Road intersection near Germantown in Maryland. The bridge is a single-span structure of a span length of 46.76 m (140 ft.), as shown in Figure 7.1. The bridge was built in 1980's and fatigue cracks were identified in some of the cross frame connection welds, as shown in Figure 7.2.

A total of five piezoelectric film AE sensors including three piezoelectric paint AE sensors were installed to monitor the growth of existing fatigue cracks in the weld connecting the lower flange plate and the connection plate. The sensor location is on the connection plate of the middle-span cross frame (70 ft. away from the bridge abutment) connecting Girder#2 and Girder#3 in the southbound part of the bridge. In this field monitoring, two types of piezoelectric film AE sensors are installed: PZT disc (7 mm diameter and 0.2 mm thickness, PZT-5A) and ½"-diameter piezoelectric paint AE sensor with a thickness of 0.5 mm (for details, see the reference by Zhang and Li, 2006).The sensors are connected to 40-dB preamplifiers and a PXI high-

speed data acquisition (DAQ) system (National Instruments model number: NI PXI-5105, 8-ch, 60 MS/s Digitizer w/512 MB Onboard Memory) for long-term AE signal collection and fatigue crack growth monitoring. 100-feet long shielded multi-conductor cable (Belden, Manufacturer #: 9535 0601000, Conductor size = 24 AWG, 5 conductors) were used to connect the preamplifier and PXI DAQ system. Figure 7.3 shows the installation of piezoelectric film AE sensors and NI monitoring system using a bucket truck.

7.2.2 Acoustic Emission Monitoring of Fatigue Crack

A remote acoustic emission monitoring system was installed on the steel I-girder bridge on June 28 2012 and its long-term performance in the field was studied in the context of fatigue crack monitoring. This remote monitoring system is comprised of three major components: sensors with signal conditioning circuits, data acquisition system and remote access. The AE events due to fatigue crack growth are monitored with piezoelectric film AE sensors with a 40-dB pre-amplifier and a band-pass filter which filters low frequency noises (< 5 kHz) induced by bridge vibration. The 5 kHz lower cutoff frequency was assigned since fatigue crack induced AE signals are usually on the order of 100 kHz. The output from the signal conditioning unit is passed to a PXI-based data acquisition system made by National Instruments. A Labview-based software program was developed and installed on the PXI system for data logging and processing. For this test, the sampling frequency was set at 2 MHz for all the channels and each triggered record has a total of 10,000 data points.

In this field test, five piezoelectric film AE sensors were used. Three were placed near the fatigue crack tip. Figure 7.4 shows the sensor configuration and a

view of the rusted area near existing fatigue crack. Two of these three piezoelectric film AE sensors (Channel 0 and 1) are made using PZT-5A discs and thus have a higher sensitivity (about 30 times higher) than the other sensor (Channel 2, made of piezoelectric paint). All triggers were made by Channel 2 at a trigger threshold level of 40 mV. Typical triggered AE signals measured by the three piezoelectric film AE sensors are shown in Figure 7.5. Note that in order to make visual inspection of the waveform easy, the signal from Channel 2 is scaled up ten times since piezoelectric paint AE sensors have a lower sensitivity than that of the PZT piezoelectric film AE sensors.

Figure 7.6 shows the average frequency spectra of all triggered AE signals from these three piezoelectric film AE sensors. A total of ninety-two AE events were triggered in the week of July 11, 2012. Averaging is done so that ambient noise could be canceled out in the frequency domain. It is seen that there is an attenuation of 7 dB from the Channel 0 signal to the Channel 1 signal. This is consistent with the $r^{-1/2}$ Rayleigh wave attenuation relationship reported by Mooney (Mooney, 1974), where r is the distance from the AE source to the sensor. It is calculated that from $r_1 = 0.98$ inches to $r_2 = 1.67$ inches, the attenuation is about -5.4 dB. The actual attenuation of -7 dB from field test data is close to this $r^{-1/2}$ Rayleigh wave attenuation relationship, especially considering the fact that additional attenuation might be caused by inherent material damping (which is not accounted for by the $r^{-1/2}$ Rayleigh wave attenuation). This attenuation relationship verifies that the triggered signal is not due to far field traffic induced noise (e.g., friction between tire and bridge deck) since for far field signal the attenuation between these two signals (Channel 0 and 1) would be much

smaller. Based on the dimensions of this bridge and sensor location, the attenuation for far field signals would be around -0.47 dB. Additionally, since Channel 1 and Channel 2 are at similar distance to the crack tip, the attenuation (-27 dB in Figure 7.6) is close to the value (-30 dB) due to sensor sensitivity difference (note that this calculation is based on original data, not the one presented in Figure 7.5 which has been scaled up ten times for ease of waveform identification in the figure). Considering this attenuation relationship reflected in the measured AE signals, it is very likely that the AE event in Figure 7.5 was triggered by AE activities associated with fatigue crack growth. Figure 7.7 shows the median frequency spectra of triggered AE signals by three piezoelectric film AE sensors. It delivers similar results to that of the average frequency spectra shown in Figure 7.6.

In order to eliminate possibilities of signals due to friction or impact of the cracked surface, a laboratory simulation was carried out with similar configurations on a 7/16″-thick steel plate. The test setup is shown in Figure 7.8. It can be seen that the test results presented in Figure 7.9 are considerably different from the AE signals obtained from the field test on the field test bridge, in both waveform characteristics and frequency contents. Therefore the AE signals collected in the field are unlikely to be caused by rubbing or fretting of the crack surfaces. This further verifies the judgment that those AE events were very likely to be associated with fatigue crack growth.

7.2.3 AE Feature Analysis

AE feature analysis of the triggered AE data acquired during the week of July 11, 2012 (with a total of 92 events for each sensor, as stated above) is presented in this

section. The AE features considered for this study include: time interval between triggered AE events, occurrence pattern of the triggered AE signals (AE hits rate in terms of hours of the day, days of the week and date in July 2012), AE energy and a variety of adjusted AE signal peak amplitude and AE energy.

7.2.3.1 Time Interval of AE events

Time interval has been used to deduce the independence of the recorded AE events (Mogi, 1962). If the AE events are completely independent, the distribution should be random. Figure 7.10 shows the distribution of time intervals between two successively triggered AE events. It can be seen that a significant number of the AE signals fall within the first bin, which represents signals with interval time less than one minute. This indicates that a lot of the AE events were related to each other and were acquired at some time instant of intensive AE activities. There are also some larger time intervals, which implied long calm period between two time instants of intensive AE activities. That's to say, after the boosting, AE activity at the source would became relatively calm for a long period. This phenomenon was also observed in the lab fatigue test of the welded tubular joint specimens discussed in the previous chapter.

7.2.3.2 Occurrence of AE events

As discussed in Chapter 2, AE hits rate is a very useful AE feature for structural health monitoring. For the field monitoring of active fatigue crack, it's natural to calculate the hits rate as the number of triggered AE signals per day. Figure 7.11(a) shows the hits rate within the one-week monitoring period in July 2012. More than half of the AE signals were recorded on July 15th, 2012. The rest of the signals were randomly distributed over the one-week monitoring period. This also suggests a time

instant of intensive AE activities in July 15th 2012 and explains why a lot of signals were related to each other.

As the host structure is a highway bridge, it's necessary to investigate the effect of traffic on AE activities. Figure 7.11(b) plots the distribution of AE events occurrence time in a day. It can be seen that most of the signals were obtained around 4 and 5pm. Since the time window (4PM to 5PM) falls within the traffic rush hours, the intensity of AE events might be related to traffic load on the bridge. However, looking at the occurrence date in the week in Figure 7.11(c), the weekend had the most AE activities. It is unclear that intensive AE activity at the weekend is accidental or due to other things such as traffic load.

7.2.3.3 Energy

Compared with the peak amplitude of the AE signal, AE energy could be more reflective of the intensity of AE source since it includes additional time information instead of just the peak amplitude of the AE signal. Figure 7.12 shows the distribution of AE energy of the 92 AE events triggered in the week of July 11, 2012. In general, the energy level in Channel 0 (i.e., Sensor 0) is larger than that of Channel 1 (i.e., Sensor 1). This is reasonable since Sensor 0 is closer to the fatigue crack than Sensor 1, as shown in Figure 7.4. In addition to this, the general trends in both sensors agree with each other. Also from Figure 7.12, it can be seen that the energy level of the AE events are concentrated in the lower range. Only several AE events have larger energy. This is analogous to earthquake, which has more low-magnitude activities and fewer large-magnitude events.

7.2.3.2 Source Intensity and Adjustment

Another way to assess AE source intensity is to use signal amplitude V_R, which is supposedly related to the source intensity if the distance between the source and sensor is fixed. Figure 7.13(a) shows the distribution of the peak amplitude of all 92 AE events triggered in the week of July 11, 2012. In general, it can be seen that the signals in Channel 0 have larger amplitude than that of Channel 1. This can be explained by the fact that Channel 0 is closer to the fatigue crack than Channel 1.

As the peak amplitude is also dependent on the surface stress wave propagation path which should be affected by the propagation distance, a study on correcting the wave travel distance effect is being carried out here. Since the Rayleigh arrival usually has the largest amplitude and it decays in amplitude according to the attenuation relation of $r^{-1/2}$, a source distance (r) adjustment is first carried out with a factor of $r^{1/2}$. The distance-adjusted result is shown in Figure 7.13(b). It can be seen that the result does not provide any additional information compared with Figure 7.13(a). A possible reason for this phenomenon could be the underlying assumption that all AE sources are located at the fatigue crack tip and accordingly a single value of the travel distance was used for this adjustment.

In practical application, estimation of the AE source location is usually difficult to do ahead of AE data analysis and thus will create a problem in determining the correction factor for the travel distance adjustment. If any parameter from the waveform can be related to source distance, it might be a good candidate for travel distance adjustment. It is known that rise time (τ) is an index measuring the time delay between the wave arrival (usually P arrival) and its peak amplitude (usually Rayleigh arrival). Since P wave and Rayleigh wave travel at different wave

speed, it is related to the travel distance between the AE source and sensor to some extent. Additionally, rise time can be determined from the signal waveform and thus a priori information on source location is not required. Figure 7.13(c) shows the distribution of the adjusted peak amplitude corrected with the rise time ($V_R\tau$ as shown in Figure 7.14). It can be seen this adjustment makes the two sensor data more uniform. It is also seen that the trend line follows an approximately exponential decay pattern which is commonly seen in seismology pattern of earthquakes.

As the Rayleigh wave attenuates along propagation path according to a relation of $r^{-1/2}$, using the square root of the rise time might be more accurate for the peak amplitude adjustment. Figure 7.13(d) shows the distribution of the AE signal peak amplitude adjusted with $\sqrt{\tau}$. The result is similar to that of the adjusted peak amplitude using the rise time τ and the exponential trend gets even clear. It's interesting to note that the $\sqrt{\tau}$ adjusted peak amplitude distribution $V_R\sqrt{\tau}$ is closely related to that of the energy.

At this point, it is interesting to explore another travel distance adjustment factor, $r^{1/2}$. The adjusted distribution of AE signal peak amplitude is shown in Figure 7.13(e). However, not too much difference can be seen between this feature distribution and that adjusted with only $\sqrt{\tau}$. Therefore, it is concluded that since in general AE source is unknown ahead of monitoring, $\sqrt{\tau}$ might be a good factor for peak amplitude adjustment to correct the travel distance effect in the AE sensors located at different distances from the AE sensors. The $\sqrt{\tau}$ is also applied for energy adjustment and the result is shown in Figure 7.13 (f). Not too much improvement is

observed in this case. Thus $\sqrt{\tau}$ might be more suitable for peak amplitude adjustment.

7.2.4 AE Source Localization

Figure 7.15(a) shows sample AE signals measured by the piezoelectric film AE sensors (Channel 0 and 1 used PZT-5A discs on backing plastic film). The corresponding frequency spectra are shown in Figure 7.15(b). After adding up the signals in Channel 0 and 1 following the procedure described in Chapter 5, the troughs in the frequency spectrum of the added signal became conspicuous. Two troughs appeared at 296.9 kHz and 501.5 kHz respectively. In fact, they should be the second and third troughs with the first trough invisible. At 99 kHz where the first trough should be expected, Rayleigh wave at this frequency could not develop due to the small plate thickness (equal to ½ inches) since the Rayleigh wave length corresponding to this frequency is larger than the plate thickness. For 296.9 kHz and 501.5 kHz, the Rayleigh wave lengths are smaller than the half-inch plate thickness and thus Rayleigh wave could develop and the sensor couple theory for AE source localization could be applied. The ratio of the second to third trough frequencies observed in these figures is equal to 0.59, which is very close to the theoretical value 3/5. Considering that the first aperture effect caused trough frequency for a 7-mm diameter piezoelectric film AE sensor is 514 kHz according to Eq. (5.11), these two trough frequencies are very likely due to the phase shift between the signals, which suggests this AE signal was induced by near-field AE source.

According to Eqn. (5.9), the source direction angle could be calculated as

$$\cos\theta = \frac{(0.5+n)c}{2(0.5d+a)f_s} = \frac{(0.5+0)(2950)}{2(7/16\times 25.4\times 10^{-3})(99\times 10^{3})} = 0.67$$

Therefore $\theta = 47.9^{\circ}$.

After the source direction angle is determined, the AE source could be localized combined with the known fatigue crack location as shown in Figure 7.16.

Another approach to source location determination is based on time of arrival. For ease of comparison, the time arrival is usually carried out on single frequency content. Taking the signals shown in Figure 7.15(a) as an example, the frequency component at 120 kHz is used for determining the difference in the time of Rayleigh wave arrivals. Figure 7.17 shows the signals after using a band-pass filter (110 to 130 kHz pass band). The frequency components between 110 kHz and 130 kHz are kept and a fourth order Butterworth filter is applied to do the filtering. It can be seen that the time difference of the main waveforms is 0.5 μs. Compared with the theoretical value of 5 μs, which can be determined from geometry and Rayleigh wave speed 2950 m/s, the two time arrival difference values apparent do not match. It's unclear at this moment what caused this discrepancy.

Figures 7.18-7.26 show the other nine signals with trough frequencies in their frequency spectra. The trough frequencies of these signals can be clustered into two groups with the second trough frequencies around 290 kHz and 337 kHz respectively. The signal with trough frequency (e.g. Figure 7.22) around 290 kHz show consistent results of that shown in Figure 7.15 and thus confirm the acquired signals are most likely be due to real AE source related to the existing fatigue crack and not due to ambient noise. For the rest of signals except signals in Figure 7.26, they are consistent

with each other and having the second trough frequency around 337 kHz. For the signals in Figure 7.26, looking from the frequency domain, it is the combination of the two cases before. This might be due to multiple sources at the same time. As discussed before, averaging these signals in the frequency domain might yield more informative results. Averaged frequency spectra of the ten signals that have troughs frequencies are shown in Figure 7.27, which indicates the frequency troughs more clearly after adding up to reduce the white noise effect in signal. However many other acquired AE signals do not show the troughs in the frequency domain (the rest 82 signals). Figures 7.28 and 7.29 show two typical signals without space phase shift (no trough frequency is observed in the frequency domain). After adding up all the 82 signals, no trough frequencies are observed at those reported frequencies, as shown in Figure 7.30. This does not suggest that those signals are not related to the fatigue cracks since a lot of factors such as multiple AE sources and crack orientation could also play a role in eliminating the trough frequencies.

It's worth noting that the signal duration might be critical for localization using sensor couple theory. Longer duration would introduce more noise contents in the frequency domain and thus reduce the SNR ratio making the trough frequencies invisible. This is especially true for signals with lower SNR ratio and for the trough frequencies in higher range where signal energy is typically less. Figures 7.31-7.33 show the result of using longer duration for source localization. It can be seen that there are some fluctuations in the frequency domain, which create difficulty for accurate trough frequency identification. This is even severe for trough frequencies in higher frequency range. However, if shorter duration is selected, it will reduce the

resolution in frequency domain. There is a trade-off between the noise effect and the frequency resolution that the user should decide.

7.3 Noise Observed in Field Test

To some extent, noise is unavoidable in sensor electronics due to a variety of potential causes such as improper grounding, manufacturing defects, and electromagnetic interference (EMI). Figure 7.34 shows the averaged frequency spectra of 50 ambient noise signals from the field tests. This gives the averaged frequency spectra of the signals a reference to compare with. It's clear that the previously presented signal frequency contents are different from that of the ambient noise, which further confirms that those signals are likely due to AE source which is related to fatigue crack propagation.

Fairly large noises induced by improper grounding were observed on the signals of the piezoelectric film AE sensor starting in August 2012 and the problems were fixed after proper grounding of the sensor. Large noises significantly degrade the data quality of the piezoelectric film AE sensor because normal AE signal level usually ranges from tens of millivolts to several volts and noise level on the order of hundreds of millivolts thus could inundate the useful AE signal and make event triggering impossible without filtering.

A typical example of the noisy signal is shown in Figure 7.35. The noise periodically occurred on the signal and later it is found that the noise is due to the ground loop caused by different electrical potential levels in the painted steel bridge girder and the sensor's ground. Therefore, for piezoelectric film AE sensors, a capacitor forms in the glued polyimide backing film between its bottom electrode

(ground) and bridge girder coated surface. Ground loops occur when voltage difference is observed between two ground potentials. This “capacitor” caused ground loops and had introduced the large noise on the signal. After eliminating the grounding loops, the sensor signal is clean again without this noise.

7.4 Conclusion

Field test of piezoelectric film AE sensors on a steel I-girder bridge located in Maryland was carried out to achieve three goals: characterizing sensor performance in the field; acquiring AE signals related to fatigue cracking and analyzing the signal characteristics and AE features; and validating the proposed AE source localization method using real-world AE data. The feasibility of using piezoelectric film AE sensors for online fatigue crack monitoring is demonstrated based on findings in this field test. Problems such as large noise due to ground loops are debugged. Based on analysis results of the triggered AE signals collected by the piezoelectric film AE sensor signals and AE feature analysis, it is believed that the recorded AE signals are likely related to the AE activities associated with fatigue crack growth. The high stress level (peak value up to 17 ksi) in the BDI strain gage data (vertically oriented, see Figure 7.4(a) for location) also support this observation that the fatigue crack is growing. From fatigue tests reported by others (Han *et al*. 2011) as well as the writer’s own experience from lab fatigue testing, fatigue crack development should be in regime II (Paris law regime, or stable crack growth regime). The sensor couple theory for AE source localization was also verified with a limited number of piezoelectric film AE sensor data. However, many AE data do not show the space

phase shift induced trough frequencies although this does not suggest these AE data are not related to the active fatigue cracking. This deserves further study.

(a)

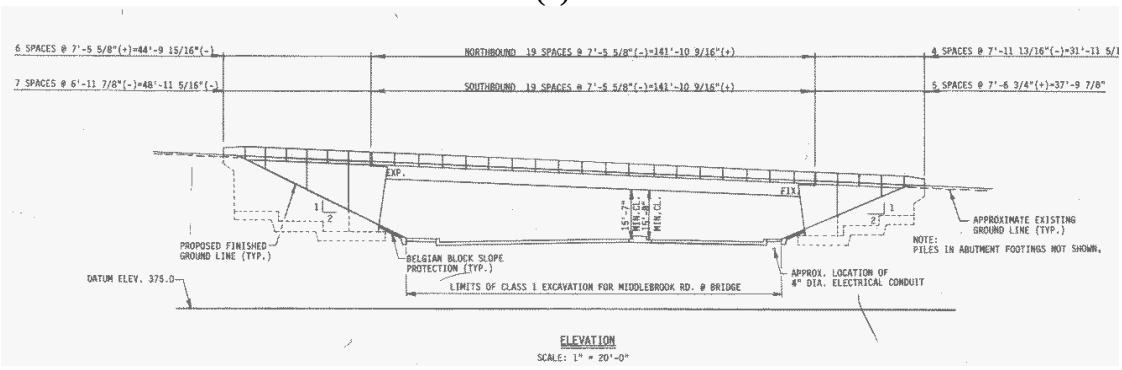

(b)

Figure 7.1: Field test bridge located at I-270/Middlebrook Road near Germantown, Maryland: (a) view of the southbound bridge from west; (b) dimensions of the bridge (courtesy of Maryland State Highway Administration)

(a)

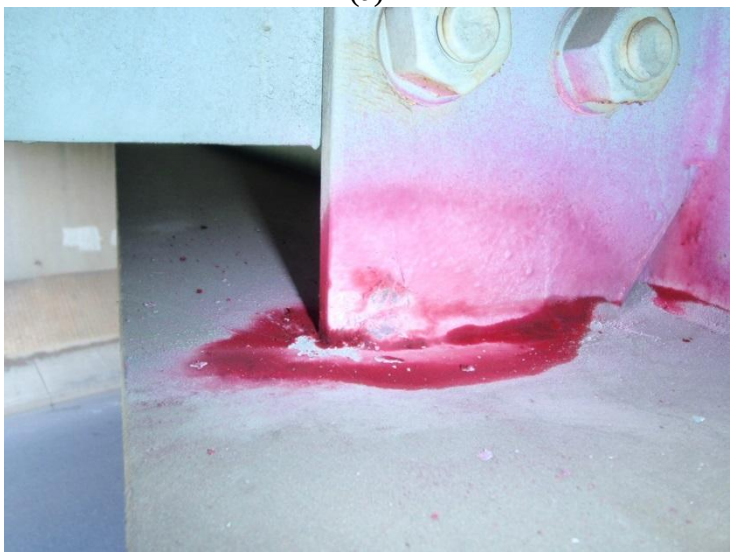

(b)

Figure 7.2: Fatigue cracks on the bridge diaphragm connection plate weld (courtesy of Dr. Y. Edward Zhou at URS Corporation)

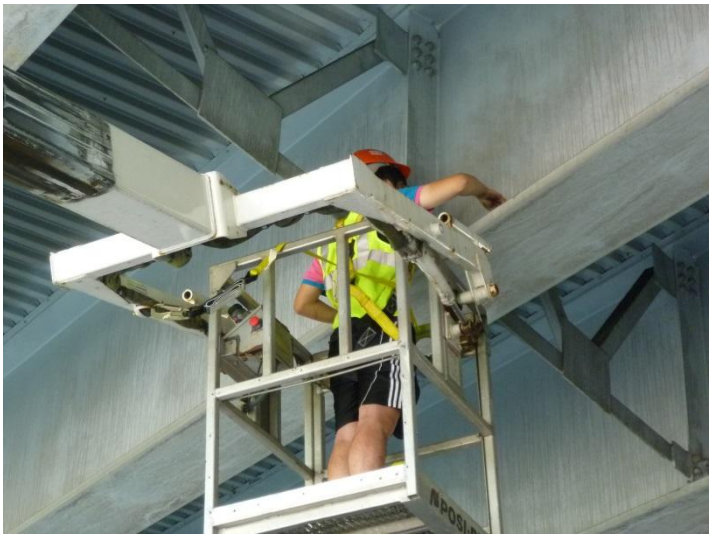

(a)

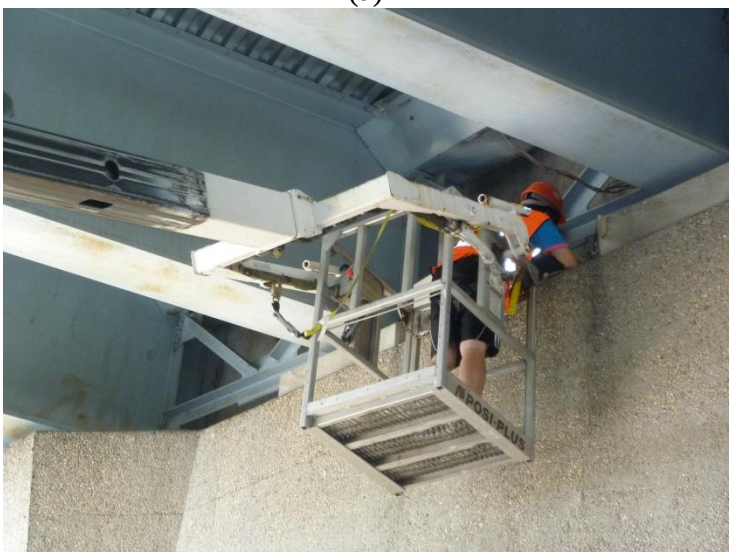

(b)

Figure 7.3: AE sensor and monitoring system installation on the field test bridge

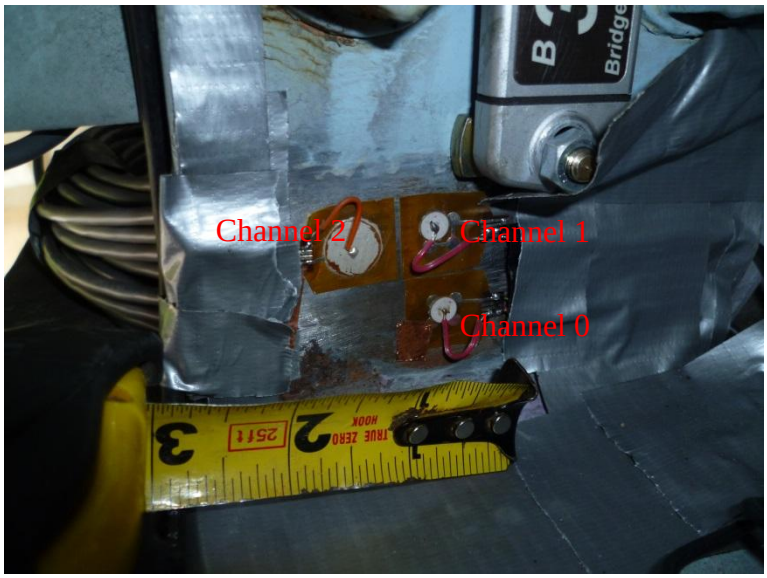

(a)

(b)

Figure 7.4: (a) Three piezoelectric film AE sensor near fatigue crack on the ½”-thick connection plate; (b) another view of the rusted area with existing fatigue crack

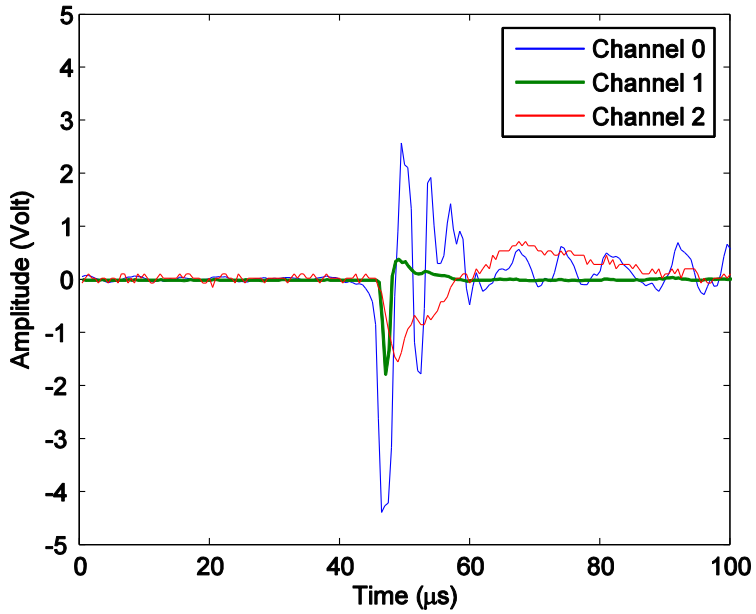

Figure 7.5: Typical AE signals measured by the three piezoelectric film AE sensors (Channel 2 signal scaled up ten times for ease in visual inspection of the waveform in this figure)

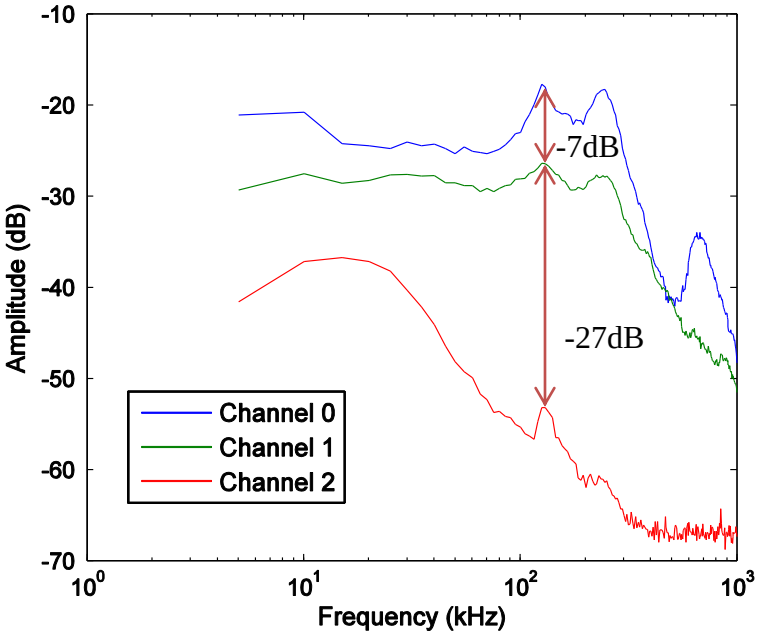

Figure 7.6: Averaged frequency spectra of triggered AE signals by three piezoelectric film AE sensors

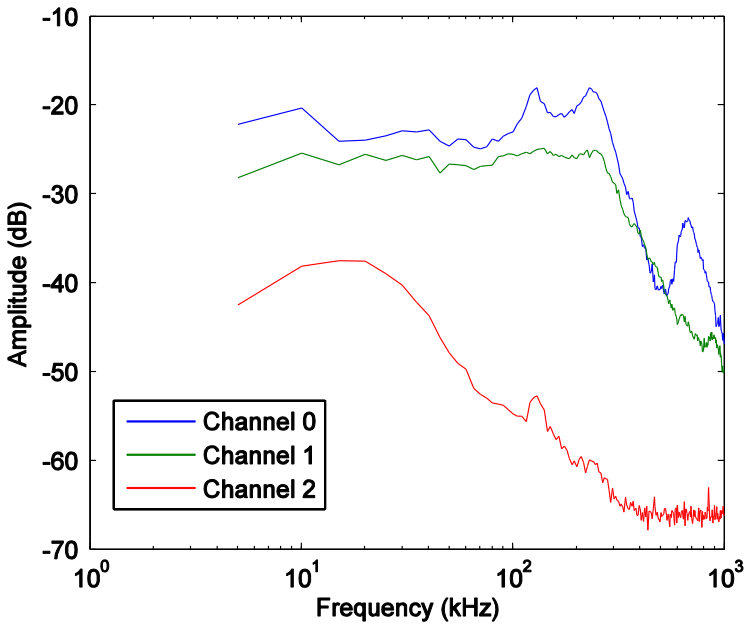

Figure 7.7: Median frequency spectra of triggered AE signals by three piezoelectric film AE sensors

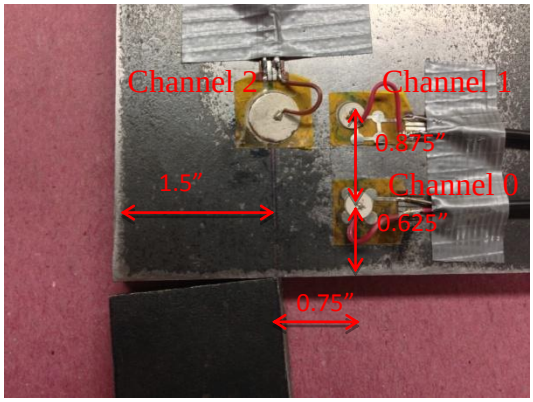

Figure 7.8: Experimental set up for lab test of impact effect on AE signal waveform

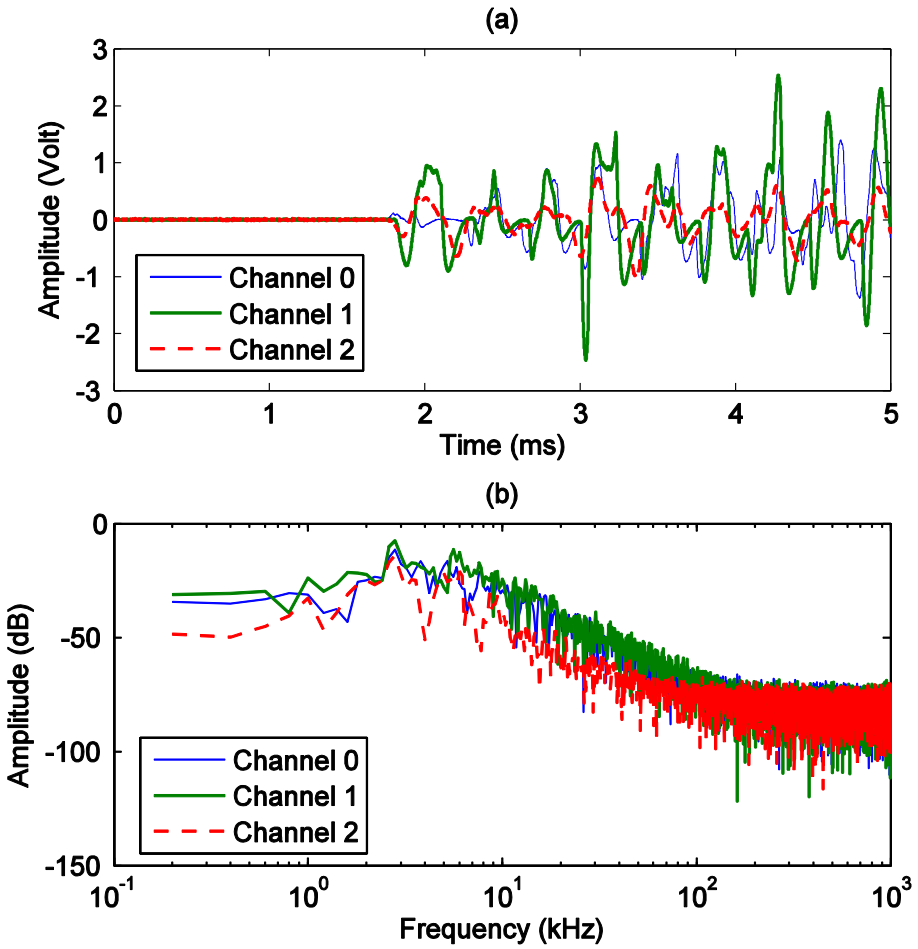

Figure 7.9: Typical AE event due to surface impact measured by the three piezoelectric AE sensors in the lab simulation: (a) time history of the signals; (b) frequency spectra

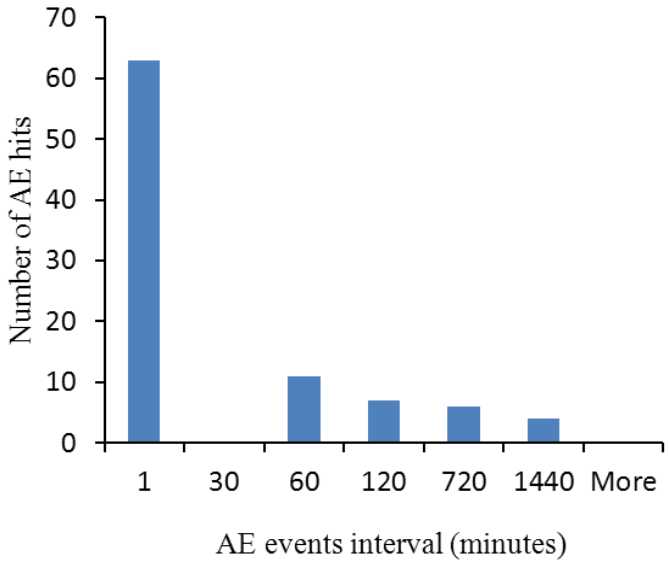

Figure 7.10: Time intervals between two successive AE events of all 92 AE records triggered in the week of July 11, 2012

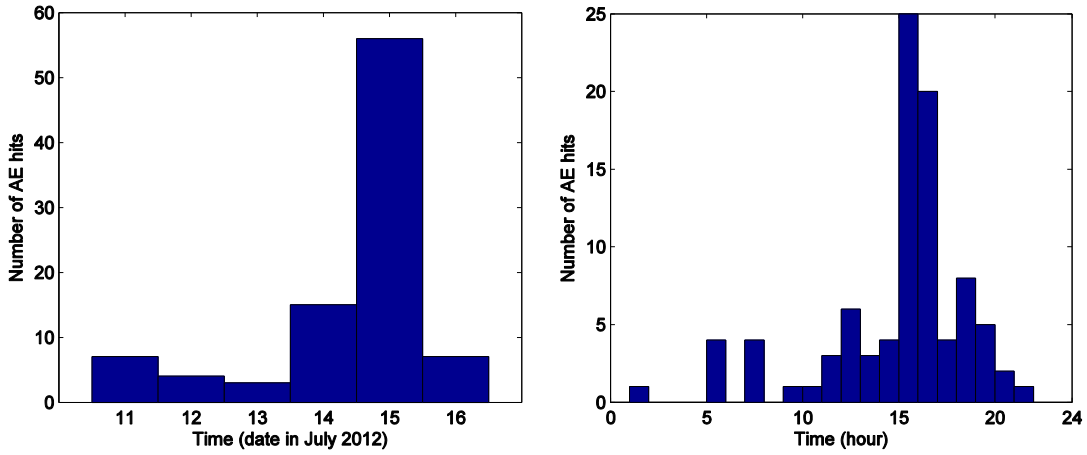

(a) (b)

Figure 7.11: (a), (b) see next page for caption

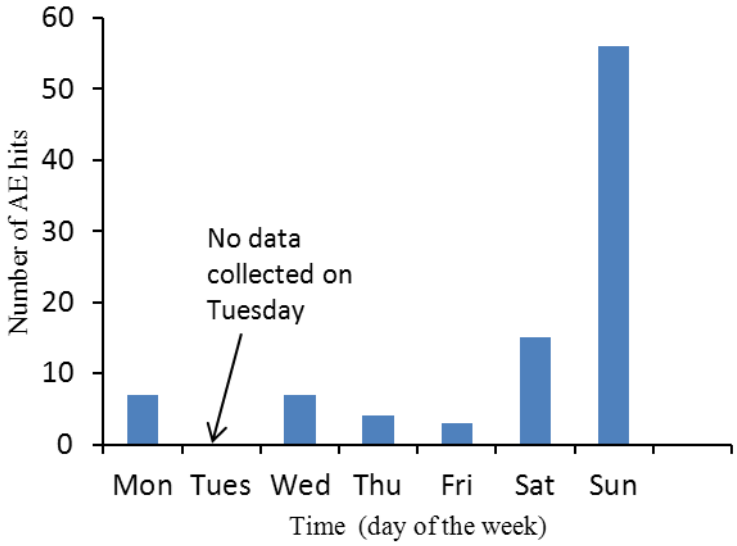

(c)

Figure 7.11: Histograms of AE events recording time: (a) date (in July 2012); (b) hours of the day; (c) days of the week

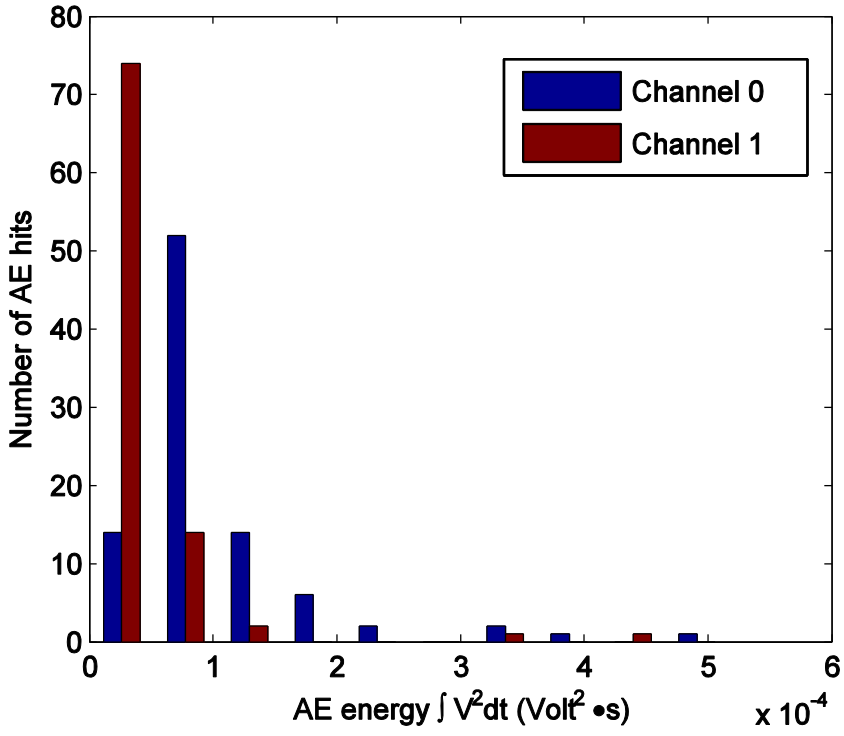

Figure 7.12: Histogram of AE energy level

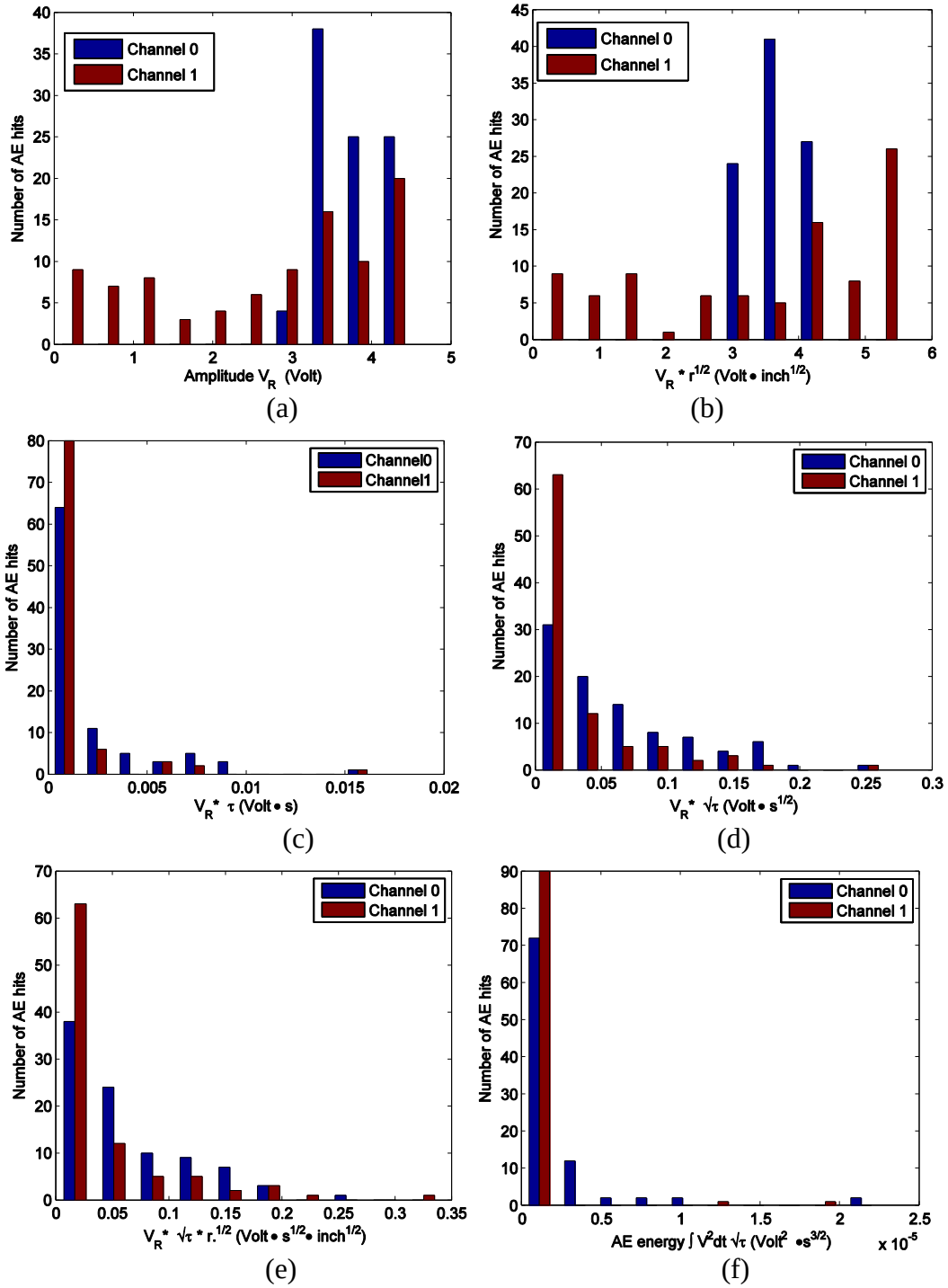

Figure 7.13: Histograms of AE event features: (a) AE signal peak amplitude (PA); (b) PA adjusted with square root of the source distance; (c) PA adjusted with the rise time; (d) PA adjusted with the square root of rise time; (e) PA adjusted with the square root of rise time and square root of source distance; (f) energy adjusted with the square root of rise time

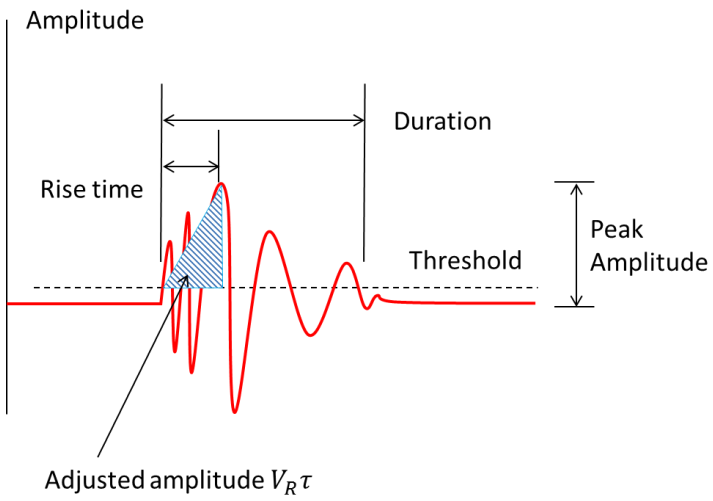

Figure 7.14: Illustration of AE parameters definition

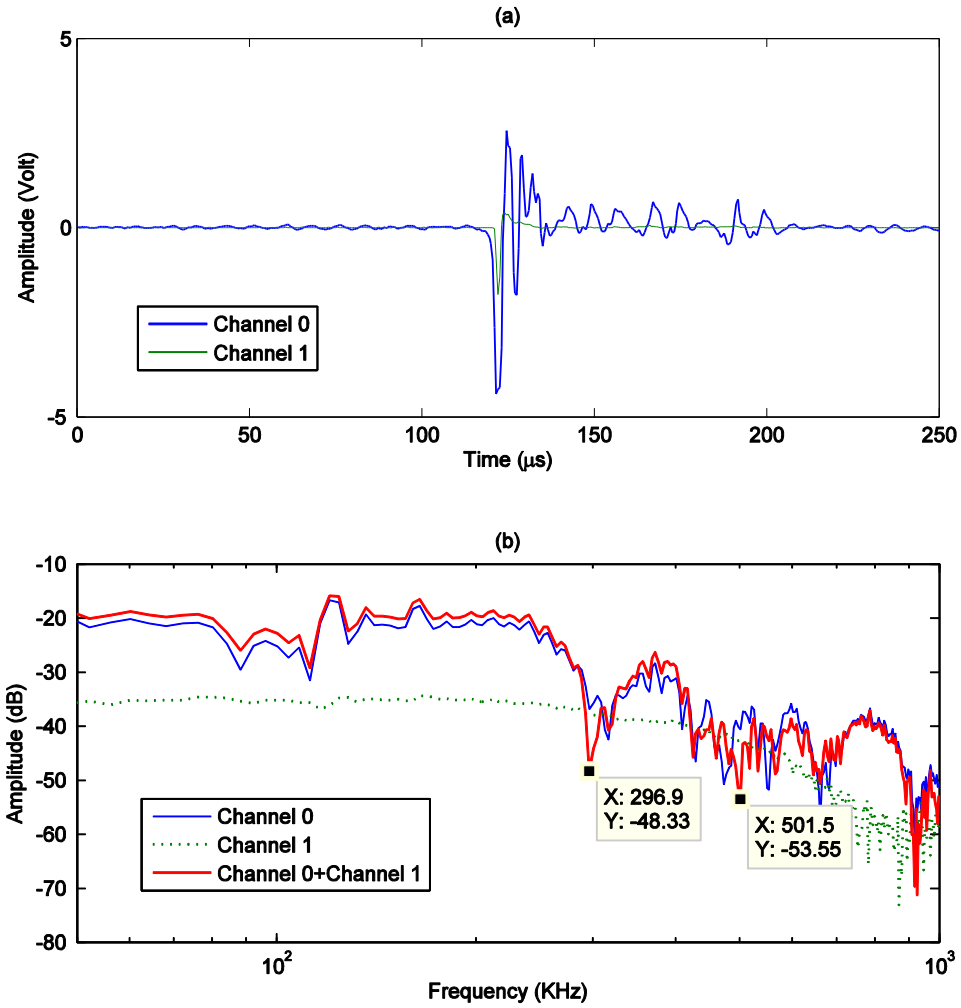

Figure 7.15: AE signal from the sensor couple acquired at 4:10pm on July 15 2012: (a) signal waveform; (b) frequency spectra

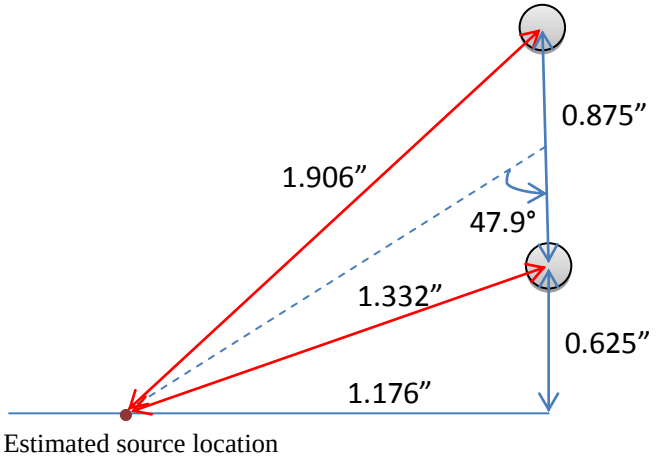

Figure 7.16: AE source location estimated using the phase shift method

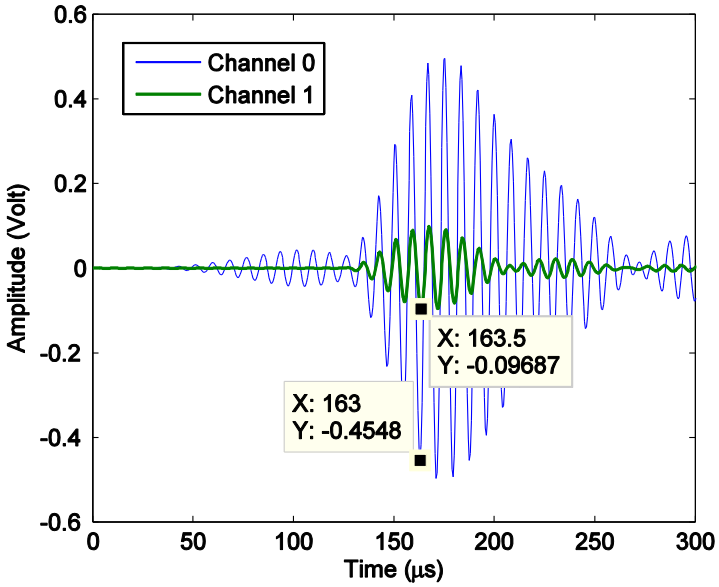

Figure 7.17: Highlighted time arrival of filtered AE signals (original AE records are shown in Figure 7.13(a)) with a band-pass frequency of 110-130 kHz

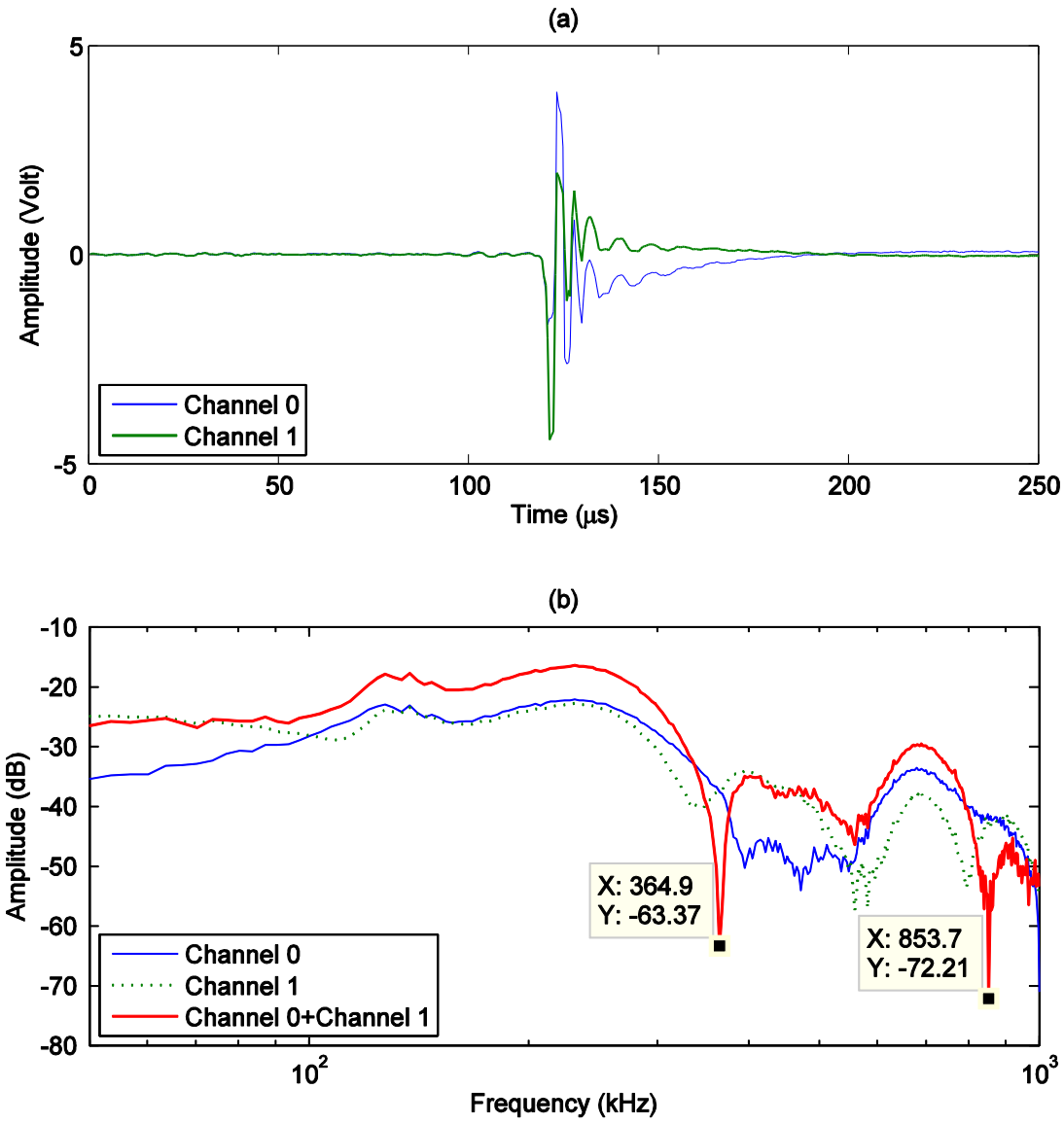

Figure 7.18: AE event measured by piezoelectric film AE sensors with troughs observed in the frequency domain of the combined sensor couple signal (signal acquired at 12:00pm on July 11, 2012): (a) signal waveform; (b) frequency spectra

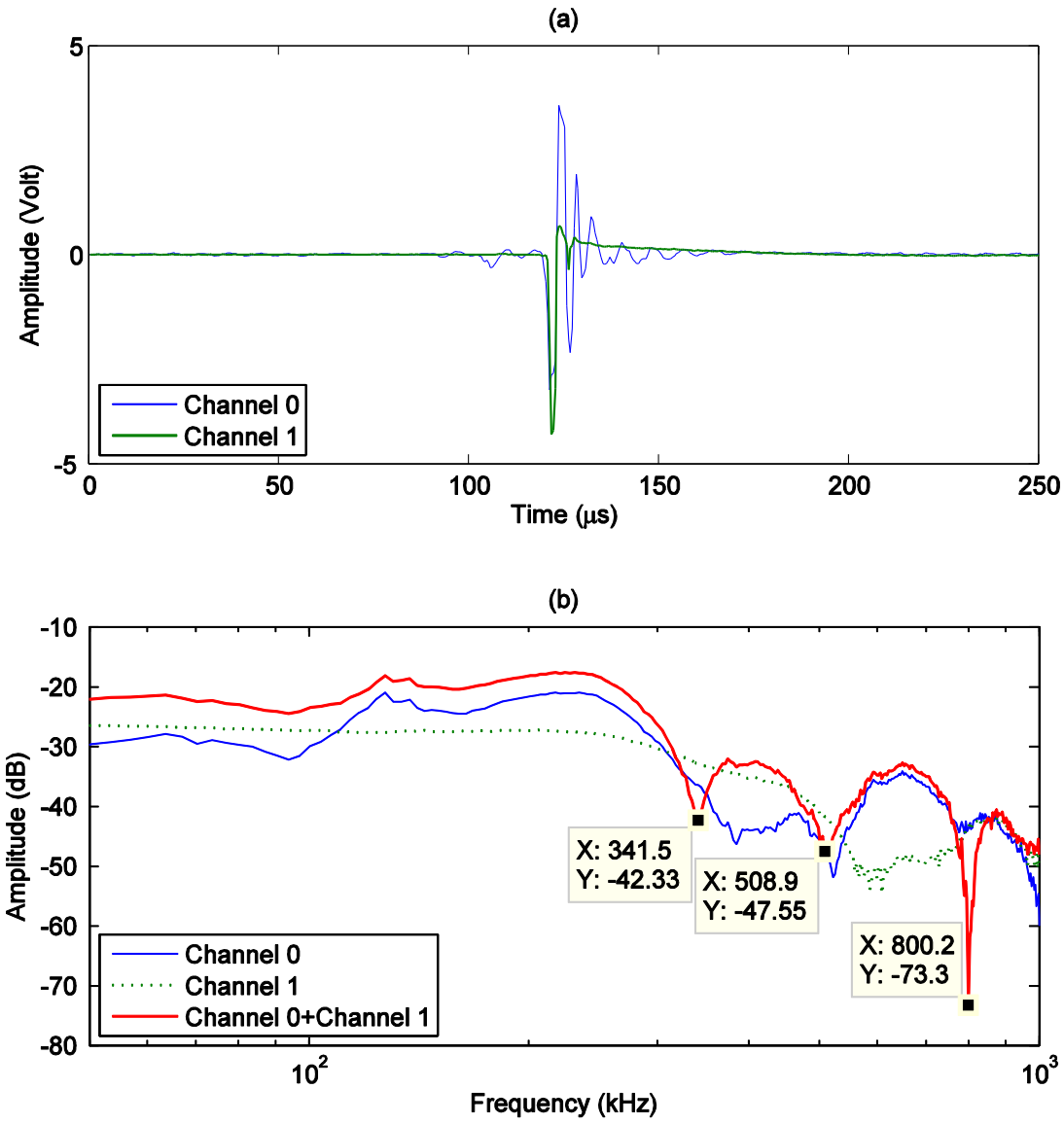

Figure 7.19: AE event measured by piezoelectric film AE sensors with troughs observed in the frequency domain of the combined sensor couple signal (signal acquired at 7:48pm on July 14, 2012): (a) signal waveform; (b) frequency spectra

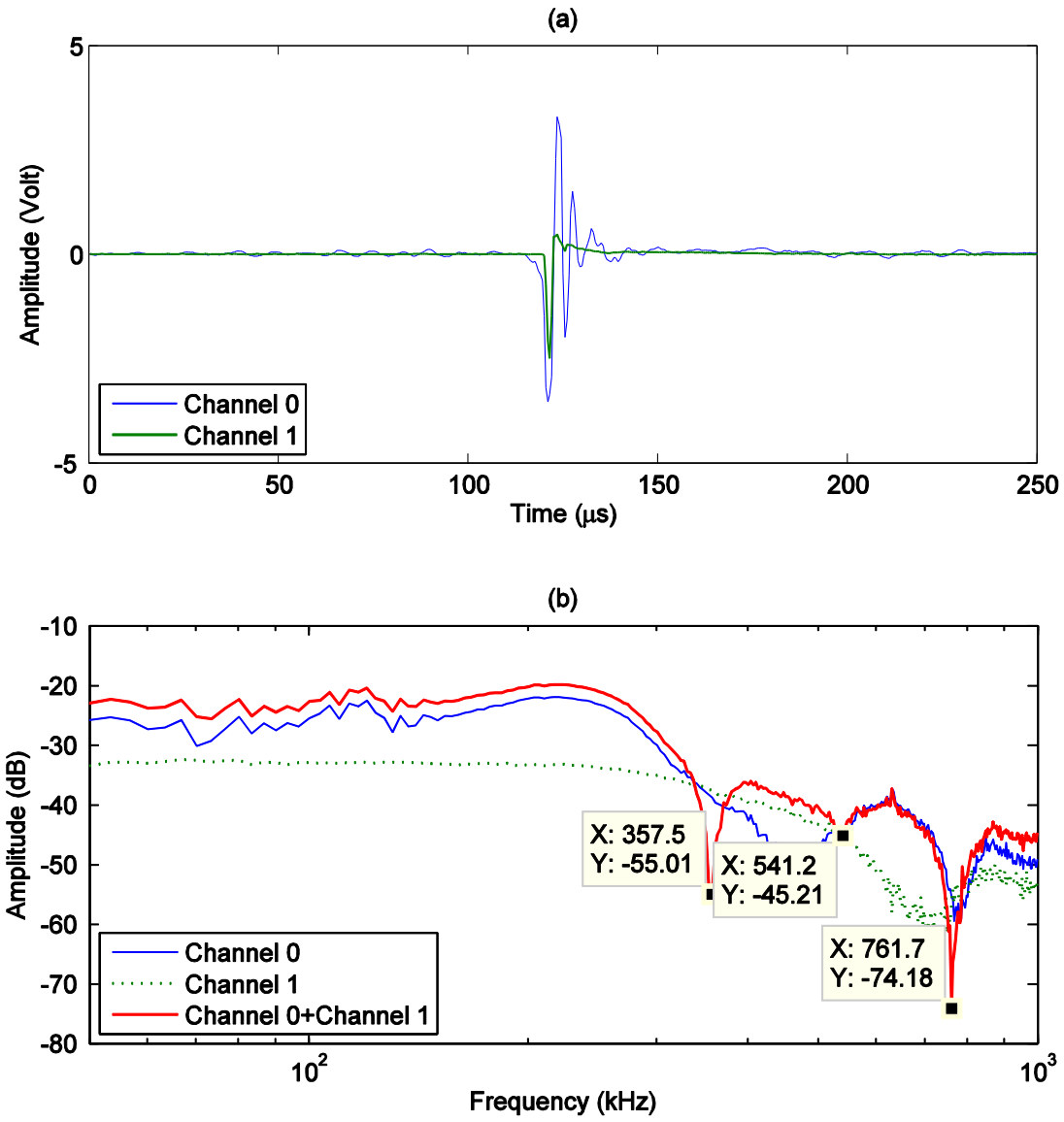

Figure 7.20: AE event measured by piezoelectric film AE sensors with troughs observed in the frequency domain of the combined sensor couple signal (signal acquired at 8:33pm on July 14, 2012): (a) signal waveform; (b) frequency spectra

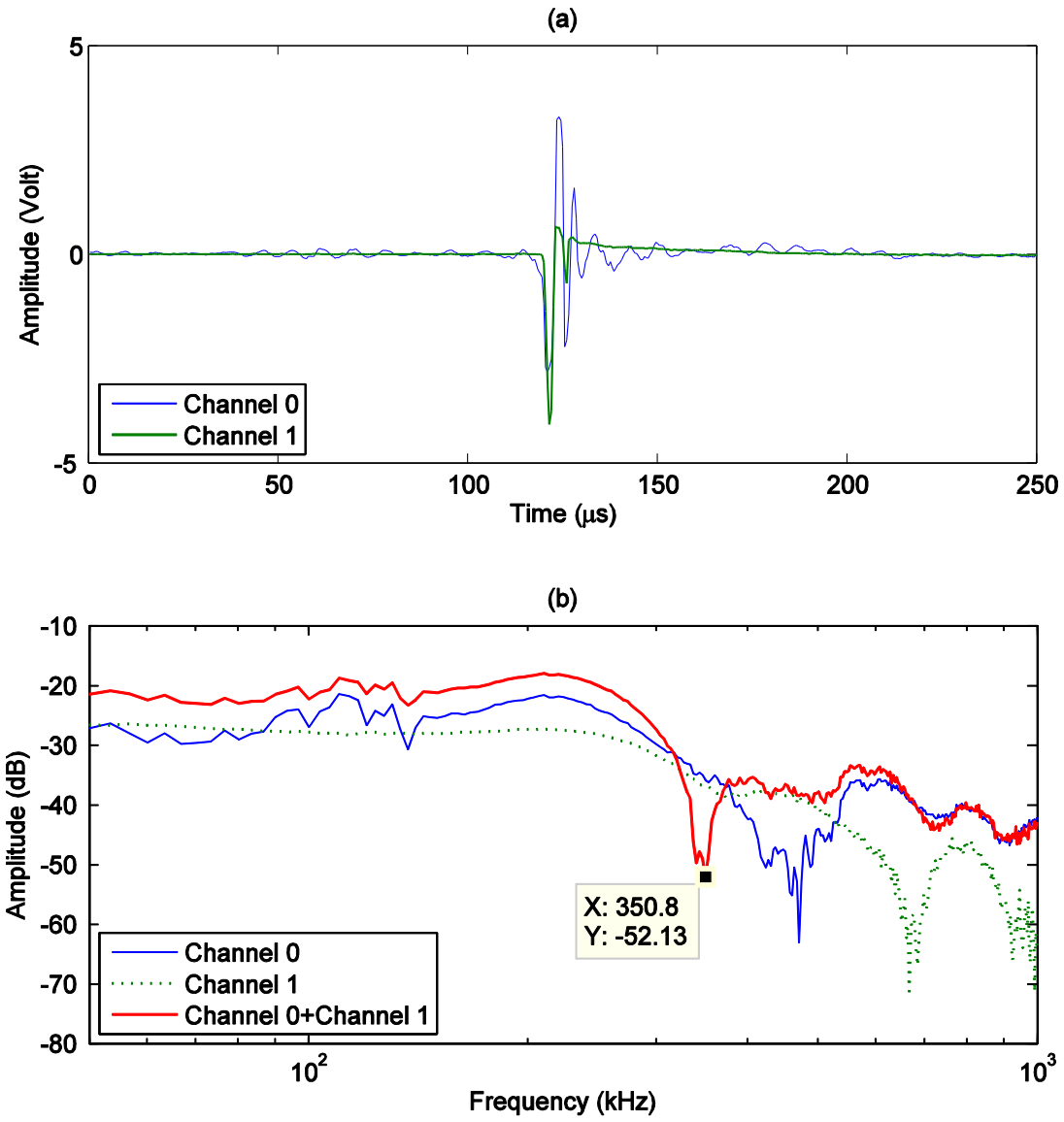

Figure 7.21: AE event measured by piezoelectric film AE sensors with troughs observed in the frequency domain of the combined sensor couple signal (signal acquired at 9:00pm on July 14, 2012): (a) signal waveform; (b) frequency spectra

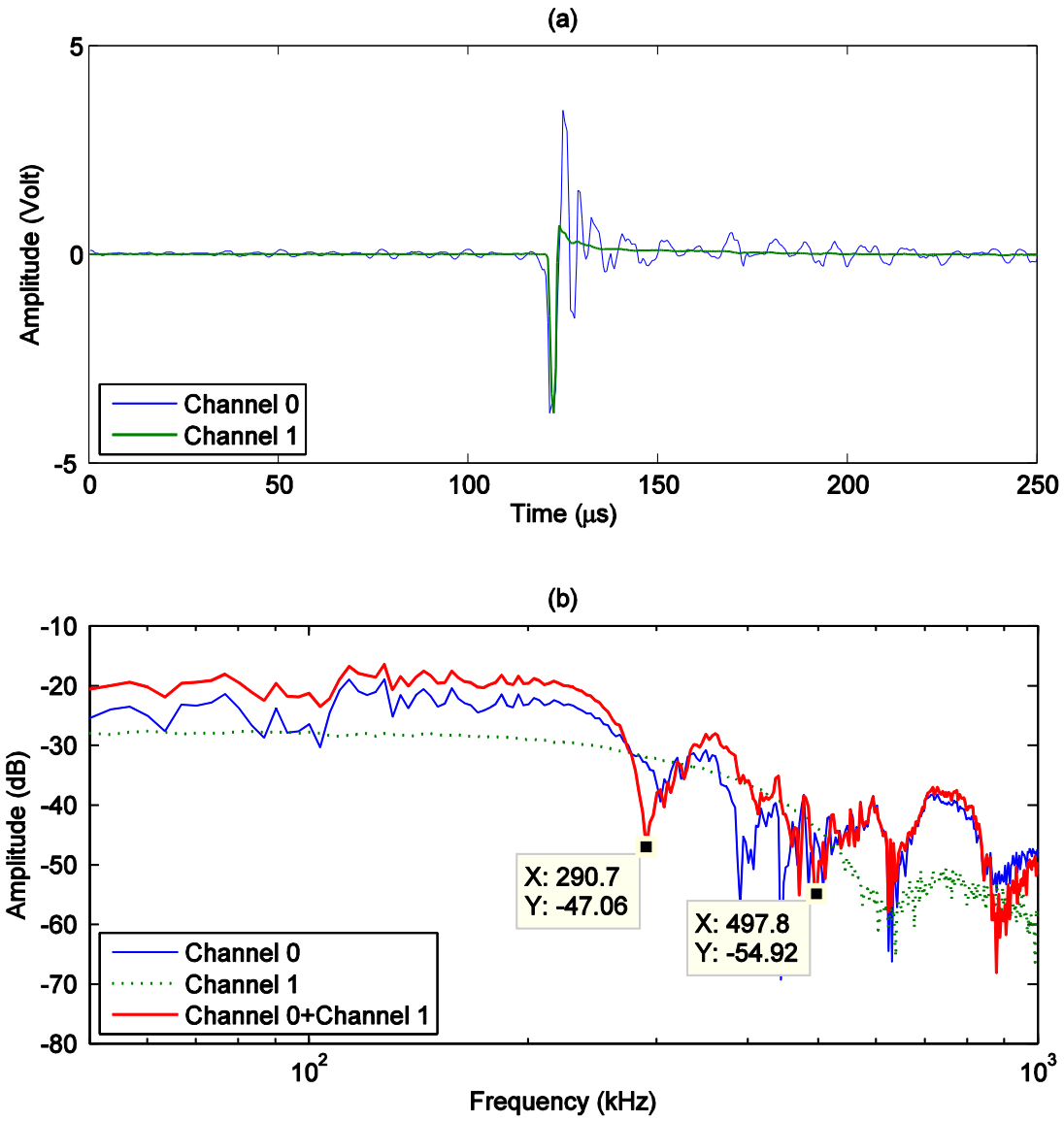

Figure 7.22: AE event measured by piezoelectric film AE sensors with troughs observed in the frequency domain of the combined sensor couple signal (signal acquired at 4:37pm on July 15, 2012): (a) signal waveform; (b) frequency spectra

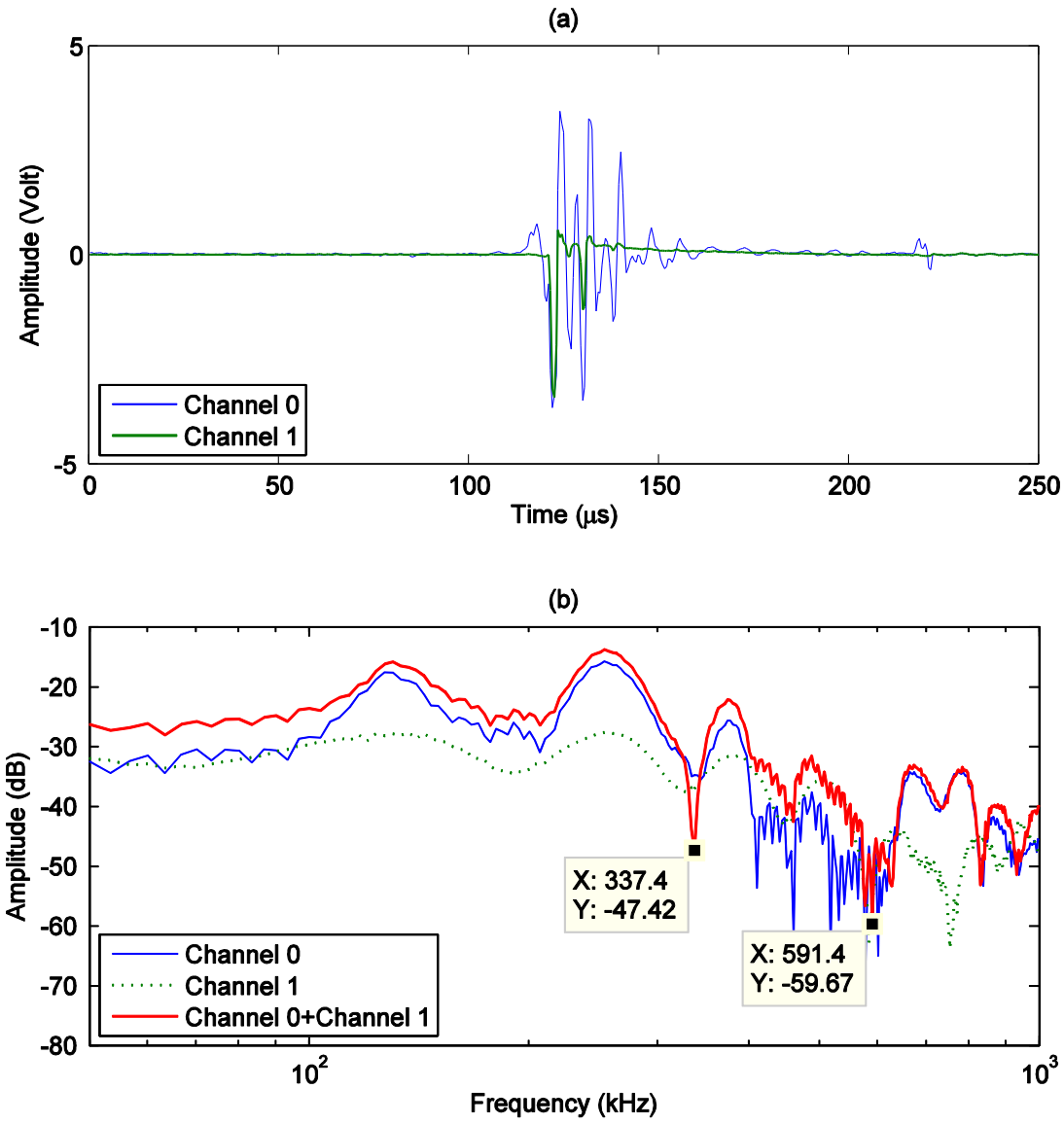

Figure 7.23: AE event measured by piezoelectric film AE sensors with troughs observed in the frequency domain of the combined sensor couple signal (signal acquired at 4:40pm on July 15, 2012): (a) signal waveform; (b) frequency spectra

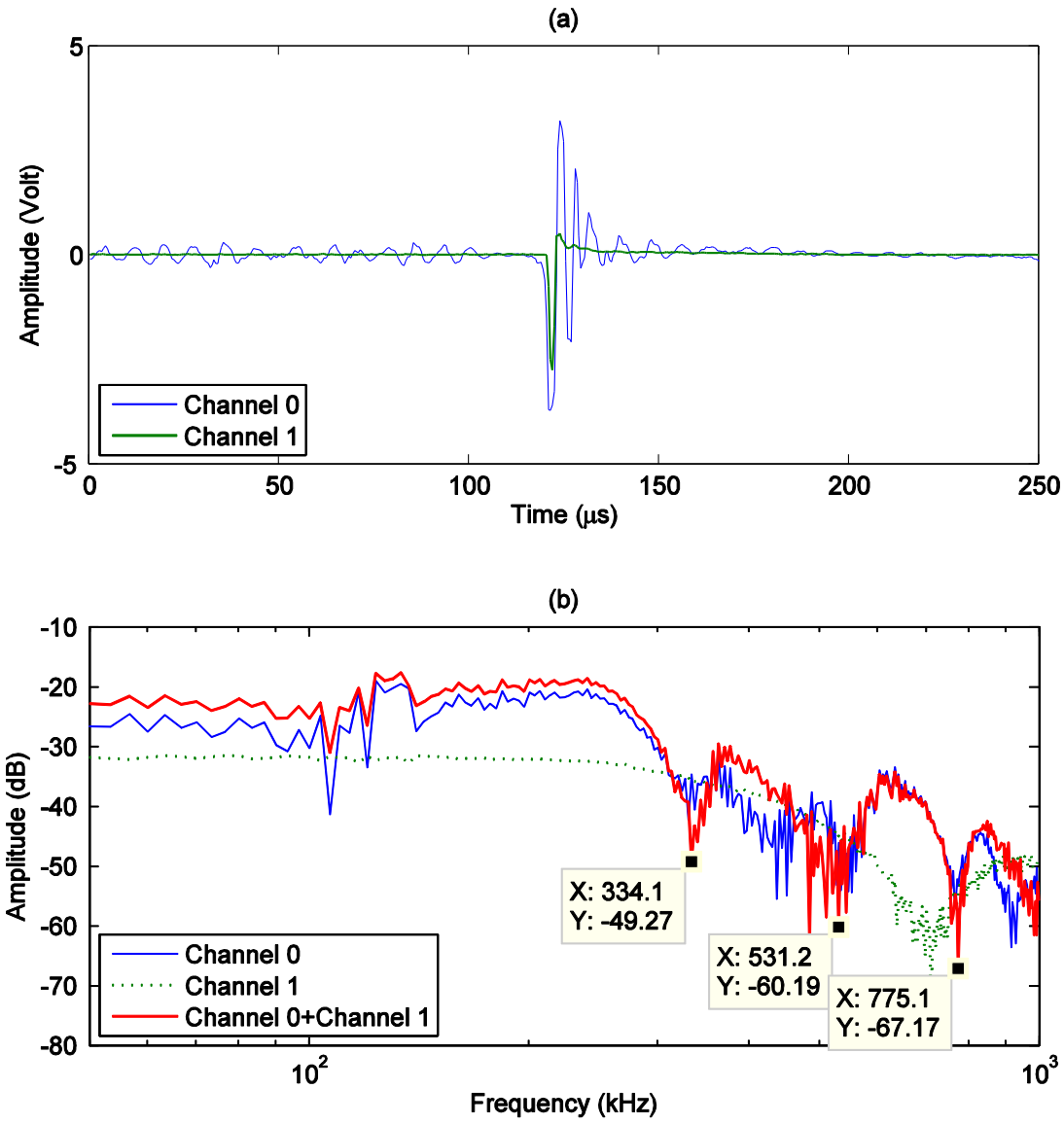

Figure 7.24: AE event measured by piezoelectric film AE sensors with troughs observed in the frequency domain of the combined sensor couple signal (signal acquired at 4:47pm on July 15, 2012): (a) signal waveform; (b) frequency spectra

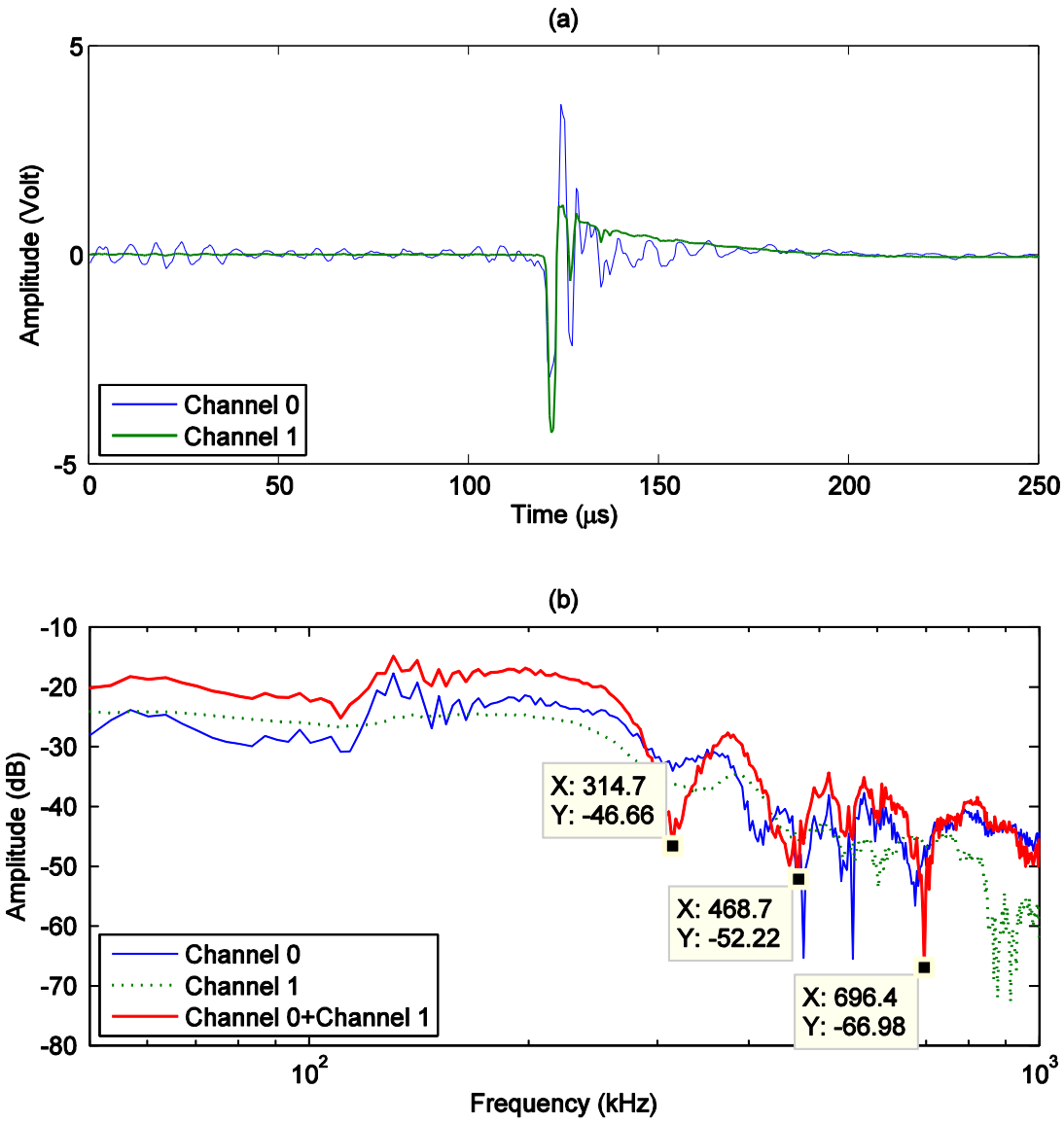

Figure 7.25: AE event measured by piezoelectric film AE sensors with troughs observed in the frequency domain of the combined sensor couple signal (signal acquired at 5:14pm on July 15, 2012): (a) signal waveform; (b) frequency spectra

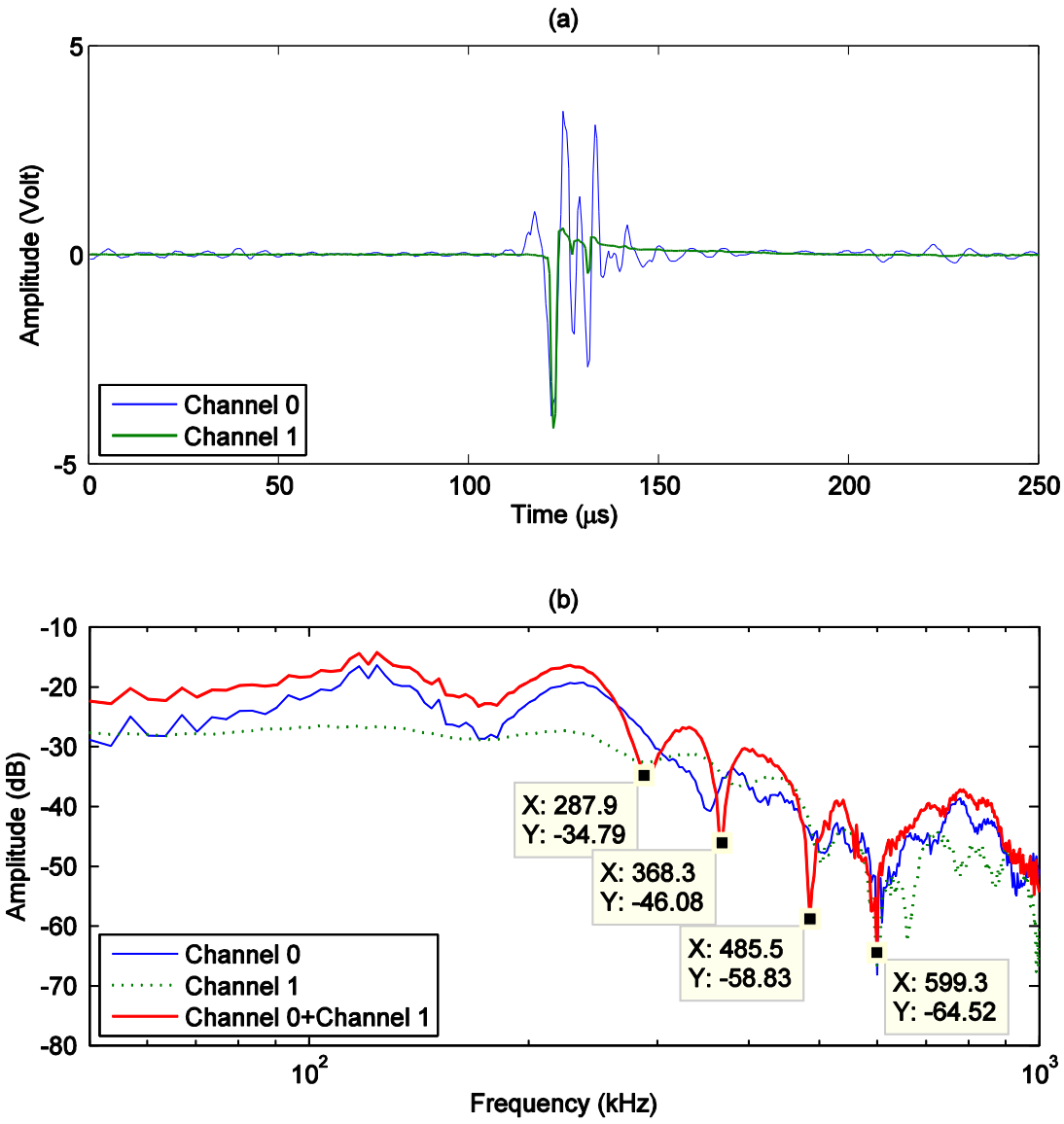

Figure 7.26: AE event measured by piezoelectric film AE sensors with troughs observed in the frequency domain of the combined sensor couple signal (signal acquired at 8:03pm on July 15, 2012): (a) signal waveform; (b) frequency spectra

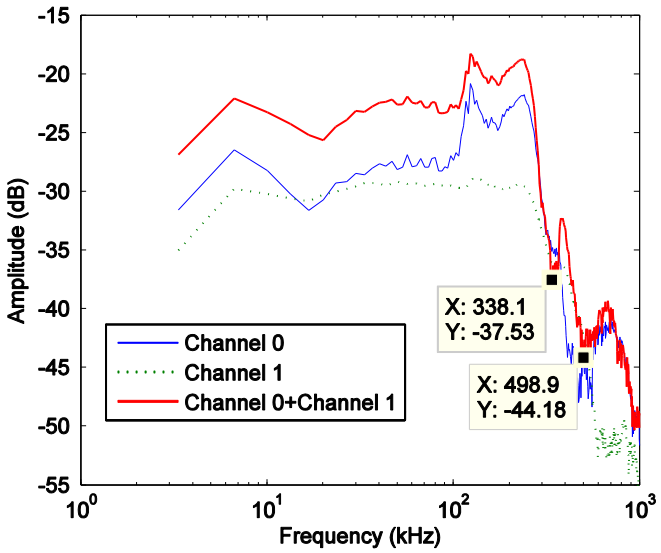

Figure 7.27: Average frequency spectrum of ten measured AE signals with space phase shift effect

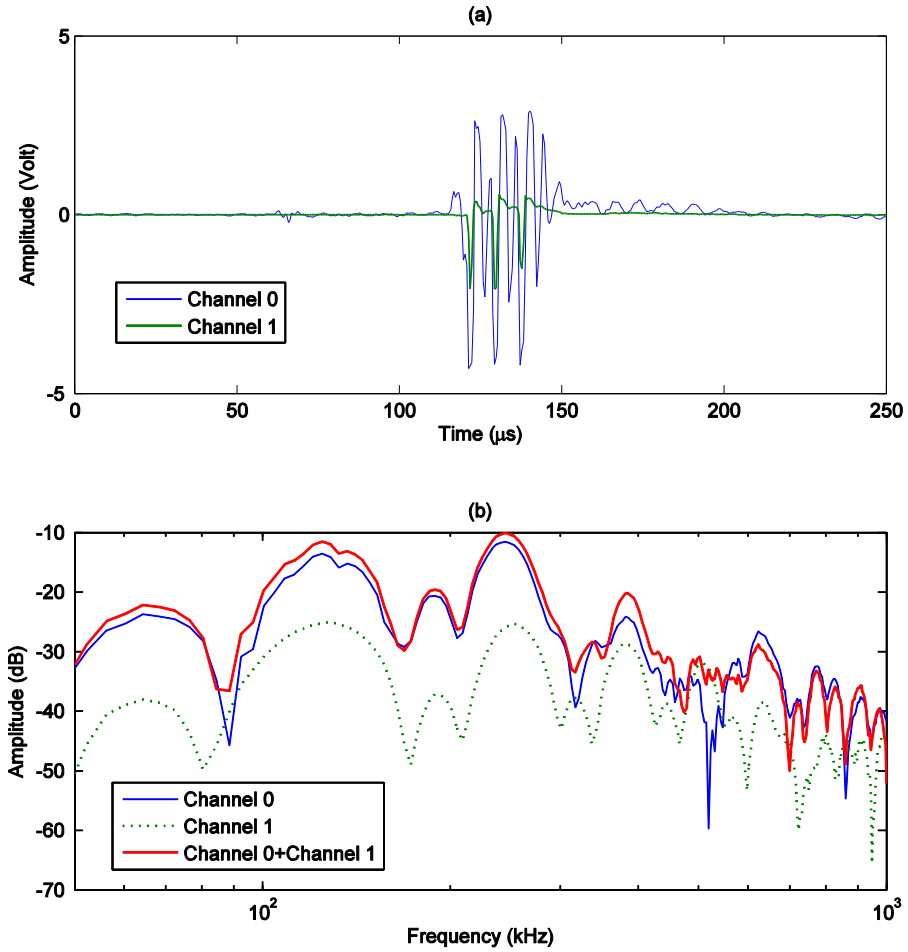

Figure 7.28: Typical AE event measured by piezoelectric film AE sensors without troughs observed in the frequency domain of the combined sensor couple signal (signal acquired at 6:42am on July 14, 2012): (a) signal waveform; (b) frequency spectra

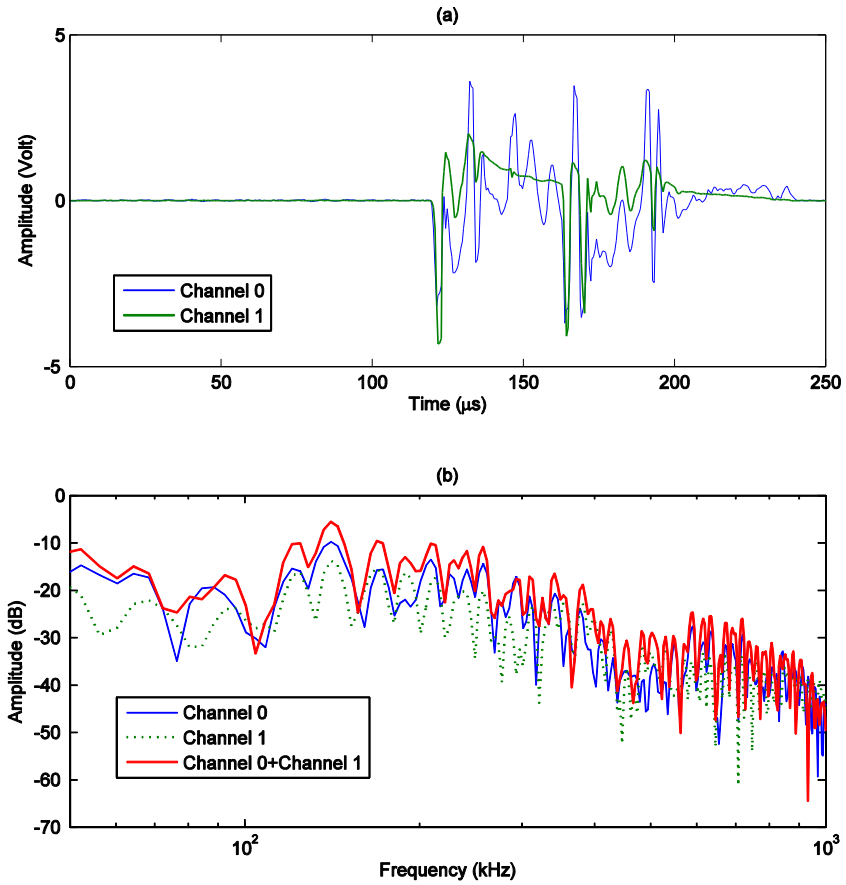

Figure 7.29: Typical AE event measured by piezoelectric film AE sensors without troughs observed in the frequency domain of the combined sensor couple signal(signal acquired at 7:58pm on July 12, 2012): (a) signal waveform; (b) frequency spectra

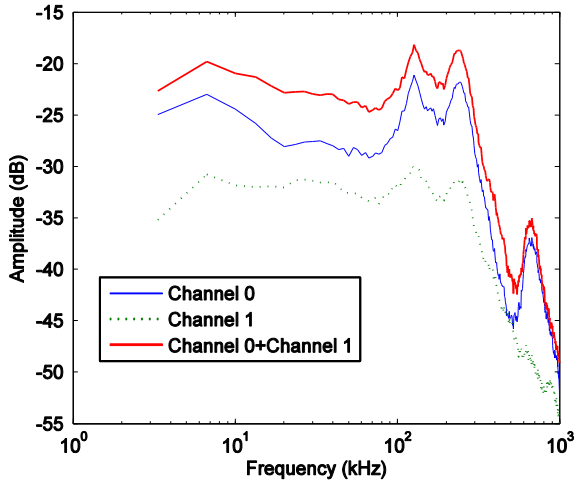

Figure 7.30: Average frequency spectra of triggered AE signals from piezoelectric film AE sensors without troughs observed in the frequency domain of the combined sensor couple signal and the combined sensor couple signal

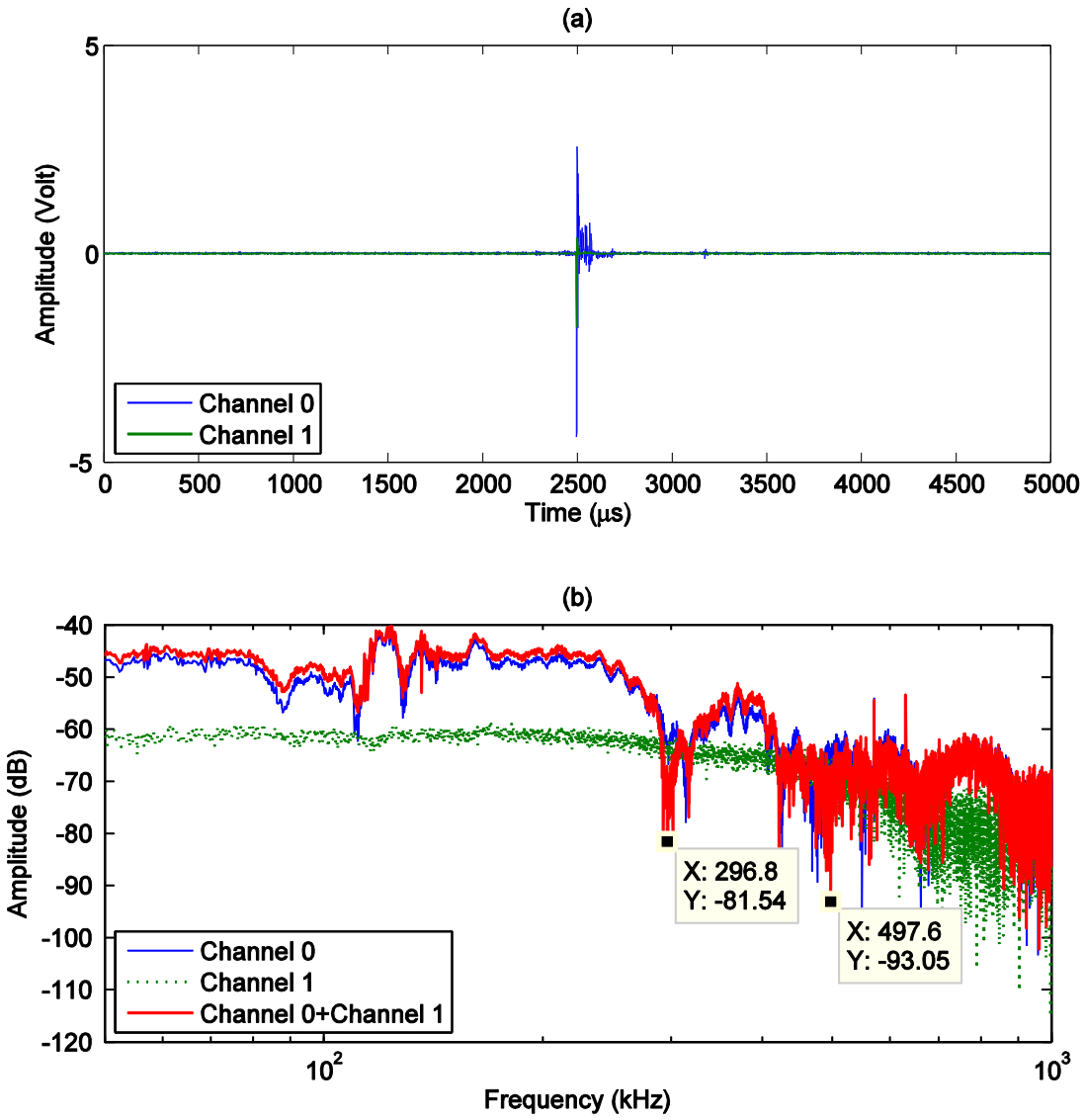

Figure 7.31: Signal duration effect on trough frequency identification (shorted duration is shown in Figure 7.15): (a) signal waveform; (b) frequency spectra

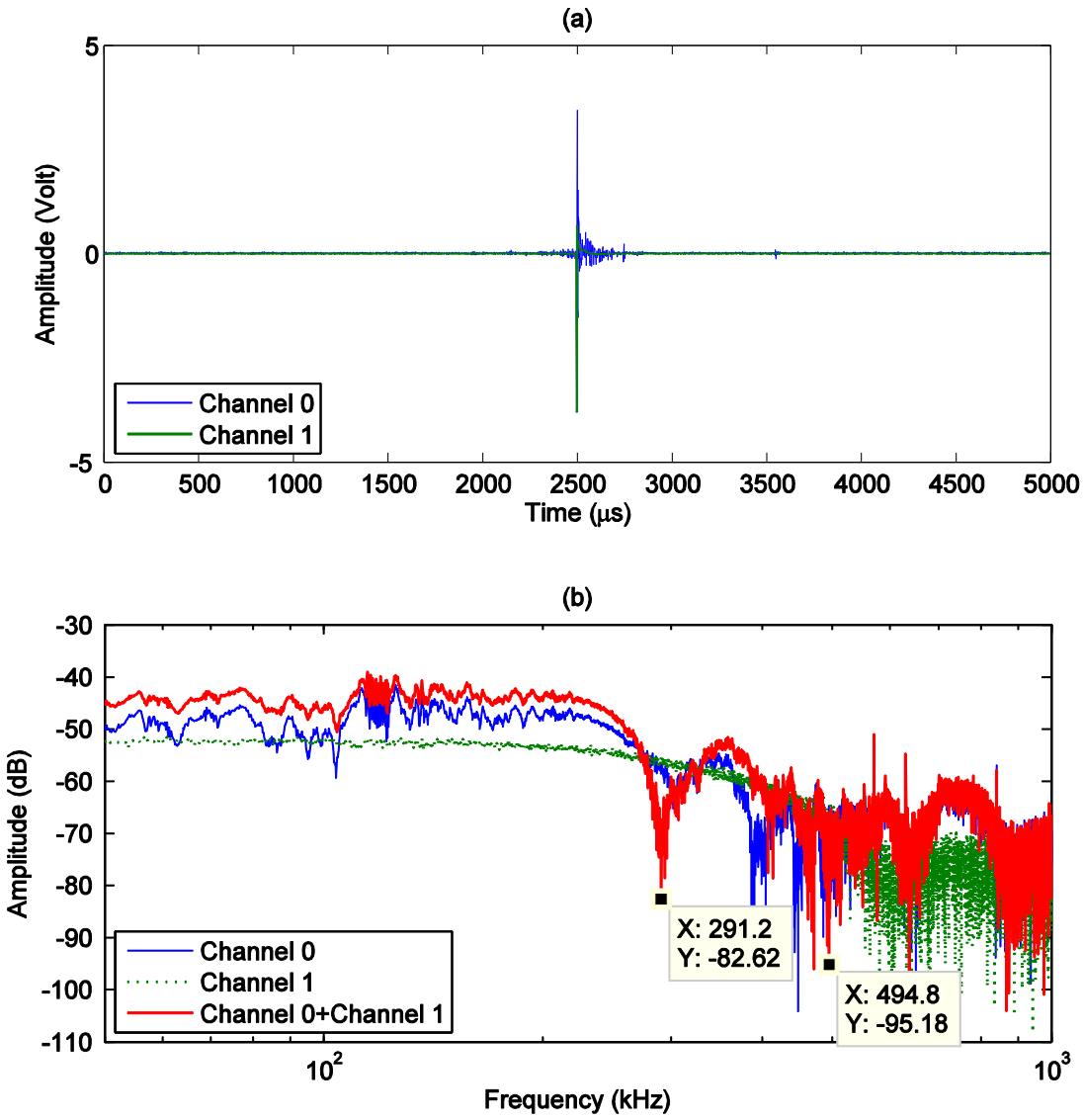

Figure 7.32: Signal duration effect on trough frequency identification (shorter duration is shown in Figure 7.22): (a) signal waveform; (b) frequency spectra

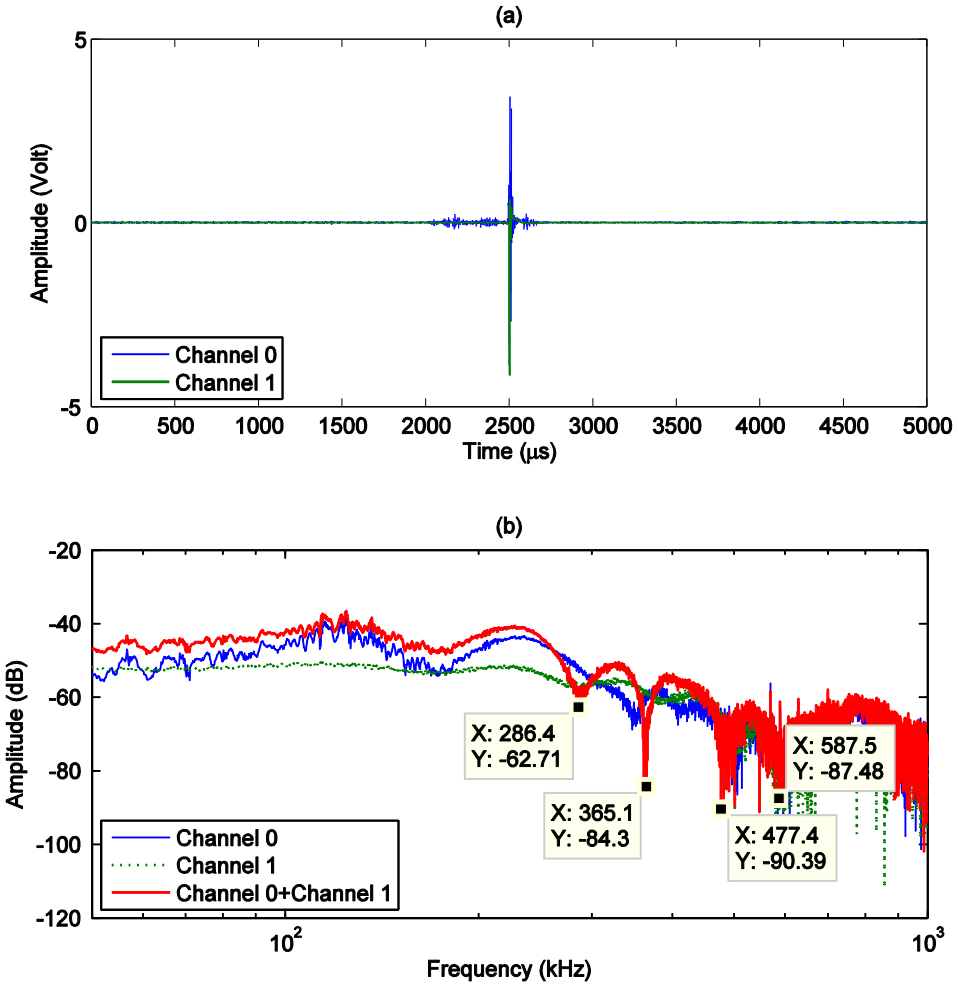

Figure 7.33: Signal duration effect on trough frequency identification (shorted duration is shown in Figure 7.26): (a) signal waveform; (b) frequency spectra

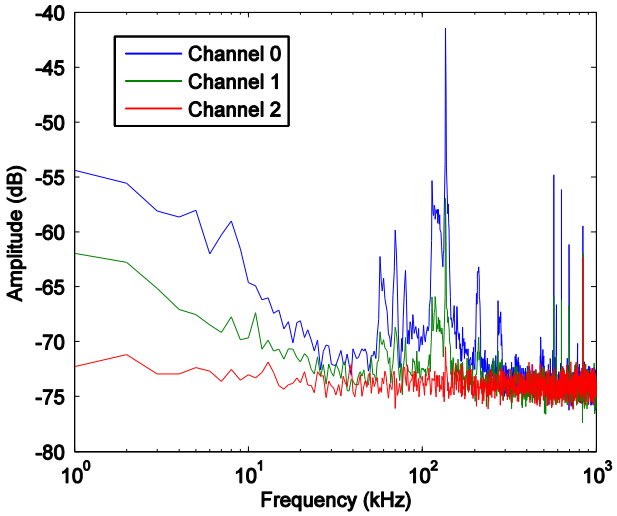

Figure 7.34: Averaged frequency spectra of 50 ambient noise signals

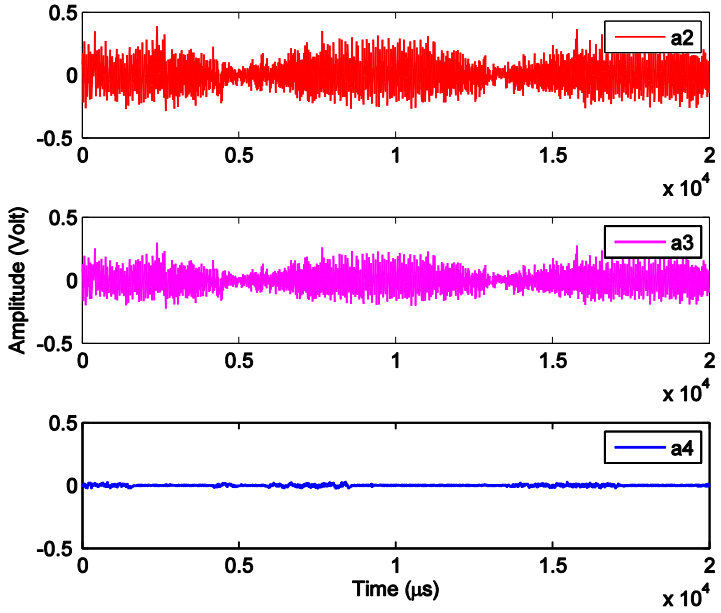

(a)

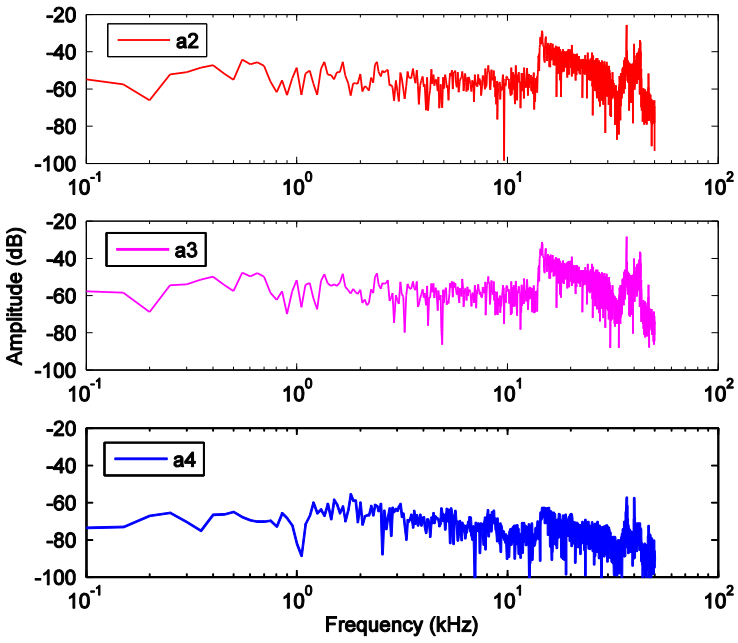

(b)

Figure 7.35: (a) Large noise due to grounding loops; (b) frequency spectra of the noise

Chapter 8: Conclusions and Future Work

8.1 Conclusions

While there are quite a few non-destructive evaluation (NDE) techniques available for fatigue crack inspection, acoustic emission (AE) sensing with piezoelectric film AE sensor has been demonstrated to be an effective approach for fatigue crack monitoring and has been attracting growing interests. The advantages using piezoelectric film AE sensor include real-time information, continuous monitoring and ability to localize AE source using the proposed near-field AE monitoring strategy.

This dissertation research aims to establish the foundation technologies for applying piezoelectric film AE sensor to fatigue crack growth monitoring and to develop the associated AE signal analysis methods such as AE source localization in both analytical and experimental approach. The performance of piezoelectric film AE sensor is verified and characterized, with simulated AE tests on a large steel block and fatigue crack monitoring on full-scale steel test specimens, as well as through field test on a real highway bridge. Specifically, the major findings of this research are summarized as follows,

- The theoretical expressions of Green's function of surface strain for half space were formulated and verified with experimental data. By avoiding the numeric error that could result from numerical differentiation of surface wave induced displacements with respect to spatial coordinates, this analytical formula has the advantage of increased accuracy in calculating AE strain signals.

- The generalized expression for stress-wave induced AE strain signal reveals the relationship between the AE strain signal and AE source mechanism. It can be used to represent different source mechanisms by combining moment tensors.
- A formula for the AE strain sensor's response to surface pulse is provided to lay the theoretical foundation for calibrating piezoelectric film based AE strain sensors. It is found that AE strain signal due to a step force on the surface of a half space has a relatively flat frequency spectrum. This suggests that the piezoelectric film AE sensor could also be used for broadband AE signal sensing.
- By comparing the experimental results and theoretical predictions of AE signals due to an approximate step force generated by glass capillary breakage, it is found that piezoelectric film AE sensor is able to record the AE signal with high fidelity and thus suitable for waveform-based AE signal analysis.
- By comparing the AE signal measured by piezoelectric film AE sensor and commercial AE sensor (Dunegan Engineering model number SE1000-HI, broadband, high sensitivity) in lab test, it's concluded that piezoelectric film AE sensors have comparable AE sensing performance to the commercial AE sensor in terms of sensitivity and frequency response. The polyimide backing film of piezoelectric film AE sensor would reduce the AE signal peak amplitude by approximately 18%.
- According to the parametric study of AE strain signals, it is found that the amplitude of Raleigh wave decays at a rate of $r^{-0.4114}$ with distance r, which is

slower than the decay of P wave with a ratio of $r^{-1.1330}$. This finding is consistent with the $r^{-1/2}$ Rayleigh wave attenuation relationship reported by other researchers. It is also seen in AE strain signals that Raleigh wave has a much larger amplitude than the P and S wave arrivals in the near-field.

- For the crack-induced AE strain signals, sharp rise can be seen and deeper crack source would have weaker AE signals. In addition, the signal attenuation with distance become more apparent when the crack source depth increases. In terms of different structural materials, the AE strain signal in steel has a slightly larger amplitude than the signal in aluminum.
- The proposed AE source localization technique with sensor couple does not require exact knowledge of the time of arrivals, which is often subject to error due to signal noise for the Time of Arrival method. By averaging multiple records in frequency domain, this method could enhance the SNR ratio for trough frequency identification and thus locate the AE source more accurately.
- Elastodynamic simulation and experimental test results validate the AE source localization technique in two independent approaches. Case studies confirmed the trough frequency caused by space phase shift in a sensor couple is only related to the source direction angle.
- Through the sensitivity analysis of frequency change to direction angle in the sensor couple theory, it is recommended that a source direction angle ranging from 30° to 60° should be arranged in sensor installation for best accuracy in AE source localization.

- Piezoelectric film AE sensor made of piezoelectric paint was found to be especially suitable for fatigue crack monitoring on tubular structure. Its flexibility made it able to conform to the curved surface of the tubular structure and avoid noise introduced by imperfect bonding which was seen for PZT disc.
- It is demonstrated that piezoelectric film AE sensor can be used for real-time fatigue crack monitoring on the welded tubular joints and the welded plate.
- Using sensor couple for source localization was experimentally validated with AE data from fatigue test of the welded plate specimens. The result is consistent with that of the conventional Time of Arrival method and the results from two different types of sensors agree with each other. Because of its higher sensitivity, the piezoelectric film AE sensor made of PZT outperforms the commercial AE sensor (SE1000-HI) when using the sensor couple theory for source localization on the fatigue test specimens. However, due to the smaller tube wall thickness of the tubular joint and its curved surface, the sensor couple based AE source localization method can not be verified on the welded tubular joint specimens.
- The feasibility of using piezoelectric film AE sensors for online fatigue crack monitoring is demonstrated in the field test. Based on the analysis of AE features including hits rate, occurrence, adjusted amplitude and energy level, it is believed that the recorded AE signals were likely to be related to the AE activities associated with fatigue crack growth. The high stress level (peak value up to 17 ksi) from the BDI strain gage data also support this observation

that the fatigue crack was growing and fatigue crack development should be in regime II (Paris law regime, or stable crack growth regime).

- The sensor couple theory for AE source localization was also verified with a limited number of piezoelectric film AE sensor data from the field test. However, many AE data do not show the space phase shift induced trough frequencies although this does not suggest these AE data are not related to the active fatigue cracking. This deserves further study.

8.2 Recommendation of Future Research

The following future research works are recommended:

- Extending the Green's function for AE strain signal from half space to plates with finite thickness could be very useful. In the present research, most of studies were conducted on thick plate, which can be approximately considered as half space. In future work, the effect of plate thickness on the AE strain signal waveform may be an interesting topic to look into, especially for plate thickness smaller than ½". The application of sensor couple theory in thin plate would also be of interest.
- The current design of piezoelectric film AE sensor has a protection and shielding layer that intends to shield the inside sensing element from environmental impact like moisture and EMI noise. However, noise level on the order of 10 mV is still observed in measured AE data, especially in field test. Future improvements of the sensor design including preamplifier/filter circuitry could be made to reduce the noise floor to below 3 mV.

- Although AE signals generated by different source mechanisms were studied here, a limited number of cases for quantitative AE analysis have been carried out. Analytical models that can describe the AE source mechanisms (e.g. fatigue cracking, friction rubbing/fretting, etc.) would be very helpful for quantitative AE analysis, which might be developed in future research.
- Current study is limited to using piezoelectric AE film sensor for fatigue crack monitoring in steel structures. Experimental study of the sensing performance of piezoelectric film AE sensor on different structural materials such as reinforce concrete and fiber reinforced polymer composite structures, would be of interest.
- Results of the present study show that piezoelectric film AE sensor provides a promising tool for fatigue crack monitoring in practice. Although field test has been carried out, more extensive field work is still needed to characterize the sensor performance in real word environment, including: (i) the effect of weather on AE monitoring, including the temperature, the moisture and humidity; (ii) the correlation between the traffic pattern on the bridge and AE signal patterns; (iii) Wireless sensor technology could be incorporated for AE data collection, which would simply the installation process and make it convenient to use by engineers.

Appendices

A.1 Matlab Code for Elastodynamic Solution of Surface Source Response in a Half Space(This Code was Used for Chapter 4 of this Dissertation)

```
% The following codes are written with Matlab
% Main file for Surface pulse calculation
clc; clear
%% Material constants
PO=0.3;       % Poisson's ratio for material (steel)
RO=7850;      % Material density (kg/m^3)
E=200e9;      % Modulus of elasticity(Pa)
NT=500;       % Number of time instants
DT=1e-7;      % Sampling time interval (s)
x0=0.025*2;   % Receiver location (m)
%% Calculate Green's function using function HGreen131_2d
G131HS=HGreen131_2d(PO,RO,E,x0,NT,DT);
% Function HGreen131_2d
% This function is to compute the 131 component of Green's function for
% half space due to a Heaviside step function: G131H
% Input: Poisson's ratio PO, Density RO, Young's modulus E
% Sampling points NT, Sampling interval DT
% The distance between receiver and the source X12
function  y=HGreen131_2d(PO,RO,E,X12,NT,DT)
% ************************************************************
% material constants:
miu=E/((1+PO)*2);   % Shear modulus
lame=2*miu*PO/(1-2*PO); % Lame constant
VP=sqrt((lame+2*miu)/RO);  % P wave velocity
VS=sqrt(miu/RO); % S wave velocity
SC=(VP/VS)^2;
% ************************************************************
% Solve the cubic function for Rayleigh wave;
% When Poisson's ratio is larger than 0.262, the cubic function has only
% one real roots which can be used to calculate the Rayleigh wave speed;
% When Poisson's ratio is smaller than 0.262, the cubic function has 3 real
% roots, and the largest root is used to calculate the Rayleigh wave speed.
A(1)=(16 - 16*SC);
A(2)=(24*SC^2 - 16*SC);
A(3)=((-8)*SC^3);
A(4)=SC^4;  % Cubic function coefficients
x=roots(A);
% Find the real roots or maximum real roots (if all 3 are real) which
% corresponds to the ratio of P wave speed to Rayleigh wave speed.
R3=max(x((x==abs(x))|(x==-abs(x))));
```

```
VR=VP/sqrt(R3); % Rayleigh wave speed
RR=x((x~=abs(x))&(x~=-abs(x)));
c=1./(16.*(SC-1).*(R3-RR(1)).*(RR(2)-R3));
c8=1/2.*c.*SC.*(SC-2.*R3).^3/R3;

t=(1:NT)*DT; % Sampling time instants t
T=VP.*t./X12; % Dimensionless time T
k1=find(T>1,1);
k2=find(T<VP/VS,1,'last');
u(1:k1-1)=0;
% Do integration
 for k=k1:k2  % When X12/VP< t <X12/VS, or 1< T <VP/VS
    u(k) = quadl(@(s)green131half1_2d(s,SC,T(k)),0,pi/2,1e-10);
    u(k) = u(k).*2.*SC/pi/VP;
 end
 for k=k2+1:NT % When t >=X12/VS, or T >=VP/VS
    u1(k)= quadl(@(s)green131half2_2d(s,SC,T(k)),0,pi/2,1e-10);
    u2(k)=-heaviside(T(k)-sqrt(R3)).*c8.*R3./sqrt(T(k).^2-R3)/VP;
    u(k)=2.*SC/pi/VP.*u1(k)+u2(k);
 end
 y=real(u)/(pi*miu*X12);
 y=diff(y)/DT; % Differentiation with respect to time

% Integral function for surface pulse: 1< T <VP/VS
function y=green131half1_2d(s,A,T)
 P2=(T.^2-1).*(sin(s)).^2+1;
 y=P2.*(P2-1).*sqrt(A-P2).*(A-2.*P2)./ ...
     ((A-2.*P2).^4-16.*(1-P2).*(A-P2).*P2.^2);

% Integral function for surface pulse:  T >=VP/VS
function y=green131half2_2d(s,A,T)
P2=(A-1).*(sin(s)).^2+1;
y=P2.*(P2-1).*(A-P2).*(A-2.*P2)./ ...
    ((A-2.*P2).^4-16.*(1-P2).*(A-P2).*P2.^2)./sqrt(T.^2-P2);
```

A.2 Matlab Code for Elastodynamic Solution of Buried Source Response in a Half Space (This Code was Used for Chapter 4 of this Dissertation)

```
% The following codes are written with Matlab
% Double derivative of Green's function
function f=SpatialG_db(X1,X2,Z,NT,DT,VP,VS,miu,index)
% VP: P-wave velocity, PO: Poisson's ratio
% RO: Mass density, X1,X2, Z:  source coordinates
% DT: sampling time; NT: sampled number
% Input of the parameters
```

```
P1=zeros(1,NT);
P2=zeros(1,NT);
G=zeros(1,NT);
T=DT.*(1:NT);
Y1=zeros(1,NT);
Y2=zeros(1,NT);
R=sqrt(X1^2+X2^2);
RZ=sqrt(R^2+Z^2); % Source distance
ST=R/RZ;
CT=Z/RZ;
SC=VS/VP;
PHI=asin(X2/R);
% Time
T1=RZ/VP;
if (ST>SC)
   T2=RZ/VP*ST+RZ*sqrt((1/VS)^2-(1/VP)^2)*CT;
   P2=sqrt((T./RZ-sqrt((1./VS).^2-(1./VP).^2).*CT).^2./ST.^2-(1./VP).^2);
else
   T2=RZ/VS;
   P2=sqrt((T./RZ).^2-(1./VS).^2);
end
% Heaviside function
P2(T<T2)=0;
P1=sqrt((T./RZ).^2-(1./VP).^2);
P1(T<T1)=0;

% Do integration first part-M{N1,N2}
I1=find(P1>0);
for i=I1:NT
      TR=T(i)/RZ;
      DP1=P1(i);
      DV1=sqrt(DP1);
      YM=quadl(@(V)FUN_M_DB(V,VP,VS,ST,CT,TR,PHI,index),0,DV1,1e-8);
      Y1(i)=YM;
end
% Do integration first part-N{N1,N2}
I2=find(P2>0);
if (ST>=SC)
   for i=I2:NT
      TR=T(i)/RZ;
      if(TR<1/VS)
         dpp2=P2(i);
         YS=quadl(@(V)FUN_ND_DB(V,VP,VS,ST,CT,TR,PHI,index),0,dpp2,1e-8);
         Y2(i)=YS;
      else
         YS1=quadl(@(V)FUN_N_DB(V,VP,VS,ST,CT,TR,PHI,index),0,pi/2,1e-8);
```

```
            dpp1=sqrt(TR^2-1/VS^2);
            dpp2=acos(dpp1/P2(i));
            YS2=quadl(@(V)FUN_ND2_DB(V,VP,VS,ST,CT,TR,PHI,index),0,dpp2,1e-
8);
            Y2(i)=-(YS1-YS2);
        end
    end
else
    display ('Deep source, implement the other case of the integral function')
end

for i=1:NT
    G(i)=(Y1(i)-Y2(i));
end
FAC1=pi^2*miu*RZ;
f=diff(G,2)./DT./DT./FAC1;
f=ConvWithSour(f,DT); % Convolute with the source function S(t)

% Function  Fun_M_DB
function  f=FUN_M_DB(V,VP,VS,ST,CT,TR,PHI,index)
P=sqrt(TR.^2-(1.0./VP).^2)-V.^2;
SA=sqrt(abs(TR.^2-(1.0./VP).^2-P.^2));
Q1=-TR.*ST;
Q2=SA.*CT;

Q=Q1+Q2*1i;
EA=sqrt((1.0./VP).^2+P.^2-Q.^2);
EB=sqrt((1.0./VS).^2+P.^2-Q.^2);
SIG=(EB.^2+P.^2-Q.^2).^2+4.0.*EA.*EB.*(Q.^2-P.^2);
SOR=sqrt(2.0*sqrt(TR.^2-(1.0./VP).^2)-V.^2);
GAMA=EB.^2+P.^2-Q.^2;
CT=cos(PHI);
ST=sin(PHI);
CT2=CT.^2;
ST2=ST.^2;
CT4=CT2.^2;
ST4=ST2.^2;

%% Referring to Eq. (4.23-4.24)
switch index
    case 1111
        M=-2*EB.*(Q.^4.*CT4-6*P.^2.*Q.^2.*ST2.*CT2+P.^4.*ST4);
    case 1121
        M=-2*EB.*(Q.^4.*CT2+3*P.^2.*Q.^2.*(-ST2+CT2)-P.^4.*ST2).*ST.*CT;
    case 1131
        M=-2*EA.*EB.*(Q.^2.*CT2-3.*P.^2.*ST2).*Q.*CT;
```

```
   case 1211
      M=-2*EB.*(Q.^4.*CT2+3*P.^2.*Q.^2.*(-ST2+CT2)-P.^4.*ST2).*ST.*CT;
   case 1221
      M=-2.*EB.*((Q.^2.*CT2-P.^2.*ST2).*(Q.^2.*ST2-
P.^2.*CT2)+4.*P.^2.*Q.^2.*ST2.*CT2);
   case 1231
      M=-2*EA.*EB.*(Q.^2.*CT2-P.^2.*ST2+2.*P.^2.*CT2).*Q.*ST;
   case 1311
      M=-2*EA.*EB.*(Q.^2.*CT2-3.*P.^2.*ST2).*Q.*CT;
   case 1321
      M=-2*EA.*EB.*(Q.^2.*CT2-P.^2.*ST2+2.*P.^2.*CT2).*Q.*ST;
   case 1331
      M=-2*EA.^2.*EB.*(Q.^2.*CT2-P.^2.*ST2);

   case 2112
      M=-2.*EB.*((Q.^2.*CT2-P.^2.*ST2).*(Q.^2.*ST2-
P.^2.*CT2)+4.*P.^2.*Q.^2.*ST2.*CT2);
   case 2122
      M=-2*EB.*(Q.^4.*ST2+3*P.^2.*Q.^2.*(ST2-CT2)-P.^4.*CT2).*ST.*CT;
   case 2132
      M=-2*EA.*EB.*(Q.^2.*ST2-P.^2.*CT2+2.*P.^2.*ST2).*Q.*CT;
   case 2212
      M=-2*EB.*(Q.^4.*ST2+3*P.^2.*Q.^2.*(ST2-CT2)-P.^4.*CT2).*ST.*CT;
   case 2222
      M=-2*EB.*(Q.^4.*ST4-6*P.^2.*Q.^2.*ST2.*CT2+P.^4.*CT4);
   case 2232
      M=-2*EA.*EB.*(Q.^2.*ST2-3.*P.^2.*CT2).*Q.*ST;
   case 2312
      M=-2*EA.*EB.*(Q.^2.*ST2-P.^2.*CT2+2.*P.^2.*ST2).*Q.*CT;
   case 2322
      M=-2*EA.*EB.*(Q.^2.*ST2-3.*P.^2.*CT2).*Q.*ST;
   case 2332
      M=-2*EA.^2.*EB.*(Q.^2.*ST2-P.^2.*CT2);
end
f=real(2*EA.*M./(SIG.*SOR));

% Function  Fun_N_DB
function  f=FUN_N_DB(V,VP,VS,ST,CT,TR,PHI,index)
P=sqrt(TR.^2-(1.0/VS).^2).*sin(V);
SB=sqrt(TR.^2-(1.0/VS).^2-P.^2);
Q1=-TR.*ST;
Q2=SB.*CT;
Q=Q1+Q2*1i;
EA=sqrt((1.0./VP).^2+P.^2-Q.^2);
EB=sqrt((1.0./VS).^2+P.^2-Q.^2);
GAMA=EB.^2+P.^2-Q.^2;
```

```
CT=cos(PHI);
ST=sin(PHI);
CT2=CT.^2;
ST2=ST.^2;
CT4=CT2.^2;
ST4=ST2.^2;
% Referring to Eq. (4.25-4.26)
switch index
   case 1111
      N=-(EB.^2.*GAMA.*(Q.^2.*CT2-P.^2.*ST2)+(-GAMA+4.*EA.*EB).*...
         ((Q.^4+P.^4+4.*P.^2.*Q.^2).*ST2.*CT2-P.^2.*Q.^2.*(ST4+CT4))./EB;
   case 1121
      N=-(EB.^2.*GAMA.*(Q.^2+P.^2)+(-GAMA+4.*EA.*EB).*...
         ((Q.^4.*ST2+3*P.^2.*Q.^2.*(ST2-CT2)-P.^4.*CT2)).*ST.*CT)./EB;
   case 1131
      N=-(EB.^2.*GAMA+(-GAMA+4.*EA.*EB).*(Q.^2.*ST2-
P.^2.*CT2+2.*P.^2.*ST2)).*Q.*CT;

   case 1211
      N=-(GAMA-4.*EA.*EB).*(Q.^4.*CT2+3*P.^2.*Q.^2.*(-ST2+CT2)-
P.^4.*ST2).*ST.*CT./EB;
   case 1221
      N=-(GAMA-4.*EA.*EB).*((Q.^2.*CT2-P.^2.*ST2).*(Q.^2.*ST2-
P.^2.*CT2)+4.*P.^2.*Q.^2.*ST2.*CT2)./EB;
   case 1231
      N=-(GAMA-4.*EA.*EB).*(Q.^2.*CT2-P.^2.*ST2+2.*P.^2.*CT2).*Q.*ST;
   case 1311
      N=GAMA.*(Q.^2.*CT2-3.*P.^2.*ST2).*Q.*CT;
   case 1321
      N=GAMA.*(Q.^2.*CT2-P.^2.*ST2+2.*P.^2.*CT2).*Q.*ST;
   case 1331
      N=EB.*GAMA.*(Q.^2.*CT2-P.^2.*ST2);

   case 2112
      N=-(GAMA-4.*EA.*EB).*((Q.^2.*CT2-P.^2.*ST2).*(Q.^2.*ST2-
P.^2.*CT2)+4.*P.^2.*Q.^2.*ST2.*CT2)./EB;
   case 2122
      N=-(GAMA-4.*EA.*EB).*(Q.^4.*ST2+3*P.^2.*Q^2.*(ST2-CT2)-
P.^4.*CT2).*ST.*CT./EB;
   case 2132
      N=-(-GAMA+4.*EA.*EB).*(Q.^2.*ST2-P.^2.*CT2+2.*P.^2.*ST2).*Q.*CT;
   case 2212
      N=-(EB.^2.*GAMA.*(Q.^2+P.^2)+(-GAMA+4.*EA.*EB).*...
         ((Q.^4.*CT2+3*P.^2.*Q^2.*(CT2-ST2)-P.^4.*ST2)).*ST.*CT)./EB;
   case 2222
      N=-(EB.^2.*GAMA.*(Q.^2.*ST2-P.^2.*CT2)+(-GAMA+4.*EA.*EB).*...
```

```
        ((Q.^4+P.^4+4.*P.^2.*Q.^2).*ST2.*CT2-P.^2.*Q.^2.*(ST4+CT4))./EB;
   case 2232
      N=-(EB.^2.*GAMA+(-GAMA+4.*EA.*EB).*...
        (Q.^2.*CT2-P.^2.*ST2+2.*P.^2.*CT2)).*Q.*ST;
   case 2312
      N=GAMA.*(Q.^2.*ST2-P.^2.*CT2+2.*P.^2.*ST2).*Q.*CT;
   case 2322
      N=GAMA.*(Q.^2.*ST2-3.*P.^2.*CT2).*Q.*ST;
   case 2332
      N=EB.*GAMA.*(Q.^2.*ST2-P.^2.*CT2);
end

SIG=(EB.^2+P.^2-Q.^2).^2+4.0*EA.*EB.*(Q.^2-P.^2);
f=real(EB.*N./SIG);

% Function  Fun_ND_DB
function  f=FUN_ND_DB(P,VP,VS,ST,CT,TR,PHI,index)
SB=sqrt(abs(TR.^2-(1.0/VS).^2-P.^2));
 HH=sqrt(TR.^2-(1.0/VS).^2-P.^2);
Q1=-TR.*ST;
Q2=SB.*CT;
Q=Q1+Q2;
EA=sqrt((1.0./VP).^2+P.^2-Q.^2);
EB=sqrt((1.0./VS).^2+P.^2-Q.^2);
GAMA=EB.^2+P.^2-Q.^2;

CT=cos(PHI);
ST=sin(PHI);
CT2=CT.^2;
ST2=ST.^2;
CT4=CT2.^2;
ST4=ST2.^2;
% Referring to Eq. (4.25-4.26)
switch index
   case 1111
      N=-(EB.^2.*GAMA.*(Q.^2.*CT2-P.^2.*ST2)+(-GAMA+4.*EA.*EB).*...
        ((Q.^4+P.^4+4.*P.^2.*Q.^2).*ST2.*CT2-P.^2.*Q.^2.*(ST4+CT4))./EB;
   case 1121
      N=-(EB.^2.*GAMA.*(Q.^2+P.^2)+(-GAMA+4.*EA.*EB).*...
        ((Q.^4.*ST2+3*P.^2.*Q.^2.*(ST2-CT2)-P.^4.*CT2)).*ST.*CT)./EB;
   case 1131
      N=-(EB.^2.*GAMA+(-GAMA+4.*EA.*EB).*(Q.^2.*ST2-
P.^2.*CT2+2.*P.^2.*ST2)).*Q.*CT;

   case 1211
```

```
      N=-(GAMA-4.*EA.*EB).*(Q.^4.*CT2+3*P.^2.*Q.^2.*(-ST2+CT2)-
P.^4.*ST2).*ST.*CT./EB;
   case 1221
      N=-(GAMA-4.*EA.*EB).*((Q.^2.*CT2-P.^2.*ST2).*(Q.^2.*ST2-
P.^2.*CT2)+4.*P.^2.*Q.^2.*ST2.*CT2)./EB;
   case 1231
      N=-(GAMA-4.*EA.*EB).*(Q.^2.*CT2-P.^2.*ST2+2.*P.^2.*CT2).*Q.*ST;
   case 1311
      N=GAMA.*(Q.^2.*CT2-3.*P.^2.*ST2).*Q.*CT;
   case 1321
      N=GAMA.*(Q.^2.*CT2-P.^2.*ST2+2.*P.^2.*CT2).*Q.*ST;
   case 1331
      N=EB.*GAMA.*(Q.^2.*CT2-P.^2.*ST2);

   case 2112
      N=-(GAMA-4.*EA.*EB).*((Q.^2.*CT2-P.^2.*ST2).*(Q.^2.*ST2-
P.^2.*CT2)+4.*P.^2.*Q.^2.*ST2.*CT2)./EB;
   case 2122
      N=-(GAMA-4.*EA.*EB).*(Q.^4.*ST2+3*P.^2.*Q^2.*(ST2-CT2)-
P.^4.*CT2).*ST.*CT./EB;
   case 2132
      N=-(-GAMA+4.*EA.*EB).*(Q.^2.*ST2-P.^2.*CT2+2.*P.^2.*ST2).*Q.*CT;
   case 2212
      N=-(EB.^2.*GAMA.*(Q.^2+P.^2)+(-GAMA+4.*EA.*EB).*...
         ((Q.^4.*CT2+3*P.^2.*Q^2.*(CT2-ST2)-P.^4.*ST2)).*ST.*CT)./EB;
   case 2222
      N=-(EB.^2.*GAMA.*(Q.^2.*ST2-P.^2.*CT2)+(-GAMA+4.*EA.*EB).*...
         ((Q.^4+P.^4+4.*P.^2.*Q.^2).*ST2.*CT2-P.^2.*Q.^2.*(ST4+CT4))).*EB;
   case 2232
      N=-(EB.^2.*GAMA+(-GAMA+4.*EA.*EB).*...
         (Q.^2.*CT2-P.^2.*ST2+2.*P.^2.*CT2)).*Q.*ST;
   case 2312
      N=GAMA.*(Q.^2.*ST2-P.^2.*CT2+2.*P.^2.*ST2).*Q.*CT;
   case 2322
      N=GAMA.*(Q.^2.*ST2-3.*P.^2.*CT2).*Q.*ST;
   case 2332
      N=EB.*GAMA.*(Q.^2.*ST2-P.^2.*CT2);
end

SIG=(EB.^2+P.^2-Q.^2).^2+4.0*EA.*EB.*(Q.^2-P.^2);
f=real(EB.*N./SIG./HH);

% Function  Fun_ND2_DB
function  f=FUN_ND2_DB(PP,VP,VS,ST,CT,TR,PHI,index)
P=1./cos(PP).*sqrt(abs(TR.^2-(1.0/VS).^2));
SB=sqrt(abs(TR.^2-(1.0/VS).^2-P.^2));
```

```
HH=1i.*sqrt(abs(TR.^2-(1.0/VS).^2-P.^2));
Q1=-TR.*ST;
Q2=SB.*CT;
Q=Q1+Q2;
EA=sqrt((1.0./VP).^2+P.^2-Q.^2);
EB=sqrt((1.0./VS).^2+P.^2-Q.^2);
GAMA=EB.^2+P.^2-Q.^2;
CT=cos(PHI);
ST=sin(PHI);
CT2=CT.^2;
ST2=ST.^2;
CT4=CT2.^2;
ST4=ST2.^2;

% Referring to Eq. (4.25-4.26)
switch index
   case 1111
      N=-(EB.^2.*GAMA.*(Q.^2.*CT2-P.^2.*ST2)+(-GAMA+4.*EA.*EB).*...
         ((Q.^4+P.^4+4.*P.^2.*Q.^2).*ST2.*CT2-P.^2.*Q.^2.*(ST4+CT4))./EB;
   case 1121
      N=-(EB.^2.*GAMA.*(Q.^2+P.^2)+(-GAMA+4.*EA.*EB).*...
         ((Q.^4.*ST2+3*P.^2.*Q.^2.*(ST2-CT2)-P.^4.*CT2)).*ST.*CT)./EB;
   case 1131
      N=-(EB.^2.*GAMA+(-GAMA+4.*EA.*EB).*(Q.^2.*ST2-
P.^2.*CT2+2.*P.^2.*ST2)).*Q.*CT;

   case 1211
      N=-(GAMA-4.*EA.*EB).*(Q.^4.*CT2+3*P.^2.*Q.^2.*(-ST2+CT2)-
P.^4.*ST2).*ST.*CT./EB;
   case 1221
      N=-(GAMA-4.*EA.*EB).*((Q.^2.*CT2-P.^2.*ST2).*(Q.^2.*ST2-
P.^2.*CT2)+4.*P.^2.*Q.^2.*ST2.*CT2)./EB;
   case 1231
      N=-(GAMA-4.*EA.*EB).*(Q.^2.*CT2-P.^2.*ST2+2.*P.^2.*CT2).*Q.*ST;
   case 1311
      N=GAMA.*(Q.^2.*CT2-3.*P.^2.*ST2).*Q.*CT;
   case 1321
      N=GAMA.*(Q.^2.*CT2-P.^2.*ST2+2.*P.^2.*CT2).*Q.*ST;
   case 1331
      N=EB.*GAMA.*(Q.^2.*CT2-P.^2.*ST2);

   case 2112
      N=-(GAMA-4.*EA.*EB).*((Q.^2.*CT2-P.^2.*ST2).*(Q.^2.*ST2-
P.^2.*CT2)+4.*P.^2.*Q.^2.*ST2.*CT2)./EB;
   case 2122
```

```
        N=-(GAMA-4.*EA.*EB).*(Q.^4.*ST2+3*P.^2.*Q^2.*(ST2-CT2)-
P.^4.*CT2).*ST.*CT./EB;
    case 2132
        N=-(-GAMA+4.*EA.*EB).*(Q.^2.*ST2-P.^2.*CT2+2.*P.^2.*ST2).*Q.*CT;
    case 2212
        N=-(EB.^2.*GAMA.*(Q.^2+P.^2)+(-GAMA+4.*EA.*EB).*...
            ((Q.^4.*CT2+3*P.^2.*Q^2.*(CT2-ST2)-P.^4.*ST2)).*ST.*CT)./EB;
    case 2222
        N=-(EB.^2.*GAMA.*(Q.^2.*ST2-P.^2.*CT2)+(-GAMA+4.*EA.*EB).*...
            ((Q.^4+P.^4+4.*P.^2.*Q.^2).*ST2.*CT2-P.^2.*Q.^2.*(ST4+CT4))).*/EB;
    case 2232
        N=-(EB.^2.*GAMA+(-GAMA+4.*EA.*EB).*...
            (Q.^2.*CT2-P.^2.*ST2+2.*P.^2.*CT2)).*Q.*ST;
    case 2312
        N=GAMA.*(Q.^2.*ST2-P.^2.*CT2+2.*P.^2.*ST2).*Q.*CT;
    case 2322
        N=GAMA.*(Q.^2.*ST2-3.*P.^2.*CT2).*Q.*ST;
    case 2332
        N=EB.*GAMA.*(Q.^2.*ST2-P.^2.*CT2);
end
SIG=(EB.^2+P.^2-Q.^2).^2+4.0*EA.*EB.*(Q.^2-P.^2);
f=real(EB.*N./SIG./1i./cos(PP));

% Source function
function EpsiConv=ConvWithSour(Epsi,fs)
% This function is to perform convolution of source mechanism (force) and spatial
derivative of Green's function
b=1; % Final crack opening
DT=1/fs;   % Sampling time interval
s=1;   %Final crack surface area, b × s is the crack volume
Rt=2e-6;     % Rise time of source-force: 2 μs
nt=Rt/DT;    % Number of time points during force rising
t=DT*(1:nt); % Time points
st1=(sin(pi*t/(nt*DT))).^4; % Source mechanism
NT=length(Epsi);            % Time points to be calculated
st2=zeros(NT-nt,1);    % Zero padding for the source force time history
st=[st1 st2'];         % Entire source kinematics (time history)
EpsiConv=conv(u1,st'); % Convolution of spatial derivative of Green's function and
source function
EpsiConv=EpsiConv(1:NT); % Truncation at NT
EpsiConv=EpsiConv.*b.*s*DT; % Multiply by crack volume
```

Bibliography

Aggelis, D.G., Barkoula, N.M., Matikas, T.E., and Paipetis, A.S. (2010). Acoustic emission monitoring of degradation of cross ply laminates. The Journal of the Acoustical Society of America *127*, EL246-51.

Aki, K. (1981). A probabilistic synthesis of precursory phenomena. In Maurice Ewing Series, W. Simpson, and G. Richards, eds. (Washington, D. C.: American Geophysical Union), pp. 566–574.

Aki, K., and Richards, P.G. (2002). Quantitative Seismology: Theory and Methods (University Science Books).

Anastassopoulos, A.A., and Philippidis, T.P. (1995). Clustering methodologies for the evaluation of AE from composites. Journal of Acoustic Emission *13*, 11–21.

ASTM (2005). ASTM E1316-05 Standard Terminology for Nondestructive Testing (ASTM International).

ASTM (2007). Standard Method for Primary Calibration of Acoustic Emission Sensors, E1106-07 (Philadelphia, Pennsylvania: ASTM International).

Berkovits, A., and Fang, D. (1995). Study of fatigue crack characteristics by acoustic emission. Engineering Fracture Mechanics *51*, 401–416.

Bourchak, M., Farrow, I., Bond, I., Rowland, C., and Menan, F. (2007). Acoustic emission energy as a fatigue damage parameter for CFRP composites. International Journal of Fatigue *29*, 457–470.

Ciampa, F., and Meo, M. (2010). Acoustic emission source localization and velocity determination of the fundamental mode A0 using wavelet analysis and a Newton-based optimization technique. Smart Materials and Structures *19*, 045027.

Colombo, I.S., Main, I.G., and Forde, M.C. (2003). Assessing damage of reinforced concrete beam using "b-value" analysis of acoustic emission signals. Journal of Materials in Civil Engineering *15*, 280–286.

Crawley, E.F. (1994). Intelligent structures for aerospace - a technology overview and assessment. AIAA Journal *32*, 1689–1699.

Dahlen, F.A., and Tromp, J. (1998). Theoretical Global Seismology (Princeton University Press).

Dahm, T. (1993). Relativmethoden zur Bestimmung der Abstrahlcharakteristik von seismischen Quellen. Doctoral thesis. University of Karlsruhe.

Dexter, R.J., and Ricker, M.J. (2002). Fatigue-resistant design of cantilevered signal, sign, and light supports (Transportation Research Board).

Egusa, S., and Iwasawa, N. (1998). Piezoelectric paints as one approach to smart structural materials with health-monitoring capabilities. Smart Materials and Structures *7*, 438–445.

Fortunko, C.M., Hamstad, M.A., and Fitting, D.W. (1992). High-fidelity acoustic-emission sensor/preamplifier subsystems: modeling and experiments. In Ultrasonics Symposium, 1992. Proceedings, IEEE 1992, 327–332.

Greenspan, M. (1987). The NBS conical transducer: Analysis. The Journal of the Acoustical Society of America *81*, 173–183.

Grosse, C.U. (1996). Quantitative zerstörungsfreie Prüfung von Baustoffen mittels Schallemissions-Analyse und Ultraschall. Doctoral thesis. Universität Stuttgart.

Grosse, C.U., and Ohtsu, M. (2008). Acoustic Emission Testing: Basics for Research - Applications in Civil Engineering (Springer).

Grosse, C.U., Reinhardt, H.W., and Finck, F. (2003). Signal-based acoustic emission techniques in civil engineering. Journal of Materials in Civil Engineering *15*, 274–279.

Gu, X., Sung, L., Ho, D.L., Michaels, C.A., Nguyen, D., Jean, Y.C., and Nguyen, T. (2002). Surface and interface properties of PVDF/Acrylic copolymer blends before and after UV exposure. In Proceedings International Coating Technology Conference.

Gutenberg, B., and Richter, C.F. (1954). Seismicity of the Earth and Associated Phenomenon (Princeton University Press).

Han, Z., Luo, H., Cao, J., and Wang, H. (2011). Acoustic emission during fatigue crack propagation in a micro-alloyed steel and welds. Materials Science and Engineering: A *528*, 7751–7756.

Harris, D.O., and Bell, R.L. (1977). The measurement and significance of energy in acoustic-emission testing. Experimental Mechanics *17*, 347–353.

Harsanyi, G. (2010). Sensors in biomedical applications: fundamentals, technology and applications (CRC Press).

Hirata, T. (1989). A correlation between the b value and the fractal dimension of earthquakes. Journal of Geophysical Research: Solid Earth *94*, 7507–7514.

Holford, K.M., Davies, A.W., Pullin, R., and Carter, D.C. (2001). Damage location in steel bridges by acoustic emission. Journal of Intelligent Material Systems and Structures *12*, 567–576.

De Hoop, A.T. (1960). A modification of cagniard's method for solving seismic pulse problems. Applied Scientific Research, Section B *8*, 349–356.

De Hoop, A.T. (1961). Theoretical determination of the surface motion of a uniform elastic half-space produced by a dilational, impulsive, point source. In Proceedings of Colloque International C.N.R.S., pp. 21–32.

Hsu, N.N. (1985). Dynamic Green's functions of an infinite plate: a computer program (U.S. Department of Commerce, National Bureau of Standards).

Ihn, J.-B., and Chang, F.-K. (2004). Detection and monitoring of hidden fatigue crack growth using a built-in piezoelectric sensor/actuator network: II. Validation using riveted joints and repair patches. Smart Materials and Structures *13*, 621.

JCMS-IIIB5706 (2003). Monitoring method for active cracks in concrete by acoustic emission. In Japan Construction Material Standards (Japan: The Federation of Construction Material Industries).

Johnson, L.R. (1974). Green's function for Lamb's problem. Geophysical Journal of the Royal Astronomical Society *37*, 99–131.

Kawai, H. (1969). The piezoelectricity of poly (vinylidene Fluoride). Japanese Journal of Applied Physics *8*, 975–976.

Kawasaki, I., Suzuki, Y., and Sato, R. (1972a). Seismic waves due to double couple source in a semi-infinite space. Zisin *25*, 207–217.

Kawasaki, I., Suzuki, Y., and Sato, R. (1972b). Seismic waves due to double couple source in a semi-infinite space. Zisin *25*, 333–342.

Kim, Y.H., and Kim, H.C. (1993). Source function determination of glass capillary breaks. Journal of Physics D: Applied Physics *26*, 253–258.

Kinsler, L.E., Frey, A.R., Coppens, A.B., and Sanders, J.V. (1999). Fundamentals of Acoustics (Wiley).

Kobayashi, M., Olding, T.., Sayer, M., and Jen, C.-K. (2002). Piezoelectric thick film ultrasonic transducers fabricated by a sol–gel spray technique. Ultrasonics *39*, 675–680.

Kobayashi, M., Jen, C.-K., Moisan, J.-F., Mrad, N., and Nguyen, S.B. (2007). Integrated ultrasonic transducers made by the sol–gel spray technique for structural health monitoring. Smart Materials and Structures *16*, 317.

Kosnik, D.E. (2009). Acoustic emission testing of a difficult-to-reach steel bridge detail. Journal of Acoustic Emission *29*, 11–17.

Lamb, H. (1904). On the propagation of tremors over the surface of an elastic solid. Philosophical Transactions of the Royal Society of London. Series A, Containing Papers of a Mathematical or Physical Character *203*, 1–42.

Landis, E.N., and Baillon, L. (2002). Experiments to relate acoustic emission energy to fracture energy of concrete. Journal of Engineering Mechanics *128*, 698–702.

Lay, T., and Wallace, T.C. (1995). Modern Global Seismology (Academic Press).

Lee, C.-K., and O'Sullivan, T.C. (1991). Piezoelectric strain rate gages. The Journal of the Acoustical Society of America *90*, 945–953.

Li, X. (2009). Electroelastic properties of piezoelectric paint for ultrasonic guided wave sensing and damage detection. Doctoral thesis. Lehigh University.

Li, Z. (2013). Fatigue test and prognosis study of welded tubular joints in signal support structures. Doctoral thesis. University of Maryland, College Park.

Li, X., and Zhang, Y. (2008). Analytical study of piezoelectric paint sensor for acoustic emission-based fracture monitoring. Fatigue & Fracture of Engineering Materials & Structures *31*, 684–694.

Liu, S.C., Chong, K.P., and Singh, M.P. (1995). Civil infrastructure systems research: hazard mitigation and intelligent material systems. Smart Materials and Structures *4*, A169–A174.

Maji, A.K., and Satpathi, D. (1995). Acoustic emission source location based on lamb waves. In Proceedings of Engineering Mechanics, pp. 597–600.

McKeefry, J.A., and Shield, C.K. (1999). Acoustic Emission Monitoring of Fatigue Cracks in Steel Bridge Girders.

Miller, R.K. (1987). Nondestructive Testing Handbook: Volume 5 Acoustic Emission Testing (American Society for Nondestructive).

Mogi, K. (1962). On the time distribution of aftershocks accompanying the recent major earthquakes in and near Japan. Bulletin of the Earthquake Research Institute, University of Tokyo *40*, 107–124.

Mohan, R., and Prathap, G. (1980). An acoustic emission energy analysis and its use to study damage in laminated composites. Journal of Nondestructive Evaluation *1*, 225–233.

Mooney, H.M. (1974). Some numerical solutions for Lamb's problem. Bulletin of the Seismological Society of America *64*, 473–491.

Ocel, J.M., Dexter, R.J., and Hajjar, J.F. (2006). Fatigue-resistant design for overhead signs, mast-arm signal poles, and lighting standards.

Ohtsu, M. (1995). Acoustic emission theory for moment tensor analysis. Research in Nondestructive Evaluation *6*, 169–184.

Ohtsu, M., and Tomoda, Y. (2008). Phenomenological model of corrosion process in reinforced concrete identified by acoustic emission. ACI Materials Journal *105*, 194-199.

Ono, K., and Ohtsu, M. (1984). A generalized theory of acoustic emission and Green's functions in a half space. Journal of Acoustic Emission *3*, 27–40.

Pao, Y.-H., Gajewski, R.R., and Ceranoglu, A.N. (1979). Acoustic emission and transient waves in an elastic plate. The Journal of the Acoustical Society of America *65*, 96–105.

Park, S., Yun, C.-B., Roh, Y., and Lee, J.-J. (2006). PZT-based active damage detection techniques for steel bridge components. Smart Materials and Structures *15*, 957–966.

Pekeris, C. (1955a). The seismic surface pulse. Proceedings of the National Academy of Sciences of the United States of America *41*, 629–639.

Pekeris, C. (1955b). The seismic buried pulse. Proceedings of the National Academy of Sciences of the United States of America *41*, 629–639.

Pinney, E. (1954). Surface motion due to a point source in a semi-infinite elastic medium. Bulletin of the Seismological Society of America *44*, 571–596.

Proctor, T.M. (1982). An improved piezoelectric acoustic emission transducer. The Journal of the Acoustical Society of America *71*, 1163–1168.

Rao, M., and Lakshmi, K.P. (2005). Analysis of b-value and improved b-value of acoustic emissions accompanying rock fracture. Current Science *89*, 1577-1582.

Ren, S.-C., Hsu, N.N., and Eitzen, D.G. (2002). Transient Green's tensor for a layered solid half-space with different interface conditions. Journal of Research of the National Institute of Standards and Technology *107*, 445–473.

Roberts, T.M., and Talebzadeh, M. (2003a). Acoustic emission monitoring of fatigue crack propagation. Journal of Constructional Steel Research *59*, 695–712.

Roberts, T.M., and Talebzadeh, M. (2003b). Fatigue life prediction based on crack propagation and acoustic emission count rates. Journal of Constructional Steel Research *59*, 679–694.

Sakamoto, W.K., Marin-Franch, P., Tunnicliffe, D., and Das-Gupta, D.K. (2001). Lead zirconate titanate/polyurethane (PZT/PU) composite for acoustic emission sensors. In Conference on Electrical Insulation and Dielectric Phenomena, 2001 Annual Report, pp. 20–23.

Sause, M.G.R. (2011). Investigation of pencil-lead breaks as acoustic emission sources. Journal of Acoustic Emission *29*, 184–196.

Shi, Z., Jarzynski, J., Bair, S., Hurlebaus, S., and Jacobs, L.J. (2000). Characterization of acoustic emission signals from fatigue fracture. In Proceedings of the Institution of Mechanical Engineers, Part C: Journal of Mechanical Engineering Science *214*, 1141.

Shiotani, T., Fujii, K., Aoki, T., and Amou, K. (1994). Evaluation of progressive failure using AE sources and improved b-value on slope model test. Progress in Acoustic Emission VII *7*, 529–534.

Shiotani, T., Ohtsu, M., and Ikeda, K. (2001). Detection and evaluation of AE waves due to rock deformation. Construction and Building Materials *15*, 235–246.

Shiotani, T., Luo, X., Haya, H., and Ohtsu, M. (2007). Damage quantification for concrete structures by improved b-value analysis of AE. Earthquakes and Acoustic Emission *1*, 181–186.

Sirohi, J., and Chopra, I. (2000). Fundamental understanding of piezoelectric strain sensors. Journal of Intelligent Material Systems and Structures *11*, 246–257.

Soulioti, D., Barkoula, N.M., Paipetis, A., Matikas, T.E., Shiotani, T., and Aggelis, D.G. (2009). Acoustic emission behavior of steel fibre reinforced concrete under bending. Construction and Building Materials *23*, 3532–3536.

Spanner, J.C. (1974). Acoustic Emission Techniques and Applications (Intex Publishing Co.).

Talebzadeh, M., and Roberts, T.M. (2001). Correlation of crack propagation and acoustic emission rates. Key Engineering Materials *204-205*, 341–350.

Vahaviolos, S.J. (1999). Acoustic Emission: Standards and Technology Update (ASTM International).

Wang, D., Liu, J., Zhou, D., and Huang, S. (1999). Using PVDF piezoelectric film sensors for in situ measurement of stayed-cable tension of cable-stayed bridges. Smart Materials and Structures *8*, 554–559.

Watanabe, T., Nishibata, S., Hashimoto, C., and Ohtsu, M. (2007). Compressive failure in concrete of recycled aggregate by acoustic emission. Construction and Building Materials *21*, 470–476.

Weiler, B. (2000). Zerstörungsfreie Untersuchung von Stahlfaserbeton (Shaker).

Weiss, J. (1997). The role of attenuation on acoustic emission amplitude distributions and b-values. Bulletin of the Seismological Society of America *87*, 1362–1367.

Wenger, M.P., Blanas, P., Shuford, R.J., and Das-Gupta, D.K. (1996). Acoustic emission signal detection by ceramic/polymer composite piezoelectrets embedded in glass-epoxy laminates. Polymer Engineering & Science *36*, 2945–2954.

Wenger, M.P., Almeida, P.L., Das-Gupta, D.K., Blanas, P., and Shuford, R.J. (1999a). The ferroelectric properties of piezoelectric ceramic/polymer composites for acoustic emission sensors. Polymer Engineering & Science *39*, 483–492.

Wenger, M.P., Blanas, P., Shuford, R.J., and Das-Gupta, D.K. (1999b). Characterization and evaluation of piezoelectric composite bimorphs for in-situ acoustic emission sensors. Polymer Engineering & Science *39*, 508–518.

Willis, J.R. (1973). Self-Similar problems in elastodynamics. Philosophical Transactions of the Royal Society of London A *274*, 435–491.

Yu, J., and Ziehl, P. (2012). Stable and unstable fatigue prediction for A572 structural steel using acoustic emission. Journal of Constructional Steel Research *77*, 173–179.

Yu, J., Ziehl, P., Zárate, B., and Caicedo, J. (2011). Prediction of fatigue crack growth in steel bridge components using acoustic emission. Journal of Constructional Steel Research *67*, 1254–1260.

Yun, C.B., Sohn, H., Lee, J.J., Park, S., Wang, M.L., Zhang, Y.F., and Lynch, J.P. (2010). US-Korea collaborative research for bridge monitoring test beds (San Diego, California).

Yuyama, S., Imanaka, T., and Ohtsu, M. (1988). Quantitative evaluation of microfracture due to disbonding by waveform analysis of acoustic emission. The Journal of the Acoustical Society of America *83*, 976–983.

Zhang, Y., and Li, X. (2006). Piezoelectric Paint Sensor for Fatigue Crack Monitoring In Steel Structures. In Proceedings of US-Korea Workshop on Smart Structures Technology for Steel Structures (Seoul Korea).

Zhou, Y.E. (2006). Assessment of bridge remaining fatigue life through field strain measurement. Journal of Bridge Engineering *11*, 737–744.

Zhou, C., and Zhang, Y. (2012). Steel bridge fatigue crack monitoring with broadband thin-film AE sensors. In Proceedings of 6th International Conference on Bridge Maintenance, Safety and Management (Stresa, Lake Maggiore, Italy).

Zhou, Y.E., and Biegalski, A.E. (2010). Investigation of large web fractures of welded steel plate girder bridge. Journal of Bridge Engineering *15*, 373–383.

Ziola, S.M., and Gorman, M.R. (1991). Source location in thin plates using cross-correlation. The Journal of the Acoustical Society of America *90*, 2551–2556.